Biomedical implications from mathematical models for the simulation of dermal wound healing

Koppenol, Daniel

DOI
10.4233/uuid:cdc7392f-4ac6-404c-9615-dc425f67efae

Publication date
2017

Document Version
Final published version

Citation (APA)
Koppenol, D. (2017). *Biomedical implications from mathematical models for the simulation of dermal wound healing*. [Dissertation (TU Delft), Delft University of Technology]. https://doi.org/10.4233/uuid:cdc7392f-4ac6-404c-9615-dc425f67efae

BIOMEDICAL IMPLICATIONS FROM MATHEMATICAL MODELS FOR THE SIMULATION OF DERMAL WOUND HEALING

BIOMEDICAL IMPLICATIONS FROM MATHEMATICAL MODELS FOR THE SIMULATION OF DERMAL WOUND HEALING

Proefschrift

ter verkrijging van de graad van doctor
aan de Technische Universiteit Delft,
op gezag van de Rector Magnificus prof. ir. K.C.A.M. Luyben,
voorzitter van het College voor Promoties,
in het openbaar te verdedigen op donderdag 15 juni 2017 om 10:00 uur

door

Daniël Cornelis KOPPENOL

Master of Science in Brain and Cognitive Sciences, Universiteit van Amsterdam,
geboren te Capelle aan den IJssel.

Dit proefschrift is goedgekeurd door de

Promotor: Prof. dr. ir. C. Vuik
Promotor: Prof. dr. P.P.M. van Zuijlen
Copromotor: Dr. ir. F.J. Vermolen
Copromotor: Dr. F.B. Niessen

Samenstelling promotiecommissie:

Rector Magnificus,	voorzitter
Prof. dr. ir. C. Vuik,	Technische Universiteit Delft, promotor
Prof. dr. P.P.M. van Zuijlen,	Vrije Universiteit Amsterdam, promotor
Dr. ir. F.J. Vermolen,	Technische Universiteit Delft, copromotor
Dr. F.B. Niessen,	Vrije Universiteit Amsterdam, copromotor
Onafhankelijke leden:	
Prof. dr. J.M. Garcia Aznar,	Universidad de Zaragoza
Prof. dr. S. Gibbs,	Vrije Universiteit Amsterdam
Prof. dr. ir. A.W. Heemink,	Technische Universiteit Delft
Prof. dr. A. Madzvamuse,	University of Sussex
Prof. dr. ir. C.W. Oosterlee,	Technische Universiteit Delft, reservelid

The research in this dissertation was financed by the Dutch Burns Foundation.

Keywords: Dermal wound healing, Fibroblasts, Collagen bundles, Wound contraction, Hypertrophic scar tissue, Contracture formation, Biomechanics, neo-Hookean solid, Morphoelasticity, Sensitivity analysis, Moving-grid finite-element method, Element resolution adaptation, Flux-corrected transport limiter, Adaptive time-stepping

Printed by: ProefschriftMaken ‖ www.proefschriftmaken.nl

Front & Back: The cover was designed by J. Kühne and R.J. Koppenol, and is based on images that were generated by D.C. Koppenol.

Biomedical implications from mathematical models for the simulation of dermal wound healing
Dissertation at Delft University of Technology

ISBN 978-94-6295-661-2

An electronic version of this dissertation is available at
http://repository.tudelft.nl/.

There are some people who live in a dream world,
and there are some who face reality;
and then there are those who turn one into the other.

Desiderius Erasmus

SUMMARY

DERMAL wounds are a significant global problem; although the treatment of these wounds has improved considerably over the last few decades, a treatment still does not result in a complete regeneration of the injured tissue. Instead, the final outcome of the healing process is scar tissue. The material properties of scar tissue are different from the material properties of uninjured dermal tissue and, therefore, the presence of scar tissue might result in complications such as a restriction in the movement of the affected skin. Subsequently, this might cause, for instance, a reduction in the radius of movement of a limb that is covered by this scar tissue.

In addition, the restoration of dermal wounds also gets perturbed many times during the initial period post-wounding and this might result in the development of, for instance, contractures and hypertrophic scar tissue. Unfortunately, the causal pathways that lead to the formation of contractures and hypertrophic scar tissue are unknown at present. Furthermore, even in the absence of complications, it is very difficult to influence the material properties of developing scar tissue. A better understanding of the mechanisms underlying the (aberrant) healing of dermal wounds will probably improve the treatment of dermal wounds, and will, consequently, reduce the probability of the occurrence of sequelae, such that the newly generated tissue in a recovered wounded area is more akin to the original tissue. Therefore, a lot of resources have been allocated to research the mechanisms with *in vivo* and *in vitro* experiments. This has resulted in the production of much knowledge about these mechanisms. However, there is still much that remains understood incompletely. This is partly due to the intrinsic complexity of the wound healing process, but it is also a consequence of the fact that it is very difficult to study the interactions between different components of the wound healing cascade with experimental studies.

A way to deal with this latter issue, is to use mathematical models. With these models it is possible to simulate components of the wound healing cascade and to investigate the interactions between these components. The results obtained with these models might aid in disentangling which components of the wound healing cascade influence the material properties of the scar tissue. Furthermore, these results might aid in providing insights into which components of the wound healing response are disrupted during the formation of contractures and hypertrophic scar tissue. For these reasons several mathematical models were developed during this investigation.

In Chapter 3 a hybrid model is presented that was used to study wound contraction and the development of the distribution of the collagen bundles in relatively small, deep dermal wounds. In this model cells are modeled as discrete, inelastic spheres while the other components are modeled as continuous entities. After obtaining baseline simulation results, the impact of macrophage depletion and the application of a transforming growth factor-β receptor antagonist on both the degree of wound contraction and overall distribution of the collagen bundles were investigated. Depletion of the macrophages

during the execution of the wound healing cascade results in a delayed healing of a wound. Furthermore, the depletion of the macrophages hardly influences the geometrical distribution of the collagen bundles in the recovering wounded area. However, the depletion does result in an increase of the final surface area of the recovered wounded area. The imitation of the application of a transforming growth factor-β receptor antagonist also results in an increase of the surface area of the recovering wounded area. In addition, the application of the antagonist results in a more uniform distribution of the collagen bundles in the recovered wounded area.

In Chapter 4 a continuum hypothesis-based model is presented that was used to investigate how certain components of the wound environment and the wound healing response might influence the contraction of the wound and the development of the geometrical distribution of collagen bundles in relatively large wounds. In this model all components are modeled as continuous entities. The dermis is modeled as an orthotropic continuous solid with bulk mechanical properties that are locally dependent on both the local concentration and the local geometrical distribution of the collagen bundles. The simulation results show that the distribution of the collagen bundles influences the evolution over time of both the shape of the recovering wounded area and the degree of overall contraction of the wounded area. Interestingly, these effects are solely a consequence of alterations in the initial overall distribution of the collagen bundles, and not a consequence of alterations in the evolution over time of the different cell densities and concentrations of the modeled constituents. In addition, the evolution over time of the shape of the wound is also influenced by the orientation of the collagen bundles relative to the wound while this relative orientation does not influence the evolution over time of the relative surface area of the wound. Furthermore, the simulation results show that ultimately the majority of the collagen molecules ends up permanently oriented toward the center of the wound and in the plane that runs parallel to the surface of the skin when the dependence of the direction of deposition / reorientation of collagen molecules on the direction of movement of cells is included into the model. If this dependence is not included, then this will result ultimately in newly generated tissue with a collagen bundle-distribution that is exactly equal to the collagen-bundle distribution of the surrounding uninjured tissue.

In Chapter 5 a continuum hypothesis-based model is presented that was used to investigate in more detail which elements of the healing response might have a substantial influence on the contraction of burns. That is, a factorial design combined with a regression analysis were used to quantify the individual contributions of variations in the values for certain parameters of the model to the dispersion in the surface area of healing burns. Solely a portion of the dermal layer was included explicitly into the model. The dermal layer is modeled as an isotropic compressible neo-Hookean solid. Wound contraction is caused in the model by temporary pulling forces. These pulling forces are generated by myofibroblasts which are present in the recovering wounded area. Based on the outcomes of the sensitivity analysis it was concluded that most of the variability in the evolution of the surface area of healing burns over time might be attributed to variability in the apoptosis rate of myofibroblasts and, to a lesser extent, the secretion rate of collagen molecules.

In Chapter 6 a continuum hypothesis-based model is presented that was used to investigate what might cause the formation of hypertrophic scar tissue. All components of the model are modeled as continuous entities. Solely a portion of the dermal layer of the skin is modeled explicitly and this portion is modeled as an isotropic compressible neo-Hookean solid. In the model pulling forces are generated by the myofibroblasts that are present in the recovering wounded area. These pulling forces are responsible for both the compaction and the increased thickness of the recovering wounded area. A comparison between the outcomes of the computer simulations obtained in this study and clinical measurements shows that a relatively high apoptosis rate of myofibroblasts results in scar tissue that behaves like normal scar tissue with respect to the evolution of the thickness of the tissue over time, while a relatively low apoptosis rate results in scar tissue that behaves like hypertrophic scar tissue with respect to the evolution of the thickness of the tissue over time. Interestingly, this result is in agreement with the suggestion put forward that the disruption of apoptosis (i.e., a low apoptosis rate) during wound healing might be an important factor in the development of pathological scarring.

In Chapter 7 a continuum hypothesis-based model is presented that was used for the simulation of contracture formation in skin grafts that cover excised burns in order to obtain suggestions regarding the ideal length of splinting therapy and when to start with this therapy such that the therapy is effective optimally. All components of the model are modeled as continuous entities. Solely a portion of the dermal layer is modeled explicitly and this portion is modeled as an isotropic morphoelastic solid. In the model pulling forces are generated by the myofibroblasts which are present in the skin graft. These pulling forces are responsible for the compaction of the skin graft. Based on the simulation results obtained with the presented model it is suggested that the optimal point in time to start with splinting therapy is directly after placement of the skin graft on its recipient bed. Furthermore, the simulation results suggest that it is desirable to continue with splinting therapy until the concentration of the signaling molecules in the grafted area has become negligible such that the formation of contractures can be prevented.

SAMENVATTING

DERMALE wonden zijn een significant globaal probleem; alhoewel de behandeling van deze wonden de afgelopen decennia aanzienlijk verbeterd is, leidt een behandeling nog steeds niet tot een volledige regeneratie van het verwonde weefsel. In plaats daarvan is de uiteindelijke uitkomst van het genezingsproces littekenweefsel. De materiaaleigenschappen van littekenweefsel verschillen van de materiaaleigenschappen van onbeschadigd dermaal weefsel en zodoende kan de aanwezigheid van littekenweefsel leiden tot complicaties zoals een beperking in de beweegbaarheid van de aangedane huid. Vervolgens kan dit bijvoorbeeld leiden tot een afname in de bewegingsradius van een ledemaat die wordt bedekt door dit littekenweefsel.

Daarnaast raakt de genezing van dermale wonden ook vaak verstoord gedurende de initiële periode na verwonding, en dit kan leiden tot de ontwikkeling van bijvoorbeeld contracturen en hypertrofisch littekenweefsel. Helaas zijn de causale paden die leiden tot de ontwikkeling van contracturen en hypertrofisch littekenweefsel op dit moment niet bekend. Verder is het moeilijk, zelfs wanneer geen complicaties optreden, om de materiaaleigenschappen van ontwikkelend littekenweefsel te beïnvloeden. Een beter begrip van de mechanismen die ten grondslag liggen aan de (afwijkende) genezing van dermale wonden zal de behandeling van dermale wonden waarschijnlijk verbeteren, en zal zodoende de kans op het ontstaan van sequels verkleinen zodat het nieuw gegenereerde weefsel meer lijkt op het oorspronkelijke weefsel. Zodoende dat veel middelen zijn ingezet om deze mechanismen te onderzoeken met *in vivo* en *in vitro* experimenten. Dit heeft geresulteerd in de productie van veel kennis over deze mechanismen. Echter, er is nog steeds veel niet volledig bekend. Dit wordt gedeeltelijk veroorzaakt door de intrinsieke complexiteit van het wondgenezingsproces, maar het is ook een gevolg van het feit dat het erg moeilijk is om de interacties tussen verschillende componenten van het wondgenezingsproces te onderzoeken met behulp van experimenteel onderzoek.

Door gebruik te maken van wiskundige modellen kan met dit laatstgenoemde probleem omgegaan worden. Met deze modellen is het mogelijk om componenten van het wondgenezingsproces te simuleren en de interactie tussen deze componenten te onderzoeken. De resultaten die met deze modellen verkregen worden, kunnen wellicht helpen bij het ontrafelen van welke componenten van het wondgenezingsproces de materiaaleigenschappen van het littekenweefsel beïnvloeden. Verder kunnen deze resultaten wellicht helpen bij het verkrijgen van inzichten in welke componenten van het wondgenezingsproces verstoord raken gedurende de vorming van contracturen en hypertrofisch littekenweefsel. Om deze redenen zijn een aantal wiskundige modellen ontwikkeld gedurende dit onderzoek.

In Hoofdstuk 3 wordt een hybride model gepresenteerd dat is gebruikt om wondcontractie en de ontwikkeling van de distributie van de collageenbundels in relatief kleine, diepe dermale wonden te onderzoeken. In dit model worden cellen gemodelleerd als discrete, inelastische bollen terwijl de andere componenten worden gemodelleerd als

continue objecten. Nadat referentiesimulaties zijn verkregen, is de invloed onderzocht van decimatie van de macrofagen en de toepassing van een transforming growth factor-β receptor antagonist, op zowel de mate van wondcontractie als de distributie van de collageenbundels. Decimatie van de macrofagen gedurende de uitvoering van het wondgenezingsproces resulteert in een vertraagde genezing van een wond. Verder beïnvloedt de decimatie van de macrofagen de geometrische distributie van de collageenbundels in het herstellende wondgebied nauwlijks. Echter, de decimatie resulteert wel in een toename van het uiteindelijke oppervlak van het herstelde wondgebied. Het nabootsen van de toepassing van een transforming growth factor-β receptor antagonist leidt ook tot een toename van het oppervlak van het herstellende wondgebied. Daarnaast leidt de toepassing van de antagonist tot een meer uniforme verdeling van de collageenbundels in het herstelde wondgebied.

In Hoofdstuk 4 wordt een model dat is gebaseerd op de continuïteitsaanname, gepresenteerd dat is gebruikt om te onderzoeken hoe bepaalde componenten van de wondomgeving en het wondgenezingsproces de contractie van de wond en de ontwikkeling van de geometrische distributie van de collageenbundels in relatief grote wonden, wellicht beïnvloeden. In dit model worden alle componenten gemodelleerd als continue objecten. De dermis wordt gemodelleerd als een orthotroop, continu vast lichaam met bulk mechanische eigenschappen die lokaal afhankelijk zijn van zowel de lokale concentratie als de lokale geometrische distributie van de collageenbundels. De simulatieresultaten laten zien dat de distributie van de collageenbundels de evolutie over de tijd van zowel de vorm van het herstellende wondgebied als de mate van contractie van het wondgebied, beïnvloeden. Het is interessant om te observeren dat deze effecten enkel het gevolg zijn van veranderingen in de initiële, globale distributie van de collageenbundels, en niet een gevolg van veranderingen in de evolutie over de tijd van de celdichtheden en de concentraties van de gemodelleerde componenten. Daarnaast wordt de evolutie van de vorm van de wond over de tijd ook beïnvloed door de relatieve oriëntatie van de collageenbundels ten opzichte van de wond terwijl deze relatieve oriëntatie de evolutie over tijd van het relatieve wondoppervlak niet beïnvloedt. Bovendien laten de simulatieresultaten zien dat uiteindelijk het merendeel van de collageenmoleculen permanent georiënteerd ligt in de richting van het middelpunt van de wond en in het vlak dat evenwijdig loopt aan het huidoppervlak wanneer de richting van afzetting / reoriëntatie van collageenmoleculen afhankelijk is van de bewegingsrichting van cellen. Als deze afhankelijkheid niet wordt opgenomen in het model, dan leidt dit uiteindelijk tot nieuw gegenereerd weefsel met een collageenbundeldistributie die exact gelijk is aan de collageenbundeldistributie van het omringende ongedeerde weefsel.

In Hoofdstuk 5 wordt een model dat is gebaseerd op de continuïteitsaanname, gepresenteerd dat is gebruikt om gedetailleerder te onderzoeken welke elementen van het genezingsproces een substantiële invloed hebben op de contractie van brandwonden. Dat wil zeggen, een factorieel ontwerp in combinatie met een regressie analyse zijn gebruikt om de afzonderlijke contributies van variaties in de waardes van bepaalde parameters van het model op de dispersie in het oppervlak van genezende brandwonden te kwantificeren. Slechts een deel van de dermale laag is expliciet opgenomen in het model. De dermale laag wordt gemodelleerd als een isotroop, samendrukbaar neo-Hookeaans vast lichaam. Wondcontractie wordt veroorzaakt in het model door tijdelijke trekkrach-

ten. Deze trekkrachten worden gegenereerd door myofibroblasten die aanwezig zijn in het herstellende wondgebied. Op basis van de uitkomsten van de gevoeligheidsanalyse wordt er geconcludeerd dat het merendeel van de variatie in de evolutie van het oppervlak van genezende brandwonden over tijd wellicht toegeschreven kan worden aan variatie in de apoptosesnelheid van myofibroblasten, en in mindere mate de secretiesnelheid van collageenmoleculen.

In Hoofdstuk 6 wordt een model dat is gebaseerd op de continuïteitsaanname, gepresenteerd dat is gebruikt om te onderzoeken wat de vorming van hypertrofisch littekenweefsel wellicht veroorzaakt. Alle componenten van het model worden gemodelleerd als continue objecten. Slechts een deel van de dermale laag van de huid wordt expliciet gemodelleerd en dit deel wordt gemodelleerd als een isotroop, samendrukbaar neo-Hookeaans vast lichaam. In het model worden trekkrachten gegenereerd door de myofibroblasten die aanwezig zijn in het herstellende wondgebied. Deze trekkrachten zijn verantwoordelijk voor zowel de contractie als de toegenomen dikte van het herstellende wondgebied. Een vergelijking tussen de uitkomsten van de computersimulaties die zijn verkregen in deze studie, en klinische metingen laat zien dat een relatief hoge apoptosesnelheid van myofibroblasten resulteert in littekenweefsel dat zich gedraagt als normaal littekenweefsel met betrekking tot de evolutie van de dikte van het weefsel over de tijd, terwijl een relatief lage apoptosesnelheid resulteert in littekenweefsel dat zich gedraagt als hypertrofisch littekenweefsel met betrekking tot de evolutie van de dikte van het weefsel over de tijd. Het is interessant dat dit resultaat in overeenstemming is met de suggestie dat de ontregeling van apoptose (ofwel een lage apoptosesnelheid) gedurende wondgenezing wellicht een belangrijke rol speelt bij pathologische littekenvorming.

In Hoofdstuk 7 wordt een model dat is gebaseerd op de continuïteitsaanname, gepresenteerd dat is gebruikt voor de simulatie van contractuurvorming in huidtransplantaten die zijn geplaatst over uitgesneden brandwonden om zo aanwijzingen te verkrijgen met betrekking tot de ideale lengte en het ideale tijdstip om te starten met spalktherapie zodat de therapie optimaal effectief is. Alle componenten van het model worden gemodelleerd als continue objecten. Slechts een deel van de dermale laag wordt expliciet gemodelleerd en dit deel wordt gemodelleerd als een isotroop, morfoelastisch vast lichaam. In het model worden trekkrachten gegenereerd door de myofibroblasten die aanwezig zijn in het huidtransplantaat. Deze trekkrachten zijn verantwoordelijk voor de contractie van het huidtransplantaat. Op basis van de simulatieresultaten verkregen met het gepresenteerde model wordt er voorgesteld dat het ideale tijdstip om te starten met spalktherapie direct na de plaatsing van het huidtransplantaat is. Bovendien suggereren de simulatieresultaten dat het gewenst is om door te gaan met spalktherapie totdat de concentratie van de signaalmoleculen in het getranspanteerde gebied verwaarloosbaar klein is geworden zodat de vorming van contracturen voorkomen kan worden.

PREFACE

THIS dissertation completes four and half years of interdisciplinary research. The aim of the investigation was the development of mathematical models with which to obtain insights that might aid in disentangling which components of the wound healing cascade influence the contraction of wounds, the geometrical distribution of collagen bundles in scar tissue, and the formation of contractures and hypertrophic scar tissue. In my opinion, this investigation has generated various interesting insights that can contribute to the design of better treatment plans with which, for instance, the probability of contracture formation in skin grafts can be reduced. Furthermore, this investigation has shown me that much more is probably possible with mathematical models in an environment of close collaboration between experimental scientists, computational scientists and mathematicians.

It has been a very interesting and valuable experience for me to conduct this research. I learned a lot about the different subjects related to the investigation, and how to combine the obtained knowledge in order to create something new. In addition, I learned a lot about how to collaborate with researchers from different fields of research. Many people contributed (indirectly) to making this possible. Here, I would like to express my gratitude to them.

I thank the Dutch burns foundation for financing this investigation. I am very grateful to the foundation for providing the financial support that made it possible to conduct this research and to attend a number of international conferences.

I acknowledge my supervisory team consisting of Kees Vuik, Paul van Zuijlen, Fred Vermolen and Frank Niessen for their trust and for the opportunity to perform this research. In addition, I thank Paul and Frank for the opportunity to shadow them during their consulting hours. These visits provided me with new insights and were very inspiring to me. I thank Fred for teaching me some courses on numerical analysis and for the opportunities he has given me to present my work at conferences. Furthermore, I want to thank you, Fred, for the informal and friendly atmosphere you created during our meetings and for the conversations we have had over the years. These conversations have taught me a lot.

I would like to thank my colleague Neil for giving me the possibility to assist him during a few courses on calculus and linear algebra. I enjoyed teaching these subjects. Moreover, I really enjoyed our discussions about politics, literature and various research topics both during class and after class. Thank you also, Neil, for the many cups of coffee.

Furthermore, I would like to thank my colleagues Matthias and Dennis for making it possible to connect the element resolution refinement / recoarsement tool of the CFD software package `FEATFLOW2` with the kernel of the software package that has been developed during this investigation. Due to this interface the computation times were reduced tremendously. This really helped me a lot. Once more, thank you very much!

I want to thank Martijn and Rohit with whom I shared an office. I enjoyed our conversations about culture, food, movies and plants. Thank you also, Martijn, for all the plants you brought to the office. Their presence really helped with the creation of a cozy atmosphere. Furthermore, I wish to thank my colleagues Reinaldo, Manuel, Guido, Gabriela, Behrouz, Thea, Jing, Yue, Luis and Joost for the interesting conversations on various topics we have had over the years. Menel, I want to thank you in particular. I really enjoyed our, sometimes lengthy, conversations. The last few months these conversations also really helped me with the completion of this research. Thank you very much for that!

I also wish to thank the anonymous reviewers of the manuscripts that I submitted to scientific journals for publication. The comments I received on these manuscripts were valuable and helped me with improving the quality of the generated work.

Besides the aforementioned colleagues, I also wish to thank some people who in their daily lifes have little to do with dermal wound healing, scar formation, numerical algorithms, computation times and so on.

Ten eerste wil ik graag vrienden en schoonfamilie bedanken. Ik heb genoten van de feesten en de etentjes. ¡Gracias! Ook wil ik mijn zus Ruth en haar partner Jero bedanken voor hun steun, hun luisterend oor en de tijd die we samen hebben doorgebracht. Dit heeft mij heel erg geholpen de afgelopen jaren. Ik heb heel erg genoten van ons samenzijn en onze vakanties in Normandië en de Belgische Ardennen. Dank jullie wel!

Ik wil ook graag mijn ouders bedanken. Pap, ik wil je bedanken voor het mij aanmoedigen om dit onderzoeksproject af te maken. Verder wil ik je bedanken voor het feit dat je mij netjes en georganiseerd hebt leren werken. Deze vaardigheden hebben mij ontzettend veel geholpen tijdens dit project. Mam, ik wil jou bedanken voor alle steun die je mij de afgelopen jaren hebt gegeven. Je hebt mij vaak een luisterend oor geboden en advies gegeven. Ik ben je hier heel erg dankbaar voor. Verder wil je bedanken voor de mini vakanties en de vele etentjes van de afgelopen jaren. Ik vond het erg gezellig.

Goed, dan wil ik nu graag twee viervoeters bedanken (ook al kunnen zij deze tekst zelf niet lezen). Dit is wellicht wat ongebruikelijk, maar zij zijn mij zeer dierbaar. Lieve Loes en Milo, ik wil jullie bedanken voor jullie liefde, jullie trouw, jullie knuffels en jullie gezelschap tijdens onze vele wandelingetjes.

Tot slot wil ik mijn grote liefde bedanken. Het is moeilijk om in woorden uit te drukken hoe dankbaar ik je ben... Je bent een fantastische vrouw en ik ben heel erg blij dat ik mijn leven met jou mag delen. Dank je wel voor alle “love, peace and understanding”.

Daniël Koppenol
Hoek van Holland, February 2017

CONTENTS

1

GENERAL INTRODUCTION

In this chapter a broad overview of the anatomy and physiology of skin tissue is presented. Subsequently, an overview of dermal wound healing is presented. It is assumed that the wounds extend deep into the dermal layer of the skin and are left to heal by secondary intention (i.e., the wounds are left open and close naturally). Furthermore, it is assumed that the healing process proceeds without complications and hence results in the formation of normal scar tissue. Thereafter, the motivation behind the study is presented. Finally, the chapter is concluded with an outline of the thesis.

1.1. THE ANATOMY AND PHYSIOLOGY OF SKIN TISSUE

SKIN tissue is a complex living material that performs many different functions such as assisting in maintaining homeostasis and protecting the body against potentially lethal environmental factors. In order to perform these functions the components of skin tissue are replaced and repaired continuously. In addition, a complex biomechanical cross-talk takes place between different components of the tissue, and between components of the tissue and other elements of the human body such as the circulatory system and the nervous system, such that these functions are performed accurately. In this section a short description of some important anatomical structures and some important physiological properties of human skin tissue is presented. More details on these subjects can be found, for instance, in the books edited by Burns *et al.* [4].

The skin of an adult human with an average posture has a surface area of approximately two square meters and is between one and two millimeters thick in most places [35, 40]. Skin tissue consists of two primary, functionally independent layers: the epidermis and the dermis. Underneath the dermis lies the hypodermis (i.e., the subcutis) which is separated from the rest of the body by a vestigial layer of striated muscle. See Figure 1.1 for a broad graphical overview of the composition and the organization of skin tissue.

Parts of this chapter are based on content of the article "A mathematical model for the simulation of the formation and the subsequent regression of hypertrophic scar tissue after dermal wounding" [23].

1

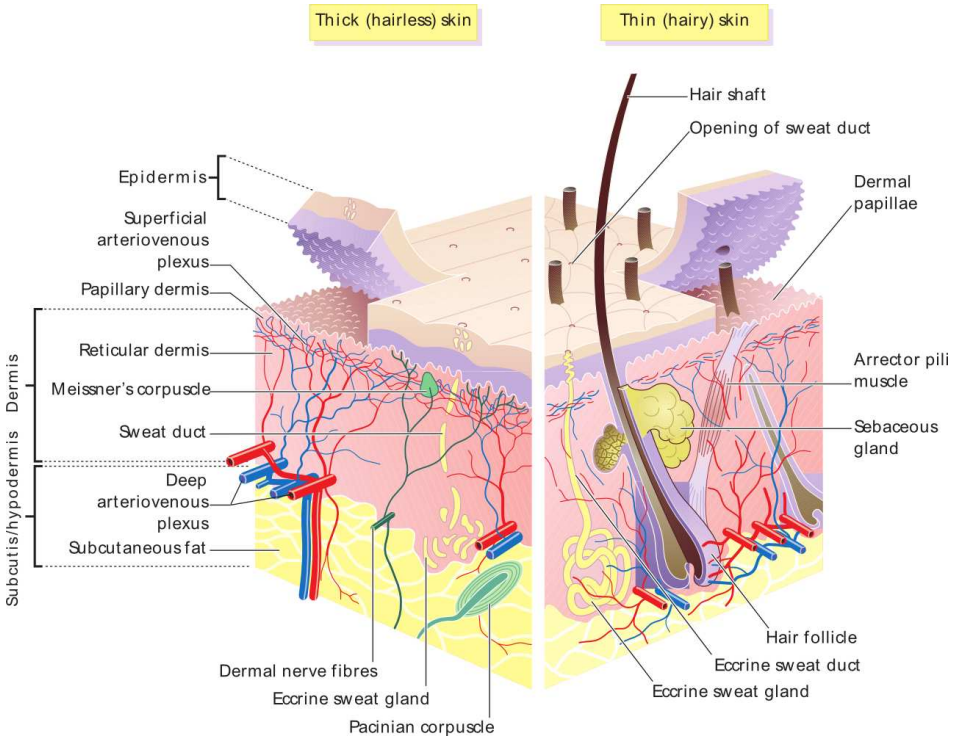

Figure 1.1: A graphical overview of the composition and the organization of human skin tissue [32]

1.1.1. THE EPIDERMIS

THE epidermis is the outermost layer of skin tissue and is in general less than 0.1 millimeters thick [42]. It is an avascular, terminally keratinized stratified squamous epithelium, which is nourished through diffusion of nutrients that leave the vascular space in the upper layer of the underlying dermis [35]. The undersurface contains downward ridge-like projections known as rete ridges that interlock with upward-projecting dermal mesenchymal cones from the papillary dermis. Between the epidermis and the papillary dermis lies a thin sheet of protein fibers which is known as the basement membrane. Through this membrane the epidermis is anchored down to the underlying dermis.

The epidermal layer consists mainly of cells. Melanocytes, Langerhans cells (i.e., epidermal dendritic cells) and Merkel cells constitute a small portion of the total amount of cells that are present in the epidermis. The majority of the remainder of the cells that constitute the cell population of the epidermis are keratinocytes. Keratinocytes move progressively from their attachment to the basement membrane toward the surface of the skin and form several well-defined layers due to a gradual differentiation from proliferating basal keratinocytes into terminally differentiated corneocytes during their ascend. While they move slowly toward the surface of the skin, the keratinocytes synthesize water-repellent keratin proteins and lipids. These molecules are major components of the physical barrier that protects the body against potentially damaging environmen-

tal factors such as pathogens and oxidative stresses [43]. Furthermore, these molecules play a crucial role in maintaining homeostasis. Besides synthesizing keratin proteins and lipids, the keratinocytes also secrete various types of signaling molecule (i.e., cytokines and growth factors) that stimulate processes such as the proliferation of cells, the active attraction of motile cells through chemotaxis and the initiation of the inflammatory response after dermal wounding [60]. Finally, the corneocytes are shed from the surface during the desquamation process [35]. During this process the corneocytes lose their cohesion and separate from the surface one by one. Due to the gradual ascend of the keratinocytes and the desquamation process, the entire epidermis is replaced by new cells over a period of approximately one month.

1.1.2. THE DERMIS

THE dermis is the skin layer between the epidermis and the hypodermis [35]. Its thickness varies, being greatest in the palms and the soles (approximately 5 millimeters) and least in the eyelids (approximately 0.5 millimeters). The dermal layer consists of fibers (i.e., protein bundles), extrafibrillar matrix components and different types of cell such as fibroblasts, endothelial cells, dermal dendritic cells, resident T lymphocytes, mast cells, Schwann cells, pericytes and mesenchymal stem cells. It should be noted that, although the dermis consists of many different cell types, the dermis is actually largely acellular. Together with the basement membrane, the fibers and the extrafibrillar matrix components form the extracellular matrix (ECM). The ECM occupies most of the dermal layer and serves many different functions such as resisting mechanical forces and regulating the intercellular communication between cells. The dermis is divided into two layers. The first layer is the superficial area adjacent to the epidermis called the papillary dermis. This layer consists of a loosely organized, randomly directed finely woven mesh of protein bundles, numerous capillary loops, lymph vessels and nerve endings. The second layer is the deep thicker layer known as the reticular dermis. This layer is less vascularized and consists of a basket weave-like pattern of thick, dense protein bundles.

Fibroblasts are the most common cell type found in the dermis. They form a heterogeneous population that displays distinct and characteristic transcriptional patterns related to the anterior-posterior, proximal-distal and dermal versus non-dermal division of the body [49, 50]. The population of dermal fibroblasts can be divided furthermore in two distinct subpopulations based on both their physical location and their phenotype: papillary fibroblasts and reticular fibroblasts. The main function of fibroblasts is to maintain the structural integrity of the dermis by continuously secreting the precursors of the components of the ECM. Furthermore, the fibroblasts secrete several other molecules besides these precursors such as various types of signaling molecule [60]. Fibroblasts are not fully differentiated or specialized which implies that these cells can differentiate further. One important example of further differentiation is the differentiation of fibroblasts into myofibroblasts [53]. A myofibroblasts is a modulated fibroblast that is, amongst other things, characterized by the presence of a certain isoform of actin in its cytoskeleton. This isoform is similar to the one observed in the cytoskeleton of vascular smooth muscle cells.

The ECM consists of four major classes of extracellular matrix components, namely

collagen bundles, elastic fibers, non-collagenous glycoproteins such as fibronectins, and proteoglycan-glycosaminoglycan complexes like the decorin-dermatan sulphate complex [19, 46]. The collagen bundles consist of individual collagen proteins. At least thirteen different types of collagen are expressed in human tissue [51]. Taken together, these thirteen types of collagen account for 90% to 95% of the dry weight of the dermis [29]. The main types of collagen found in the dermis are types I, III and V. Type I collagen, the most abundant type overall, is the predominant type of collagen in the reticular dermis and accounts for approximately 80% of the total dry weight of the collagen molecules. Type III collagen accounts for about 10% to 15% of the total dry weight of the collagen molecules found in the adult human dermis and is the predominant type of collagen in the papillary dermis. Type V collagen represents less than 5% of the total dry weight of the collagen molecules. Type I collagen associates with type III collagen to form an interconnected network of collagen bundles. Within the dermis type V collagen is located primarily on the surface of the collagen bundles. The primary function of type V collagen is the regulation of the diameter of the collagen bundles. The network as a whole provides most of the tensile strength to the dermal tissue [45]. In addition, the collagen bundles facilitate together with glycoproteins the migration of cells such as endothelial cells and fibroblasts, by providing scaffolding and contact guidance [37].

Many processes and proteins play a role in the synthesis, cross-linking and degradation of collagen molecules. An important example of a group of proteins that is involved in the degradation of collagen molecules is the group of metalloproteinases (MMPs) [30, 39]. MMPs are secreted by a variety of cell types such as fibroblasts, endothelial cells and leukocytes, and the group as a whole is capable of breaking down every type of collagen found in human tissue. In addition, MMPs are capable of cleaving many signaling molecules and their receptors [34, 52].

Within the dermal layer lies an extensive blood vessel network consisting of both a superficial and a deep arteriovenous plexus, and numerous arteriovenous anastomoses that connect the two plexuses [35]. The superficial plexus is located at the boundary between the papillary dermis and the reticular dermis. The deep plexus is located at the boundary between the dermis and the subcutaneous adipose tissue. Besides the blood vessel network, the dermis also contains several skin appendages such as hair follicles, pilosebaceous apparatuses and sweat glands. These appendages are derived from invaginated epidermal tissue and are often found projecting deep into the dermis.

1.2. DERMAL WOUND HEALING

DERMAL wounds may cause a variety of potentially lethal pathological conditions and therefore the speedy and effective restoration of the integrity of affected skin is crucial. In order to accomplish this, humans have evolved sophisticated processes for the healing of wounds. In the case of deep dermal wounds that are created after birth and are left to heal by secondary intention (i.e., the wounds are left open and close naturally), the final outcome of the execution of the restoration processes is usually a thin, flat scar when the restoration of the wounded area proceeds without complications [16, 56]. The processes that bring about the formation of this type of scar are often divided up in four sequential, partially overlapping phases: haemostasis, inflammation, proliferation and maturation / remodeling [11, 43].

1.2.1. HAEMOSTATIC PHASE

NEAR instantly after the disruption of blood vessels due to injury the wound healing cascade is set in motion. Wound healing starts with haemostasis. Haemostasis is the process that causes a bleeding to stop. If the lining of blood vessels is broken due to wounding, then the nearby uninjured blood vessels constrict in order to minimize the loss of blood [3]. In addition, nearby platelets are activated, and due to that these platelets adhere to the site of injury and to each other [12]. This results in the plugging of the injury. The platelets have receptors on their outer cell membrane that bind the protease thrombin present in the serum of blood. As a consequence of the action of thrombin the soluble protein fibrinogen which is also present in the serum of blood, is converted into the insoluble protein fibrin at the site of injury. Fibrin forms bundles in the extracellular space that are bound to the platelets. Under the influence of the coagulation factor $XIII$ these bundles are cross-linked to form a firm provisional fibrin-based ECM.

While bleeding stops, activated platelets also start releasing the contents of different types of granule into the extracellular space. These granules contain several chemical substances such as fibronectins that adhere to the provisional ECM [18] and various types of signaling molecule that influence the behavior of, for instance, leukocytes, fibroblasts and endothelial cells by stimulating amongst other things chemotaxis, cell differentiation and cell division [2, 60].

During the healing of a wound the fibrin-based ECM is broken down by the protease plasmin [5]. Plasmin is released by the liver into the blood stream as the zymogen plasminogen. During the formation of a blood clot plasminogen molecules become entrapped within the clot and under the influence of tissue plasminogen activator (tPA) and other proteases these plasminogen molecules are converted into active plasmin molecules. tPA is released into the blood stream very slowly by the damaged endothelium of the blood vessels in order to accomplish that the fibrin mesh is broken down slowly.

1.2.2. INFLAMMATORY PHASE

THE initial vasoconstriction of the nearby blood vessels is reversed quickly after injury and is succeeded by vasodilatation and increased permeability of the walls of these vessels [3, 37]. These changes are brought about by the complex and highly regulated interplay between the nervous system and various signaling molecules. Effectively, this results in the leakage of plasma from the intravascular space into the extravascular space and the transmigration of various types of leukocyte, such as polymorphonuclear leukocytes (PMNs), monocytes (i.e., immature cells that can differentiate into macrophages) and T lymphocytes, from the intravascular space into the extravascular space. The transmigration marks the start of the inflammatory phase and is mediated through the presence of a variety of chemoattractants in the wounded area (which are in part present here due to the release of the contents of the aforementioned granules) [26, 48].

Early in the wound healing cascade, macrophages and neutrophils are the dominant types of leukocyte in the injured area (with neutrophils arriving first) [7, 10]. The macrophages in the wounded area can display two different functional phenotypes: M1 macrophages and M2 macrophages [33]. Whether a monocyte differentiates into a M1

macrophage or a M2 macrophage depends on the types of molecule it encounters in the recovering wounded area [7]. During normal wound repair the macrophages that are present early in the healing process mainly display a M1 phenotype [6]. At day 5 after wounding, the dominating phenotype in the wounded area has become the M2 macrophage [31]. After activation, the neutrophils and the M1 macrophages start cleaning the wounded area by removing bacteria and debris through phagocytosis and the release of different types of MMP. The M2 macrophages suppress further inflammatory responses, but also remove debris, and stimulate angiogenesis [7]. Furthermore, this latter cell type stimulates a successful completion of the immune response. Besides cleaning the wounded area, both macrophages and neutrophils also secrete various signaling molecules. These signaling molecules are very important for successful completion of the wound healing cascade because of the fact that they affect, for instance, both fibroblasts and keratinocytes in various processes such as protein production, cell division and cell migration [28, 60]. T lymphocytes become the dominant type of leukocyte in the wounded area during the later stages of the wound healing cascade [10]. T lymphocytes are the main effectors of the cell-mediated immune response, and are major sources of signaling molecules that regulate important processes such as the proliferation and the cell differentiation of various cell types present in wounded area [37].

1.2.3. PROLIFERATIVE PHASE

SOON after the initiation of the inflammatory phase, the proliferative phase of the wound healing cascade commences [11]. The subprocesses that take place during the proliferative phase are reepithelialization, angiogenesis, fibroplasia and wound contraction [37, 28, 48]. Reepithelialization encompasses the subprocesses that bring about the restoration of the epidermis and angiogenesis comprises a sequence of subprocesses through which new capillaries in the wounded area are formed from preexisting blood vessels. Due to the restoration of the epidermis, a crucial part of the protective physical barrier is restored. The renewed presence of blood vessels in the injured area is very important since it improves the delivery of nutrients and oxygen to the reconstituting dermal tissue, and contributes to the enhancement of the influx of leukocytes and other cell types by providing both more and more proximate locations for these cells to infiltrate the wounded area.

Fibroplasia encompasses the subprocesses that cause the restoration of the presence of fibroblasts and the production of a new ECM in the injured area. Traditionally, it was thought that the repopulation of the wounded area by fibroblasts is realized through the active migration of nearby fibroblasts into the evolving ECM, and through the cell division of fibroblasts that are present in this matrix [26]. However, experimental evidence gathered over the last 20 years suggests that this repopulating population of fibroblasts probably accrues from a variety of sources. Besides containing fibroblasts that originate from nearby, uninjured tissue, the population might consist of differentiated cells of the epidermis and the inner lining of blood vessels, differentiated bone marrow- and tissue-derived mesenchymal stem cells, differentiated pericytes and differentiated fibrocytes [1, 13, 21, 25, 38, 44]. Taken together, the heterogeneous population of fibroblasts is responsible for the adjustment of other wound healing processes through the release of various signaling molecules, and is the main producer of the constituents of the new

collagen-rich ECM that replaces the provisional fibrin-based ECM [2, 3, 60]. Furthermore, cells from the population of fibroblasts can differentiate into myofibroblasts [53]. Fibroblast differentiation is stimulated by transforming growth factor β (TGF-β) [8], but stimulation by this growth factor will only be effective in the presence of fibronectin and sufficient mechanical stiffness [47, 58]. Like fibroblasts, myofibroblasts are responsible for both the production of constituents of the new collagen-rich ECM and the release of MMPs. During the final stages of the wound healing cascade, myofibroblasts undergo apoptosis and only a few fibroblasts remain to finish the remodeling of the ECM [9]. De-differentiation of myofibroblasts back to fibroblasts has not been demonstrated clearly *in vivo* [25].

Wound contraction is the process that causes the circumferential inward movement of surrounding uninjured skin tissue toward the injured area [43]. The amount of contraction is dependent on the size, shape, depth, and anatomical location of the wound [3, 28, 37]. Due to the contraction of the wounded area, the exposed surface area of the wound is decreased relatively fast without the production of new wound-covering tissue. For instance, due to wound contraction, typical full-thickness wounds in humans may undergo a reduction in wound surface area of up to 40% over a period of several weeks, while rapid wound contraction in rats may even be responsible for up to 90% of the closure of a wounded area [28, 36]. Given that the production of mature scar tissue of sufficient quality takes longer and fast closure of the wounded area is necessary so that the influx of, for instance, bacteria is minimized as much as possible, it is advantageous in general that the surface area of a wound reduces as consequence of wound contraction.

1.2.4. REMODELING PHASE

WITH the onset of the proliferative phase, the remodeling of the evolving ECM also commences [3, 11]. However, contrary to the proliferative phase, which is relatively short under normal circumstances, the remodeling of the ECM takes place over a much longer period of time. The subprocesses that underlie the remodeling process are active mostly during the first year post-wounding, but they remain active thereafter [28]. During remodeling the nature of the ECM changes as a consequence of alterations in the balances between the production and the breakdown of various constituents of the ECM [37]. For instance, the total amount of collagen and the relative levels of fibronectin, proteoglycans, and type III collagen decrease over time, while the relative levels of type I collagen increase over time. Furthermore, the ECM also changes as a consequence of adjustments in the way that the collagen molecules are aligned and interconnected. The initial mesh of newly formed, delicate collagen bundles is transformed slowly into a mesh consisting of thicker, extensively cross-linked collagen bundles that are oriented more parallel to the surface of the skin compared to the collagen bundles of uninjured dermal tissue [54, 59]. These alterations are brought about by present fibroblasts and certain types of molecule, such as particular types of MMP, which are released by these fibroblasts [37]. Finally, the cell densities of various cells such as the cell densities of endothelial cells and (myo)fibroblasts, decrease over time during the remodeling of the scar tissue. Taken together, these alterations result effectively in relatively acellular, thin and flat scar tissue of gradually increasing strength [16].

1.3. STUDY MOTIVATION

DERMAL wounds are a significant global problem. This can be illustrated clearly by presenting some figures related to a particular type of wound, namely burns. Every year approximately 250,000 citizens of the United Kingdom get injured due to burning while about half a million citizens of the United States require medical treatment as a result of thermal injury each year [14, 17]. In the United Kingdom and the United States the majority of these injuries are minor and do not require specialized care. However, a small portion of the injuries are extensive and as a consequence roughly 13,000 individuals in the United Kingdom and approximately 40,000 individuals in the United States are admitted to a hospital or burn center for treatment each year. While this number has decreased by about 50% over the last two decades due to effective prevention strategies and advances in therapy strategies, it is in general still very difficult to prevent the development of sequelae [22].

For example, even in the absence of complications, if skin tissue gets damaged after birth, then the restoration of deep dermal wounds does not result in scar-free healing (i.e., healing that results in a complete regeneration of the injured tissue). Instead the final outcome of the restoration processes is relatively acellular, thin and flat scar tissue in which the collagen bundles are oriented more parallel to the surface of the skin [54, 59]. Given that the behavior of dermal tissues in response to mechanical forces is influenced strongly by the geometrical distribution of the collagen bundles [20, 61], the abnormal distribution of collagen bundles in scar tissue might result in complications such as a restriction in the movement of the affected skin. Subsequently, this might cause, for instance, a reduction in the radius of movement of a limb that is covered by this scar tissue.

In addition, the restoration of dermal wounds also gets perturbed many times during the initial period post-wounding and this might result in the development of, for instance, hypertrophic scar tissue [41, 56]. There are many factors that influence the properties of hypertrophic scar tissue, but in general the growing tissue becomes firm and thick and has a dark red appearance. After the initial expansion phase, the hypertrophy of the tissue usually regresses gradually over an extended period of time, and ultimately the outcome of the perturbed restoration process is ordinarily a relatively flat and inflexible scar [16].

Severe burns are usually not treated by letting these wounds heal by secondary intention. Instead the treatment of burns usually consists of the following two subparts. First most of the burnt skin is excised surgically and thereafter the newly created wound is covered by a skin graft. The use of a skin graft to cover a newly created wound has two widely recognized benefits compared to the situation where these wounds are left to heal by secondary intention; in general it reduces both the overall contraction of the wounded area and the development of hypertrophic scar tissue in these areas [57]. However, many times skin grafts still contract considerably after placement on their recipient bed and this may result then in substantial shrinkage of the grafts and hence the development of contractures in these tissues [24]. The development of contractures is a serious complication that has a significant impact on an affected person's quality of life, and often requires substantial further corrective surgery [27].

Unfortunately, the causal pathways that lead to the formation of contractures and hypertrophic scar tissue are unknown at present [15, 25, 55]. Furthermore, it is very dif-

ficult to alter the distribution of collagen bundles and the degree of wound contraction during healing. A better understanding of the mechanisms underlying the (aberrant) healing of dermal wounds will probably improve the treatment of dermal wounds, and will, consequently, reduce the probability of the occurrence of sequelae, such that the newly generated tissue in the recovered wounded area is more akin to the original tissue. Therefore, a lot of resources have been allocated to research the mechanisms with *in vivo* and *in vitro* experiments. This has resulted in the production of much knowledge about these mechanisms [3, 4, 15, 25, 28, 37, 55]. However, there is still much that remains understood incompletely. This is partly due to the intrinsic complexity of the wound healing process, but it is also a consequence of the fact that it is very difficult to study the interactions between different components of the wound healing cascade with experimental studies.

A way to deal with this latter issue, is to use mathematical models. With these models it is possible to simulate components of the wound healing cascade and to investigate the interactions between these components. The results obtained with these models might aid in disentangling which components of the wound healing cascade influence, for instance, the degree of wound contraction and the geometrical distribution of collagen bundles in scar tissue. Furthermore, these results might aid in providing insights into which components of the wound healing response are disrupted during the formation of contractures and hypertrophic scar tissue. Subsequently, this might help the design of better treatment plans that can reduce, for instance, the probability of hypertrophic scar tissue formation. In addition, these insights might help the design of treatment plans that are better capable of guiding the degree of wound contraction and the overall geometrical distribution of the collagen bundles. For these reasons several mathematical models were developed during this investigation.

1.4. OUTLINE OF THE THESIS

BEFORE presenting the models and the obtained results, the background of the models is presented in Chapter 2. Subsequently, three models are presented that were developed to investigate the impact of various components of the wound healing response on the degree of wound contraction and the development of the geometrical distribution of the collagen bundles in evolving scar tissue.

In Chapter 3 a hybrid model is presented that was used to study wound contraction and the development of the distribution of the collagen bundles in relatively small wounds. In this model cells are modeled as discrete inelastic spheres while the other components are modeled as continuous variables. A tensorial approach was used for the representation of the collagen bundles. After obtaining baseline simulation results, the impact of macrophage depletion and the application of a TGF-β receptor antagonist on both the degree of wound contraction and overall distribution of the collagen bundles were investigated with this model.

In Chapter 4 a continuum hypothesis-based model is presented that was used to study wound contraction and the development of the distribution of the collagen bundles in relatively large wounds. In this model all components are modeled as continuous variables. Furthermore, the bulk mechanical properties of the involved dermal tissues such as the Young's moduli and the Poisson ratios depend locally on the local

concentration and the local geometrical distribution of the collagen bundles. Using this model, the impact on the contraction of the wounded area of the distribution of the collagen bundles and the position of the wound relative to the dominant direction of the collagen bundles, were investigated. In addition, the impact of the movement of the (myo)fibroblasts on the development of the geometrical distribution of the collagen bundles in the recovering injured area was investigated with this model.

In Chapter 5 a continuum hypothesis-based model is presented that was used to study the contraction of burns more rigorously. That is, a factorial design combined with a regression analysis were used to quantify the individual contributions of variations in the values for certain parameters of the model to the dispersion in the surface area of healing burns. Furthermore, a probabilistic analysis was used to investigate in more detail the effect of variability in the values for certain parameters of the model on certain aspects of the healing process.

In order to help with gaining more insight into what might cause the formation of hypertrophic scar tissue, a mechano-chemical continuum hypothesis-based model was developed. The model and the results obtained with the model are presented in Chapter 6. Furthermore, the implications of the obtained results are discussed at the end of the chapter.

In Chapter 7 a morphoelastic continuum hypothesis-based model is presented that was used to study the formation of contractures in skin grafts that cover excised burns. Based on the insights obtained with the model, suggestions are presented regarding how splinting therapy, which is the main therapy for the prevention of contracture formation in current usage, should be applied such that the therapy is effective optimally. In addition, some alternative ideas on how to diminish the degree of contracture formation are put forward that are not based on a mechanical intervention.

Finally, the thesis is concluded in Chapter 8 with an overview of the most important conclusions that were drawn from the results obtained with the models, and an overview of recommendations for future research in Chapter 9.

REFERENCES

[1] Abe R, Donneley S, Peng T, Bucala R, Metz C (2001) Peripheral blood fibrocytes: differentiation pathway and migration to wound sites. J Immunol 166:756–762

[2] Barrientos S, Stojadinovic O, Golinko M, Brem H, Tomic-Canic M (2008) Growth factors and cytokines in wound healing. Wound Repair Regen 16:585–601

[3] Baum C, Arpey C (2005) Normal cutaneous wound healing: clinical correlation with cellular and molecular events. Dermatol Surg 31:674–686

[4] Burns D, Breathnach S, Cox N, Griffiths C (2010) Rook's Textbook of Dermatology, 8th edn. Blackwell Publishing Ltd, West Sussex, United Kingdom

[5] Cesarman-Maus G, Hajjar K (2005) Molecular mechanisms of fibrinolysis. Br J Haematol 129:307–321

[6] Daley J, Brancato S, Thomay A, Reichner J, Albina J (2010) The phenotype of murine wound macrophages. J Leukoc Biol 87:59–67

[7] Delavary B, Van der Veer W, Van Egmond M, Niessen F, Beelen R (2011) Macrophages in skin injury and repair. Immunobiology 216:753–762

[8] Desmoulière A, Geinoz A, Gabbiani F, Gabbiani G (1993) Transforming growth factor-β1 induces α-smooth muscle actin expression in granulation tissue myofibroblasts and in quiescent and growing cultured fibroblasts. J Cell Biol 122:103–111

[9] Desmoulière A, Redard M, Darby I, Gabbiani G (1995) Apoptosis mediates the decrease in cellularity during the transition between granulation tissue and scar. Am J Pathol 146:56–66

[10] Eming S, Krieg T, Davidson J (2007) Inflammation in wound repair: Molecular and cellular mechanisms. J Invest Dermatol 127:514–525

[11] Enoch S, Leaper D (2007) Basic science of wound healing. Surgery 26:31–37

[12] Gale A (2011) Current understanding of hemostasis. Toxicol Pathol 39:273–280

[13] Gharzi A, Reynolds A, Jahoda C (2003) Plasticity of hair follicle dermal cells in wound healing and induction. Exp Dermatol 12:126–136

[14] Gibran N, Wiechman S, Meyer W, Edelman L, Fauerbach J, Gibbons L, et al (2013) American burn association consensus statements. J Burn Care Res 34:361–365

[15] Harrison C, MacNeil S (2008) The mechanism of skin graft contraction: An update on current research and potential future therapies. Burns 34:153–163

[16] Hawkins H, Finnerty C (2012) Pathophysiology of the burn scar. In: Herndon D (ed) Total Burn Care, 4th edn, Elsevier Inc, Philadelphia, Pennsylvania, chap 45, pp 507–516.e3

[17] Hettiaratchy S, Dziewulski P (2004) ABC of burns. Introduction. BMJ 328:1366–1368

[18] Hynes R (1986) Fibronectins. Sci Am 254:42–61

[19] Jarvelainen H, Sainio A, Koulu M, Wight T, Penttinen R (2009) Extracellular matrix molecules: potential targets in pharmacotherapy. Pharmacol Rev 61:198–223

[20] Jor J, Nash M, Nielsen P, Hunter P (2011) Estimating material parameters of a structurally based constitutive relation for skin mechanics. Biomech Model Mechanobiol 10:767–778

[21] Kalluri R, Neilson E (2003) Epithelial-mesenchymal transition and its implications for fibrosis. J Clin Invest 112:1776–1784

[22] Keck M, Herndon D, Kamolz L, Frey M, Jeschke M (2009) Pathophysiology of burns. Wien Med Wochenschr 159:327–336

[23] Koppenol D, Vermolen F, Niessen F, Van Zuijlen P, Vuik K (2017) A mathematical model for the simulation of the formation and the subsequent regression of hypertrophic scar tissue after dermal wounding. Biomech Model Mechanobiol 16:15–32, DOI: 10.1007/s10237-016-0799-9

[24] Kraemer M, Jones T, Deitch E (1988) Burn contractures: incidence, predisposing factors, and results of surgical therapy. J Burn Care Rehabil 9:261–265

[25] Kwan P, Desmoulière A, Tredget E (2012) Molecular and cellular basis of hypertrophic scarring. In: Herndon D (ed) Total Burn Care, 4th edn, Elsevier Inc, Philadelphia, Pennsylvania, chap 45, pp 495–505.e5

[26] Lawrence W (1998) Physiology of the acute wound. Clin Plast Surg 25:321–340

[27] Leblebici B, Adam M, Bagis S, Tarim A, Noyan T, Akman M, Haberal M (2006) Quality of life after burn injury: The impact of joint contracture. J Burn Care Res 27:864–868

[28] Li J, Chen J, Kirsner R (2007) Pathophysiology of acute wound healing. Clin Dermatol 25:9–18

[29] Linares H, Kischer C, Dobrkovsky M, Larson D (1972) The histiotypic organization of the hypertrophic scar in humans. J Invest Dermatol 59:323–331

[30] Lindner D, Zietsch C, Becher P, Schulze K, Schultheiss HP, Tschöpe C, Westermann D (2012) Differential expression of matrix metalloproteases in human fibroblasts with different origins. Biochemistry Research International 2012:1–10

[31] Lucas T, Waisman A, Ranjan R, Roes J, Krieg T, Muller W, Roers A, Eming S (2010) Differential roles of macrophages in diverse phases of skin repair. J Immunol 184:3964–3977

[32] Madhero88 (2011) A graphical overview of the composition and the organization of human skin tissue. https://upload.wikimedia.org/wikipedia/commons/3/36/Skin_layers.png, Downloaded on: 2017-01-19

[33] Mantovani A, Sozzani S, Locati M, Allavena P, Sica A (2002) Macrophage polarization: tumor-associated macrophages as a paradigm for polarized M2 mononuclear phagocytes. Trends Immunol 23:549–555

[34] Mast B, Schultz G (1996) Interactions of cytokines, growth factors, and proteases in acute and chronic wounds. Wound Repair Regen 4:411–420

[35] McGrath J, Uitto J (2010) Anatomy and organization of human skin. In: Burns D, Breathnach S, Cox N, Griffiths C (eds) Rook's Textbook of Dermatology, 8th edn, Blackwell Publishing Ltd, West Sussex, United Kingdom, chap 3, pp 3.1–3.53

[36] McGrath M, Simon R (1983) Wound geometry and the kinetics of wound contraction. Plast Reconstr Surg 72:66–72

[37] Monaco J, Lawrence W (2003) Acute wound healing: an overview. Clin Plast Surg 30:1–12

[38] Mori L, Bellini A, Stacey M, Schmidt M, Mattoli S (2005) Fibrocytes contribute to the myofibroblast population in wounded skin and originate from the bone marrow. Exp Cell Res 304:81–90

[39] Nagase H, Visse R, Murphy G (2006) Structure and function of matrix metalloproteinases and TIMPs. Cardiovasc Res 69:562–573

[40] Nedelec B, Correa J, De Oliveira A, LaSalle L, Perrault I (2014) Longitudinal burn scar quantification. Burns 40:1504–1512

[41] Niessen F, Spauwen P, Schalkwijk J, Kon M (1999) On the nature of hypertrophic scars and keloids: A review. Plast Reconstr Surg 104:1435–1458

[42] Oliveira G, Chinkes D, Mitchell C, Oliveras G, Hawkins H, Herndon D (2005) Objective assessment of burn scar vascularity, erythema, pliability, thickness, and planimetry. Dermatol Surg 31:48–58

[43] O'Toole E, Mellerio J (2010) Wound healing. In: Burns D, Breathnach S, Cox N, Griffiths C (eds) Rook's Textbook of Dermatology, 8th edn, Blackwell Publishing Ltd, West Sussex, United Kingdom, chap 14, pp 14.1–14.27

[44] Quan T, Cowper S, Wu S, Bockenstedt L, Bucala R (2004) Circulating fibrocytes: collagen-secreting cells of the peripheral blood. Int J Biochem Cell B 36:598–606

[45] Rozario T, DeSimone D (2010) The extracellular matrix in development and morphogenesis: a dynamic view. Dev Biol 341:126–140

[46] Schaefer L, Schaefer R (2010) Proteoglycans: from structural compounds to signaling molecules. Cell Tissue Res 339:237–246

[47] Serini G, Bochaton-Piallat M, Ropraz P, Geinoz A, Borsi L, Zardi L, Gabbiani G (1998) The fibronectin domain ED-A is crucial for myofibroblastic phenotype induction by transforming growth factor-beta1. J Cell Biol 142:873–881

[48] Singer A, Clark R (1999) Cutaneous wound healing. N Engl J Med 341:738–746

[49] Sorrell J, Caplan A (2004) Fibroblast heterogeneity: more than skin deep. J Cell Sci 117:667–675

[50] Sorrell J, Baber M, Caplan A (2008) Human dermal fibroblast subpopulations; differential interactions with vascular endothelial cells in coculture: nonsoluble factors in the extracellular matrix influence interactions. Wound Repair Regen 16:300–309

[51] Stadelmann W, Digenis A, Tobin G (1998) Physiology and healing dynamics of chronic cutaneous wounds. Am J Surg 176:26S–38S

[52] Sternlicht M, Werb Z (2001) How matrix metalloproteinases regulate cell behavior. Annu Rev of Cell Dev Biol 17:463–516

[53] Tomasek J, Gabbiani G, Hinz B, Chaponnier C, Brown R (2002) Myofibroblasts and mechano-regulation of connective tissue remodelling. Nat Rev Mol Cell Bio 3:349–363

[54] Van Zuijlen P, Ruurda J, Van Veen H, Van Marle J, Van Trier A, Groenevelt F, Kreis R, Middelkoop E (2003) Collagen morphology in human skin and scar tissue: no adaptation in response to mechanical loading at joints. Burns 29:423–431

[55] Van der Veer W, Bloemen M, Ulrich M, Molema G, Van Zuijlen P, Middelkoop E, Niessen F (2009) Potential cellular and molecular causes of hypertrophic scar formation. Burns 35:15–29

[56] Verhaegen P, Van Zuijlen P, Pennings N, Van Marle J, Niessen F, Van der Horst C, Middelkoop E (2009) Differences in collagen architecture between keloid, hypertrophic scar, normotrophic scar, and normal skin: An objective histopathological analysis. Wound Repair Regen 17:649–656

[57] Walden J, Garcia H, Hawkins H, Crouchet J, Traber L, Gore D (2000) Both dermal matrix and epidermis contribute to an inhibition of wound contraction. Ann Plast Surg 45:162–166

[58] Van de Water L, Varney S, Tomasek J (2013) Mechanoregulation of the myofibroblast in wound contraction, scarring, and fibrosis: Opportunities for new therapeutic intervention. Adv Wound Care 2:122–141

[59] Welch M, Odland G, Clark R (1990) Temporal relationships of *F*-actin bundle formation, collagen and fibronectin matrix assembly, and fibronectin receptor expression to wound contraction. J Cell Biol 110:133–145

[60] Werner S, Grose R (2003) Regulation of wound healing by growth factors and cytokines. Physiol Rev 83:835–870

[61] Wilkes G, Brown I, Wildnauer R (1973) The biomechanical properties of skin. CRC Crit Rev Bioeng 1:453–495

2

THE STORY BEHIND THE DEVELOPED MODELS

In this chapter a description of previously developed mathematical frameworks and models that served as basis for the models that were developed in this study, is presented. Furthermore, reasons for the development of the new models that are presented in the subsequent chapters, are provided, and a description is given of how these new models differ from the models that have been developed previously.

2.1. INTRODUCTION

FOR approximately the last 25 years the mathematical modeling of processes involved in the healing of dermal wounds has been an active area of research. Over these years a large number of models has been developed for the investigation of different components of the wound healing cascade. Focusing on the types of mathematical framework used for the development of these models, surveys such as those compiled by Sherratt and Dallon [34], Buganza Tepole and Kuhl [4], Valero *et al.* [42] and Jorgensen and Sanders [17] indicate that the majority of the models can be placed into one of three categories: continuum hypothesis-based models, discrete cell-based models and hybrid models. In this latter type of model components of the continuum hypothesis-based framework are combined with components of the discrete cell-based framework. Furthermore, the continuum hypothesis-based models are often divided in three subcategories: (bio)chemical models, mechanical models and mechano-(bio)chemical models. The models in the first subcategory are based on the conservation of mass, those in the second subcategory are based in principle on the conservation of linear momentum, and those in the third subcategory are based in principle on the conservation of both

Parts of this chapter are based on content of the articles "A biomechanical mathematical model for the collagen bundle distribution-dependent contraction and subsequent retraction of healing dermal wounds" [20], "A mathematical model for the simulation of the contraction of burns" [19] and "Biomedical implications from a morphoelastic continuum model for the simulation of contracture formation in skin grafts that cover excised burns" [18].

mass and linear momentum. Particular previously developed mechano-(bio)chemical continuum hypothesis-based models and hybrid models served as basis for the models developed during this investigation. A short overview of these models is presented here. Descriptions of other mathematical models developed over the last 25 years can be found, for instance, in the aforementioned surveys [4, 17, 34, 42]. Furthermore, reasons for the development of the new models that are presented in the subsequent chapters, are provided, and a description is given of how these new models differ from the models that have been developed previously.

2.2. MECHANICS

IN order to help with gaining more insight into the mechanisms underlying wound contraction, Tranquillo and Murray [37] formulated the first mathematical framework for the modeling of the mechanical component of the wound healing response in dermal tissues. This framework is based on the continuum hypothesis and the conservation of both mass and linear momentum. Using this framework Tranquillo and Murray developed several models. First, a basic model was developed. With respect to the constituents of the recovering dermal tissue, the following components were selected as primary model components in this basic model: fibroblasts and the extracellular matrix (ECM). The dermal tissues were modeled as isotropic linear viscoelastic solids.

Next, the basic model was extended in several different ways after the addition of a signaling molecule to the basic model. Here it was assumed that the concentration profile of the signaling molecule is static (i.e., the concentration of the signaling molecule at a certain location within the dermal tissue does not change over time). The first extension to the basic model was to let the the traction force generated by the fibroblasts vary with the local concentration of the signaling molecule. The second extension was to let the maximum cell density of the fibroblasts vary with the local concentration of the signaling molecule. The third extension was to incorporate the directed movement of the fibroblasts up the gradient of the signaling molecule and the final extension was to include the production of ECM molecules into the model. Due to the fact that fibroblasts produce isotropic stresses in the models, Tranquillo and Murray were able to replicate the experimental data on wound contraction in rats that were collected by McGrath and Simon [23] with all different extensions to the basic model.

Subsequently, the basic model developed by Tranquillo and Murray was extended by Olsen *et al.* [28]. In this model, all of the aforementioned extensions to the basic model developed by Tranquillo and Murray were included. However, the applied functional forms for the inclusion of these extensions are different. Furthermore, the general ECM was replaced by collagen molecules as a primary model variable, and the concentration of the signaling molecule changes dynamically over time in the model developed by Olsen *et al.* Over the years numerous studies have demonstrated that myofibroblasts are present in the recovering wounded area [14]. Therefore, myofibroblasts were also added as a primary model component to the model developed by Olsen *et al.* The dermal tissues were modeled again as isotropic linear viscoelastic solids. In the model both fibroblasts and myofibroblasts produce isotropic stresses that work on the dermal tissues. Due to this, Olsen *et al.* were also able to replicate the experimental data on wound contraction that were collected by McGrath and Simon [23].

In order to investigate the impact of the addition and the adaptation of various components of the wound healing cascade on different aspects of the wound healing response, the models developed by Tranquillo and Murray, and Olsen *et al.* served as basis for the development of new models in several more recent studies [9, 15, 26, 31, 32, 36, 38, 39, 43]. In this study it was decided to use the (bio)chemical components of the model developed by Olsen *et al.* for the (bio)chemical components of the continuum hypothesis-based models presented in Chapters 4 through 7. However, there are also some differences between the models presented in this thesis and the model developed by Olsen *et al.*

For instance, while in the model developed by Olsen *et al.* solely the fibroblasts are actively motile, in the models presented here both fibroblasts and myofibroblasts are actively motile. Thampatty and Wang [35] have demonstrated previously that both fibroblasts and myofibroblasts are actively motile. Therefore, it seems reasonable to incorporate this phenomenon into the models.

Furthermore, the random movement of cells is modeled by means of cell density-dependent Fickian diffusion instead of linear Fickian diffusion in the models presented in this thesis. Traditionally, linear diffusion is used to model the random dispersal of cells in continuum hypothesis-based models [15, 26, 28, 43]. As is also mentioned by Olsen *et al.* [28], this is the standard representation of random cell movement in mathematical models. However, Hillen and Painter [13] point out that it is actually far more likely that the random movement of cells depends on the density of these cells. They also show in their study that this type of dependence can show up naturally during the derivation of a Keller-Segel type of system. Hence it was assumed in the models presented in this thesis that the random movement of the cells increases with an increasing cell density [13, 21].

Finally, the degradation of both signaling molecules and collagen molecules was incorporated into the models by means of proteolytic cleavage by a generic MMP instead of by means of natural decay or very general enzymatic degradation which were used in the model developed by Olsen *et al.* For this end, the phenomenological relationship given in Equation (4.9) was used which is based on the deduction presented in the accompanying paragraph.

Additionally, the mechanical components of the models presented in Chapters 4 through 7 are also different. Traditionally, the dermis is treated as a linear (visco)elastic solid in mechano-chemical continuum models for (certain aspects of) dermal wound healing [15, 26, 28, 31, 32, 39, 40, 43]. However, the experimental data by Wang *et al.* [44] and Nedelec *et al.* [27] that were used, respectively, in Chapter 5 and Chapter 6, indicate that it is probably inappropriate to assume that the generated strains in the dermal tissues are infinitesimally small. Therefore, it was decided to model the dermal tissues as isotropic compressible neo-Hookean solids in the models presented in Chapter 5 and Chapter 6. Although the models presented in these chapters are not the first models within the context of the modeling of dermal wound healing where dermal tissues are modeled as hyperelastic materials (See for example the studies by Valero *et al.* [38, 41]), it is not a standard approach. Furthermore, these models are the first models wherein an explicit description of the dynamics of a myofibroblast population is combined with the modeling of dermal tissues as hyperelastic materials.

In the model presented in Chapter 4 the dermis is modeled as an orthotropic con-

tinuous solid with bulk mechanical properties that are locally dependent on both the local concentration and the local geometrical distribution of the collagen bundles (See Section 2.4 for further details). Finally, in the model presented in Chapter 7 the dermis is modeled as an isotropic morphoelastic solid (See Section 2.5 for further details).

2.3. GEOMETRICAL DISTRIBUTION OF COLLAGEN BUNDLES

ALTHOUGH the mathematical models developed by Olsen *et al.* [28] and Tranquillo and Murray [37] contain functional descriptions of several components of the wound healing cascade, they all lack a description of the geometrical distribution of the collagen bundles. Consequently is is not possible to investigate, for instance, the bidirectional interaction between the direction of movement of cells such as fibroblasts, and the way that the collagen bundles are aligned and interconnected into sheets and bundles.

Barocas and Tranquillo [1] formulated the first framework that includes a description of the dynamic regulation of the geometrical distribution of collagen bundles by fibroblasts. This framework is also based on the continuum hypothesis and the conservation of both mass and linear momentum. For the representation of the collagen bundles, Barocas and Tranquillo used a tensorial approach. The ECM is modeled as an anisotropic, biphasic medium consisting of a fibrillar network and an interstitial solution. The two phases display intraphase viscoelasticity and interphase frictional drag due to the relative motion of the two phases. The fibrillar network orients the fibroblasts. This results in anisotropic cell migration and anisotropic traction forces. Furthermore, the fibrillar network is oriented by the inhomogeneous deformation of the network due to the traction forces generated by the fibroblasts. With the developed models that are based on the framework, Barocas and Tranquillo were able to replicate qualitatively the alignment of collagen bundles in tissue-equivalents (i.e., cell-populated collagen gels).

Subsequently, Olsen *et al.* [29, 30] also formulated a continuum hypothesis-based framework that includes a description of the dynamic regulation of the geometrical distribution of either one type or two types of bundle. In this framework the fibroblasts are oriented by the geometrical distribution of the bundles. Furthermore, the bundles are oriented by the direction of movement of the fibroblasts and / or the stresses generated by the fibroblasts. However, compared to the framework developed by Barocas and Tranquillo, the framework of Olsen *et al.* has a clear disadvantage. Olsen *et al.* model the alignment of collagen bundles in their model by considering two orthogonal configurations and assuming that the transition between these two configurations is a dynamic and reversible process. The major disadvantage of this approach is that this representation cannot provide an accurate representation of the collagen bundles when this orientation is continuously distributed. The tensorial approach used by Barocas and Tranquillo does not suffer from this drawback.

Dallon *et al.* [6, 8, 7, 22, 30] also developed a theoretical framework in order to study the dynamic regulation of the distribution of collagen bundles. Given that wound healing is actually a process that involves the interplay between elements that vary widely in nature and size, Dallon *et al.* developed a new approach to model aspects of the wound healing cascade that is different from the approaches used by Barocas and Tranquillo [1] and Olsen *et al.* [29, 30]. While in the latter approaches it is assumed that it is appropriate to model all constituents of the skin as continuous entities, in the hybrid framework

developed by Dallon *et al.* constituents of the skin are represented by models of a different type. For instance, cells are modeled as discrete entities while collagen bundles and signaling molecules are modeled as continuous entities. In the hybrid framework the direction of movement of the cells is influenced by the local orientation of the collagen bundles while the orientation of the bundles is in turn dependent on the polarity of the cells in the vicinity.

More recently, the hybrid framework developed by Dallon *et al.* has been extended by Cumming *et al.* [5]. Compared to the framework developed by Dallon *et al.*, the framework of Cumming *et al.* has two benefits. In the framework of Dallon *et al.* cells are represented as discrete points. In the framework of Cumming *et al.* cells occupy a circular region of the domain of computation. Due to this the latter approach allows the inclusion of cell-cell interactions such as contact inhibition and collisions. Furthermore, Cumming *et al.* used a tensorial approach for the representation of the collagen bundles, similar to the approach used by Barocas and Tranquillo [1], while Dallon *et al.* use a vector-based approach for the representation of the collagen bundles. The use of a vector-based approach has two clear disadvantages. Firstly, the vector-based approach does not provide any information about the degree of isotropy of collagen bundles at individual material points within the dermal layer. Secondly, due to the use of a vector representation, collagen bundles are treated basically as unidirectional entities. Given that fiber alignment is actually bidirectional, this may lead to duality when one wishes to determine the degree of alignment of the collagen bundles. These two disadvantages are not present when a tensorial approach is used.

Given the elegance of the framework developed by Cumming *et al.*, this framework was chosen by Boon *et al.* [2] for the development of a new mathematical model. However, the modeling framework developed by Cumming *et al.* does not contain a mechanical component. Consequently, it is not possible to investigate with this framework how certain components of the wound healing cascade might influence the contraction of wounds. Therefore, a mechanical component was added to the framework of Cumming *et al.* by Boon *et al.* through the incorporation of a mechanical force balance into the framework. In the study presented in Chapter 3 an extended version of the model developed by Boon *et al.*, was used in order to investigate how certain components of the wound healing response might influence the degree of wound contraction.

2.4. COLLAGEN DISTRIBUTION DEPENDENT MECHANICS

ALTHOUGH the frameworks discussed in the previous two sections are elegant, they either do not contain a mechanical component at all, or they lack an incorporation of the effect of the geometrical distribution of the collagen bundles on the bulk mechanical behavior of the involved dermal tissues. Hence, it is not possible with the models which are based on these frameworks, to investigate the direct influence of the composition and the topology of the constituents of the ECM on the behavior of dermal tissues in response to mechanical forces such as wound contraction.

Recently, two models have been formulated that do incorporate the effect of the geometrical arrangement of constituents of the ECM on the bulk mechanical behavior of the tissues these constituents are embedded in [41, 46]. Due to the organization of the collagen molecules into interconnected sheets and bundles, the geometrical distribu-

tion of the collagen bundles, in particular, has a huge impact on the response of dermal tissues to mechanical forces [16]. Therefore, the bulk mechanical behavior is influenced in the models by the geometrical distribution of the collagen bundles. However, each of these two models has a serious limitation. Due to the fact that the model developed by Yang *et al.* [46] uses a hybrid framework similar to the one developed by Dallon *et al.* [6], the domain of computation, and hence the simulated wound, has to be small so that the computation times and the computer memory requirements remain acceptable. Consequently, they used a domain of computation of 4 mm^2 and created circular wounds with a radius of solely 400 μm. Because of the fact that the model developed by Valero *et al.* [41] is a continuum hypothesis-based model, it is possible to simulate the healing of deep dermal wounds that cover a large surface area with this model. However, this latter model lacks a dynamic regulation of the geometrical distribution of the collagen bundles (i.e., the geometrical distribution of the collagen bundles is static in this model). Given that the proportion of the collagen bundles that runs parallel to the surface of the skin increases considerably in general during the execution of the wound healing processes [45], it is a limitation of the model developed by Valero *et al.* that the dynamic regulation of the geometrical distribution of the collagen bundles is not included in this model.

Given the limitations associated with the models developed by Yang *et al.* and Valero *et al.*, it was decided to develop a new, fully continuum hypothesis-based model in order to become able to investigate how certain components of the wound environment and the wound healing response might influence the contraction of the wound and the development of the geometrical distribution of collagen bundles in the recovering wounded area. In this model the bulk mechanical behavior of the involved dermal tissues is dependent on the geometrical distribution of the collagen bundles. That is, the bulk mechanical properties of the tissues such as the Young's moduli and the Poisson ratios depend locally on the local concentration and the local geometrical distribution of the collagen bundles. Furthermore, the dynamic change of the geometrical distribution of the collagen bundles was incorporated into this new model similar to how this process has been incorporated into the model developed by Olsen *et al.* [29]. A tensorial approach, similar to the one proposed by Barocas and Tranquillo [1] and Cumming *et al.* [5], was used for the representation of the collagen bundles. A detailed derivation of the model is presented in Chapter 4.

2.5. CONTRACTURE FORMATION

WITH the frameworks discussed in the previous sections it is not straightforward to investigate the formation of contractures unless artificial assumptions are added to the resulting models. For instance, Olsen *et al.* [28] were able to simulate the permanent contraction of a recovered injured area. However, in order to accomplish this the collagen kinetics had to be removed from the model. Given that the production and the breakdown of components of the ECM are actually key components of the wound healing response [24], removing the collagen kinetics from the model seriously reduces the accuracy of the representation of reality.

Therefore, like in the models developed by Murphy *et al.* [25] and Bowden *et al.* [3], a morphoelastic framework was applied in the model presented in Chapter 7 in order to incorporate the formation of contractures in a more realistic way. More specifically

the theory of morphoelasticity developed by Hall [12] was used in the model presented in Chapter 7. Central to this theory is the assumption that the classical deformation gradient tensor (i.e., **F**) can be decomposed into a product of two tensors (i.e., **F** = **AZ**) [11, 12, 33]. The tensor **Z** can be thought of as the locally-defined deformation gradient tensor that describes how infinitesimal line segments in the fixed reference configuration are transformed into infinitesimal line segments in a hypothetical configuration (i.e., a zero stress state [10]) wherein the internal stresses around all individual points in the dermal layer are relieved. The tensor **A** can be thought of as the locally-defined deformation gradient tensor that describes how infinitesimal line segments in the hypothetical configuration are transformed into infinitesimal line segments in the current configuration of the dermal layer.

Based on the decomposition of the classical deformation gradient tensor, Hall derived several related evolution equations that describe mathematically the change over time of the effective strain (i.e., the local measure for the difference between the current configuration of the dermal layer and a hypothetical configuration of the dermal layer where the tissue is mechanically relaxed). Hence, these equations basically give a mathematical description of the remodeling of the dermal layer over time. In this study it was assumed that the effective strains are small. Consequently, the evolution equation that describes the dynamic change of the infinitesimal effective strain over time (i.e., Equation (7.1c) in Chapter 7 and Equation (5.64) in the PhD thesis of Hall [12]) was used. Furthermore, the general conservation equations for linear momentum and mass were used to describe mathematically the dynamic change over time of, respectively, the linear momentum, and the cell densities and concentrations of the modeled constituents of the dermal layer.

The derivation of the evolution equation that describes the dynamic change of the infinitesimal effective strain over time, is rather lengthy and contains numerous subtleties. Therefore, solely the finally derived equation is presented in this thesis. The full derivation of the evolution equation can be found in the PhD thesis of Hall [12].

REFERENCES

[1] Barocas V, Tranquillo R (1997) An anisotropic biphasic theory of tissue-equivalent mechanics: the interplay among cell traction, fibrillar network deformation, fibril alignment, and cell contact guidance. AMSE J Biomech Eng 119:137–145

[2] Boon W, Koppenol D, Vermolen F (2016) A multi-agent cell-based model for wound contraction. J Biomech 49:1388–1401

[3] Bowden L, Byrne H, Maini P, Moulton D (2016) A morphoelastic model for dermal wound closure. Biomech Model Mechanobiol 15:663–681

[4] Buganza Tepole A, Kuhl E (2013) Systems-based approaches toward wound healing. Pediatr Res 73:553–563

[5] Cumming B, McElwain D, Upton Z (2010) A mathematical model of wound healing and subsequent scarring. J R Soc Interface 7:19–34

[6] Dallon J, Sherratt J, Maini P (1999) Mathematical modelling of extracellular matrix dynamics using discrete cells: fiber orientation and tissue regeneration. J Theor Biol 199:449–471

[7] Dallon J, Sherratt J, Maini P, Ferguson M (2000) Biological implications of a discrete mathematical model for collagen deposition and alignment in dermal wound repair. IMA J Math Appl Med Biol 17:379–393

[8] Dallon J, Sherratt J, Maini P (2001) Modeling the effects of transforming growth factor-β on extracellular matrix alignment in dermal wound repair. Wound Repair Regen 9:278–286

[9] Friedman A, Hu B, Xue C (2012) A three dimensional model of wound healing: Analysis and computation. Discrete Cont Dyn-B 17:2691–2712

[10] Fung Y (1993) Biomechanics, 2nd edn. Springer Science & Business Media, Berlin, Germany

[11] Goriely A, Ben Amar M (2007) On the definition and modeling of incremental cumulative, and continuous growth laws in morphoelasticity. Biomech Model Mechanobiol 6:289–296

[12] Hall C (2009) Modelling of some biological materials using continuum mechanics. PhD thesis, Queensland University of Technology

[13] Hillen T, Painter K (2009) A user's guide to PDE models for chemotaxis. J Math Biol 58:183–217

[14] Hinz B (2007) Formation and function of the myofibroblast during tissue repair. J Invest Dermatol 127:526–537

[15] Javierre E, Moreo P, Doblaré M, García-Aznar J (2009) Numerical modeling of a mechanochemical theory for wound contraction analysis. Int J Solids Struct 46:3597–3606

[16] Jor J, Nash M, Nielsen P, Hunter P (2011) Estimating material parameters of a structurally based constitutive relation for skin mechanics. Biomech Model Mechanobiol 10:767–778

[17] Jorgensen S, Sanders J (2016) Mathematical models of wound healing and closure: a comprehensive review. Med Biol Eng Comput 54:1297–1316

[18] Koppenol D, Vermolen F (2017) Biomedical implications from a morphoelastic continuum model for the simulation of contracture formation in skin grafts that cover excised burns. Biomech Model Mechanobiol DOI: 10.1007/s10237-017-0881-y

[19] Koppenol D, Vermolen F, Koppenol-Gonzalez G, Niessen F, Van Zuijlen P, Vuik K (2016) A mathematical model for the simulation of the contraction of burns. J Math Biol DOI: 10.1007/s00285-016-1075-4

[20] Koppenol D, Vermolen F, Niessen F, Van Zuijlen P, Vuik K (2017) A biomechanical mathematical model for the collagen bundle distribution-dependent contraction and subsequent retraction of healing dermal wounds. Biomech Model Mechanobiol 16:345–361, DOI: 10.1007/s10237-016-0821-2

[21] Kowalczyk R (2005) Preventing blow-up in a chemotaxis model. J Math Anal Appl 305:566–588

[22] McDougall S, Dallon J, Sherratt J, Maini P (2006) Fibroblast migration and collagen deposition during dermal wound healing: mathematical modelling and clinical implications. Phil Trans R Soc 364:1385–1405

[23] McGrath M, Simon R (1983) Wound geometry and the kinetics of wound contraction. Plast Reconstr Surg 72:66–72

[24] Monaco J, Lawrence W (2003) Acute wound healing: an overview. Clin Plast Surg 30:1–12

[25] Murphy K, Hall C, McCue S, McElwain D (2011) A two-compartment mechanochemical model of the roles of transforming growth factor β and tissue tension in dermal wound healing. J Theor Biol 272:145–159

[26] Murphy K, Hall C, Maini P, McCue S, McElwain D (2012) A fibrocontractive mechanochemical model of dermal wound closure incorporating realistic growth factor kinetics. B Math Biol 74:1143–1170

[27] Nedelec B, Correa J, De Oliveira A, LaSalle L, Perrault I (2014) Longitudinal burn scar quantification. Burns 40:1504–1512

[28] Olsen L, Sherratt J, Maini P (1995) A mechanochemical model for adult dermal wound contraction and the permanence of the contracted tissue displacement profile. J Theor Biol 177:113–128

[29] Olsen L, Sherratt J, Maini P, Marchant B (1998) Simple modelling of extracellular matrix alignment in dermal wound healing I. Cell flux induced alignment. J Theor Med 1:172–192

[30] Olsen L, Maini P, Sherratt J, Dallon J (1999) Mathematical modelling of anisotropy in fibrous connective tissue. Math Biosci 158:145–170

[31] Ramtani S (2004) Mechanical modelling of cell/ECM and cell/cell interactions during the contraction of a fibroblast-populated collagen microsphere: theory and model simulation. J Biomech 37:1709–1718

[32] Ramtani S, Fernandes-Morin E, Geiger D (2002) Remodeled-matrix contraction by fibroblasts: numerical investigations. Comput Biol Med 32:283–296

[33] Rodriguez E, Hoger A, McCulloch A (1994) Stress-dependent finite growth in soft elastic tissues. J Biomech 27:455–467

[34] Sherratt J, Dallon J (2002) Theoretical models of wound healing: past successes and future challenges. C R Biol 325:557–564

[35] Thampatty B, Wang JC (2007) A new approach to study fibroblast migration. Cell Motil Cytoskeleton 64:1–5

[36] Tracqui P, Woodward D, Cruywagen G, Cook J, Murray J (1995) A mechanical model for fibroblast-driven wound healing. J Biol Systems 3:1075–1084

[37] Tranquillo R, Murray J (1992) Continuum model of fibroblast-driven wound contraction: inflammation-mediation. J Theor Biol 158:135–172

[38] Valero C, Javierre E, García-Aznar J, Gómez-Benito M (2013) Numerical modelling of the angiogenesis process in wound contraction. Biomech Model Mechanobiol 12:349–360

[39] Valero C, Javierre E, García-Aznar J, Gómez-Benito M (2014) A cell-regulatory mechanism involving feedback between contraction and tissue formation guides wound healing progression. PLoS ONE 9:e92,774

[40] Valero C, Javierre E, García-Aznar J, Gómez-Benito M (2014) Nonlinear finite element simulations of injuries with free boundaries: Application to surgical wounds. Int J Numer Meth Biomed Engng 30:616–633

[41] Valero C, Javierre E, García-Aznar J, Gómez-Benito M, Menzel A (2015) Modeling of anisotropic wound healing. J Mech Phys Solids 79:80–91

[42] Valero C, Javierre E, García-Aznar J, Menzel A, Gómez-Benito M (2015) Challenges in the modeling of wound healing mechanisms in soft biological tissues. Ann Biomed Eng 43:1654–1665

[43] Vermolen F, Javierre E (2012) A finite-element model for healing of cutaneous wounds combining contraction, angiogenesis and closure. J Math Biol 65:967–996

[44] Wang XQ, Kravchuk O, Winterford C, Kimble R (2011) The correlation of in vivo burn scar contraction with the level of α-smooth muscle actin expression. Burns 37:1367–1377

[45] Welch M, Odland G, Clark R (1990) Temporal relationships of F-actin bundle formation, collagen and fibronectin matrix assembly, and fibronectin receptor expression to wound contraction. J Cell Biol 110:133–145

[46] Yang L, Witten T, Pidaparti R (2013) A biomechanical model of wound contraction and scar formation. J Theor Biol 332:228–248

3

IMPLICATIONS FROM A HYBRID MODEL FOR THE SIMULATION OF THE HEALING OF SMALL WOUNDS

A mechano-chemical hybrid model is presented for the simulation of the healing of small, deep dermal wounds in order to investigate how certain components of the wound healing response might influence the degree of wound contraction and the development of the geometrical distribution of collagen bundles in a recovered wounded area. Solely the dermal layer of the skin is modeled explicitly and it is modeled as an anisotropic continuous linear elastic solid. With respect to the constituents of the recovering dermal layer, the following components were selected as primary model components: fibroblasts, macrophages, the signaling molecule transforming growth factor-β, the signaling molecule platelet derived growth factor, fibrin bundles, collagen bundles and the protease tissue plasminogen activator. The cells are modeled as discrete inelastic spheres. The signaling molecules and the protease are modeled as continuous entities. For the representation of the collagen bundles a tensorial approach was used. Wound contraction and the development of residual forces are caused in the model by temporary pulling forces and permanent plastic forces. The pulling forces are generated by fibroblasts and the plastic forces are caused by the remodeling of the extracellular matrix. The newly secreted collagen molecules are secreted by the fibroblasts in their direction of movement.

With the model certain components of the healing response can be reproduced quite reasonably. For instance, the amount of time it takes to restore the presence of a collagen-rich extracellular matrix in the recovering wounded area and the time window during which macrophages are present in the wounded area coincide quite nicely with in vivo experimental observations. Furthermore, the initial compaction and subsequent partial dilatation of the recovering wounded area can be reproduced as well as the development

Parts of this chapter are based on content of the article "A multi-agent cell-based model for wound contraction" [4].

of residual stresses within the dermal layer. In addition, it is possible to reproduce that the majority of the collagen bundles ends up permanently oriented toward the center of the wound, parallel to the surface of the skin.

In accordance with experimental observations, depletion of the macrophages in the model during the execution of the wound healing cascade results in a delayed healing of a wound. Furthermore, the depletion of the macrophages hardly influences the geometrical distribution of the collagen bundles in the recovering wounded area. However, the depletion does result in an increase of the final surface area of the recovered wounded area.

The application of a transforming growth factor-β receptor antagonist in the model also results in an increase of the surface area of the recovering wounded area. In addition, the application of the antagonist results in a more uniform distribution of the collagen bundles in the recovered wounded area. These observations are also in accordance with experimental observations.

3.1. INTRODUCTION

In Section 3.2 a detailed description of the model is presented. Subsequently, a description of the applied numerical algorithm for obtaining computer simulations is provided in Section 3.3. The simulation results are presented in Section 3.4. Finally, the simulation results are discussed in Section 3.5.

3.2. DEVELOPMENT OF THE MATHEMATICAL MODEL

In order to simulate wound contraction and the deposition of collagen bundles, the following processes that take place after completion of the haemostatic phase of the wound healing cascade were incorporated into the model [9]. Firstly, the gradual breakdown of the fibrin mesh which developed during the clotting of blood after injury, was incorporated into the model. Secondly, the influx of monocytes from the intravascular space into the extravascular space was included into the model. Thirdly, the restoration of the presence of fibroblasts and a collagen-rich extracellular matrix (ECM) in the injured area were incorporated. Fourthly, the initial compaction and subsequent (partial) dilatation of the wounded area were included. Finally, the development of residual stresses in the wounded area due to the remodeling of the ECM was incorporated into the model.

Since wound contraction mainly takes place in the dermal layer of the skin, solely a portion of this layer was included explicitly into the model. The dermis is modeled as an anisotropic continuous linear elastic solid. With respect to the mechanical component of the model, the displacement of the dermal layer ($\mathbf{u}$) was selected as primary model variable. In addition, the following constituents of the recovering dermal tissue were selected as primary model variables: fibroblasts (N), macrophages ($M\Phi$), the signaling molecules TGF-β (c_β) and platelet derived growth factor (c_P), fibrin bundles (Ω^f), collagen bundles (Ω^c) and tissue plasminogen activator (c_t). Hence, in this model no distinction is made between M1 macrophages and M2 macrophages, and between fibroblasts and myofibroblasts. The proportion of bound receptors on the outer cell membrane of each individual fibroblast (i.e, n_N^i with $i \in \{1,\ldots,T_N(t)\}$ where $T_N(t)$ is the total num-

ber of fibroblasts present at time t) and the proportion of bound receptors on the outer cell membrane of each individual macrophage (i.e., $n^i_{M\Phi}$ with $i \in \{1,\ldots,T_{M\Phi}(t)\}$ where $T_{M\Phi}(t)$ is the total number of macrophages present at time t) were also selected as primary model variables.

3.2.1. THE SIGNALING MOLECULES

THE following general advection-diffusion-reaction equation was used to describe the change over time of the concentration of a generic signaling molecule c mathematically:

$$\frac{\partial z_c}{\partial t} + \nabla \cdot [z_c \mathbf{v}] = -\nabla \cdot [-D_c \nabla z_c] + S_c. \tag{3.1}$$

Here z_c represents the concentration of the generic signaling molecule c, $\mathbf{v}$ represents the displacement velocity of the dermal layer, S_c represents the chemical kinetics associated with the generic signaling molecule, and $-D_c \nabla z_c$ represents the flux per unit area due to diffusion. In the model the Fickian diffusion coefficient D_c may be a function of space and time. In order to simplify notation z_c has been replaced by c in the remainder of the text of this chapter. Hence, z_{c_β} has been replaced by c_β, z_{c_P} has been replaced by c_P, z_{c_t} has been replaced by c_t and so on.

PLATELET DERIVED GROWTH FACTOR (PDGF)

With respect to the signaling molecule PDGF it was assumed that the diffusion rate of the molecules is constant over space and time. Furthermore, it was assumed that the net change of the concentration of PDGF due to local chemical kinetics, such as the secretion of the molecule and the proteolytic breakdown of the molecule, is equal to zero (i.e., $S_c = 0$). Taken together, this results in

$$\frac{\partial c_P}{\partial t} + \nabla \cdot [c_P \mathbf{v}] = D_{c_P} \Delta c_P, \tag{3.2}$$

where D_{c_P} is the Fickian diffusion coefficient of the PDGF molecules.

TRANSFORMING GROWTH FACTOR-β (TGF-β)

With respect to the signaling molecule TGF-β it was assumed that the diffusion rate of the molecules is linearly dependent on the local concentration of the fibrin molecules [5]. Furthermore, the secretion of TGF-β by macrophages was included into the model [37]. Taken together, this gives

$$\frac{\partial c_\beta}{\partial t} + \nabla \cdot [c_\beta \mathbf{v}] = \nabla \cdot \left[D_{c_\beta}\left(\rho^f\right) \nabla c_\beta \right] + k_{c_\beta} \sum_{i=1}^{T_{M\Phi}(t)} \delta\left(\mathbf{x} - \mathbf{x}^i_{M\Phi}(t)\right), \tag{3.3}$$

with

$$D_{c_\beta}\left(\rho^f\right) = \left[a^I_\rho \rho^f \right] D^{\min}_{c_\beta} + \left[1 - a^I_\rho \rho^f \right] D^{\max}_{c_\beta}. \tag{3.4}$$

Here $D^{\min}_{c_\beta}$ and $D^{\max}_{c_\beta}$ represent, respectively, the minimum and maximum diffusion rate of the TGF-β molecules, a^I_ρ is a de-dimensionalization constant, ρ^f is the concentration

of the fibrin molecules, k_{c_β} is the secretion rate of TGF-β molecules by macrophages, $\mathbf{x}^i_{M\Phi}(t)$ is the position of the cell center of macrophage i at time t within the domain of computation, and $\delta(\cdot)$ is the Dirac delta distribution.

3.2.2. THE EXTRACELLULAR MATRIX MOLECULES

TWO types of extracellular matrix molecule were incorporated explicitly into the model as primary model variables. The first type of molecule is fibrin and the second type of molecule is collagen. Both types of molecule form bundles in the extracellular space and therefore both types of molecule are modeled as such. For the representation of the bundles a tensorial approach similar to the one proposed by Barocas and Tranquillo [3] and Cumming *et al.* [5] was used. The orientation of the bundles and the concentration of the molecules at location $\mathbf{x}$ and time t within the dermal layer are represented together by the general symmetric tensor

$$\Omega^i(\mathbf{x},t) = \int_0^{\pi/2}\int_0^{\pi} \left[\mathbf{p}(\theta,\varphi)\left(\mathbf{p}(\theta,\varphi)\right)^{\mathrm{T}} \rho^i(\mathbf{x},\theta,\varphi,t)\right] \mathrm{d}\theta\,\mathrm{d}\varphi, \tag{3.5}$$

with $i \in \{f,c\}$, $(\mathbf{p}(\theta,\varphi))^{\mathrm{T}} = [\sin(\varphi)\cos(\theta), \sin(\varphi)\sin(\theta), \cos(\varphi)]$ the unit vector in the direction of azimuthal angle θ and polar angle φ, and $\rho^i(\mathbf{x},\theta,\varphi,t)$ the concentration of bundle type i at location $\mathbf{x}$ and time t with angle θ and angle φ. The concentration of the molecules of type i at location $\mathbf{x}$ and time t (i.e., $\rho^i(\mathbf{x},t)$) can be recovered from the above tensor by either adding its eigenvalues or determining its trace.

Due to the symmetry of the above tensor, the tensor is orthogonal diagonalizable. Hence the tensor can be decomposed as a sum of weighed outer products of orthonormal eigenvectors:

$$\Omega^i(\mathbf{x},t) = \sum_{j=1}^{3} \lambda^i_j(\mathbf{x},t)\left[\mathbf{v}^i_j(\mathbf{x},t)\left(\mathbf{v}^i_j(\mathbf{x},t)\right)^{\mathrm{T}}\right]. \tag{3.6}$$

Here $(\lambda^i_j, \mathbf{v}^i_j)$ are the eigenpairs of the tensor. These eigenpairs can be used to measure the degree of anisotropy of the dermal layer and have been used for the graphical presentation of the degree of anisotropy within the modeled portion of dermal layer in Section 3.4. The larger the difference between the different (positive, real) eigenvalues, the more anisotropic the dermal layer. The eigenvector corresponding to the largest eigenvalue provides the dominant direction of the bundles. If all eigenvalues are equal, then the dermal layer is perfectly isotropic.

FIBRIN BUNDLES & TISSUE PLASMINOGEN ACTIVATOR (TPA)

The breakdown of the provisional fibrin-based ECM was incorporated into the model. In order to keep the model concise, it was assumed that the degradation rate of the fibrin bundles is directly proportional to the the product of the concentration of tPA and the concentration of the fibrin bundles themselves [5]. Hence, for $j,k \in \{1,2,3\}$,

$$\frac{\partial \Omega^f_{jk}}{\partial t} + \nabla\cdot\left[\Omega^f_{jk}\mathbf{v}\right] = -\delta_\rho\left[c_t\Omega^f_{jk}\right], \tag{3.7}$$

where δ_ρ is the degradation rate of the fibrin bundles.

With respect to the release of the protease tPA, it was assumed that this release solely takes place at the interface between injured and uninjured dermal tissue. Furthermore, it was assumed that the diffusion rate of the protease tPA is linearly dependent on the local concentration of the fibrin molecules [5]. Taken together, this results in

$$\frac{\partial c_t}{\partial t} + \nabla \cdot [c_t \mathbf{v}] = \nabla \cdot \left[D_{c_t}\left(\rho^f\right) \nabla c_t \right] + k_{c_t} \delta_{\Gamma_t}, \tag{3.8}$$

with

$$D_{c_t}\left(\rho^f\right) = \left[a_\rho^I \rho^f \right] D_{c_t}^{\min} + \left[1 - a_\rho^I \rho^f \right] D_{c_t}^{\max}. \tag{3.9}$$

Here $D_{c_t}^{\min}$ and $D_{c_t}^{\max}$ represent, respectively, the minimum and maximum diffusion rate of tPA, and k_{c_t} represents the secretion rate of the protease tPA by damaged endothelial cells. Furthermore, the distribution $\delta_{\Gamma_t} : \Omega_{\mathbf{x},t} \to \mathbb{R}_{\geq 0}$, where $\Omega_{\mathbf{x},t}$ is the domain of computation in Eulerian coordinates at time t, is defined as

$$\delta_{\Gamma_t}(\mathbf{x}) \begin{cases} = 0 & \text{if } \mathbf{x} \notin \Gamma_t, \\ > 0 & \text{if } \mathbf{x} \in \Gamma_t, \end{cases} \tag{3.10}$$

such that for any $A \subset \Omega_{\mathbf{x},t}$

$$\int_A \delta_{\Gamma_t}(\mathbf{x}) \, \mathrm{d}\Omega_{\mathbf{x},t} = \frac{\mu(A \cap \Gamma_t)}{\mu(\Gamma_t)}. \tag{3.11}$$

Depending on whether the domain of computation is two- or three-dimensional, Γ_t represents either the curve or the surface that describes the position of the interface between injured and uninjured dermal tissue over time, and the measure $\mu : \Gamma \to \mathbb{R}_{>0}$ represents either the length of the curve Γ or the surface area of the surface Γ.

COLLAGEN BUNDLES

As has been mentioned before, the restoration of a collagen-rich ECM in the injured area was also incorporated. In the model the collagen molecules are secreted by the fibroblasts in the direction of movement of the fibroblasts. It was assumed that the secreted collagen molecules are attached to the ECM instantaneously. Hence, the active movement of these molecules is equal to zero. Furthermore, it was assumed that the secretion rate of collagen molecules by each individual fibroblast is dependent on the proportion of the receptors on its outer cell membrane that is bound to the signaling molecule TGF-β [5, 29]. Finally, it was assumed that the secretion rate of collagen molecules by each individual fibroblast is also dependent on the local concentration of both the fibrin molecules and the collagen molecules. Taken together, this results in

$$\begin{aligned} \frac{\partial \Omega_{jk}^c}{\partial t} + \nabla \cdot \left[\Omega_{jk}^c \mathbf{v} \right] = \left\{ 1 - a_\rho^I \left[\rho^f + \rho^c \right] \right\} \times \\ \sum_{i=1}^{T_N(t)} \left\{ \left[k_\rho^I + \left[k_\rho^{II} - k_\rho^I \right] n_N^i \right] \left[\mathbf{r}_N^i(t) \left(\mathbf{r}_N^i(t) \right)^{\mathrm{T}} \right]_{jk} \delta\left(\mathbf{x} - \mathbf{x}_N^i(t) \right) \right\} \end{aligned} \tag{3.12}$$

for $j,k \in \{1,2,3\}$, where ρ^c is the concentration of the collagen molecules, k_ρ^I is the minimum secretion rate of collagen molecules by fibroblasts, k_ρ^{II} is the maximum secretion rate of collagen molecules by fibroblasts, $\mathbf{r}_N^i(t) = [\mathrm{d}\mathbf{x}_N^i(t) - \mathbf{v}\,\mathrm{d}\,t]/\|[\mathrm{d}\mathbf{x}_N^i(t) - \mathbf{v}\,\mathrm{d}\,t]\|_2$ is the direction of active movement of fibroblast i at time t (See also Equation (3.19)), and $\mathbf{x}_N^i(t)$ is the position of the cell center of fibroblast i at time t.

3.2.3. THE CELLS

CELLS are modeled as discrete, inelastic spheres with radius r_c. Every individual cell receives cues from its environment and these cues determine the behavior of the cell. In this model the behavior of a cell can be influenced by the local gradient of the concentration of one of the modeled signaling molecules, the proximity of nearby cells, the proportion of the receptors on the outer cell membrane that is bound to one of the modeled signaling molecules, the local geometrical distribution of the collagen bundles and the concentration of both the fibrin bundles and the collagen bundles. These properties of the environment can affect both the speed and the direction of movement of the individual cells. Depending on the cell type, the aforementioned properties can also affect other behaviors of each cell. In the subsequent paragraphs this is described in more detail per cell type.

MACROPHAGES

It was assumed that the receptors on the outer membrane of the macrophages selectively bind to PDGF molecules. Furthermore, it was assumed that PDGF molecules can unbind from these receptors, and it was assumed that the number of receptors on each individual macrophage is fixed. The following ordinary differential equation (ODE) was used to describe the change over time of the the proportion of the receptors that is bound to PDGF molecules on the outer cell membrane of macrophage i [5]:

$$\frac{\mathrm{d}\,n_{M\Phi}^i}{\mathrm{d}\,t} = -\gamma_m^u n_{M\Phi}^i + \gamma_m^b c_P(\mathbf{x}_{M\Phi}^i(t), t)\left[1 - n_{M\Phi}^i\right]. \tag{3.13}$$

Here γ_m^u and γ_m^b represent, respectively, the receptor unbinding rate and the receptor binding rate of the PDGF molecules.

It was assumed that the maximum speed of the biased movement of a macrophage diminishes with an increase in the combined concentration of both ECM bundle types [5]. Furthermore, it was assumed that the speed of biased movement is dependent on the proportion of the receptors on the outer membrane that is bound to PDGF molecules. In this study, a bell-shaped curve was used to describe the relationship between the proportion of bound receptors and the speed of biased movement. This curve attains its maximum value when half of the receptors are bound to PDGF molecules and the speed of biased movement is equal to zero when either none or all of the receptors are bound to PDGF molecules. Taken together, the speed of the biased movement of macrophage i due to chemotaxis at time t is given by

$$v^i_{M\Phi}(t) = v\left\{S\left(n^i_{M\Phi}(t)\right)\left[1 - S\left(n^i_{M\Phi}(t)\right)\right]\right\} \times \left\{\frac{2 - a^I_\rho\left[\rho^f\left(\mathbf{x}^i_{M\Phi}(t), t\right) + \rho^c\left(\mathbf{x}^i_{M\Phi}(t), t\right)\right]}{2}\right\}, \quad (3.14)$$

with

$$S(r) = \frac{1}{2}\left[1 + \sin\left(\left[r - \frac{1}{2}\right]\pi\right)\right], \quad (3.15)$$

and v a fixed constant.

Deuel *et al.* [7] have demonstrated previously that monocytes migrate up the gradient of PDGF molecules. In this study no distinction is made between monocytes and macrophages. Hence, the direction of biased movement of a macrophage due to chemotaxis is determined in the model by the local gradient of the PDGF molecules. Furthermore, the random movement of macrophages was incorporated into the model, as well as the displacement of macrophages due to collisions with other cells. In the model the distance between the cell centers of all present cells is computed. If the distance between two cells is less than the sum of both cell radii, then these cells are displaced over the line that connects the cell centers such that there is no overlap anymore between the colliding cells [33]. Finally, the displacement of macrophages due to mechanical drag as a result of local deformation of the dermal layer was also incorporated. Taken together, the following stochastic differential equation (SDE) was obtained for the mathematical description of the displacement of macrophage i at time t:

$$\mathrm{d}\mathbf{x}^i_{M\Phi}(t) = v^i_{M\Phi}(t)\left[\frac{\nabla c_P\left(\mathbf{x}^i_{M\Phi}(t), t\right)}{\gamma + \left\|\nabla c_P\left(\mathbf{x}^i_{M\Phi}(t), t\right)\right\|_2}\right]\mathrm{d}\,t + \mathbf{v}\left(\mathbf{x}^i_{M\Phi}(t), t\right)\mathrm{d}\,t + \mathbf{v}_c(t)\,\mathrm{d}\,t + \sqrt{2D_{M\Phi}}\,\mathrm{d}\mathbf{W}(t). \quad (3.16)$$

Here the term $\mathbf{v}_c(t)\,\mathrm{d}\,t$ represents the displacement of a macrophage due to collisions with other cells. Furthermore, $\mathbf{W}$ denotes a vector Wiener process where $[\mathbf{W}(t) - \mathbf{W}(s)]$ is normally distributed with zero mean and variance $[t - s]$ (under the assumption that $t > s$) [30], and $D_{M\Phi}$ is the macrophage random motility coefficient. The constant γ is a very small positive value that is added to the model to prevent the division by zero in the case that the gradient of the PDGF molecules is equal to zero locally. In this study, γ is set equal to 10^{-12} g/mm^4.

As described in Chapter 1, monocytes transmigrate from the intravascular space of small blood vessels in the vicinity of the injured area into the extravascular space during the inflammatory phase of the wound healing cascade. After migration to the ECM, these monocytes are stimulated by several types of molecule to differentiate into macrophages. The transmigration process and the differentiation process are not modeled explicitly. Solely the appearance of new macrophages in the extravascular space (i.e., the domain of computation) is modeled explicitly. Hence, the appearance of new

macrophages at the interface between the injured and the uninjured dermal tissue during the early stages of the wound healing response was incorporated into the model. The number of macrophages that enter the domain of computation per time step Δt is dependent on the concentration of the PDGF molecules at the interface between the injured and the uninjured dermal tissue (i.e, Γ_t). It was assumed that monocytes solely transmigrate into the extravascular space when the average concentration of PDGF at the interface (i.e., $\hat{c}_P$) exceeds a lower limit $\beta^l_{M\Phi}$. If this lower limit is exceeded, then the number of monocytes that transmigrate per time step is determined by drawing a single sample from a Poisson distribution with an expected value of $\beta_{M\Phi}[\hat{c}_P \mu(\Gamma_t)]\Delta t$. Here $\beta_{M\Phi}$ is a fixed constant and $\mu(\Gamma_t)$ is the measure that has been introduced in Subsection 3.2.2.

The new macrophages enter the domain of computation at the interface between the injured and the uninjured dermal tissue. The location on the interface where a macrophage enters the domain of computation is random. If the interface is a curve, then the position of a newly transmigrated macrophage can be determined by drawing a single sample from a continuous uniform probability distribution with lower bound 0 and upper bound $\mu(\Gamma_t)$. The value of this sample determines the location on the curve where the macrophage enters the domain of computation. If the interface is a surface, then the position of a newly transmigrated macrophage can be determined in two steps. First, the surface is transformed into an unit square through an appropriate mapping (assuming that such a mapping exists). Subsequently, two samples are drawn from a continuous uniform probability distribution with lower bound 0 and upper bound 1. The values of these samples provide together a random position on the unit square, and hence the location on the surface that forms the interface where the macrophage enters the domain of computation. All receptors on the outer membrane of the newly transmigrated macrophage are assumed to be unbound.

Finally, the apoptosis (i.e., the programmed cell death) of macrophages present in the domain of computation was also incorporated into the model. Apoptosis is treated as a stochastic process where it was assumed that the probability of apoptosis is memoryless. Hence, the probability that a macrophage dies within a time interval Δt does not depend on the evolution of this cell before this time interval. Furthermore, it was assumed that the life span of a macrophage depends on the local concentration of the PDGF molecules. In this study, an exponential probability distribution with an expected value of $d_{M\Phi} c_P(\mathbf{x}^i_{M\Phi}(t), t)$ was chosen to determine whether macrophage i dies or survives over a time interval Δt. Here $d_{M\Phi}$ is a fixed constant. That is, per macrophage a single sample is drawn from the exponential probability distribution. If the value of this sample is smaller than the size of the time interval Δt, then the macrophage dies. Otherwise, the macrophage stays alive during the time interval Δt.

FIBROBLASTS

It was assumed that the receptors on the outer membrane of the fibroblasts selectively bind to TGF-β molecules. Furthermore, it was assumed that TGF-β molecules can unbind from these receptors, and it was assumed that the amount of receptors on each individual fibroblast is fixed. The following ODE was used to describe the change over time of the proportion of the receptors that is bound to TGF-β molecules on the outer cell membrane of fibroblast i:

$$\frac{\mathrm{d}\, n_N^i}{\mathrm{d}\, t} = -\gamma_f^u n_N^i + \gamma_f^b c_\beta(\mathbf{x}_N^i(t), t)\left[1 - n_N^i\right]. \tag{3.17}$$

Here γ_f^u and γ_f^b represent, respectively, the receptor unbinding rate and the receptor binding rate of the TGF-β molecules.

For the determination of the speed of the biased movement of fibroblast i due to chemotaxis the following equation was used (See the text preceding Equation (3.14) for more information about the derivation of this function):

$$v_N^i(t) = v\left\{S\left(n_N^i(t)\right)\left[1 - S\left(n_N^i(t)\right)\right]\right\}\left\{\frac{2 - a_\rho^I\left[\rho^f\left(\mathbf{x}_N^i(t), t\right) + \rho^c\left(\mathbf{x}_N^i(t), t\right)\right]}{2}\right\}. \tag{3.18}$$

Postlethwaite *et al.* [27] have demonstrated that fibroblasts migrate up the gradient of TGF-β molecules. Furthermore, Dickinson *et al.* [8] have demonstrated that the direction of migration is also influenced by the geometrical distribution of the collagen bundles over space. Therefore, the direction of the biased movement of a fibroblast due to chemotaxis and contact guidance is determined in the model by the local gradient of the TGF-β molecules and the geometrical distribution of the collagen bundles. Furthermore, the random movement of fibroblasts and the displacement of fibroblasts due to collisions with other cells were incorporated into the model. The latter was implemented in the same way as how this has been implemented for macrophages. Finally, the displacement of fibroblasts due to mechanical drag was also incorporated. Taken together, the following SDE was obtained for the description of the displacement of fibroblast i at time t:

$$\begin{aligned}\mathrm{d}\mathbf{x}_N^i(t) = v_N^i(t)\left\{\left[1 - a_\rho^I\rho^c\left(\mathbf{x}_N^i(t), t\right)\right]\mathbf{I} + \left[a_\rho^I\rho^c\left(\mathbf{x}_N^i(t), t\right)\right]\hat{\Omega}^c\left(\mathbf{x}_N^i(t), t\right)\right\} \times \\ \left[\frac{\nabla c_\beta\left(\mathbf{x}_N^i(t), t\right)}{\gamma + \left\|\nabla c_\beta\left(\mathbf{x}_N^i(t), t\right)\right\|_2}\right]\mathrm{d}\, t + \mathbf{v}\left(\mathbf{x}_N^i(t), t\right)\mathrm{d}\, t + \mathbf{v}_c(t)\,\mathrm{d}\, t + \sqrt{2D_N}\,\mathrm{d}\mathbf{W}(t).\end{aligned} \tag{3.19}$$

Here $\mathbf{I}$ is the second-order identity tensor, $\hat{\Omega}^c(\mathbf{x}, t)$ represents the tensor related to the collagen bundles with rows normalized to a length of one, and D_N is the fibroblast random motility coefficient.

As described in Chapter 1, the population of fibroblasts that repopulate the wounded area probably accrues from a variety of sources besides the nearby, uninjured tissue. The population might also consist of differentiated cells of the epidermis and the inner lining of nearby blood vessels, differentiated bone marrow- en tissue-derived mesenchymal stem cells, differentiated pericytes and differentiated fibrocytes [1, 11, 15, 16, 22, 28]. Therefore, the appearance of new fibroblasts due to differentiation of cells, such as pericytes and fibrocytes, was incorporated into the model. The differentiation process is not modeled explicitly. Solely the appearance of new fibroblasts in the domain of computation is modeled explicitly. Given the variety of the sources that contribute probably to the repopulating population of fibroblasts, it was assumed that new fibroblasts can enter the domain of computation at all positions. Furthermore, it was assumed that the

modeled portion of dermal layer has a maximum capacity s_N^u with respect to the number of fibroblasts it can contain. The number of new fibroblasts that enter the domain of computation during a time interval Δt is determined in the following way. First the difference between the current number of fibroblasts present in the dermal layer and the maximum capacity s_N^u is determined. Subsequently, a sample the size of this difference, is drawn from an exponential probability distribution with an expected value of s_N. The number of fibroblasts that enter the domain of computation is determined finally by determining the number of draws that exceeds Δt. The location where a new fibroblasts enters the domain of computation is completely random. That is, every position in the domain of computation has an equal probability of being the location where a new fibroblast enters the domain of computation. All receptors on the outer membrane of a new fibroblast are assumed to be unbound.

In the model new fibroblasts can also appear due to proliferation of fibroblasts that are already present in the modeled portion of dermal layer. It was assumed that fibroblasts can proliferate solely when a certain proportion of the receptors on the outer membrane of a fibroblast (i.e., p_N^l) has been bound to TGF-β molecules for a sufficient amount of time p_N. In addition, it was assumed that crowding can prevent a fibroblast from proliferating. In the model this was implemented by preventing a fibroblast which is ready to proliferate, from dividing when the minimum distance between the cell center of this fibroblast and all other fibroblasts is less than 4 times the size of the radius of a fibroblast. A new fibroblast appears at the position of the fibroblast that has just proliferated. All TGF-β molecules unbind from the receptors of the fibroblast that has just proliferated, and all receptors on the outer cell membrane of the new fibroblast are unbound.

Finally, the apoptosis of fibroblasts present in the domain of computation was also incorporated into the model. Again apoptosis is treated as a stochastic process where it was assumed that the probability of apoptosis is memoryless. In this study, an exponential probability distribution with an expected value of d_N was chosen to determine whether a fibroblast dies or survives over a time interval Δt. Here d_N is a fixed constant. The actual implementation of the apoptosis mechanism in the model is done in the same way as how this has been done for macrophages.

3.2.4. THE FORCE BALANCE

THE following partial differential equation (PDE) was used to describe the force balance for the modeled portion of dermal layer:

$$-\nabla \cdot \sigma = \mathbf{f}. \tag{3.20}$$

This equation is the reduced conservation equation for the linear momentum of the dermal layer in local form. It was assumed that the inertial forces that work on the dermal layer are negligible and as a consequence the conservation equation for the linear momentum reduces to the above force balance equation [23, 24, 32, 35]. Within the above equation, σ represents the Cauchy stress tensor and $\mathbf{f}$ represents the total body force working on the dermal layer.

The dermis is modeled as a continuous linear elastic solid and therefore, the following constitutive stress-strain relation was chosen [17]:

$$\sigma = \frac{E}{1+\nu}\left\{\epsilon + \mathrm{tr}(\epsilon)\left[\frac{\nu}{1-2\nu}\right]\mathbf{I}\right\}. \tag{3.21}$$

Here E is the Young's modulus of the dermal tissues, ν is Poisson's ratio and ϵ is the infinitesimal strain tensor. Furthermore,

$$\epsilon = \frac{1}{2}\left[\nabla\mathbf{u} + (\nabla\mathbf{u})^{\mathrm{T}}\right]. \tag{3.22}$$

Finally, two additive (body) forces were incorporated into the model. The first type of force is a temporary force (i.e., $\mathbf{f}_t$). This temporary force represents the pulling force of fibroblasts on their surroundings as they move around through the dermal layer. The second type of force is a plastic force (i.e., $\mathbf{f}_p$). This plastic force is a residual force that remains after completion of the wound healing cascade. It is caused by the remodeling of the ECM which results in a modification of the way that the collagen molecules are interconnected. Due to this modification, the distances between collagen molecules are changed permanently and this leads to the development of residual stresses in the recovering dermal tissues. In the model the residual stresses are modeled phenomenologically by treating them as point loading forces. For the actual incorporation of the two types of force into the model, the general formalism proposed by Vermolen and Gefen [34] was used.

THE TEMPORARY FORCES

In order to derive the incorporation of the pulling forces generated by a fibroblast i into the model, the cell boundary Γ_N^i of fibroblast i was subdivided into either a set of line segments, if the domain of computation is two-dimensional, or a set of equilateral triangular surface segments, if the domain of computation is three-dimensional (where the cell boundary is treated as either a polygon in the two-dimensional setting or a spherical polyhedron in the three-dimensional setting). It was assumed that an inward directed pulling force is generated at the midpoint (centroid) of every segment in the direction perpendicular to the line segment (normal to the surface segment). Then the total temporary force generated by all fibroblasts present in the modeled portion of dermal layer at time t is given by

$$\mathbf{f}_t = \sum_{i=1}^{T_N(t)} \sum_{j=1}^{N_S^i} P(\mathbf{x},t)\mathbf{n}(\mathbf{x})\delta(\mathbf{x}-\mathbf{x}_j^i(t))\Delta\Gamma_N^{i,j}. \tag{3.23}$$

Here N_S^i is the total number of segments on the cell boundary of fibroblast i, $P(\mathbf{x},t)$ is the magnitude of the pulling force density that is generated at position $\mathbf{x}(t)$ and time t per unit length (per unit surface area), $\mathbf{n}(\mathbf{x})$ is the unit inward pointing normal vector at position $\mathbf{x}$, $\mathbf{x}_j^i(t)$ is the position of the midpoint (centroid) of segment j on fibroblast i at time t, and $\Delta\Gamma_N^{i,j}$ is the length (surface area) of line segment j (surface segment j). Presuming that the magnitude of the pulling force density is integrable over the boundary of a cell, and letting $N_S^i \to \infty$ for all fibroblasts present in the modeled portion of dermal

layer (i.e., letting $\Delta\Gamma_N^{i,j} \to 0$ for all segments j), the following integral was obtained in addition for the mathematical description of the temporary forces that are generated by all fibroblasts together at time t:

$$\mathbf{f}_t = \sum_{i=1}^{T_N(t)} \int_{\partial\Omega_N^i} P(\mathbf{x}, t)\mathbf{n}(\mathbf{x})\delta(\mathbf{x} - \mathbf{x}_s^i(t))\, \mathrm{d}\Gamma_N^i. \tag{3.24}$$

Here $\mathbf{x}_s^i(t)$ represents a position on the cell boundary of fibroblast i at time t. In this study the generated pulling force is assumed to be constant over space and time. Hence, $P(\mathbf{x}, t) = P_0$, where P_0 is a constant.

THE PLASTIC FORCES

In order to incorporate the plastic forces into the model, an approach was used that is similar to the approach that was used for the incorporation of the pulling forces. The main difference is that the plastic forces are not generated at the boundary of a cell, but at the boundary of a control surface, if the domain of computation is two-dimensional, or a control volume, if the domain of computation is three-dimensional. The control surfaces (volumes) are generated by subdividing the domain of computation into control surfaces (volumes). These surfaces (volumes) coincide with the elements of the conforming triangulation of the domain of computation that has been generated for the application of the finite-element method (See Section 3.3). It was assumed that an inward directed plastic force can be generated at the midpoint (centroid) of all edges (faces) of every control surface (volume) in the direction perpendicular to the edge (normal to the face). Then the total plastic force present in the modeled portion of dermal layer at time t is given by

$$\mathbf{f}_p = \sum_{i=1}^{N_E} \sum_{e=1}^{N_e^i} Q(\tau^i)\mathbf{n}(\mathbf{x})\delta(\mathbf{x} - \mathbf{x}_e^i(t))\Delta\Gamma_E^{i,e}. \tag{3.25}$$

Here N_E is the total number of control surfaces (volumes) in the triangulation, N_e^i is the total number of edges (faces) of control surface (volume) i, $Q(\tau^i)$ is the magnitude of the plastic force density that is generated at effective fibroblast exposure time τ^i per unit length (per unit surface area) at an edge (face) of control surface (volume) i, $\mathbf{n}(\mathbf{x})$ is the unit inward pointing normal vector at position $\mathbf{x}$, $\mathbf{x}_e^i(t)$ is the position of the midpoint (centroid) of edge (face) e of control surface (volume) i at time t, and $\Delta\Gamma_E^{i,e}$ is the length (surface area) of edge (face) e of control surface (volume) i.

The magnitude of the plastic force density that is generated at the boundary of control surface (volume) i is dependent on the effective fibroblast exposure time τ^i. In this study, the change over time of τ^i is a function of the percentage of the area (volume) of control surface (volume) i that is occupied by fibroblasts at time t, the concentration of the signaling molecule TGF-β at the centroid of the control surface (volume) i at time t, and the concentration of the collagen molecules at the centroid of the control surface (volume) i at time t. Taken together, this results in

$$\frac{\mathrm{d}\tau^i}{\mathrm{d}t} = k_\tau c_\beta(\mathbf{x}_E^i(t), t)\left[1 - a_\rho^I \rho^c(\mathbf{x}_E^i(t), t)\right]\left\{\frac{\mathscr{A}\left(\Omega_E^i(t) \cap \left[\cup_j \Omega_N^j(t)\right]\right)}{\mathscr{A}\left(\Omega_E^i(t)\right)}\right\}. \tag{3.26}$$

Here k_τ is the increment rate of the effective fibroblast exposure time, $\mathbf{x}_E^i(t)$ is the position of the centroid of the control surface (volume) i at time t, $\Omega_E^i(t)$ is the region occupied by control surface (volume) i at time t, $\Omega_N^j(t)$ is the region occupied by fibroblast j at time t, and $\mathscr{A}(\cdot)$ denotes the area (volume). Finally, it was assumed in this study that the magnitude of the plastic force density is related to the effective fibroblast exposure time according to the following phenomenological relation:

$$Q(\tau) = Q_0\left[1 - e^{-\tau}\right]. \tag{3.27}$$

Here Q_0 is the maximum of the magnitude of the plastic force density that can be generated per unit length (per unit surface area) at an edge (face) of a control surface (volume).

3.2.5. THE DOMAIN OF COMPUTATION

IT was assumed that $u = 0$ and $\partial v/\partial x = \partial w/\partial x = 0$ hold within the modeled portion of dermal layer, with the yz-plane running parallel to the surface of the skin and $\mathbf{u} = (u, v, w)^{\mathrm{T}}$. Furthermore, it was assumed that the derivatives of the concentrations of the modeled constituents of the dermal layer are equal to zero in the direction perpendicular to the surface of the skin. It was also presumed that all cells solely move randomly in the direction parallel to the yz-plane and that the cell centers of all (newly introduced) cells in the model lie in a plane parallel to the yz-plane. In addition, it was assumed that the plastic forces work solely in the direction parallel to the yz-plane. Finally, it was presumed that a fibroblast generates pulling forces solely at the intersection of its cell boundary, and the plane that passes through the cell center of the fibroblast and that runs parallel to the yz-plane. Taken together, these assumptions imply that the calculations can be performed on an arbitrary, infinitely thin slice of dermal layer oriented parallel to the surface of the skin. Using Lagrangian coordinates $\mathbf{X} = (X, Y, Z)^{\mathrm{T}}$, the following domain of computation $\Omega_{\mathbf{X}}$ was used therefore in this study:

$$\Omega_{\mathbf{X}} \in \{X = 0\ \mathrm{mm},\ -5\ \mathrm{mm} \leq Y \leq 5\ \mathrm{mm},\ -5\ \mathrm{mm} \leq Z \leq 5\ \mathrm{mm}\}. \tag{3.28}$$

3.2.6. THE INITIAL CONDITIONS AND THE BOUNDARY CONDITIONS

THE initial conditions give a description of the positions of the cells and the concentrations of the modeled constituents of the dermal layer at the onset of the inflammatory phase of the wound healing cascade. In addition, initial conditions are provided for the displacement field at the onset of the inflammatory phase and the proportion of the receptors on the outer cell membrane of each cell that is bound by a signaling molecule. For the mathematical description of the shape of the wounded area, the following general function was used:

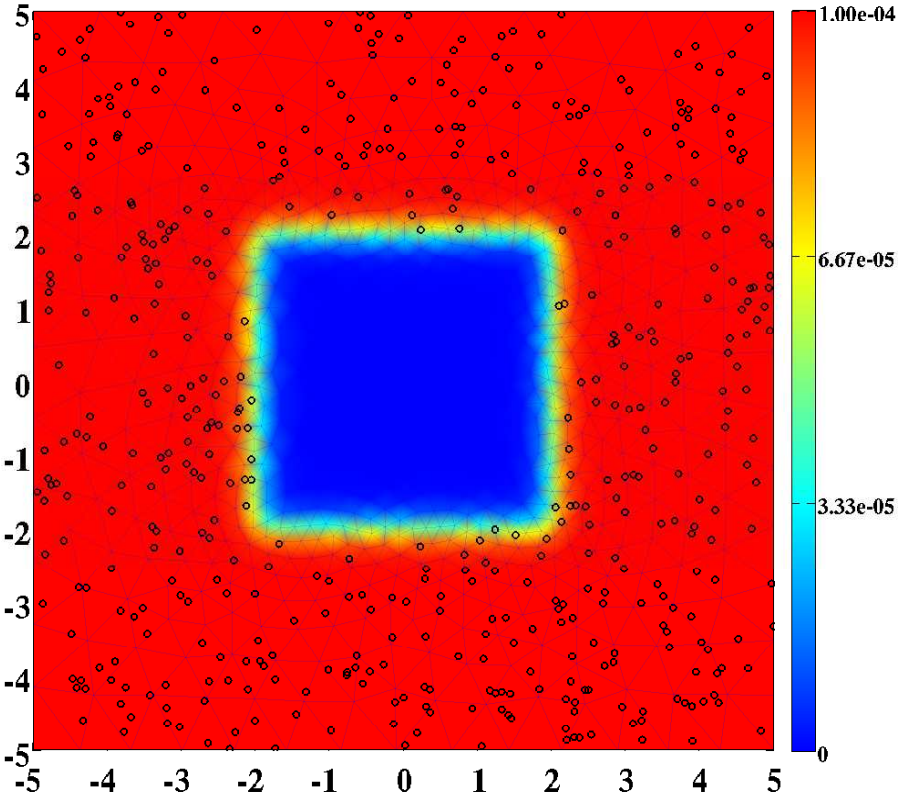

Figure 3.1: A graphical representation of the initial conditions. Depicted are the initial shape of the wounded area and, in color scale, the initial concentration of the collagen molecules (g/mm^3). The scale along both axes is in millimeters. The black circles mark the initial positions of the fibroblasts present in the modeled portion of dermal layer

$$w(\mathbf{X}) = \frac{1}{16}\left[1+\tanh\left(\frac{s_1-X}{2}\right)\right]\left[1+\tanh\left(\frac{s_1+X}{2}\right)\right]\times \left[1+\tanh\left(\frac{s_2-Y}{2}\right)\right]\left[1+\tanh\left(\frac{s_2+Y}{2}\right)\right]. \quad (3.29)$$

The values for the parameters s_1 and s_2 determine, respectively, the positions of the vertical segments of the wound boundary and the positions of the horizontal segments of the wound boundary. In this study $s_1 = s_2 = 2$ mm.

In the model PDGF molecules are present initially in the wounded area due to the early secretion of this signaling molecule by platelets that got trapped in the developing fibrin clot during coagulation. Using the general function for the shape of the wounded area, the following initial condition was used for the PDGF molecules:

$$c_P(\mathbf{X},0) = w(\mathbf{X})\, c^w. \tag{3.30}$$

Here c^w represents the maximum initial concentration of the signaling molecule in the wounded area. Furthermore, it was assumed that there are no TGF-β molecules and tPA molecules present at the onset of the inflammatory phase. Hence,

$$c_\beta(\mathbf{X},0) = 0, \tag{3.31}$$
$$c_t(\mathbf{X},0) = 0. \tag{3.32}$$

It was assumed that the geometrical distribution of the formed fibrin bundles is uniform throughout the wounded area. Therefore, the following initial condition was used for the fibrin bundles:

$$\Omega^f(\mathbf{X},0) = \left[\frac{w(\mathbf{X})}{3a_\rho^I}\right]\mathbf{I}. \tag{3.33}$$

In uninjured skin, the majority of the collagen bundles of the dermal layer run parallel to the surface of the skin, while only a small portion of the fibers are oriented out-of-plane [2, 13]. In this study, it was assumed that all collagen bundles are oriented parallel to the surface of the skin. Within the plane that runs parallel to the surface of the skin, it was assumed that the geometrical distribution of the collagen bundles is uniform. Hence, the following initial condition was used for the collagen bundles:

$$\Omega^c(\mathbf{X},0) = \left[\frac{1-w(\mathbf{X})}{2a_\rho^I}\right]\begin{bmatrix}0&0&0\\0&1&0\\0&0&1\end{bmatrix}. \tag{3.34}$$

At the onset of the inflammatory phase, there are no macrophages present in the domain of computation. Hence, $T_{M\Phi}(0) = 0$. Furthermore, it was presumed that there are 500 fibroblasts present in the portion of the dermal layer that is uninjured while there are no fibroblasts present in the wounded area. Hence, $T_N(0) = 500$. The initial position of the present fibroblasts in the unwounded dermis is random. Finally, all receptors on the outer cell membrane of all fibroblasts present initially in the domain of computation are unbound. Hence,

$$n_N^i(0) = 0 \quad \forall\, i \in \{1,\ldots,T_N(0)\}. \tag{3.35}$$

With respect to the initial condition for the displacement field, it was assumed that the displacements of the dermal tissue at the onset of the inflammatory phase are negligible. Hence,

$$\mathbf{u}(\mathbf{x},0) = \mathbf{0} \quad \forall \mathbf{x} \in \Omega_{\mathbf{x},0}. \tag{3.36}$$

In addition, it was assumed that the remodeling of the ECM has not yet begun at the onset of the inflammatory phase. Hence the effective fibroblast exposure time initially satisfies

$$\tau^i(0) = 0 \quad \forall i \in \{1, \ldots, N_E\}. \tag{3.37}$$

See Figure 3.1 for a graphical representation of initial conditions that have been used in this study.

With respect to the boundary conditions for the modeled constituents of the dermal, the following Robin boundary conditions were used for all time t and for all $\mathbf{x} \in \partial\Omega_{\mathbf{x},t}$, where $\partial\Omega_{\mathbf{x},t}$ is the boundary of the domain of computation in Eulerian coordinates:

$$\mathbf{n} \cdot \left[D_{c_P} \nabla c_P(\mathbf{x}, t) \right] = -\kappa c_P(\mathbf{x}, t), \tag{3.38}$$

$$\mathbf{n} \cdot \left[D_{c_\beta} \left(\rho^f(\mathbf{x}, t) \right) \nabla c_\beta(\mathbf{x}, t) \right] = -\kappa c_\beta(\mathbf{x}, t), \tag{3.39}$$

$$\mathbf{n} \cdot \left[D_{c_t} \left(\rho^f(\mathbf{x}, t) \right) \nabla c_t(\mathbf{x}, t) \right] = -\kappa c_t(\mathbf{x}, t). \tag{3.40}$$

Here κ is a constant that determines the rate with which the molecules leave the domain of computation on the boundary, and $\mathbf{n}$ is the unit outward pointing normal vector to the boundary. Finally, the following Dirichlet boundary condition was used for the mechanical component of the model for all time t and for all $\mathbf{x} \in \partial\Omega_{\mathbf{x},t}$:

$$\mathbf{u}(\mathbf{x}, t) = \mathbf{0}. \tag{3.41}$$

3.2.7. THE (RANGES OF THE) VALUES FOR THE PARAMETERS

Table 3.1 provides an overview of the (ranges of the) values for the parameters of the model. Unfortunately, accurate estimates for the values for many of the parameters of the model are, to the best of my knowledge, at present not available in the literature. A few values were taken directly from previously conducted studies. Furthermore, some values were estimated from results obtained in previously conducted studies. However, the majority of the values were estimated in this study. These latter values were chosen in such a way that a reasonable reproduction of the wound healing cascade in the case of healing by secondary intention is generated.

Table 3.1: An overview of the (ranges of the) values for the parameters of the model. The last column contains the references to the studies that were used for obtaining (estimates of) the values for the parameters. If (the range of) the value for a parameter was estimated in this study, then this is indicated by the abbreviation TW

Parameter	Value	Dimensions	Reference
D_{c_P}	10^{-2}	mm^2/h	[12]
$D_{c_\beta}^{\min}$	1.06×10^{-2}	mm^2/h	[5] & [23]
$D_{c_\beta}^{\max}$	1.06×10^{-1}	mm^2/h	[5] & [23]
a_ρ^I	10^4	mm^3/g	[24]
k_{c_β}	2.5×10^{-14}	$\mathrm{g}/(\mathrm{mm}^3\,\mathrm{h})$	TW
δ_ρ	1.5×10^{10}	$\mathrm{mm}^3/(\mathrm{g}\,\mathrm{h})$	[5]
$D_{c_t}^{\min}$	$7,11 \times 10^{-3}$	mm^2/h	[5] & [23]
$D_{c_t}^{\max}$	$1,41 \times 10^{-1}$	mm^2/h	[5] & [23]
k_{c_t}	5×10^{-14}	$\mathrm{g}/(\mathrm{mm}^3\,\mathrm{h})$	TW

Continued on the next page

Table 3.1 – *Continued from the previous page*

Parameter	Value	Dimensions	Reference
k_ρ^I	5×10^{-8}	g/(mm^3 h)	TW
k_ρ^{II}	10^{-7}	g/(mm^3 h)	TW
r_c	1.7×10^{-2}	mm	[26]
γ_m^u	1	1/h	[5]
γ_m^b	5×10^{11}	mm^3/(g h)	[5]
v	2.5×10^{-1}	mm/h	TW
$D_{M\Phi}$	3.33×10^{-4}	mm^2/h	TW
$\beta_{M\Phi}^l$	3.33×10^{-12}	g/mm^3	TW
$\beta_{M\Phi}$	$(0 - 7.50) \times 10^{10}$	mm^2/(g h)	TW
$d_{M\Phi}$	7.2×10^{12}	mm^3/g	TW
γ_f^u	1	1/h	[5]
γ_f^b	$(1 - 5) \times 10^{11}$	mm^3/(g h)	[5]
D_N	3.33×10^{-4}	mm^2/h	TW
s_N^u	9×10^2	–	TW
s_N	4.8×10	–	TW
p_N^l	7.5×10^{-1}	–	TW
p_N	4.8×10	h	TW
d_N	1.20×10^2	–	TW
E	10×10^{-1}	N/mm^2	[20]
ν	4.9×10^{-1}	–	[20]
P_0	2.08	N/mm^4	TW
k_τ	10^{11}	mm^3/(g h)	TW
Q_0	3.3×10^{-1}	N/mm^4	TW
c^w	10^{-11}	g/mm^3	[24]
κ	1	1/mm	TW

3.3. THE APPLIED NUMERICAL ALGORITHM

THE system of mathematical relations presented in the Section 3.2 is a complex system of equations that consists of various PDEs, SDEs, ODEs and stochastic processes. Consequently, obtaining an approximation of the solution for the primary variables of the model is not straightforward. Here an overview is presented of the different components that together form the core of the applied numerical algorithm.

For the kernel of the concrete expression of the algorithm, `MATLAB` was used [31]. Furthermore, the mesh generator developed by Persson and Strang was used for the generation of a conforming triangulation of the domain of computation [25]. The resulting mesh consisted of triangles that were gradually refined toward the boundary of the wounded area (See Figure 3.1 for a graphical representation of the triangulation of the domain of computation). A fixed time step Δt of half an hour was chosen. This time step was sufficiently small to obtain numerical stability.

Preceding the execution of the time-integration, the initial conditions for both the signaling molecules and the extracellular matrix molecules were mapped to the nodes of the generated mesh. Furthermore, the initial positions of the fibroblasts present in the uninjured portion of dermal layer were determined. After that, the time-integration was executed.

Every time step the change in the position of the cell centers of all cells present in the modeled portion of dermal layer due to chemotaxis, contact guidance and random movement was determined first. For this end, the Euler-Maruyama method was applied on the related portions of Equation (3.16) and Equation (3.19). In order to simulate the random movement of each cell, two independent samples were drawn from a Gaussian normal distribution with zero mean and variance Δt for each cell. The values of these samples provide the random displacement along both axes for each cell per time step.

Subsequently, new fibroblasts were added to the domain of computation at the positions of fibroblasts that were ready and able to proliferate, and fibroblasts that died due to apoptosis, were removed from the domain of computation. Then, new macrophages that transmigrated from the intravascular space to the extravascular space were added to the domain of computation and present macrophages that died due to apoptosis, were removed from the domain of computation. After that, differentiated cells such as differentiated pericytes and differentiated fibrocytes, were added to the domain of computation as new fibroblasts. Next, the change in the position of every individual cell due to collisions with other cells was determined and the positions of all cells were updated. Finally, cells that left the domain of computation due to, for example, random movement and collisions, were replaced by new cells. These latter new cells were placed on the boundary of the domain of computation at a random position. See Subsection 3.2.3 for more details about the implementation of processes such as proliferation, transmigration and apoptosis. Given that linear basis functions were used on the triangular elements of the triangulation, linear interpolation based on these basis functions was used to map the approximation of the solution for the concentrations of the PDGF molecules and the TGF-β molecules from the nodes of the mesh to the centers of the cells.

Next, the effective fibroblast exposure times of the elements in the triangulation were updated by using an IMEX method on Equation (3.26). That is, the positions of the cell centers of the fibroblasts were evaluated at the new point in time while the concentrations of the collagen molecules and the TGF-β molecules at the centroids of the elements were evaluated at the previous point in time. Linear interpolation was used to map the approximations of the solutions for the concentrations from the nodes of the mesh to the centroids of the elements.

Subsequently, the displacement field at the new point in time was determined by finding an approximate solution for the displacement field from Equation (3.20). For the discretization of this equation, a moving-grid finite-element method was used [10]. Here, the positions of the nodes of the triangulation were taken at the previous point in time, while the positions of the cell centers of the fibroblasts were evaluated at the new point in time. In order to simplify matters and save computation time, all cell boundaries were approximated by squares with a side length of $\sqrt{\pi} r_c$ mm. Consequently, Equation (3.23) was used for the mathematical description of the temporary forces. Based on the new displacement field, the position of the nodes of the triangulation, the position of the boundary of the wound and the positions of the centers of the cells were updated. Linear interpolation was used to map the approximation of the solution for the displacement field from the nodes of the mesh on the boundary of the wound and onto the centers of the cells.

After these steps, the approximations of the solutions for the concentrations of the

PDGF molecules, the tPA molecules, the fibrin bundles and the TGF-β molecules were determined consecutively from, respectively, Equation (3.2), Equation (3.8), Equation (3.7) and Equation (3.3). For the discretization of these equations, the moving-grid finite-element method was used together with either an IMEX method or the backward Euler time-integration method. The new positions of the cell centers of the macrophages, the new positions of the nodes of the triangulation and the new position of the boundary of the wound were used here. Furthermore, approximations of the solutions for other primary model variables at the new point in time were used in these equations where possible. If these values were not yet available, then approximations at the previous point in time were used.

Next, the proportion of the receptors on the outer membrane of each individual cell that was bound to a signaling molecule was updated by using the backward Euler time-integration method on Equation (3.13) and Equation (3.17). Hence, the approximations of the solutions for the concentrations of the PDGF molecules and the TGF-β molecules were taken at the new point in time. Linear interpolation was used to map the approximations of the solutions for the concentrations of the PDGF molecules and the TGF-β molecules from the nodes of the mesh to the centers of the cells.

Finally, the concentration and the orientation of the collagen bundles were updated by using the moving-grid finite-element method together with the backward Euler time-integration method on Equation (3.12). Hence, the approximation of the solution for the concentration of the fibrin bundles, the approximations of the proportion of the receptors on the outer membrane of the fibroblasts that were bound to a signaling molecule, the approximation of the direction of active movement of the fibroblasts, and the position of the cell centers of the fibroblasts were taken at the new point in time.

3.4. SIMULATION RESULTS

BASELINE simulation results are presented in Figures 3.2 through 3.5. Looking at Figure 3.2, it can be observed that the fibrin bundles in the wounded area are broken down gradually. The degradation of the fibrin bundles starts at the boundary of the wounded area as a consequence of the fact that the tPA molecules are released at the interface between the injured and the uninjured dermal tissue. Due to the slow diffusion of the tPA molecules throughout the modeled portion of dermal layer, the concentration of the tPA molecules rises gradually in the wounded area. This causes that the fibrin bundles deeper into the wounded area are also broken down in the long run. As can be observed in Figure 3.2, roughly all fibrin bundles in the wounded area have been broken down after 12 days.

Due to the early secretion of PDGF molecules by platelets that got trapped in the developing fibrin clot during coagulation, initially the concentration of this signaling molecule is high in the wounded area. This can be observed in Figure 3.2. Subsequently, the concentration of the PDGF molecules drops slowly over time due to diffusion. The diffusion of the PDGF molecules results in the development of a nonzero gradient profile for this signaling molecule. This causes a biased movement of macrophages present at the boundary of the wounded area, toward the center of the wound. This biased movement can be observed clearly in Figure 3.3. Furthermore, the diffusion of the PDGF molecules also leads to a gradual diminishing of the concentration of this molecule at

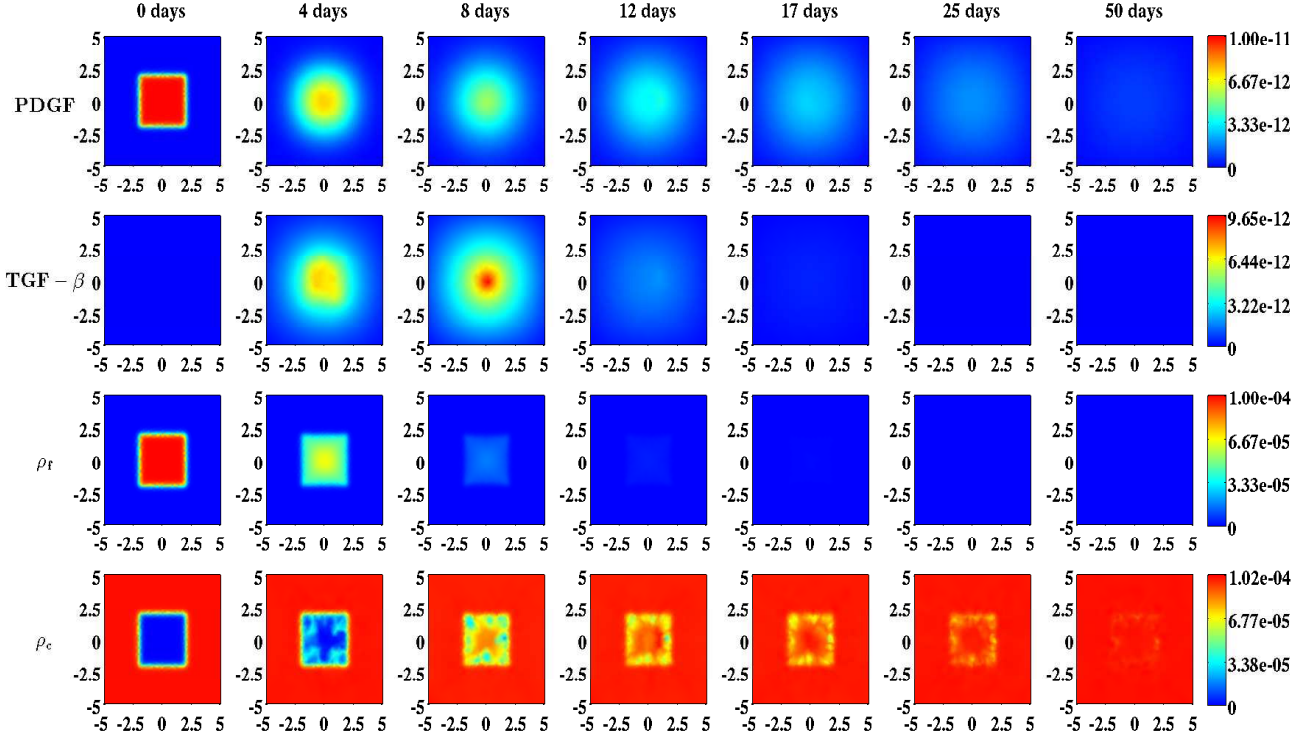

Figure 3.2: An overview of simulation results for continuous primary variables of the model when the value for the constant $\beta_{M\Phi}$ is 7.50×10^{10} mm^2/(g h) and the value for the receptor binding rate of the TGF-β molecules is 5×10^{11} mm^3/(g h). The values for the other parameters are equal to those depicted in Table 3.1. From top to bottom, the rows show the evolution over time of the concentration of, respectively, the PDGF molecules, the TGF-β molecules, the fibrin molecules and the collagen molecules. The color scales represent the concentrations, measured in g/mm^3. Within the subfigures, the scale along both axes is in millimeters

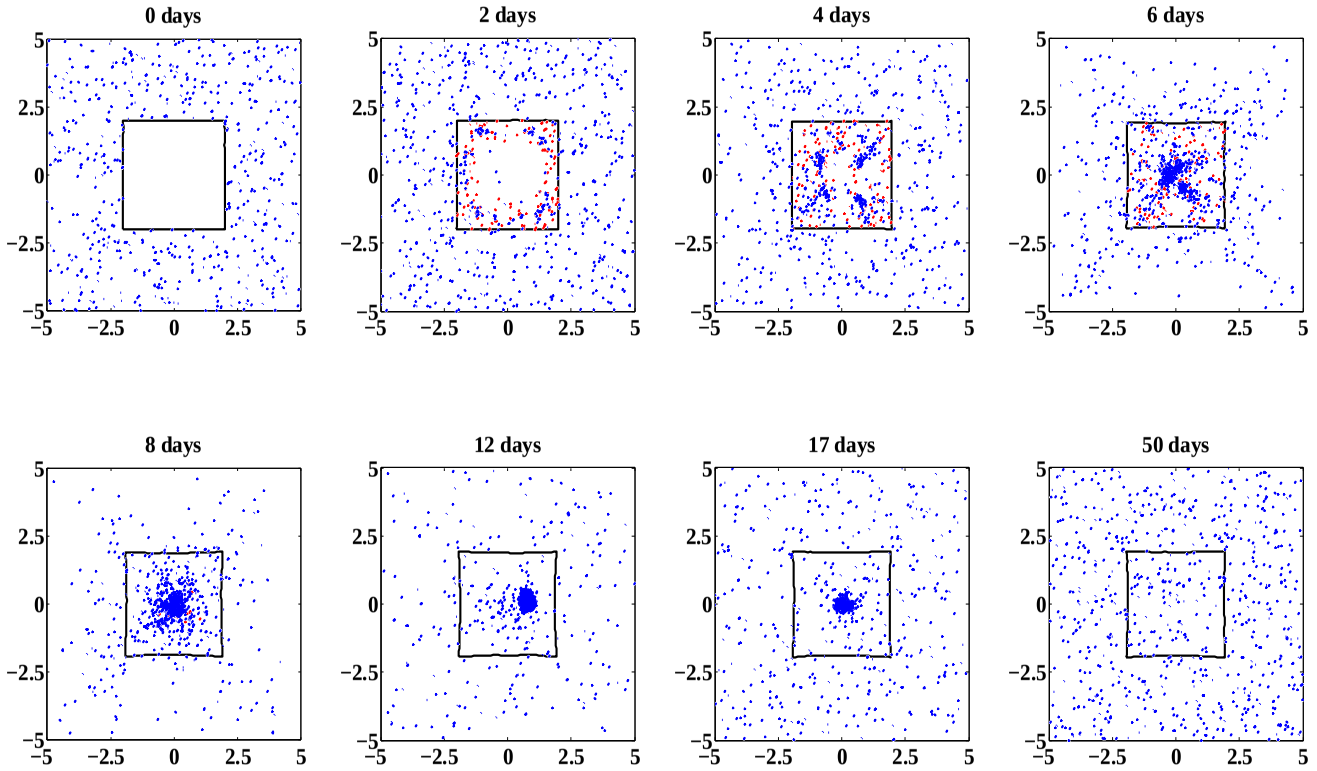

Figure 3.3: An overview of simulation results for the cell types of the model when the value for the constant $\beta_{M\Phi}$ is 7.50×10^{10} mm^2/(g h) and the value for the receptor binding rate of the TGF-β molecules is 5×10^{11} mm^3/(g h). The values for the other parameters are equal to those depicted in Table 3.1. The blue circles mark the positions of the cell centers of the fibroblasts and the red circles mark the positions of the cell centers of the macrophages. The black squares within the subfigures represent the (displaced) interface between the uninjured dermal tissue and the recovering wounded area. Within the subfigures, the scale along both axes is in millimeters

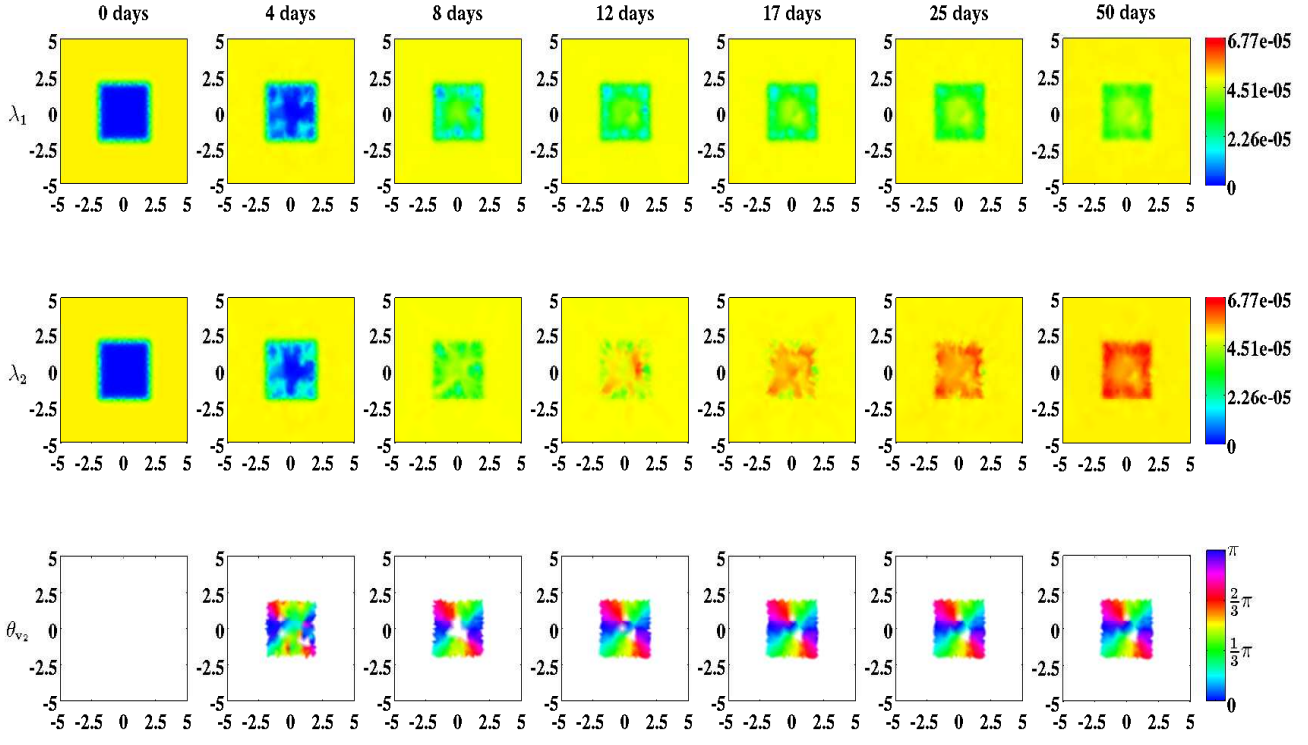

Figure 3.4: An overview of the evolution over time of the geometrical distribution of the collagen bundles during the healing of the wound. In this simulation the value for the constant $\beta_{M\Phi}$ is 7.50×10^{10} mm^2/(g h) and the value for the receptor binding rate of the TGF-β molecules is 5×10^{11} mm^3/(g h). The values for the other parameters are equal to those depicted in Table 3.1. λ_1 and λ_2 are the nonzero eigenvalues of the tensor Ω^c and $\theta_{\mathbf{v}2}$ is the angle between the eigenvector related to the largest eigenvalue λ_2 (where the third element of this eigenvector is larger than/equal to zero) and the positive horizontal axis. Within the subfigures on the bottom row the transparency (i.e., $\alpha(\mathbf{x},t)$) is set to either zero (opaque) or one (fully transparent) based on the following rule: if $(\lambda_2(\mathbf{x},t)-\lambda_1(\mathbf{x},t))/\lambda_1(\mathbf{x},t)>0.2$, then $\alpha(\mathbf{x},t)=0$, else $\alpha(\mathbf{x},t)=1$

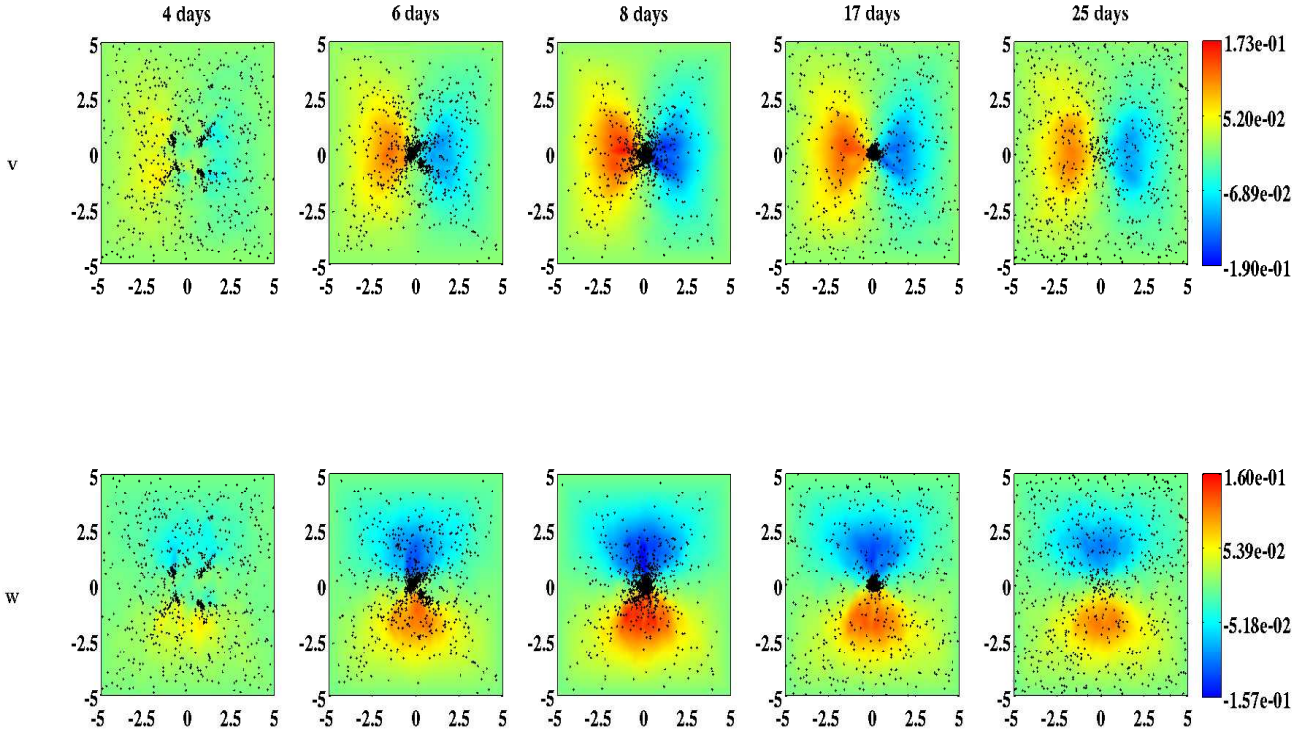

Figure 3.5: An overview of simulation results for the demonstration of the relationship between the position of the cell centers of the fibroblasts and the nonzero components of the displacement field. In this simulation the value for the constant $\beta_{M\Phi}$ is 7.50×10^{10} mm^2/(g h) and the value for the receptor binding rate of the TGF-β molecules is 5×10^{11} mm^3/(g h). The values for the other parameters are equal to those depicted in Table 3.1. The rows show the evolution over time of the displacement in, respectively, the horizontal direction and the vertical direction. The color scales represent the displacement, measured in mm. The black circles mark the positions of the cell centers of the fibroblasts. Within the subfigures, the scale along both axes is in millimeters

the interface between the uninjured and injured dermal tissue. Due to this, the concentration of the PDGF molecules becomes so low at a certain point in time that the transmigration of macrophages from the intravascular space to the extravascular space stops. This is also clearly visible in Figure 3.3. Subsequently, the number of macrophages drops slowly toward zero due to apoptosis. After 12 days, no more macrophages are present in the modeled portion of dermal layer.

The secretion of TGF-β molecules by macrophages results in a gradual rise of the concentration of this molecule. Together with the diffusion of this molecule, this leads to the development of a nonzero gradient profile for this signaling molecule. This can be observed in Figure 3.2. Subsequently, this causes a biased movement of fibroblasts present in the uninjured dermal tissue, toward the center of the wound. This biased movement can be observed clearly in Figure 3.3. Due to the fact that the number of macrophages drops slowly toward zero, the secretion of the TGF-β molecules gradually drops as well and finally the concentration of the TGF-β molecules diminishes toward zero as a consequence of the diffusion of the molecules. This leads to a reduction in the biased movement of the fibroblasts and finally the distribution of the cell density of the fibroblasts over the modeled portion of dermal layer becomes more or less uniform. This can be observed in Figure 3.3.

As soon as the fibroblasts enter the injured dermal tissue, these cells start secreting collagen molecules. As is clearly visible in Figure 3.2, this results in a gradual increase of the concentration of the collagen molecules in the wounded area. Since the fibroblasts are treated as discrete entities in the model, and since it was assumed that the secreted collagen molecules attach to the ECM instantaneously, the concentration profiles of the collagen molecules exhibit a discontinuous, spiky pattern over space for an extended period of time. After approximately 50 days, the concentration of the collagen molecules in the recovered wounded area has become more or less equal to the concentration of this molecule in the surrounding uninjured dermal tissue. However, contrary to the surrounding uninjured dermal tissue, the geometrical distribution of the new collagen bundles in the recovered wounded area is no longer uniform in the plane. Due to the biased movement of the fibroblasts toward the center of the wound during healing, the majority of the new collagen bundles are secreted in the direction of the center of the wounded area. This can be observed clearly in Figure 3.4.

Due to the gradually increasing cell density of the fibroblasts in the wounded area during healing, the generated temporary (pulling) forces become relatively large in the wounded area. Furthermore, the presence of fibroblasts in the wounded area causes the development of residual (plastic) forces in the wounded area as a consequence of the remodeling of the ECM. Taken together, this results in the development of a nonzero displacement field in the modeled portion of dermal layer and compaction of the wounded area (i.e., the inward movement of the interface between the injured and uninjured dermal tissue). These phenomena can be observed, respectively, in Figure 3.5 and Figure 3.3. As the cell density of the fibroblasts declines in the wounded area, the magnitude of the displacement field also declines. However, due to the remodeling of the ECM and hence the development of residual forces, the displacement field does not become approximately equal to zero throughout the modeled portion of dermal layer when the distribution of the cell density of the fibroblasts over the modeled portion of dermal layer

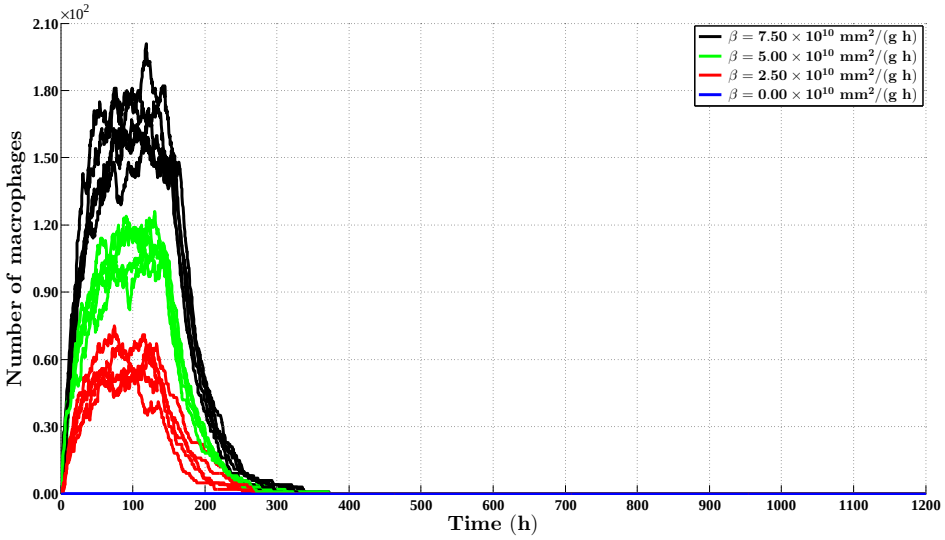

Figure 3.6: The evolution over time of the total number of macrophages present in the modeled portion of dermal layer for different values for the constant $\beta_{M\Phi}$ related to the number of monocytes that transmigrate per time step. In these simulations the value for the receptor binding rate of the TGF-β molecules is 5×10^{11} mm^3/(g h)). The values for the other parameters are equal to those depicted in Table 3.1. Each curve represents a separate simulation

becomes more or less uniform. This can be observed clearly in Figure 3.5. Consequently, this implies that the surface area of the recovered wounded area has diminished permanently. This can also be observed in Figure 3.7.

3.4.1. MACROPHAGE DEPLETION

In order to investigate the impact of macrophage depletion on the wound healing response, the value for the constant $\beta_{M\Phi}$ related to the number of monocytes that transmigrate per time step, was decreased in steps to zero over simulations. Decreasing the value for this constant has a clear influence on the maximum of the total number of macrophages that are present in the modeled portion of dermal layer. This can be observed in Figure 3.6. Looking at Figure 3.8, it can be observed that a gradual reduction in the total number of macrophages present in the wounded area results in a gradual increase of the amount of time that is needed to restore the presence of a collagen-rich ECM in the wounded area. If fewer macrophages are present in the wounded area, then the concentration of the TGF-β molecules in the wounded area is lower. Consequently, the proportion of the receptors on the outer cell membrane of the fibroblasts that is bound to TGF-β molecules is lower. This causes that the secretion rate of collagen molecules is lower, which subsequently results in an increase of the amount of time that is needed to restore the presence of a collagen-rich ECM. Interestingly, reducing the total number of macrophages present in the wounded area hardly changes the final geometrical distribution of the new collagen bundles in the recovered wounded area. Solely when the total number of macrophages present in the wounded area is equal to zero during

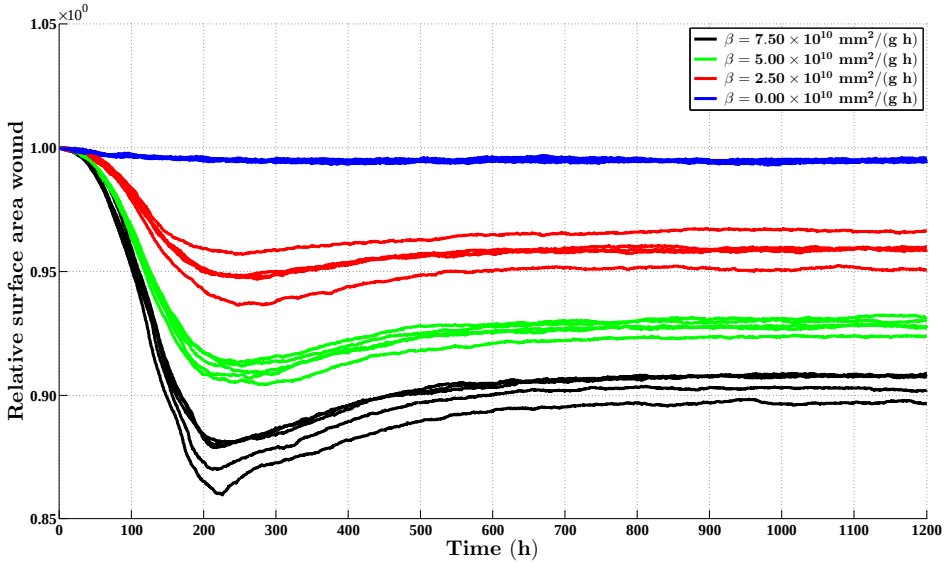

Figure 3.7: The evolution over time of the relative surface area of wounds for different values for the constant $\beta_{M\Phi}$ related to the number of monocytes that transmigrate per time step. In these simulations the value for the receptor binding rate of the TGF-β molecules is 5×10^{11} mm^3/(g h). The values for the other parameters are equal to those depicted in Table 3.1. Each curve represents a separate simulation

the entire simulation, the final distribution of the collagen bundles is far more uniform. This can be observed in Figure 3.9. If the total number of macrophages is equal to zero during the entire simulation, then no TGF-β molecules are secreted into the wounded area. Consequently, the fibroblasts will not display a biased movement, which implies subsequently that the orientation of the newly secreted collagen molecules will be random. Furthermore, it is interesting to observe in Figure 3.7 that a decrease in the total number of macrophages present in the wounded area has a positive effect on the final surface area of the recovered wounded area. That is, the lower the total number of macrophages, the higher the final surface area of the recovered wounded area. This latter effect is caused by the fact that less residual forces are generated when the concentration of the TGF-β molecules is lower.

3.4.2. APPLICATION OF A RECEPTOR ANTAGONIST

THE effect of adding a TGF-β receptor antagonist that does not activate the signal transduction pathways in fibroblasts, but competes with TGF-β molecules for binding to the receptors on the outer membrane of these cells, was mimicked by gradually decreasing the receptor binding rate of the TGF-β molecules. As can be observed in Figure 3.10, decreasing the binding rate has a clear impact on the maximum of the total number of fibroblasts present in the modeled portion of dermal layer. Due to the fact that a reduction in the binding rate leads to a reduction in the proportion of the receptors that is bound to TGF-β molecules, fewer fibroblasts will become ready to proliferate and this causes the observed reduction in the maximum of the total number of fibroblasts.

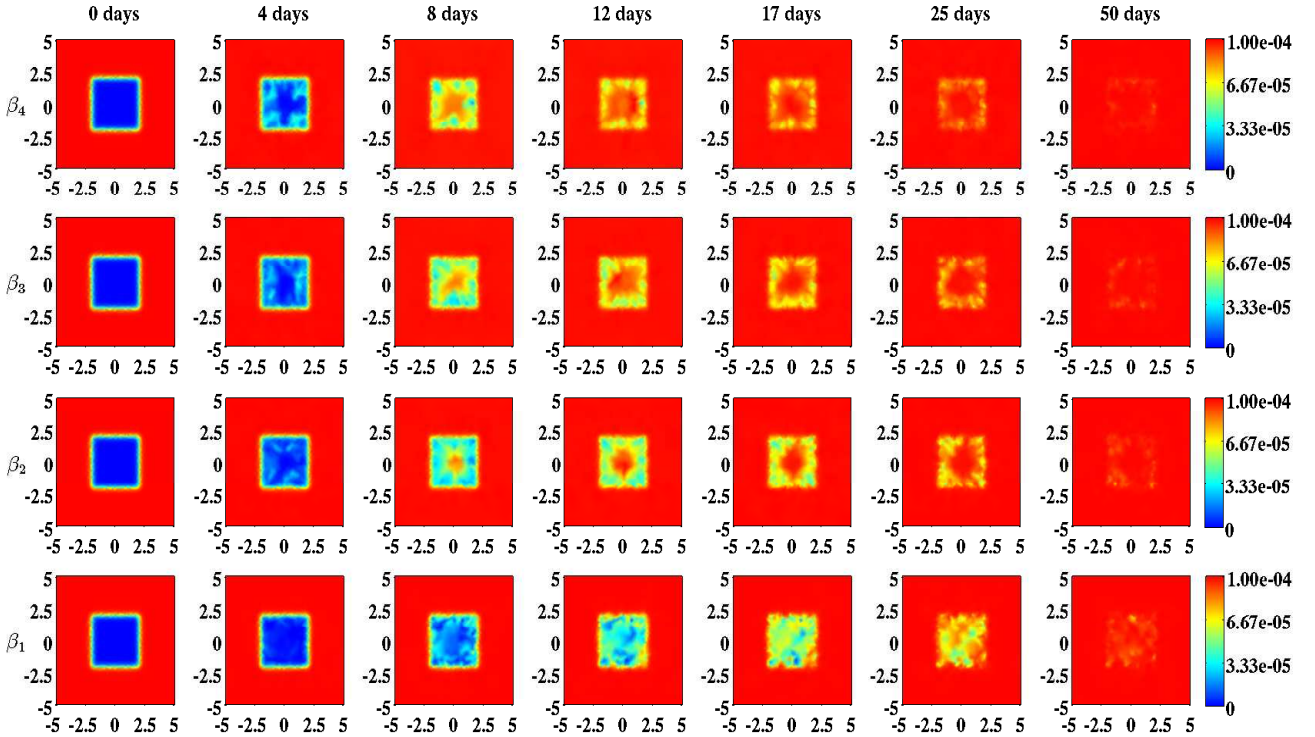

Figure 3.8: An overview of the evolution over time of the concentration of the collagen molecules for different values for the constant $\beta_{M\Phi}$ related to the number of monocytes that transmigrate per time step. Here $\beta_1 = 0.00 \times 10^{10}$ mm^2/(g h), $\beta_2 = 2.50 \times 10^{10}$ mm^2/(g h), $\beta_3 = 5.00 \times 10^{10}$ mm^2/(g h) and $\beta_4 = 7.50 \times 10^{10}$ mm^2/(g h). In these simulations the value for the receptor binding rate of the TGF-β molecules is 5×10^{11} mm^3/(g h). The values for the other parameters are equal to those depicted in Table 3.1. The color scales represent the concentrations, measured in g/mm^3. Within the subfigures, the scale along both axes is in millimeters

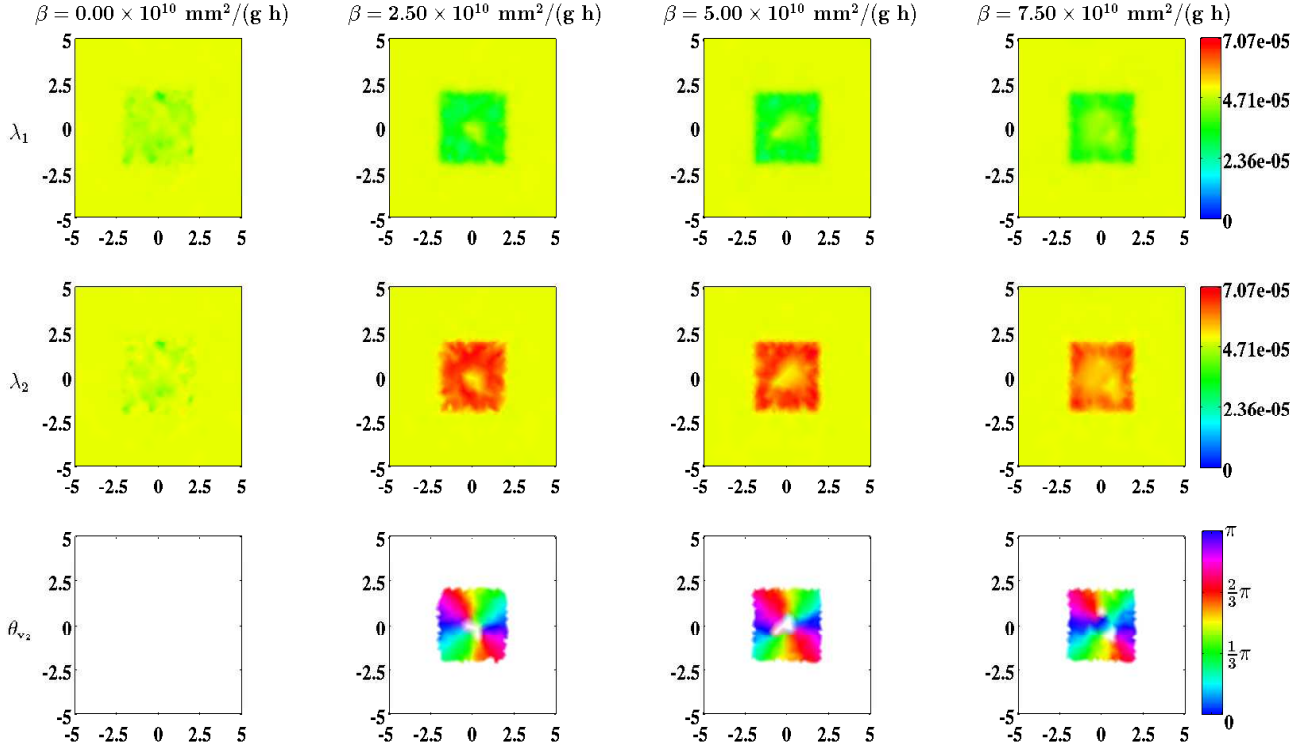

Figure 3.9: An overview of the geometrical distribution of the collagen bundles at day 50 for different values for the the constant $\beta_{M\Phi}$ related to the number of monocytes that transmigrate per time step. In these simulations the value for the receptor binding rate of the TGF-β molecules is 5×10^{11} mm^3/(g h). The values for the other parameters are equal to those depicted in Table 3.1. λ_1 and λ_2 are the nonzero eigenvalues of the tensor Ω^c and $\theta_{\mathbf{v}2}$ is the angle between the eigenvector related to the largest eigenvalue λ_2 (where the third element of this eigenvector is larger than/equal to zero) and the positive horizontal axis. Within the subfigures on the bottom row the transparency (i.e., $\alpha(\mathbf{x}, t)$) is set to either zero (opaque) or one (fully transparent) based on the following rule: if $(\lambda_2(\mathbf{x}, t) - \lambda_1(\mathbf{x}, t))/\lambda_1(\mathbf{x}, t) > 0.2$, then $\alpha(\mathbf{x}, t) = 0$, else $\alpha(\mathbf{x}, t) = 1$

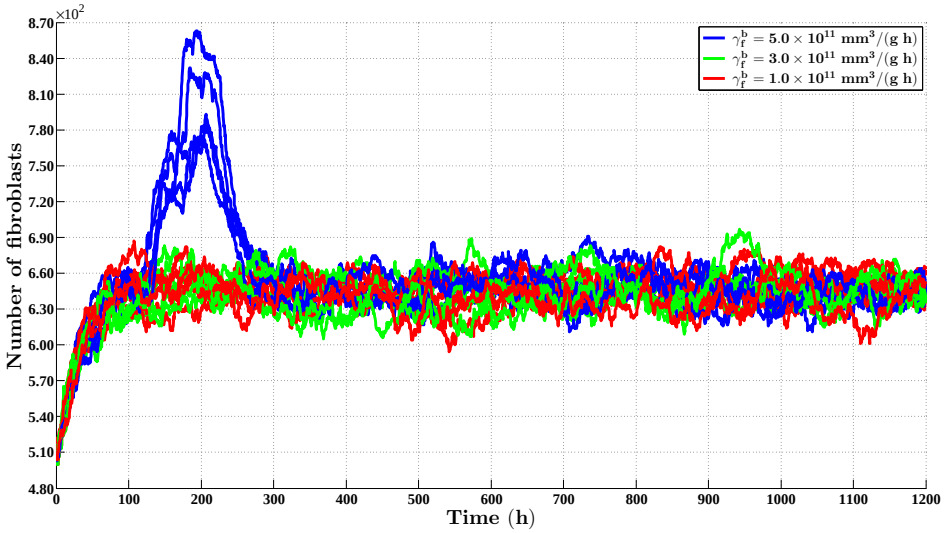

Figure 3.10: The evolution over time of the total number of fibroblasts present in the modeled portion of dermal layer for different values for the receptor binding rate of the TGF-β molecules. In these simulations the value for the constant $\beta_{M\Phi}$ is 7.50×10^{10} mm^2/(g h). The values for the other parameters are equal to those depicted in Table 3.1. Each curve represents a separate simulation

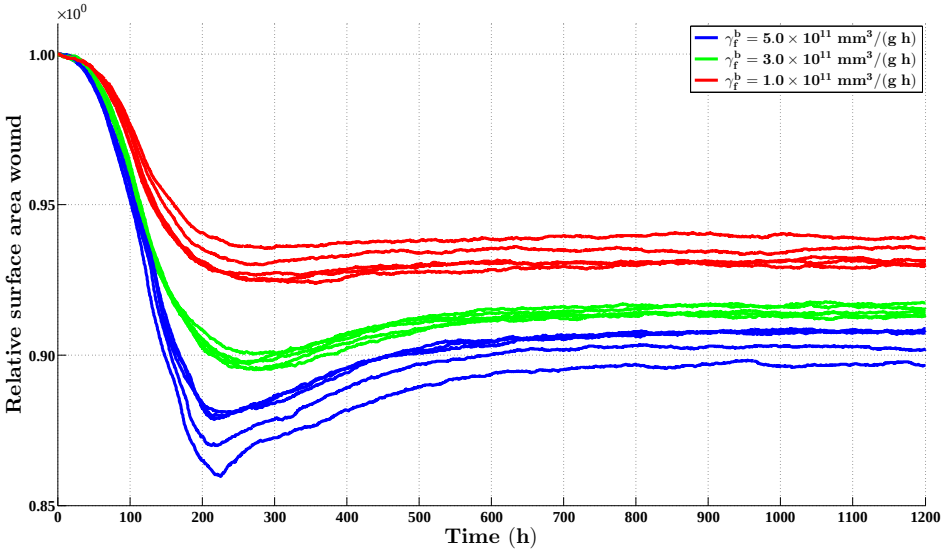

Figure 3.11: The evolution over time of the relative surface area of wounds for different values for the receptor binding rate of the TGF-β molecules. In these simulations the value for the constant $\beta_{M\Phi}$ is 7.50×10^{10} mm^2/(g h). The values for the other parameters are equal to those depicted in Table 3.1. Each curve represents a separate simulation

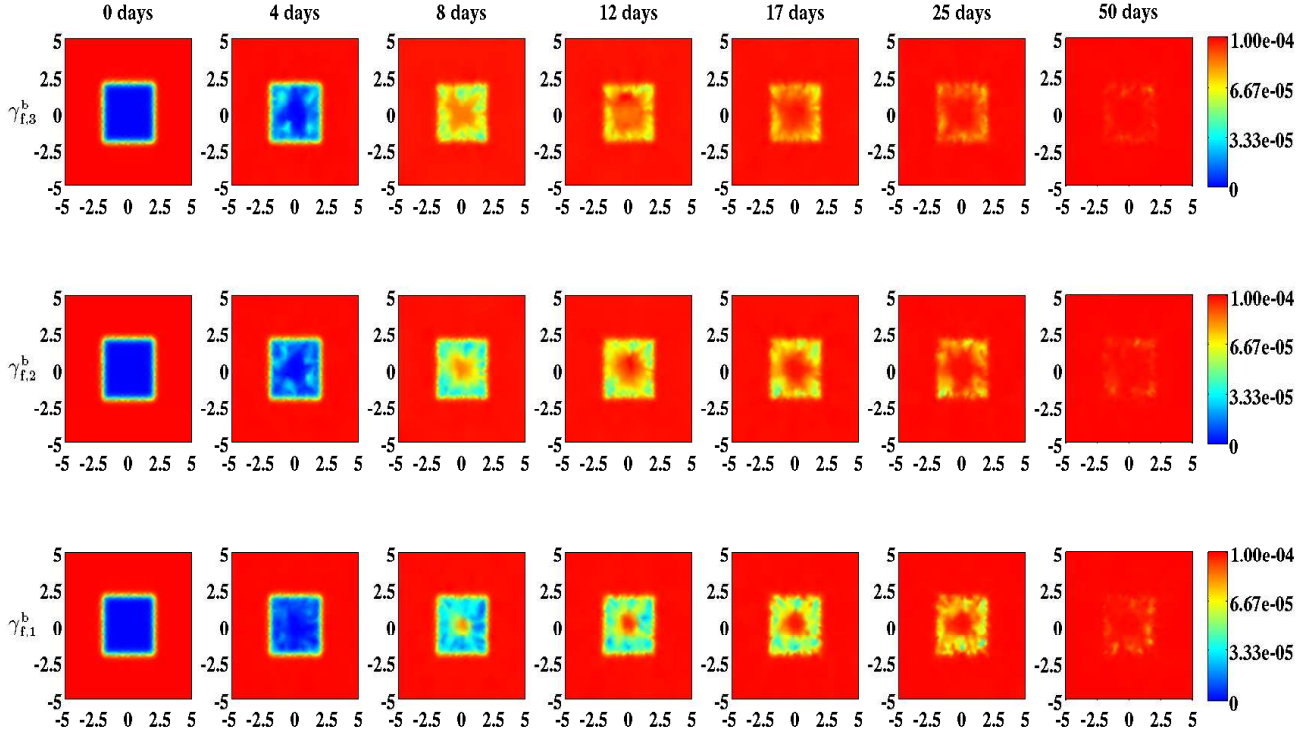

Figure 3.12: An overview of the evolution over time of the concentration of the collagen molecules for different values for the receptor binding rate of the TGF-β molecules. In these simulations the value for the constant $\beta_{M\Phi}$ is 7.50×10^{10} mm^2/(g h). The values for the other parameters are equal to those depicted in Table 3.1. The color scales represent the concentrations, measured in g/mm^3. Within the subfigures, the scale along both axes is in millimeters. Here $\gamma^b_{f,1} = 1 \times 10^{11}$ mm^3/(g h), $\gamma^b_{f,2} = 3 \times 10^{11}$ mm^3/(g h) and $\gamma^b_{f,3} = 5 \times 10^{11}$ mm^3/(g h)

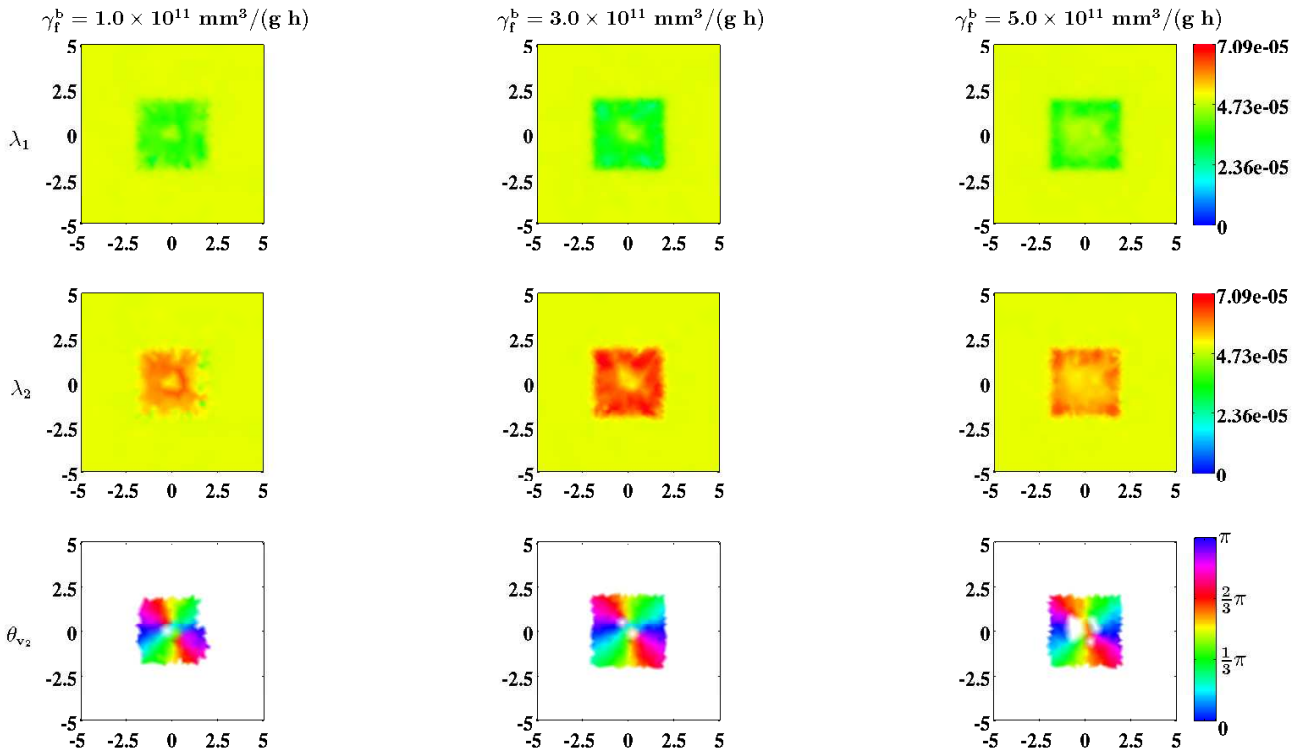

Figure 3.13: An overview of the geometrical distribution of the collagen bundles at day 50 for different values for the receptor binding rate of the TGF-β molecules. In these simulations the value for the constant $\beta_{M\Phi}$ is 7.50×10^{10} mm^2/(g h). The values for the other parameters are equal to those depicted in Table 3.1. λ_1 and λ_2 are the nonzero eigenvalues of the tensor Ω^c and $\theta_{\mathbf{v}2}$ is the angle between the eigenvector related to the largest eigenvalue λ_2 (where the third element of this eigenvector is larger than/equal to zero) and the positive horizontal axis. Within the subfigures on the bottom row the transparency (i.e., $\alpha(\mathbf{x}, t)$) is set to either zero (opaque) or one (fully transparent) based on the following rule: if $(\lambda_2(\mathbf{x}, t) - \lambda_1(\mathbf{x}, t))/\lambda_1(\mathbf{x}, t) > 0.2$, then $\alpha(\mathbf{x}, t) = 0$, else $\alpha(\mathbf{x}, t) = 1$

Furthermore, it is interesting to observe in Figure 3.11 that a reduction in the binding rate results in an increase of the final surface area of the recovered wounded area. This is probably mainly caused by the fact that fewer fibroblasts are present in the wounded area when the binding rate is lower. As a consequence, the build-up of residual forces in the wounded area is smaller, which implies subsequently that final surface area of the recovered wounded area is larger.

Looking at Figure 3.12, it can be observed that a reduction in the binding rate of the TGF-β molecules also results in an increase of the amount of time that is needed to restore the presence of a collagen-rich ECM in the wounded area. This latter effect is caused by the fact that the reduction in the binding rate of the TGF-β molecules results in both a reduction in the secretion rate of collagen molecules, and a reduction in the total number of fibroblasts that are present in the wounded area. Finally, it is interesting to observe in Figure 3.13 that an average binding rate results in the highest proportion of the collagen bundles being secreted in the direction of the center of the wounded area while both a relatively high and a relatively low binding rate result in a lower proportion of the collagen bundles being secreted in the direction of the center of the wounded area. Looking more closely at Figure 3.13, it can be observed that the proportion of the collagen bundles that is secreted in the direction of the center of the wound is especially lower when the binding rate is relatively low.

3.5. CONCLUSIONS

In this chapter an extended version of the mechano-chemical hybrid model developed by Boon *et al.* [4] has been presented in order to investigate how certain components of the wound healing response might influence the degree of wound contraction and the development of the geometrical distribution of newly formed collagen bundles in these wounds. Looking at the baseline simulation results presented in Figures 3.2 through 3.5, it can be observed that certain components of the healing response in the case small wounds that heal by secondary intention without complications, can be reproduced quite reasonably. For instance, the time window during which macrophages are present in the wounded area and the amount of time it takes to restore the presence of a collagen-rich ECM in the recovering wounded area coincide quite nicely with *in vivo* experimental observations [9, 19]. In addition, it is interesting to observe that, in accordance with experimental observations, the majority of the newly secreted collagen bundles is oriented toward the center of the wound [36]. Furthermore, the development of residual stresses within the dermal layer can be reproduced, as well as the initial compaction and subsequent partial dilatation of the recovering wounded area (if the transmigration of monocytes into the extravascular space is sufficiently large (See Figure 3.7)).

One of the most important cell types involved in the healing of dermal wounds is the macrophage [6]. Macrophages perform several important functions such as antigen-presentation to T lymphocytes and phagocytosis of debris. Furthermore, this cell type secretes many different signaling molecules that stimulate important processes such as angiogenesis, collagen synthesis and cell differentiation [19]. Therefore, it is no surprise that previously obtained experimental results demonstrated that a lack of properly functioning macrophages in the recovering wounded area resulted in a delayed wound healing response [18, 21]. Interestingly, the simulation results depicted in Figure 3.8 also

show that the depletion of macrophages results in a delayed wound healing response.

Furthermore, the simulation results presented in Figure 3.9 show that reducing the total number of macrophages present in the wounded area hardly reduces the non-uniformity of the geometrical distribution of the new collagen bundles in the recovering wounded area at day 50. Solely when the total number of macrophages present in the wounded area is equal to zero during the entire simulation, the distribution of the collagen bundles in the recovering wounded area becomes approximately similar to the distribution of the bundles in the surrounding uninjured dermal tissue. In addition, the simulation results presented in Figure 3.7 show that a reduction in the total number of macrophages results in an increase of the final surface area of the recovered wounded area.

Finally, looking at the results presented in Figure 3.11 and Figure 3.13, related to the imitation of the application of a TGF-β receptor antagonist, it is interesting to observe that, in accordance with experimental results obtained by Huang *et al.* [14], the application of such an antagonist resulted in an increase of the surface area of the recovering wounded area and a more uniform distribution of the collagen bundles in the recovering wounded area when sufficient amounts of antagonist are applied on the wounded area.

REFERENCES

[1] Abe R, Donneley S, Peng T, Bucala R, Metz C (2001) Peripheral blood fibrocytes: differentiation pathway and migration to wound sites. J Immunol 166:756–762

[2] Annaidh A, Bruyère K, Destrade M, Gilchrist M, Maurini C, Otténio M, Saccomandi G (2012) Automated estimation of collagen fibre dispersion in the dermis and its contribution to the anisotropic behaviour of skin. Ann Biomed Eng 40:1666–1678

[3] Barocas V, Tranquillo R (1997) An anisotropic biphasic theory of tissue-equivalent mechanics: the interplay among cell traction, fibrillar network deformation, fibril alignment, and cell contact guidance. AMSE J Biomech Eng 119:137–145

[4] Boon W, Koppenol D, Vermolen F (2016) A multi-agent cell-based model for wound contraction. J Biomech 49:1388–1401

[5] Cumming B, McElwain D, Upton Z (2010) A mathematical model of wound healing and subsequent scarring. J R Soc Interface 7:19–34

[6] Delavary B, Van der Veer W, Van Egmond M, Niessen F, Beelen R (2011) Macrophages in skin injury and repair. Immunobiology 216:753–762

[7] Deuel T, Senior R, Huang J, Griffin G (1982) Chemotaxis of monocytes and neutrophils to platelet-derived growth factor. J Clin Invest 69:1046–1049

[8] Dickinson R, Guido S, Tranquillo R (1994) Biased cell migration of fibroblasts exhibiting contact guidance in oriented collagen gels. Ann Biomed Eng 22:342–356

[9] Enoch S, Leaper D (2007) Basic science of wound healing. Surgery 26:31–37

[10] George U, Stéphanou A, Madzvamuse A (2013) Mathematical modelling and numerical simulations of actin dynamics in the eukaryotic cell. J Math Biol 66:547–593

[11] Gharzi A, Reynolds A, Jahoda C (2003) Plasticity of hair follicle dermal cells in wound healing and induction. Exp Dermatol 12:126–136

[12] Haugh J (2006) Deterministic model of dermal wound invasion incorporating receptor-mediated signal transduction and spatial gradient sensing. Biophys J 90:2297–2308

[13] Holzapfel G (2001) Biomechanics of soft tissue. In: Lemaître J (ed) Handbook of materials behavior models, 1st edn, Academic Press, Cambridge, United Kingdom, chap 10.11, pp 1057–1071

[14] Huang J, Wang Y, Ling T, Chuang S, Johnson F, Huang S (2002) Synthetic TGF-beta antagonist accelerates wound healing and reduces scarring. FASEB J 16:1269–1270

[15] Kalluri R, Neilson E (2003) Epithelial-mesenchymal transition and its implications for fibrosis. J Clin Invest 112:1776–1784

[16] Kwan P, Desmoulière A, Tredget E (2012) Molecular and cellular basis of hypertrophic scarring. In: Herndon D (ed) Total Burn Care, 4th edn, Elsevier Inc, Philadelphia, Pennsylvania, chap 45, pp 495–505.e5

[17] Lai W, Rubin D, Krempl E (1999) Introduction to Continuum Mechanics, 3rd edn. Butterworth Heinemann Ltd, Waltham, Massachusetts

[18] Leibovich S, Ross R (1975) The role of the macrophage in wound repair. A study with hydrocortisone and antimacrophage serum. Am J Pathol 78:71–100

[19] Li J, Chen J, Kirsner R (2007) Pathophysiology of acute wound healing. Clin Dermatol 25:9–18

[20] Liang X, Boppart S (2010) Biomedical properties of *in vivo* human skin from dynamic optical coherence elastography. IEEE T Bio-Med Eng 57:953–959

[21] Lucas T, Waisman A, Ranjan R, Roes J, Krieg T, Muller W, Roers A, Eming S (2010) Differential roles of macrophages in diverse phases of skin repair. J Immunol 184:3964–3977

[22] Mori L, Bellini A, Stacey M, Schmidt M, Mattoli S (2005) Fibrocytes contribute to the myofibroblast population in wounded skin and originate from the bone marrow. Exp Cell Res 304:81–90

[23] Murphy K, Hall C, Maini P, McCue S, McElwain D (2012) A fibrocontractive mechanochemical model of dermal wound closure incorporating realistic growth factor kinetics. B Math Biol 74:1143–1170

[24] Olsen L, Sherratt J, Maini P (1995) A mechanochemical model for adult dermal wound contraction and the permanence of the contracted tissue displacement profile. J Theor Biol 177:113–128

[25] Persson PO, Strang G (2004) A simple mesh generator in MATLAB. SIAM Rev 46:329–345

[26] Pizzo A, Kokini K, Vaughn L, Waisner B, Voytik-Harbin S (2005) Extracellular (ECM) microstructural composition regulates local cell-ECM biomechanics and fundamental fibroblast behavior: a multidimensional perspective. J Appl Physiol 98:1909–1921

[27] Postlethwaite A, Keski-Oja J, Moses H, Kang A (1987) Stimulation of the chemotactic migration of human fibroblasts by transforming growth factor β. J Exp Med 165:251–256

[28] Quan T, Cowper S, Wu S, Bockenstedt L, Bucala R (2004) Circulating fibrocytes: collagen-secreting cells of the peripheral blood. Int J Biochem Cell B 36:598–606

[29] Roberts A, Sporn M, Assoian R, Smith J, Roche N, Wakefiled L, Heine U, Liotta L, Falanga V, Kehrl J, Fauci A (1986) Transforming growth factor type β: Rapid induction of fibrosis and angiogenesis *in vivo* and stimulation of collagen formation *in vitro*. P Natl Acad Sci USA 83:4167–4171

[30] Steele J (2001) Stochastic calculus and financial applications, vol 45. Springer Science & Business Media, Berlin, Germany

[31] The MathWorks Inc (2014) `MATLAB` version 8.3.0.532 (R2014a)

[32] Tranquillo R, Murray J (1992) Continuum model of fibroblast-driven wound contraction: inflammation-mediation. J Theor Biol 158:135–172

[33] Vermolen F, Gefen A (2012) A semi-stochastic cell-based formalism to model the dynamics of migration of cells in colonies. Biomech Model Mechanobiol 11:183–195

[34] Vermolen F, Gefen A (2015) Semi-stochastic cell-level computational modelling of cellular forces: application to contractures in burns and cyclic loading. Biomech Model Mechanobiol 14:1181–1195

[35] Vermolen F, Javierre E (2012) A finite-element model for healing of cutaneous wounds combining contraction, angiogenesis and closure. J Math Biol 65:967–996

[36] Welch M, Odland G, Clark R (1990) Temporal relationships of *F*-actin bundle formation, collagen and fibronectin matrix assembly, and fibronectin receptor expression to wound contraction. J Cell Biol 110:133–145

[37] Wu L, Yu Y, Galiano R, Roth S, Mustoe T (1997) Macrophage colony-stimulating factor accelerates wound healing and upregulates TGF-β1 mRNA levels through tissue macrophages. J Surg Res 72:162–169

4

IMPLICATIONS FROM A CONTINUUM MODEL FOR THE SIMULATION OF THE HEALING OF LARGE WOUNDS

A continuum hypothesis-based model is presented for the simulation of the healing of large wounds in order to investigate how certain components of the wound environment and the wound healing response might influence the contraction of the wound and the development of the geometrical distribution of collagen bundles in the recovering wounded area. Since wound contraction mainly takes place in the dermal layer of the skin, solely a portion of this layer was included explicitly into the model. This portion of dermal layer is modeled as an orthotropic continuous solid with bulk mechanical properties that are locally dependent on both the local concentration and the local geometrical distribution of the collagen bundles. With respect to the constituents of the recovering dermal layer, the following components were selected as primary model variables: fibroblasts, myofibroblasts, a generic signaling molecule and collagen bundles. All components of the model are modeled as continuous entities. For the representation of the collagen bundles a tensorial approach was used. Wound contraction is caused in the model by temporary pulling forces. These pulling forces are generated by myofibroblasts which are present in the recovering wounded area. With respect to the dynamic regulation of the geometrical distribution of the collagen bundles, it was assumed that a portion of the collagen molecules are deposited and reoriented in the direction of movement of the (myo)fibroblasts. The remainder of the newly secreted collagen molecules are deposited by ratio in the direction of the present collagen bundles.

This chapter is based on content of the articles "A biomechanical mathematical model for the collagen bundle distribution-dependent contraction and subsequent retraction of healing dermal wounds" [16] and "A mathematical model for the simulation of the contraction of burns" [15].

With the developed model, it is possible to reproduce certain qualitative features of the dermal wound healing response. Firstly, the restoration of the presence of fibroblasts in the wounded area can be reproduced. Secondly, the initial expansion and subsequent reduction of the myofibroblast population in the wounded area during the execution of the wound healing response can be reproduced. Thirdly, it is possible to reproduce the restoration of a collagen-rich extracellular matrix in the recovering wounded area. Fourthly, the contraction and the subsequent retraction of the wounded area can be reproduced. Finally, in accordance with experimental observations, it is also possible to reproduce the permanent increase in the portion of the collagen bundles that runs parallel to the surface of the skin as a consequence of the execution of the wound healing process.

Simulation results show that the distribution of the collagen bundles influences the evolution over time of both the shape of the recovering wounded area and the degree of overall contraction of the wounded area. Interestingly, these effects are solely a consequence of alterations in the initial overall distribution of the collagen bundles, and not a consequence of alterations in the evolution over time of the different cell densities and concentrations of the modeled constituents. In addition, the evolution over time of the shape of the wound is also influenced by the orientation of the collagen bundles relative to the wound while this relative orientation does not influence the evolution over time of the relative surface area of the wound.

Finally, the simulation results show that ultimately the majority of the collagen molecules ends up permanently oriented toward the center of the wound and in the plane that runs parallel to the surface of the skin when the dependence of the direction of deposition / reorientation of collagen molecules on the direction of movement of cells is included into the model. If this dependence is not included, then this will result ultimately in newly generated tissue with a collagen bundle-distribution that is exactly equal to the collagen-bundle distribution of the surrounding uninjured tissue.

4.1. INTRODUCTION

IN Section 4.2 a detailed description of the model is presented. In Section 4.3, a short overview of the applied numerical algorithm for the generation of the computer simulations is presented. The simulation results are presented in Section 4.4. Finally, the simulation results are discussed in Section 4.5.

4.2. DEVELOPMENT OF THE MATHEMATICAL MODEL

IN order to simulate the deposition of collagen bundles and the contraction process, some of the subprocesses that take place during the proliferative phase and the remodeling phase of the wound healing cascade were included into the model [7]. With respect to the subprocesses that are executed during the proliferative phase the following subprocesses were selected: fibroplasia and wound contraction.

Since wound contraction mainly takes place in the dermal layer of the skin, solely a portion of this layer was included explicitly into the model. The dermal layer is modeled as an anisotropic continuous solid with bulk mechanical properties that are locally dependent on both the local concentration and the local geometrical distribution of the

collagen bundles. Due to the fact that the collagen bundles are represented by means of a symmetric tensor, the dermal layer has material properties that differ locally along three mutually-orthogonal twofold axes of rotational symmetry. These axes coincide with the lines that pass through the individual material points of the dermal layer and run parallel to the individual eigenvectors of the tensor that represents the collagen bundles (See Subsection 4.2.3 for further details). Therefore, the dermal layer is actually modeled as an orthotropic material [18]. In addition, it was assumed that it is appropriate to apply the infinitesimal strain theory in this model. With respect to the mechanical component of the model, the displacement of the dermal layer ($\mathbf{u}$) was chosen as primary model variable. Furthermore, the following four constituents of the dermal layer were selected as primary model variables: fibroblasts (N), myofibroblasts (M), collagen bundles (Ω^{ρ}) and a generic signaling molecule (c).

The continuum hypothesis-based framework of Tranquillo and Murray [41] was used as basis for the model. This framework consists of the following general set of conservation equations:

$$\frac{\partial z_i}{\partial t} + \nabla \cdot [z_i \mathbf{v}] = -\nabla \cdot \mathbf{J}_i + R_i, \tag{4.1a}$$

$$-\nabla \cdot \sigma = \mathbf{f}. \tag{4.1b}$$

Equation (4.1a) is the mass conservation equation for the cell density / concentration of constituent i of the dermal layer and Equation (4.1b) is the reduced conservation equation for the linear momentum of the dermal layer. It was assumed that the inertial forces that work on the dermal layer are negligible, and therefore, the conservation equation for the linear momentum of the dermal layer reduced to the above force balance equation. Within the above equations, z_i represents the cell density / concentration of constituent i, $\mathbf{v}$ represents the displacement velocity of the dermal layer, $\mathbf{J}_i$ represents the flux associated with constituent i per unit area, R_i represents the (bio)chemical kinetics associated with constituent i, σ represents the Cauchy stress tensor associated with the dermal layer, and $\mathbf{f}$ represents the total body force working on the dermal layer. Given the chosen primary model variables, $i \in \{N, M, c, \Omega^{\rho}_{jk}\}$ holds with $j,k \in \{1,2,3\}$. In the remainder of the text of this chapter, z_N has been replaced by N, z_M has been replaced by M, z_c has been replaced by c, and $z_{\Omega^{\rho}_{jk}}$ has been replaced by Ω^{ρ}_{jk}.

4.2.1. THE CELLS

THE random movement of both fibroblasts and myofibroblasts through the dermal layer and the directed movement of both fibroblasts and myofibroblasts up the gradient of the signaling molecule were incorporated into the model. The random movement of the cells is modeled by means of cell density-dependent Fickian diffusion and the directed movement of the cells is modeled by means of a simple model for chemotaxis [10]:

$$\mathbf{J}_N = -D_F F \nabla N + \chi_F N \nabla c, \tag{4.2}$$

$$\mathbf{J}_M = -D_F F \nabla M + \chi_F M \nabla c, \tag{4.3}$$

where

$$F = N + M. \tag{4.4}$$

The parameter D_F is the cell density-dependent (myo)fibroblast random motility coefficient. The parameter χ_F is the chemotactic parameter that depends on both the binding rate and the unbinding rate of the signaling molecule with its receptor, and the concentration of this receptor on the cell surface of the (myo)fibroblasts. The signaling molecule transforming growth factor-β (TGF-β) is a good example of a molecule that act as a strong attracting stimulus for (myo)fibroblasts [35].

Furthermore, the proliferation of both fibroblasts and myofibroblasts were incorporated into the model by using two nearly identical adjusted logistic growth models. The difference between the two growth models is that myofibroblasts solely divide in the presence of the signaling molecule while fibroblasts also divide without the presence of the signaling molecule. The actual proliferation rate of both cell types is dependent on the concentration of the signaling molecule. Additionally, the cell differentiation of fibroblasts into myofibroblasts under the influence of the signaling molecule was incorporated into the model. Examples of signaling molecules that can stimulate both the up-regulation of the proliferation rate and the cell differentiation rate of fibroblasts into myofibroblasts are certain members of the family of TGF-β molecules [48]. Finally, the removal of (myo)fibroblasts from the dermal layer by means of apoptosis was also incorporated into the model. Taken together, the following was obtained:

$$R_N = r_F \left[1 + \frac{r_F^{\max} c}{a_c^I + c} \right] [1 - \kappa_F F] N^{1+q} - k_F c N - \delta_N N, \tag{4.5}$$

$$R_M = r_F \left\{ \frac{\left[1 + r_F^{\max}\right] c}{a_c^I + c} \right\} [1 - \kappa_F F] M^{1+q} + k_F c N - \delta_M M. \tag{4.6}$$

Here r_F is the proliferation rate, $r_F^{\max}$ is the maximum factor with which the proliferation rate can be enhanced due to the presence of the signaling molecule, a_c^I is the concentration of the signaling molecule that causes the half-maximum enhancement of the proliferation rate, $\kappa_F F$ represents the reduction in the proliferation rate due to crowding, q is a fixed constant, k_F is the signaling molecule-dependent cell differentiation rate of fibroblasts into myofibroblasts, δ_N is the apoptosis rate of fibroblasts and δ_M is the apoptosis rate of myofibroblasts.

4.2.2. THE SIGNALING MOLECULES

IT was assumed that both fibroblasts and myofibroblasts secrete and consume the signaling molecules. The functional form for these processes is based on chemical interactions between the signaling molecules and receptors for these molecules on the cell

surfaces of the (myo)fibroblasts. The derivation of the functional form (i.e., the first term on the right hand side of Equation (4.8)) can be found in the appendix of the article by Olsen *et al.* [30]. Furthermore, the removal of signaling molecules from the dermal layer by means of proteolytic breakdown was incorporated into the model. Finally, it was assumed that the signaling molecules diffuse through the dermal layer according to linear Fickian diffusion. Taken together this results in

$$\mathbf{J}_c = -D_c \nabla c, \tag{4.7}$$

$$R_c = k_c \left[\frac{c}{a_c^{II} + c} \right] \left[N + \eta M \right] - \delta_c g\left(F, c, \Omega^\rho\right) c. \tag{4.8}$$

Here D_c is the Fickian diffusion coefficient of the generic signaling molecule, k_c is the maximum net secretion rate of the signaling molecule, η is the ratio of myofibroblasts to fibroblasts in the maximum net secretion rate of the signaling molecule, a_c^{II} is the concentration of the signaling molecule that causes the half-maximum net secretion rate of the signaling molecule, and δ_c is the proteolytic breakdown rate of the signaling molecules.

The last term of R_c requires some more explanation. In the model the signaling molecules are removed from the dermal layer by means of proteolytic breakdown by a generic metalloproteinase (MMP) [24, 44]. It is known that MMPs are involved in the breakdown of collagen-rich fibrils during the remodeling of the extracellular matrix (ECM) and the maintenance of the ECM [4, 22, 29]. Furthermore, it is known that (myo)fibroblasts are important producers of MMPs [22] and that the production of MMPs can be reduced in the presence of signaling molecules like TGF-β [32]. Therefore, it was assumed that the concentration of the generic MMP (i.e., $g(F, c, \Omega^\rho)$) is proportional to the cell density of the (myo)fibroblast population, the concentration of the collagen bundles and the concentration of the signaling molecules according to the following formula:

$$g\left(F, c, \Omega^\rho\right) \propto \frac{\mathrm{tr}\left(\Omega^\rho\right) F}{1 + a_c^{III} c}. \tag{4.9}$$

Here $1/[1 + a_c^{III} c]$ represents the inhibition of the secretion of the generic MMP due to the presence of the signaling molecule and $\mathrm{tr}\left(\Omega^\rho\right)$ represents the concentration of the collagen molecules.

4.2.3. THE COLLAGEN BUNDLES

FOR the representation of the collagen bundles a tensorial approach similar to the one proposed by Barocas and Tranquillo [2] and Cumming *et al.* [5] was used. The orientation of the bundles and the concentration of the molecules at location $\mathbf{x}$ and time t within the dermal layer are represented together by the general symmetric tensor

$$\Omega^\rho(\mathbf{x}, t) = \int_0^{\pi/2} \int_0^{\pi} \left[\mathbf{p}(\theta, \varphi) \left(\mathbf{p}(\theta, \varphi)\right)^{\mathrm{T}} \rho(\mathbf{x}, \theta, \varphi, t) \right] \mathrm{d}\theta \, \mathrm{d}\varphi, \tag{4.10}$$

with $\left(\mathbf{p}(\theta, \varphi)\right)^{\mathrm{T}} = [\sin(\varphi)\cos(\theta), \sin(\varphi)\sin(\theta), \cos(\varphi)]$ the unit vector in the direction of azimuthal angle θ and polar angle φ, and $\rho(\mathbf{x}, \theta, \varphi, t)$ the concentration of the collagen

bundles at location $\mathbf{x}$ and time t with angle θ and angle φ. The concentration of the collagen molecules at location $\mathbf{x}$ and time t can be recovered from the above tensor by either adding its eigenvalues or determining its trace.

Due to the symmetry of the above tensor, the tensor is orthogonal diagonalizable. Hence the tensor can be decomposed as a sum of weighed outer products of orthonormal eigenvectors:

$$\Omega^{\rho}(\mathbf{x},t)=\sum_{i=1}^{3}\lambda_i(\mathbf{x},t)\left[\mathbf{q}_i(\mathbf{x},t)\left(\mathbf{q}_i(\mathbf{x},t)\right)^{\mathrm{T}}\right]. \tag{4.11}$$

Here $(\lambda_i,\mathbf{q}_i)$ are the eigenpairs of the tensor. These eigenpairs can be used to measure the degree of anisotropy of the dermal layer and have been used for the graphical presentation of the degree of anisotropy within the modeled portion of dermal layer in Section 4.4. The larger the difference between the different (positive, real) eigenvalues, the more anisotropic the dermal layer. The eigenvector corresponding to the largest eigenvalue provides the dominant direction of the bundles. If all eigenvalues are equal, then the dermal layer is perfectly isotropic. In the remainder of the text of this chapter all eigenvalues are ordered such that $\lambda_3\geq\lambda_2\geq\lambda_1$.

It was assumed that the secreted collagen molecules are attached to the ECM instantaneously. Hence the flux associated with the $(j,k)^{\text{th}}$ entry of the tensor Ω^{ρ} is

$$\mathbf{J}_{\Omega^{\rho}_{jk}}=\mathbf{0}. \tag{4.12}$$

Furthermore, the secretion of collagen molecules by both fibroblasts and myofibroblasts was incorporated into the model. Similar to the mechanism proposed by Olsen *et al.* [31], it was assumed that a portion of the collagen molecules is deposited and reoriented in the direction of movement of the (myo)fibroblasts. The remainder of the newly secreted collagen molecules is deposited by ratio in the direction of the present collagen bundles. The ratio of the amount of molecules that is deposited in the direction of movement of the cells to the amount of molecules that is deposited in the direction of the present collagen bundles is determined by the walking speed of the cells (i.e., the magnitude of the cell fluxes). It was assumed that the secretion rate of the molecules is enhanced in the presence of the signaling molecule. Examples of signaling molecules that can up-regulate the secretion of collagen molecules by (myo)fibroblasts are certain members of the family of TGF-β molecules [48]. Finally, the proteolytic breakdown of the collagen molecules was incorporated into the model analogously to how this has been incorporated for the breakdown of the signaling molecules. This removal takes place by ratio. Taken together, the following was obtained for the $(j,k)^{\text{th}}$ entry of the tensor Ω^{ρ}:

$$\begin{aligned}R_{\Omega^{\rho}_{jk}}=k_{\rho}\left\{1+\left[\frac{k_{\rho}^{\max}c}{a_c^{IV}+c}\right]\right\}\left\{\left[N\left[e^{-\beta_{\rho}\|\mathbf{J}_N\|}\right]+\eta M\left[e^{-\beta_{\rho}\|\mathbf{J}_M\|}\right]\right]\left[\frac{\Omega^{\rho}_{jk}}{\operatorname{tr}(\Omega^{\rho})}\right]+\\ N\left[\frac{1-e^{-\beta_{\rho}\|\mathbf{J}_N\|}}{\left[\max\left(\|\mathbf{J}_N\|,\gamma\right)\right]^2}\right]\left[\mathbf{J}_N\left(\mathbf{J}_N\right)^{\mathrm{T}}\right]_{jk}+\eta M\left[\frac{1-e^{-\beta_{\rho}\|\mathbf{J}_M\|}}{\left[\max\left(\|\mathbf{J}_M\|,\gamma\right)\right]^2}\right]\left[\mathbf{J}_M\left(\mathbf{J}_M\right)^{\mathrm{T}}\right]_{jk}\Bigg\}-\\ \delta_{\rho}g\left(F,c,\Omega^{\rho}\right)\Omega^{\rho}_{jk}.\end{aligned} \tag{4.13}$$

Here k_ρ is the collagen molecule secretion rate, $k_\rho^{\max}$ is the maximum factor with which this rate can be enhanced due to the presence of the signaling molecule, a_c^{IV} is the concentration of the signaling molecule that causes the half-maximum enhancement of the secretion rate, β_ρ represents the sensitivity of (myo)fibroblasts to deposit and reorient (newly secreted) collagen molecules in the direction of cell movement, η is the ratio of myofibroblasts to fibroblasts in the maximum net secretion rate of collagen molecules, and δ_ρ is the proteolytic breakdown rate of the collagen molecules. The constant γ is a small positive value that was added to the model to prevent the division by zero in the case of no flux of either cell type. In this study, γ is set equal to 10^{-8} cells/(cm^2 day).

4.2.4. THE FORCE BALANCE

GIVEN that the dermal layer is modeled as an orthotropic material, the following general constitutive stress-strain relationship was used:

$$\sigma' = \mathbf{C}'\epsilon' \tag{4.14}$$

with

$$\mathbf{C}' = \begin{bmatrix} \frac{[-1+\nu_{23}\nu_{32}]E_1}{\Delta} & \frac{-[\nu_{21}+\nu_{23}\nu_{31}]E_1}{\Delta} & \frac{-[\nu_{31}+\nu_{21}\nu_{32}]E_1}{\Delta} & 0 & 0 & 0 \\ \frac{-[\nu_{12}+\nu_{13}\nu_{32}]E_2}{\Delta} & \frac{[-1+\nu_{13}\nu_{31}]E_2}{\Delta} & \frac{-[\nu_{32}+\nu_{12}\nu_{31}]E_2}{\Delta} & 0 & 0 & 0 \\ \frac{-[\nu_{13}+\nu_{23}\nu_{12}]E_3}{\Delta} & \frac{-[\nu_{23}+\nu_{13}\nu_{21}]E_3}{\Delta} & \frac{[-1+\nu_{12}\nu_{21}]E_3}{\Delta} & 0 & 0 & 0 \\ 0 & 0 & 0 & G_{23} & 0 & 0 \\ 0 & 0 & 0 & 0 & G_{13} & 0 \\ 0 & 0 & 0 & 0 & 0 & G_{12} \end{bmatrix}, \tag{4.15}$$

$$\Delta = \nu_{13}\nu_{21}\nu_{32} + \nu_{23}\nu_{12}\nu_{31} + \nu_{13}\nu_{31} + \nu_{12}\nu_{21} + \nu_{23}\nu_{32} - 1 \tag{4.16}$$

and

$$G_{jk} = \frac{E_j}{2\left[1+\nu_{jk}\right]}. \tag{4.17}$$

Here $(\sigma')^{\mathrm{T}} = [\sigma_{11}, \sigma_{22}, \sigma_{33}, \sigma_{23}, \sigma_{13}, \sigma_{12}]$, $\nu_{..}$ are the Poisson ratios, $E_.$ are the Young's moduli, $G_{..}$ are the shear moduli, and $(\epsilon')^{\mathrm{T}} = [\epsilon_{11}, \epsilon_{22}, \epsilon_{33}, 2\epsilon_{23}, 2\epsilon_{13}, 2\epsilon_{12}]$ [19]. The axes of the material coordinate system coincide locally with the principal axes of the sample (i.e., the axes of the material coordinate system run parallel to the eigenvectors of the tensor Ω^ρ). In order to make the bulk material properties dependent on the local geometrical arrangement of the collagen bundles, the following definitions are proposed for these properties:

$$E_j(\mathbf{x}, t) = E\lambda_j(\mathbf{x}, t), \tag{4.18}$$

$$\nu_{jk}(\mathbf{x}, t) = \nu\left[\frac{\lambda_j(\mathbf{x}, t)}{\sum_l \lambda_l(\mathbf{x}, t)}\right]. \tag{4.19}$$

Here E and ν are constants. Using these definitions has two nice consequences: the symmetry of the elasticity tensor $\mathbf{C}'$ is guaranteed and the positivity of the stored strain

energy density in the dermal layer is guaranteed. The elasticity tensor is symmetric when the equality

$$\frac{\nu_{jk}}{E_j} = \frac{\nu_{kj}}{E_k} \tag{4.20}$$

holds for $j,k \in \{1,2,3\}$ and $j \neq k$ [19]. The stored strain energy density is positive when the elasticity tensor is positive definite. This is the case when the inequalities

$$E_j > 0, \quad G_{jk} > 0, \quad \Delta < 0, \quad \text{and} \quad \frac{E_j}{E_k} > \nu_{jk}^2 \tag{4.21}$$

hold [19]. Taken together the dynamics and the initial conditions of the modeled constituents of the dermal layer imply $\lambda_i(\mathbf{x},t) > 0$ for all $\mathbf{x} \in \Omega_{\mathbf{x},t}$, for all time t and $i \in \{1,2,3\}$ (with $\Omega_{\mathbf{x},t}$ the domain of computation in Eulerian coordinates at time t). Combined with the proposed definitions for the bulk material properties of the dermal layer and the values chosen for the constants E and ν, these are sufficient conditions to guarantee that the above equalities and inequalities hold; checking this is straightforward. Hence, the elasticity tensor is indeed symmetric, positive definite and consequently the stored strain energy density in the system is always positive.

Notice furthermore that if the distribution of the collagen bundles is uniform (i.e., $\lambda_1 = \lambda_2 = \lambda_3$), then all Poisson ratios are equal. Likewise, all Young's moduli and shear moduli are equal. This implies that the elasticity tensor becomes equal to the elasticity tensor of an isotropic material [18]. This is a nice property because this is exactly what you would expect given the uniformity of the distribution of the collagen bundles in the dermal layer.

The tensors in Equation (4.14) need to be transformed so that they coincide with the global coordinate system (i.e., the Eulerian coordinate system). Due to the made assumptions with respect to the derivatives of the cell densities (See Subsection 4.2.5), the chosen initial conditions for the distribution of the collagen bundles (See Equation (4.35)), and the included dynamics for the production of collagen molecules (See Equation (4.13)), the first axis of the local material coordinate system always runs parallel to the first axis of the global coordinate system. This implies that the following transformations can be used to transform the tensors from Equation (4.14):

$$\sigma' = \mathbf{T}_1 \sigma \tag{4.22}$$

$$\epsilon' = \mathbf{T}_2 \epsilon \tag{4.23}$$

$$\mathbf{T}_1 \mathbf{C} = \mathbf{C}' \mathbf{T}_2, \tag{4.24}$$

with

$$\mathbf{T}_1 = \begin{bmatrix} 1 & 0 & 0 & 0 & 0 & 0 \\ 0 & m^2 & n^2 & -2nm & 0 & 0 \\ 0 & n^2 & m^2 & 2nm & 0 & 0 \\ 0 & nm & -nm & m^2 - n^2 & 0 & 0 \\ 0 & 0 & 0 & 0 & m & n \\ 0 & 0 & 0 & 0 & -n & m \end{bmatrix} \tag{4.25}$$

and

$$\mathbf{T}_2 = \begin{bmatrix} 1 & 0 & 0 & 0 & 0 & 0 \\ 0 & m^2 & n^2 & -nm & 0 & 0 \\ 0 & n^2 & m^2 & nm & 0 & 0 \\ 0 & 2nm & -2nm & m^2-n^2 & 0 & 0 \\ 0 & 0 & 0 & 0 & m & n \\ 0 & 0 & 0 & 0 & -n & m \end{bmatrix}. \tag{4.26}$$

Here $\sigma = \mathbf{C}\epsilon$, $(\sigma)^{\mathrm{T}} = [\sigma_{xx}, \sigma_{yy}, \sigma_{zz}, \sigma_{yz}, \sigma_{xz}, \sigma_{xy}]$, $(\epsilon)^{\mathrm{T}} = [\epsilon_{xx}, \epsilon_{yy}, \epsilon_{zz}, 2\epsilon_{yz}, 2\epsilon_{xz}, 2\epsilon_{xy}]$, $m = \cos(\varphi_r)$, $n = \sin(\varphi_r)$ and φ_r is the angle of the clockwise rotation that, respectively, aligns the second and the third axis of the local material coordinate system (i.e., the second and third eigenvector of the tensor Ω^{ρ}) with the second and the third axis of the global coordinate system. (Please note that the following holds: $(\mathbf{T}_1(\varphi_r))^{-1} = \mathbf{T}_1(-\varphi_r)$. This equality simplifies the calculation of the elasticity tensor $\mathbf{C}$ from Equation (4.24).) Furthermore,

$$\epsilon = \frac{1}{2}\left[\nabla\mathbf{u} + (\nabla\mathbf{u})^{\mathrm{T}}\right]. \tag{4.27}$$

Finally, the generation of an isotropic stress by the myofibroblasts due to their pulling on the ECM was incorporated into the model. This stress is proportional to the product of the cell density of the myofibroblasts and a simple function of the concentration of the collagen molecules [30]. No other forces were incorporated into the model. Taken together, the following was obtained:

$$\mathbf{f} = \nabla \cdot \psi, \tag{4.28}$$

$$\psi = \xi M \left\{ \frac{\mathrm{tr}\,(\Omega^{\rho})}{R_{\rho}^2 + [\mathrm{tr}\,(\Omega^{\rho})]^2} \right\} \mathbf{I}. \tag{4.29}$$

Here ψ is the total generated stress by the myofibroblast population, ξ is the generated stress per unit cell density and the inverse of the unit collagen molecule concentration, and R_{ρ} is a fixed constant.

4.2.5. THE DOMAIN OF COMPUTATION

It was assumed that $u = 0$ and $\partial v/\partial x = \partial w/\partial x = 0$ hold within the modeled portion of the dermal layer, with the yz-plane running parallel to the surface of the skin and $\mathbf{u} = (u, v, w)^{\mathrm{T}}$. Furthermore, it was assumed that the derivatives of the cell densities and the concentrations of the modeled constituents of the dermal layer are equal to zero in the direction perpendicular to the surface of the skin. Taken together, these assumptions imply that the calculations can be performed on an arbitrary, infinitely thin slice of dermal layer oriented parallel to the surface of the skin, and that the results from these calculations are valid for every infinitely thin slice oriented parallel to the surface of the skin. Using Lagrangian coordinates ($\mathbf{X} = (X, Y, Z)^{\mathrm{T}}$), the domain of computation ($\Omega_{\mathbf{X}}$) is described mathematically by

$$\Omega_{\mathbf{X}} \in \{X = 0\ \mathrm{cm}, -10\ \mathrm{cm} \leq Y \leq 10\ \mathrm{cm}, -10\ \mathrm{cm} \leq Z \leq 10\ \mathrm{cm}\}. \tag{4.30}$$

4.2.6. THE INITIAL CONDITIONS AND THE BOUNDARY CONDITIONS

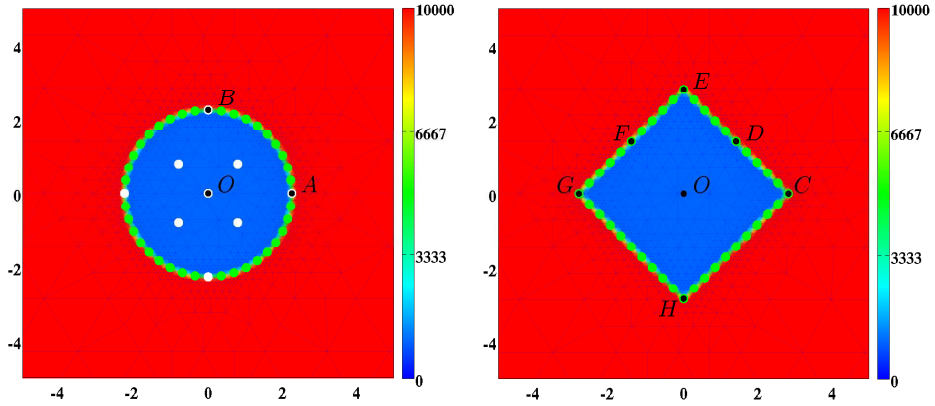

(a) (b)

Figure 4.1: Graphical representations of the initial conditions. Depicted are in both subfigures, the initial shape of the wound and, in color scale, the initial cell density of the fibroblasts (cells/cm^3). In both subfigures the scale along both axes is in centimeters. In Subfigure 4.1a, the white dots mark the material points where the evolution of the cell density / concentration of the different modeled constituents was traced over time for the generation of some of the figures in Section 4.4. In both subfigures, the green dots mark the material points that were used to trace the evolution over time of the surface area of the wound. That is, at each time point the area of the polygon with vertices located at the displaced green material points has been determined. Finally, the material points labeled with a letter have been used to study the evolution over time of the shape of the wound. See Section 4.4 for more details on this matter

THE initial conditions give a description of the cell densities and the concentrations at the onset of the proliferative phase of the wound healing cascade. For the generation of the simulation results, two wound shapes were used: a circular shape and a square shape. For the construction of these shapes, the following general indicator function was used:

$$I(r,s_1,s_2)=\begin{cases}0 & \text{if } r<[s_1-s_2]\,,\\ \frac{1}{2}\left[1+\sin\left(\frac{[r-s_1]\pi}{2s_2}\right)\right] & \text{if } |r-s_1|\le s_2,\\ 1 & \text{if } r>[s_1+s_2]\,.\end{cases} \tag{4.31}$$

The values for the parameters s_1 and s_2 determine respectively the location and the steepness of the boundary of the wounded area. In order to construct circular wounds, the following function was used:

$$w_c(\mathbf{X})=I\left(\|\mathbf{X}\|,\sqrt{16/\pi},0.10\right). \tag{4.32}$$

In order to construct square wounds with the same surface area as the circular wounds, the following function was used:

$$w_s(\mathbf{X}_r)=1-[1-I(Y_r,2,0.10)]\,[1-I(Z_r,2,0.10)]\,I(Y_r,2,0.10)\,I(Z_r,2,0.10)\,, \tag{4.33}$$

with $\mathbf{X}_r = \mathbf{R}(\theta_r)\mathbf{X} = (X_r, Y_r, Z_r)^{\mathrm{T}}$ and $\theta_r = \pi/4$ rad, where $\mathbf{R}(\theta)$ is the counterclockwise rotation matrix that rotates vectors by an angle θ about the X-axis. For $i \in \{c, s\}$, $w_i = 0$ corresponds to completely wounded dermis and $w_i = 1$ corresponds to unwounded dermis.

Based on these general functions for the shapes of the wound, the following initial conditions were used for the cell densities and the concentration of the signaling molecule:

$$\begin{aligned} N(\mathbf{X},0) &= \left\{I^w + \left[1 - I^w\right] w_i(\mathbf{X})\right\} \overline{N}, \\ M(\mathbf{X},0) &= \overline{M}, \\ c(\mathbf{X},0) &= \left[1 - w_i(\mathbf{X})\right] c^w. \end{aligned} \tag{4.34}$$

Here $\overline{N}$ and $\overline{M}$ represent the equilibrium cell density of, respectively, the fibroblast population and the myofibroblast population of the unwounded dermis. The constant c^w represents the maximum initial concentration of the signaling molecule in the wounded area. It was assumed that there are some fibroblasts and collagen bundles present in the wounded area; the parameter I^w determines the minimum amount of fibroblasts and collagen bundles present initially in the wounded area. For the initial distribution of the collagen bundles the following was used:

$$\Omega^{\rho}(\mathbf{X},0) = \left\{\left[I^w + \left[1 - I^w\right] w_i(\mathbf{X})\right]\left\{\frac{1}{1+r_a}\left[\hat{\mathbf{e}}_X(\hat{\mathbf{e}}_X)^{\mathrm{T}}\right] + \frac{r_a}{1+r_a}\left[\frac{r_b}{1+r_b}\left[\hat{\mathbf{e}}_Y(\hat{\mathbf{e}}_Y)^{\mathrm{T}}\right] + \frac{1}{1+r_b}\left[\hat{\mathbf{e}}_Z(\hat{\mathbf{e}}_Z)^{\mathrm{T}}\right]\right]\right\}\right\}\overline{\rho}, \tag{4.35}$$

with

$$\hat{\mathbf{e}}_j = \mathbf{R}(\theta_b)\mathbf{e}_j, \tag{4.36}$$

for $j \in \{X, Y, Z\}$, where $\mathbf{e}_j$ is the unit vector that runs parallel to the j^{th} coordinate axis. The value for the parameter r_a determines which portion of the collagen bundles is oriented in the direction perpendicular to the surface of the skin, and which portion of the collagen bundles is running parallel to the surface of the skin. In uninjured skin the majority of the collagen bundles of the dermal layer runs parallel to the surface of the skin while only a small portion of the fibers is oriented out-of-plane [1, 11]. Therefore, the parameter r_a is set to a relatively large value. The values for the parameter r_b and the angle θ_b together determine the overall distribution of the collagen bundles that run parallel to the surface of the skin. Over simulations the values for these latter two parameters were varied in order to investigate the effect of such a variation on the contraction of wounds. The used (ranges of) values are depicted in Table 4.1. The parameter $\overline{\rho}$ is the equilibrium concentration of the collagen molecules in the unwounded dermis.

With respect to the initial conditions for the displacement of the dermal layer, the following can be observed. The initial cell density of the myofibroblasts is equal to zero everywhere in the domain of computation. Looking at Equation (4.29), this implies $\mathbf{f}(\mathbf{x},0) = \mathbf{0}$. Therefore,

$$\mathbf{u}(\mathbf{x},0)=\mathbf{0} \quad \forall \mathbf{x}\in\Omega_{\mathbf{x},0}. \tag{4.37}$$

See Figure 4.1 for graphical representations of the initial conditions that have been used in this study.

With respect to the boundary conditions for the modeled constituents of the dermal layer, the following Dirichlet boundary conditions were used for all time t and for all $\mathbf{x}\in\partial\Omega_{\mathbf{x},t}$, where $\partial\Omega_{\mathbf{x},t}$ is the boundary of the domain of computation in Eulerian coordinates:

$$N(\mathbf{x},t)=\overline{N},\ \ M(\mathbf{x},t)=\overline{M},\ \ c(\mathbf{x},t)=\overline{c}. \tag{4.38}$$

Here $\overline{c}$ is the equilibrium concentration of the signaling molecules in the unwounded dermis. Finally, the following Dirichlet boundary condition was used for the mechanical component of the model for all time t and for all $\mathbf{x}\in\partial\Omega_{\mathbf{x},t}$:

$$\mathbf{u}(\mathbf{x},t)=\mathbf{0}. \tag{4.39}$$

4.2.7. THE (RANGES OF THE) VALUES FOR THE PARAMETERS

TABLE 4.1 provides an overview of the (ranges of the) values for the parameters of the model. The majority of these values was either obtained directly from previously conducted studies or estimated from results of previously conducted studies. In addition, the values for three more parameters could be determined due to the fact that these values are a necessary consequence of the values chosen for other parameters. These are the equilibrium signaling molecule concentration of the unwounded dermis ($\overline{c}$), the constant q and the collagen molecule degradation rate (δ_ρ). If $\overline{\rho}=0.1$ g/cm^3, $\overline{N}=10^4$ cells/cm^3, and $\overline{M}=0$ cells/cm^3 in the unwounded dermis, then $c=0$ g/cm^3 is an attracting equilibrium in the vicinity of $c=0$ g/cm^3. Hence $\overline{c}=0$ g/cm^3. Furthermore, if $\overline{N}=10^4$ cells/cm^3, $\overline{M}=0$ cells/cm^3 and $\overline{c}=0$ g/cm^3, then $q=[\log(\delta_N)-\log(r_F[1-\kappa_F\overline{N}])]/\log(\overline{N})$. Finally, if $\overline{M}=0$ cells/cm^3 and $\overline{c}=0$ g/cm^3, then $k_\rho=\delta_\rho\overline{\rho}^2$ g/(cells day).

Table 4.1: An overview of the (ranges of the) values for the parameters of the model. The last column contains the references to the studies that were used for obtaining (estimates of) the values for the parameters. If (the range of) the value for a parameter has been estimated in this study, then this is indicated by the abbreviation TW. If the value for a parameter is a necessary consequence of the values chosen for the other parameters, then this is indicated by the abbreviation NC

Parameter	Value	Dimensions	Reference
D_F	10^{-7}	cm^5/(cells day)	[38]
χ_F	2×10^{-3}	cm^5/(g day)	[28]
q	-4.2×10^{-1}	–	NC
r_F	9.24×10^{-1}	cm^{3q}/(cells^q day)	[8]
$r_F^{\max}$	2	–	[39]
a_c^I	10^{-8}	g/cm^3	[9]
κ_F	10^{-6}	cm^3/cells	[46]
k_F	5.4×10^6	cm^3/(g day)	[6]

Continued on the next page

Table 4.1 – *Continued from the previous page*

Parameter	Value	Dimensions	Reference
δ_N	2×10^{-2}	/day	[30]
δ_M	2×10^{-2}	/day	[17]
D_c	2.9×10^{-3}	cm^2/day	[28]
k_c	4×10^{-13}	g/(cells day)	[30]
η	2	–	[27] & [37]
a_c^{II}	10^{-8}	g/cm^3	[30]
δ_c	5×10^{-4}	cm^6/(cells g day)	[30]
a_c^{III}	2×10^8	cm^3/g	[32]
k_ρ	6×10^{-8}	g/(cells day)	NC
$k_\rho^{\max}$	10	–	[30]
a_c^{IV}	10^{-9}	g/cm^3	[36]
β_ρ	10^{-1}	(cm^2 day)/cells	TW
δ_ρ	6×10^{-6}	cm^6/(cells g day)	[17]
E	3.00×10^2	(N cm)/g	[21]
ν	4.9×10^{-1}	–	[21]
ξ	2×10^{-4}	(N g)/(cells cm^2)	[13] & [49]
R_ρ	3×10^{-1}	g/cm^3	[30]
$\overline{N}$	10^4	cells/cm^3	[30]
$\overline{M}$	0	cells/cm^3	[30]
$\overline{c}$	0	g/cm^3	NC
$\overline{\rho}$	10^{-1}	g/cm^3	[30]
I^w	10^{-1}	–	TW
c^w	10^{-8}	g/cm^3	[30]
r_a	9	–	[1] & [11]
r_b	$1-5$	–	TW
θ_b	$0-\pi/4$	rad	TW

4.3. THE APPLIED NUMERICAL ALGORITHM

In order to express the kernel of the algorithm and generate simulation results, `MATLAB` was used together with `MATLAB`'s Parallel Computing Toolbox [40]. Furthermore, the kernel was interfaced consecutively with a slightly adapted version of the mesh generator developed by Persson and Strang for the generation of a base triangulation of the domain of computation [34], the element resolution refinement / recoarsement tool of the computational fluid dynamics (CFD) software package `FEATFLOW2` for the adjustment of the resolution of the elements of the base triangulation [42], and the permutation routine `HSL_MC64` for the permutation of the $n \times n$ matrices related to the resulting systems of linear algebraic equations after full discretization of the model equations such that the matrices have n entries on their diagonal [12]. The equations of the model were non-dimensionalised furthermore by applying the following non-dimensionalisation:

$$\begin{aligned} x &= Lx^*, \qquad t = \left[L^2/\left[D_F\overline{N}\right]\right]t^*, \quad \Omega^\rho = \overline{\rho}\Omega^{\rho *}, \\ N &= \overline{N}N^*, \quad M = \overline{N}M^*, \qquad c = c^w c^*, \\ \mathbf{u} &= L\mathbf{u}^*, \qquad \mathbf{v} = \left[\left[D_F\overline{N}\right]/L\right]\mathbf{v}^*, \qquad \sigma = \left[\left[\xi\overline{N}\right]/\overline{\rho}\right]\sigma^*. \end{aligned} \tag{4.40}$$

Here $L = 1$ cm is the length scale of the model. The variables with the asterisks are the non-dimensionalised variables.

In order to find an approximation of the solution for the primary model variables from Equation (4.1), the standard fixed-point defect correction method was used together with the method of lines [43]. The two equations of the system were solved in a segregated way. That is, each time step approximations of the solutions for the modeled constituents of the dermal layer were determined first and subsequently an approximation of the solution for the displacement of the dermal layer was determined. This scheme was iterated until certain standard convergence criteria were met. For the discretization of the system of equations the first-order backward Euler time-integration method was used together with a moving-grid finite-element method [23]. On the discretized system of equations that describe the dynamics of the modeled constituents of the dermal layer a semi-implicit flux-corrected transport (FCT) limiter and a source term splitting procedure were applied in order to enforce positivity of the approximations of the solutions for the constituents of the dermal layer [25, 33]. Finally, an automatically adaptive time-stepping method was used to select the sizes of the individual time steps [14]. More details about the algorithm and the procedure surrounding the adjustment of the resolution of the elements of the base triangulation can be found in Section 5.3.

4.4. SIMULATION RESULTS

IN order to obtain some insight into the dynamics of the model, an overview of a simulation is presented in Figure 4.2. Figure 4.3 shows what the impact is of changing the initial distribution of the collagen bundles that run parallel to the surface of the skin, on the contraction of a circular wound. Due to the symmetry properties of a circular wound, it is not interesting to vary the value for the angle θ_b. (In the case of a perfectly circular wound, changing the value for the angle θ_b will merely rotate the solution counterclockwisely through an angle θ_b.) Hence, solely the value for the ratio r_b is changed over simulations. Note that changing the value for the ratio r_b not only influences the degree of overall contraction of the wounded area (as measured by the evolution over time of the relative surface area of the wound compared to the surface area of the wound at day 0), but also the evolution over time of the shape of the wounded area (as measured by the evolution over time of the (ratio of the) lengths of the line segments $\overline{OA}$ and $\overline{OB}$). Furthermore, note that the evolution over time of the cell densities and the concentrations of the different modeled constituents is hardly influenced by changing the value for the ratio r_b.

Figure 4.4 shows what the impact is of changing the initial distribution of the collagen bundles that run parallel to the surface of the skin, on the contraction of a square wound. (Note that if $r_b = 1$, then the solution is not dependent on the value for the angle θ_b. Looking at Equation (4.35), this becomes clear straight away.) Contrary to the case where the wound is circular, it is interesting to change both the value for the angle θ_b and the value for the ratio r_b in the case of a square wound. Due to the symmetry properties of a square wound, it is sufficient to vary the angle θ_b between 0 rad and $\pi/4$ rad. (A solution for an angle larger than $\pi/4$ rad can be obtained from a solution for an angle between 0 rad and $\pi/4$ rad by applying a proper reflection and / or rotation on this latter solution.) Similar to the case of a circular wound, changing the value for the ratio r_b

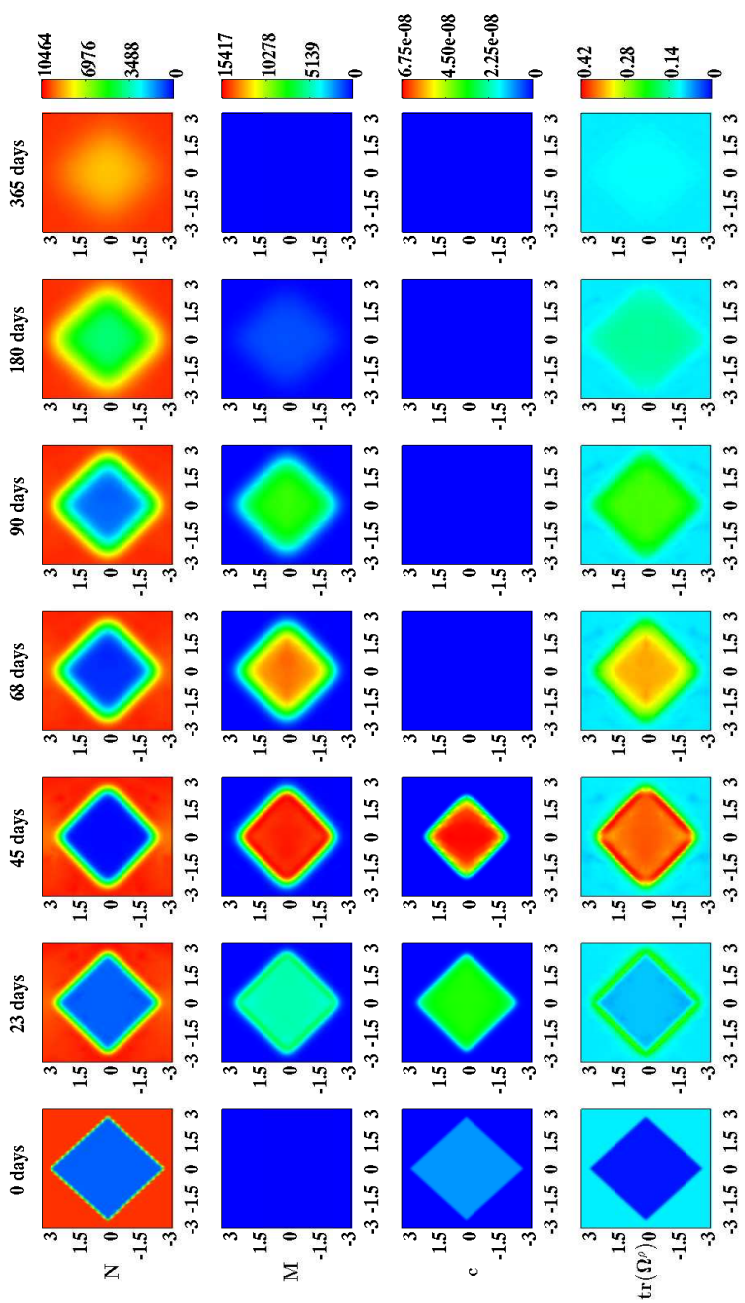

Figure 4.2: An overview of a simulation with a square wound, $r_b = 5$ and $\theta_b = 0$ rad. The values for the remaining parameters are equal to those depicted in Table 4.1. The first two rows show the evolution over time of the cell density of respectively the fibroblast population, and the myofibroblast population. The color scales represent the cell densities, measured in cells/cm^3. The last two rows show the evolution over time of the concentration of respectively the signaling molecules, and the collagen molecules. The color scales represent the concentrations, measured in g/cm^3. Within the subfigures, the scale along both axes is in centimeters

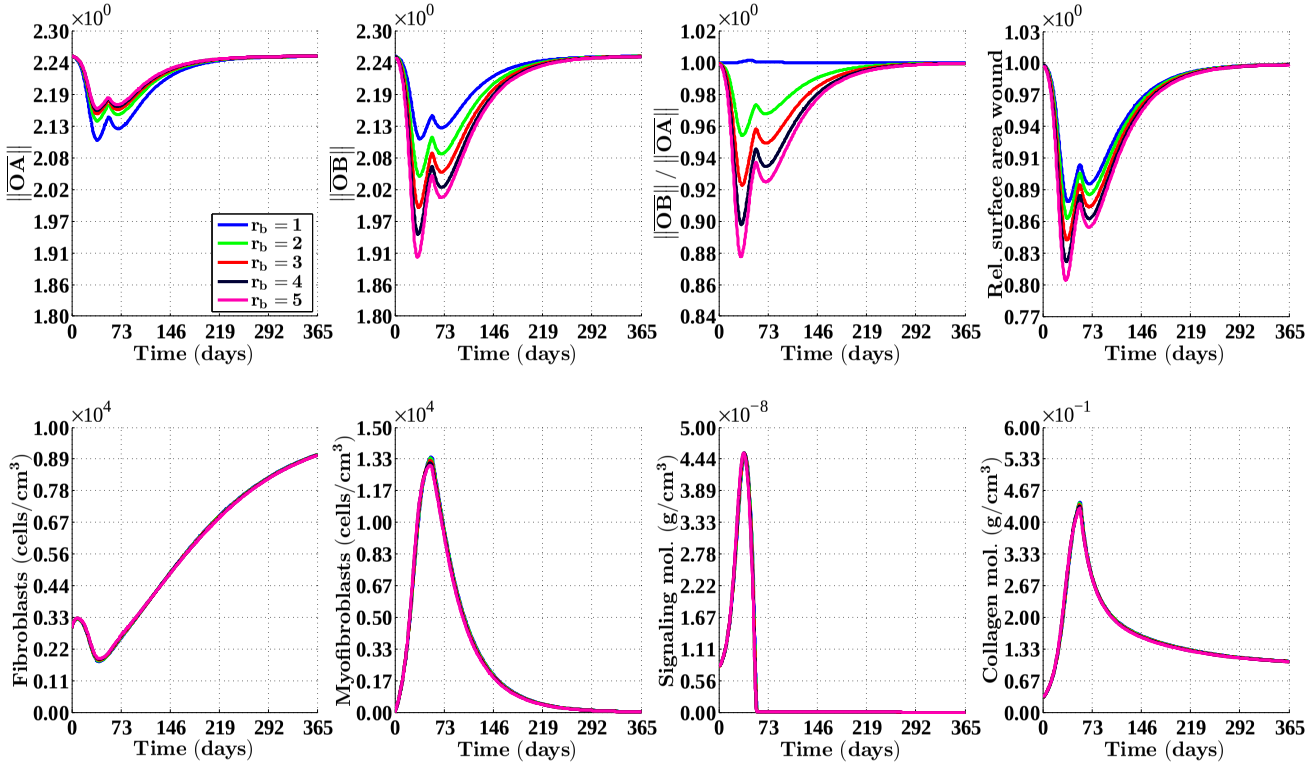

Figure 4.3: An overview of the healing response in the case of a circular wound, $\theta_b = 0$ rad and different values for the ratio r_b. The values for the remaining parameters are equal to those depicted in Table 4.1. See Subfigure 4.1a for a depiction of the line segments $\overline{OA}$ and $\overline{OB}$, and a depiction of where the cell densities and the concentrations of the modeled constituents were measured over time. The subfigures on the bottom row show the averages of these latter measurements. See also Subfigure 4.1a for a depiction of how the surface area of the wound was measured over time. The legend displayed in the top-left subfigure applies to all subfigures. Due to the fact that the curves depicted in the subfigures on the bottom row are situated more or less on top of each other, most of them are hardly visible

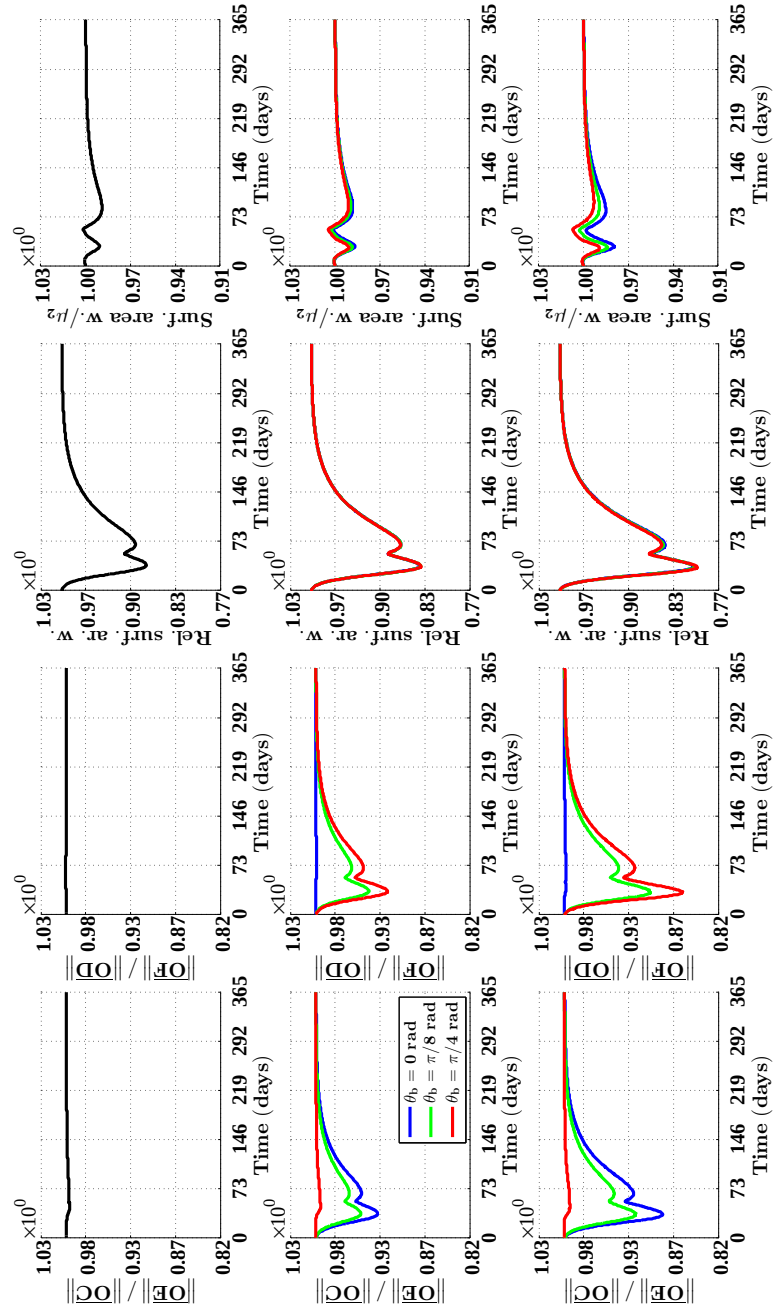

Figure 4.4: An overview of the healing response in the case of a square wound and different values for both the ratio r_b and the angle θ_b. The values for the remaining parameters are equal to those depicted in Table 4.1. See Subfigure 4.1b for a depiction of the line segments $\overline{OC}$, $\overline{OD}$, $\overline{OE}$ and $\overline{OF}$. See also Subfigure 4.1b for a depiction of how the surface area of the wound was measured over time. μ_2 equals the surface area of the quadrilateral *CEGH*. See again Subfigure 4.1b for a depiction of the vertices of this quadrilateral. The subfigures on the top row show overviews for $r_b = 1$ and $\theta_b = 0$ rad, the subfigures on the middle row show overviews for $r_b = 3$, and the subfigures on the bottom row show overviews for $r_b = 5$. The legend displayed in the middle row applies to all subfigures on the middle row and the bottom row. Due to the fact that the curves depicted in the subfigures related to the relative surface area of the wound are situated more or less on top of each other, solely one curve is mostly visible

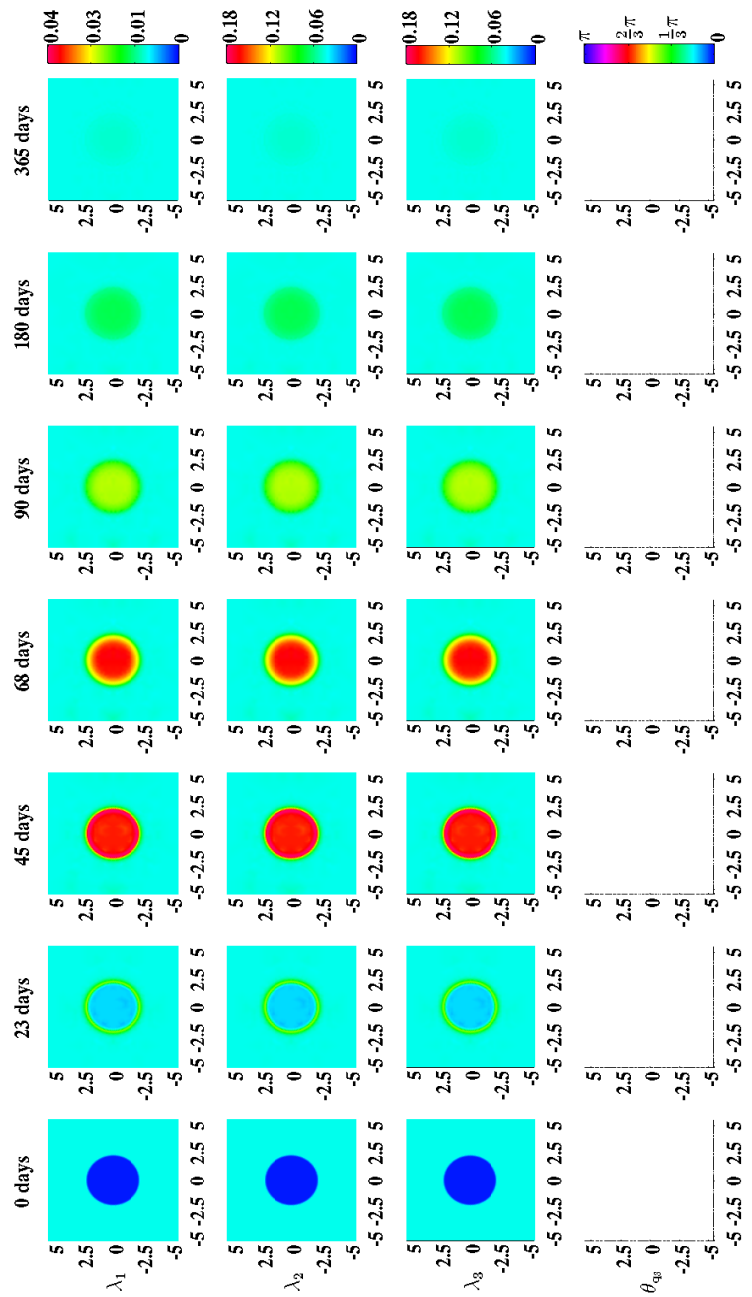

Figure 4.5: An overview of the evolution over time of the geometrical distribution of the collagen bundles during the healing of a circular wound. For the generation of these simulation results $r_b = 1$, $\theta_b = 0$ rad and $\beta_\rho = 0$ (cm^2 day)/cells. The values for the remaining parameters are equal to those depicted in Table 4.1. λ_1, λ_2 and λ_3 are the eigenvalues of the tensor Ω^ρ and $\theta_{\mathbf{q}_3}$ is the angle between the eigenvector related to the largest eigenvalue λ_3 (where the third element of this eigenvector is larger than / equal to zero) and the positive horizontal axis. Within the subfigures on the bottom row the transparency (i.e., $a(\mathbf{x}, t)$) is set to either zero (opaque) or one (fully transparent) based on the following rule: if $(\lambda_3(\mathbf{x}, t) - \lambda_2(\mathbf{x}, t))/\lambda_2(\mathbf{x}, t) > 0.2$, then $a(\mathbf{x}, t) = 0$, else $a(\mathbf{x}, t) = 1$

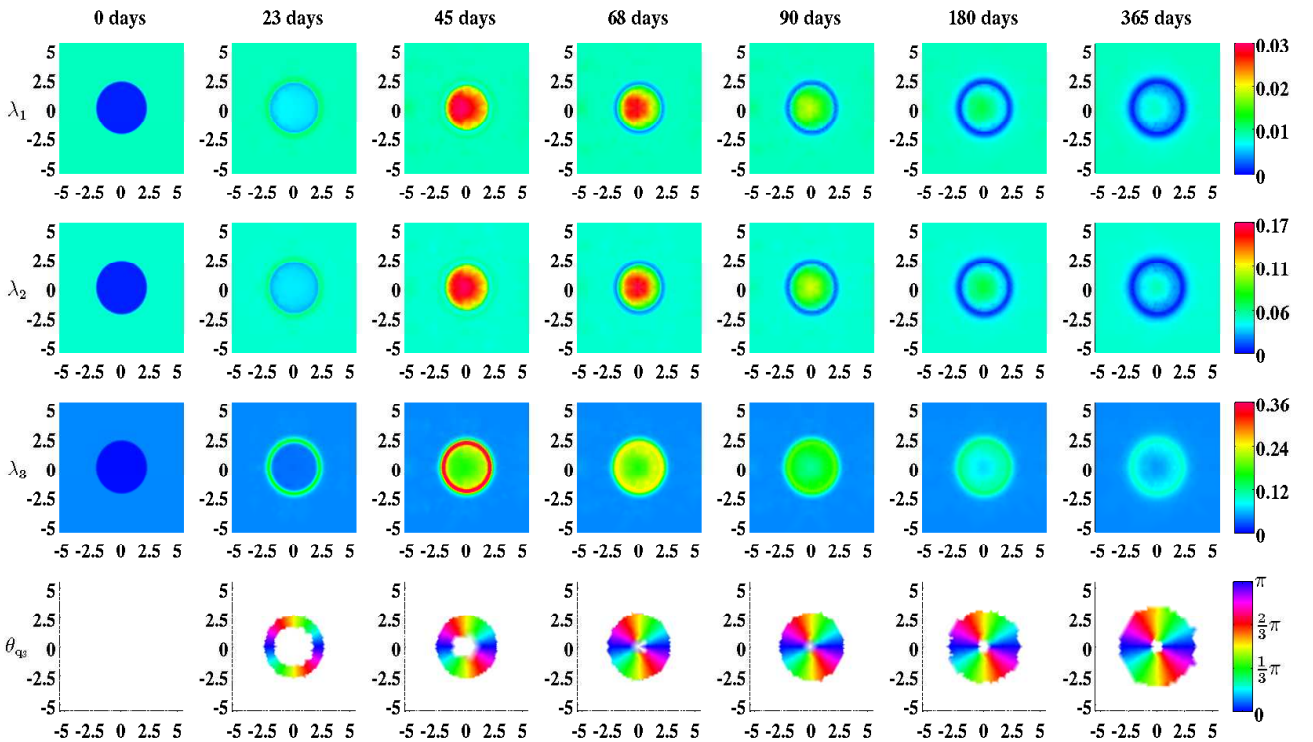

Figure 4.6: An overview of the evolution over time of the geometrical distribution of the collagen bundles during the healing of a circular wound. For the generation of these simulation results $r_b = 1$, $\theta_b = 0$ rad and $\beta_\rho = 10^{-1}$ (cm^2 day)/cells. The values for the remaining parameters are equal to those depicted in Table 4.1. λ_1, λ_2 and λ_3 are the eigenvalues of the tensor Ω^ρ and $\theta_{\mathbf{q}_3}$ is the angle between the eigenvector related to the largest eigenvalue λ_3 (where the third element of this eigenvector is larger than / equal to zero) and the positive horizontal axis. Within the subfigures on the bottom row the transparency (i.e., $\alpha(\mathbf{x}, t)$) is set to either zero (opaque) or one (fully transparent) based on the following rule: if $(\lambda_3(\mathbf{x}, t) - \lambda_2(\mathbf{x}, t))/\lambda_2(\mathbf{x}, t) > 0.2$, then $\alpha(\mathbf{x}, t) = 0$, else $\alpha(\mathbf{x}, t) = 1$

influences both the degree of overall contraction of the wounded area (as measured by the evolution over time of the relative surface area of the wound compared to the surface area at day 0), and the evolution over time of the shape of the wounded area (as measured by the evolution over time of the ratio of the lengths of the line segments $\overline{OC}$ and $\overline{OE}$, the ratio of the lengths of the line segments $\overline{OD}$ and $\overline{OF}$, and the surface area of the wound relative to the surface area of the quadrilateral $CEGH$).

Furthermore, Figure 4.4 shows that the evolution over time of the shape of the recovering wounded area is also influenced by the orientation of the collagen bundles relative to the wound in the case of a square wound. Interestingly, this relative orientation of the collagen bundles has hardly any influence on the evolution over time of the surface area of the wound relative to the surface area at day 0. Although not depicted in Figure 4.4, the evolution over time of the cell densities and the concentrations of the different modeled constituents is hardly influenced by changing the values for the ratio r_b and the angle θ_b.

Finally, Figures 4.5 and 4.6 show the evolution over time of the geometrical distribution of the collagen bundles during the healing of a circular wound. In order to demonstrate the effect of either including the deposition / reorientation of collagen molecules in the direction of cell movement or not, β_ρ was set to zero for the generation of the simulation results in Figure 4.5 and was set to the standard value depicted in Table 4.1 for the generation of the simulation results in Figure 4.6. (See the text next to Equation (4.13) for a description of the parameter β_ρ.) If $\beta_\rho = 0$ (cm^2 day)/cells, then this will result ultimately in newly generated tissue with a collagen bundle-distribution that is exactly equal to the collagen-bundle distribution of the surrounding uninjured tissue. If $\beta_\rho = 10^{-1}$ (cm^2 day)/cells, then ultimately the majority of the collagen molecules ends up permanently oriented toward the center of the wound and in the plane that runs parallel to the surface of the skin.

4.5. CONCLUSIONS

WITH the developed model, it is possible to reproduce some general qualitative features of the dermal wound healing response [3, 7, 20, 26]. Firstly, the restoration of the presence of fibroblasts in the wounded area can be reproduced. Secondly, the initial expansion and subsequent reduction of the myofibroblast population in the wounded area during the execution of the wound healing response can be reproduced. Thirdly, it is possible to reproduce the restoration of a collagen-rich ECM in the recovering wounded area. Fourthly, the contraction and the subsequent retraction of the wounded area can be reproduced. Finally, in accordance with experimental observations [45, 47], it is also possible to reproduce the permanent increase in the portion of the collagen bundles that runs parallel to the surface of the skin as a consequence of the execution of the wound healing process.

With respect to the simulation of the collagen bundle distribution-dependent contraction and subsequent retraction of healing dermal wounds, the following can be observed. Figures 4.3 and 4.4 show clearly the impact of changing the initial geometrical distribution of the collagen bundles that run parallel to the surface of the skin. The distribution of the collagen bundles influences the evolution over time of both the shape of the wounded area and the degree of overall contraction of the wounded area. Inter-

estingly, Figure 4.3 shows that these effects are solely a consequence of alterations in the initial overall distribution of the collagen bundles, and not a consequence of alterations in the evolution over time of the different cell densities and concentrations of the modeled constituents. Furthermore, it is very interesting to observe in Figure 4.4 that the evolution over time of the shape of the wound is also influenced by the orientation of the collagen bundles relative to the wound while this relative orientation does not influence the evolution over time of the relative surface area of the wound compared to the surface area of the wound at day 0.

Figures 4.5 and Figure 4.6 show clearly the effect of either including into the model the dependence of the development of the geometrical distribution of collagen bundles in the recovering wounded area on the direction of movement of cells, or not. If it is included, then an increased portion of the collagen bundles ultimately ends up permanently in the plane running parallel to the surface of the skin, and the majority of these bundles is oriented toward the center of the wound. If the deposition / reorientation of collagen molecules in the direction of cell movement is not included, then all the newly secreted collagen molecules are deposited by ratio in the direction of the present collagen bundles. As demonstrated in Figure 4.5, this will result ultimately in newly generated tissue with a collagen bundle-distribution that is exactly equal to the collagen-bundle distribution of the surrounding uninjured tissue.

REFERENCES

[1] Annaidh A, Bruyère K, Destrade M, Gilchrist M, Maurini C, Otténio M, Saccomandi G (2012) Automated estimation of collagen fibre dispersion in the dermis and its contribution to the anisotropic behaviour of skin. Ann Biomed Eng 40:1666–1678

[2] Barocas V, Tranquillo R (1997) An anisotropic biphasic theory of tissue-equivalent mechanics: the interplay among cell traction, fibrillar network deformation, fibril alignment, and cell contact guidance. AMSE J Biomech Eng 119:137–145

[3] Baum C, Arpey C (2005) Normal cutaneous wound healing: clinical correlation with cellular and molecular events. Dermatol Surg 31:674–686

[4] Chakraborti S, Mandal M, Das S, Mandal A, Chakraborti T (2003) Regulation of matrix metalloproteinases: An overview. Mol Cell Biochem 253:269–285

[5] Cumming B, McElwain D, Upton Z (2010) A mathematical model of wound healing and subsequent scarring. J R Soc Interface 7:19–34

[6] Desmoulière A, Geinoz A, Gabbiani F, Gabbiani G (1993) Transforming growth factor-β1 induces α-smooth muscle actin expression in granulation tissue myofibroblasts and in quiescent and growing cultured fibroblasts. J Cell Biol 122:103–111

[7] Enoch S, Leaper D (2007) Basic science of wound healing. Surgery 26:31–37

[8] Ghosh K, Pan Z, Guan E, Ge S, Liu Y, Nakamura T, Ren ZD, Rafailovich M, Clark R (2007) Cell adaptation to a physiologically relevant ECM mimic with different viscoelastic properties. Biomaterials 28:671–679

[9] Grotendorst G (1992) Chemoattractants and growth factors. In: Cohen I, Diegelmann R, Lindblad W (eds) Wound Healing: Biochemical and Clinical Aspects, 1st edn, W.B. Saunders, Philadelphia, Pennsylvania, chap 15, pp 237–246

[10] Hillen T, Painter K (2009) A user's guide to PDE models for chemotaxis. J Math Biol 58:183–217

[11] Holzapfel G (2001) Biomechanics of soft tissue. In: Lemaître J (ed) Handbook of materials behavior models, 1st edn, Academic Press, Cambridge, United Kingdom, chap 10.11, pp 1057–1071

[12] HSL (2013) A collection of fortran codes for large scale scientific computation. URL http://www.hsl.rl.ac.uk

[13] Javierre E, Moreo P, Doblaré M, García-Aznar J (2009) Numerical modeling of a mechanochemical theory for wound contraction analysis. Int J Solids Struct 46:3597–3606

[14] Kavetski D, Binning P, Sloan S (2002) Adaptive backward Euler time stepping with truncation error control for numerical modelling of unsaturated fluid flow. Int J Numer Meth Eng 53:1301–1322

[15] Koppenol D, Vermolen F, Koppenol-Gonzalez G, Niessen F, Van Zuijlen P, Vuik K (2016) A mathematical model for the simulation of the contraction of burns. J Math Biol DOI: 10.1007/s00285-016-1075-4

[16] Koppenol D, Vermolen F, Niessen F, Van Zuijlen P, Vuik K (2017) A biomechanical mathematical model for the collagen bundle distribution-dependent contraction and subsequent retraction of healing dermal wounds. Biomech Model Mechanobiol 16:345–361, DOI: 10.1007/s10237-016-0821-2

[17] Koppenol D, Vermolen F, Niessen F, Van Zuijlen P, Vuik K (2017) A mathematical model for the simulation of the formation and the subsequent regression of hypertrophic scar tissue after dermal wounding. Biomech Model Mechanobiol 16:15–32, DOI: 10.1007/s10237-016-0799-9

[18] Lai W, Rubin D, Krempl E (1999) Introduction to Continuum Mechanics, 3rd edn. Butterworth Heinemann Ltd, Waltham, Massachusetts

[19] Lempriere B (1968) Poisson's ratio in orthotropic materials. AIAA Journal 6:2226–2227

[20] Li J, Chen J, Kirsner R (2007) Pathophysiology of acute wound healing. Clin Dermatol 25:9–18

[21] Liang X, Boppart S (2010) Biomedical properties of *in vivo* human skin from dynamic optical coherence elastography. IEEE T Bio-Med Eng 57:953–959

[22] Lindner D, Zietsch C, Becher P, Schulze K, Schultheiss HP, Tschöpe C, Westermann D (2012) Differential expression of matrix metalloproteases in human fibroblasts with different origins. Biochemistry Research International 2012:1–10

[23] Madzvamuse A, Wathen A, Maini P (2003) A moving grid finite element method applied to a model biological pattern generator. J Comput Phys 190:478–500

[24] Mast B, Schultz G (1996) Interactions of cytokines, growth factors, and proteases in acute and chronic wounds. Wound Repair Regen 4:411–420

[25] Möller M, Kuzmin D, Kourounis D (2008) Implicit FEM-FCT algorithms and discrete Newton methods for transient convection problems. Int J Numer Meth Fluids 57:761–792

[26] Monaco J, Lawrence W (2003) Acute wound healing: an overview. Clin Plast Surg 30:1–12

[27] Moulin V, Castilloux G, Auger F, Garrel D, O'Connor-McCourt M, Germain L (1998) Modulated response to cytokines of human wound healing myofibroblasts compared to dermal fibroblasts. Exp Cell Res 238:283–293

[28] Murphy K, Hall C, Maini P, McCue S, McElwain D (2012) A fibrocontractive mechanochemical model of dermal wound closure incorporating realistic growth factor kinetics. B Math Biol 74:1143–1170

[29] Nagase H, Visse R, Murphy G (2006) Structure and function of matrix metalloproteinases and TIMPs. Cardiovasc Res 69:562–573

[30] Olsen L, Sherratt J, Maini P (1995) A mechanochemical model for adult dermal wound contraction and the permanence of the contracted tissue displacement profile. J Theor Biol 177:113–128

[31] Olsen L, Sherratt J, Maini P, Marchant B (1998) Simple modelling of extracellular matrix alignment in dermal wound healing I. Cell flux induced alignment. J Theor Med 1:172–192

[32] Overall C, Wrana J, Sodek J (1991) Transcriptional and post-transcriptional regulation of 72-kda gelatinase/ type IV collagenase by transforming growth factor-β1 in human fibroblasts. J Biol Chem 266:14,064–14,071

[33] Patankar S (1980) Numerical Heat Transfer and Fluid Flow, 1st edn. McGraw-Hill, New York City, New York

[34] Persson PO, Strang G (2004) A simple mesh generator in MATLAB. SIAM Rev 46:329–345

[35] Postlethwaite A, Keski-Oja J, Moses H, Kang A (1987) Stimulation of the chemotactic migration of human fibroblasts by transforming growth factor β. J Exp Med 165:251–256

[36] Roberts A, Sporn M, Assoian R, Smith J, Roche N, Wakefiled L, Heine U, Liotta L, Falanga V, Kehrl J, Fauci A (1986) Transforming growth factor type β: Rapid induction of fibrosis and angiogenesis *in vivo* and stimulation of collagen formation *in vitro*. P Natl Acad Sci USA 83:4167–4171

[37] Rudolph R, Vande Berg J (1991) The myofibroblast in Dupuytren's contracture. Hand Clin 7:683–692

[38] Sillman A, Quang D, Farboud B, Fang K, Nuccitelli R, Isseroff R (2003) Human dermal fibroblasts do not exhibit directional migration on collagen 1 in direct-current electric fields of physiological strength. Exp Dermatol 12:396–402

[39] Strutz F, Zeisberg M, Renziehausin A, Raschke B, Becker V, Van Kooten C, Muller G (2001) TGF-β1 induces proliferation in human renal fibroblasts via induction of basic fibroblast growth factor (FGF-2). Kidney Int 59:579–592

[40] The MathWorks Inc (2014) `MATLAB` version 8.3.0.532 (R2014a)

[41] Tranquillo R, Murray J (1992) Continuum model of fibroblast-driven wound contraction: inflammation-mediation. J Theor Biol 158:135–172

[42] Turek S (1998) FEATFLOW Finite element software for the incompressible Navier-Stokes equations: User Manual. University of Heidelberg, Heidelberg, Germany, 1st edn

[43] Van Kan J, Segal A, Vermolen F (2014) Numerical Methods in Scientific Computing, 2nd edn. Delft Academic Press, Delft, The Netherlands

[44] Van Lint P, Libert C (2007) Chemokine and cytokine processing by matrix metalloproteinases and its effect on leukocyte migration and inflammation. J Leukocyte Biol 82:1375–1381

[45] Van Zuijlen P, Ruurda J, Van Veen H, Van Marle J, Van Trier A, Groenevelt F, Kreis R, Middelkoop E (2003) Collagen morphology in human skin and scar tissue: no adaptation in response to mechanical loading at joints. Burns 29:423–431

[46] Vande Berg J, Rudolph R, Poolman W, Disharoon D (1989) Comparative growth dynamics and active concentration between cultured human myofibroblasts from granulating wounds and dermal fibroblasts from normal skin. Lab Invest 61:532–538

[47] Welch M, Odland G, Clark R (1990) Temporal relationships of *F*-actin bundle formation, collagen and fibronectin matrix assembly, and fibronectin receptor expression to wound contraction. J Cell Biol 110:133–145

[48] Werner S, Grose R (2003) Regulation of wound healing by growth factors and cytokines. Physiol Rev 83:835–870

[49] Wrobel L, Fray T, Molloy J, Adams J, Armitage M, Sparrow J (2002) Contractility of single human dermal myofibroblasts and fibroblasts. Cell Motil Cytoskelet 52:82–90

5

IMPLICATIONS FROM A SENSITIVITY ANALYSIS PERFORMED ON A MODEL FOR THE SIMULATION OF THE CONTRACTION OF BURNS

A continuum hypothesis-based model is presented in order to investigate in more detail which elements of the healing response might have a substantial influence on the contraction of burns. Solely a portion of the dermal layer was included explicitly into the model. The dermal layer is modeled as an isotropic compressible neo-Hookean solid. Furthermore, fibroblasts, myofibroblasts, collagen molecules and a generic signaling molecule were selected as primary model components. All components of the model are modeled as continuous entities. Wound contraction is caused in the model by temporary pulling forces. These pulling forces are generated by myofibroblasts which are present in the recovering wounded area.

After the presentation of the model and a more detailed presentation of the custom-made numerical algorithm for the generation of simulations, good agreement is demonstrated with respect to the variability in the evolution of the surface areas of burns over time between the outcomes of computer simulations obtained with the model and measurements obtained in a previously conducted experimental study. In the model this variability is brought about by varying the values for some of its parameters simultaneously. In order to quantify the individual contributions of these parameter value variations to the dispersion in the surface area of healing burns and hence gain insight into which subprocesses have the largest influence on the contraction of such wounds, a factorial design in combination with a multiple linear regression analysis was used to analyze the simulation

This chapter is based on content of the article "A mathematical model for the simulation of the contraction of burns" [16].

data. This analysis shows that almost all variability in the surface area can be explained by variability in the value for the myofibroblast apoptosis rate and, to a lesser extent, the value for the collagen molecule secretion rate. This suggests that most of the variability in the evolution of the surface area of burns over time in the experimental study might be attributed to variability in these two rates. Finally, a probabilistic analysis was used to investigate in more detail the effect of variability in the values for the myofibroblast apoptosis rate and the collagen molecule secretion rate, on certain components of the healing process. Results of this latter analysis are also presented and discussed in this chapter.

5.1. INTRODUCTION

THE development of the model is presented in Section 5.2. In order to generate computer simulations a custom-made numerical algorithm had to be developed. An overview of this algorithm is presented in Section 5.3. Thereafter some details of the factorial design and the regression analysis which were used for the sensitivity analysis, are presented in Section 5.4. A probabilistic analysis was also used in this study in order to investigate in more detail the effect of variability in the values for the myofibroblast apoptosis rate and the collagen molecule secretion rate on certain aspects of the healing process. More details of this probabilistic analysis are also presented in Section 5.4. Simulation results and the results obtained with the statistical analyses are presented in Section 5.5. Finally, the results are discussed in Section 5.6.

5.2. DEVELOPMENT OF THE MATHEMATICAL MODEL

IN order to simulate the contraction process, some of the subprocesses that take place during the proliferative phase of the wound healing cascade were included into the model [7]. With respect to the subprocesses that are executed during the proliferative phase the following subprocesses were selected: fibroplasia and wound contraction.

Given that wound contraction mainly takes place in the dermal layer of the skin, solely a portion of this layer was incorporated explicitly into the model. The dermal layer is modeled as an isotropic compressible neo-Hookean solid [45]. With respect to the mechanical component of the model the displacement of the dermal layer ($\mathbf{u}$) was selected as primary model variable. In addition, the following four constituents of the dermal layer were selected as primary model variables: fibroblasts (N), myofibroblasts (M), a generic signaling molecule (c) and collagen molecules (ρ). Please note that while in the model presented in Chapter 4 both the concentration and the orientation of the collagen bundles were selected as primary model components, in the model presented in the current chapter solely the concentration of the collagen molecules was selected as a primary model component.

The continuum hypothesis-based framework of Tranquillo and Murray [44] was used as basis for the model. This framework consists of the following general set of conserva-

tion equations (See Section 4.2 for more details about these equations):

$$\frac{\partial z_i}{\partial t} + \nabla \cdot [z_i \mathbf{v}] = -\nabla \cdot \mathbf{J}_i + R_i, \tag{5.1a}$$

$$-\nabla \cdot \sigma = \mathbf{f}. \tag{5.1b}$$

Within the above equations, z_i represents the cell density / concentration of constituent i, $\mathbf{v}$ represents the displacement velocity of the dermal layer, $\mathbf{J}_i$ represents the flux associated with constituent i per unit area, R_i represents the (bio)chemical kinetics associated with constituent i, σ represents the Cauchy stress tensor associated with the dermal layer, and $\mathbf{f}$ represents the total body force working on the dermal layer. Given the chosen primary model variables, $i \in \{N, M, c, \rho\}$ holds. In the remainder of the text of this chapter, z_N has been replaced by N, z_M has been replaced by M, z_c has been replaced by c and z_ρ has been replaced by ρ.

5.2.1. THE CELLS

THE functional forms for the movement of the (myo)fibroblasts and the functional forms for the biochemical kinetics associated with these cells are identical to the functional forms that have been introduced in Chapter 4. For completeness the functional forms are presented here as well. More details about the functional forms can be found in Chapter 4. The functional forms for the cell fluxes are

$$\mathbf{J}_N = -D_F F \nabla N + \chi_F N \nabla c, \tag{5.2}$$

$$\mathbf{J}_M = -D_F F \nabla M + \chi_F M \nabla c, \tag{5.3}$$

where

$$F = N + M. \tag{5.4}$$

The parameter D_F is the cell density-dependent (myo)fibroblast random motility coefficient and χ_F is the chemotactic coefficient. The functional forms for the biochemical kinetics associated with the (myo)fibroblasts are

$$R_N = r_F \left[1 + \frac{r_F^{\max} c}{a_c^I + c} \right] [1 - \kappa_F F] N^{1+q} - k_F c N - \delta_N N, \tag{5.5}$$

$$R_M = r_F \left\{ \frac{\left[1 + r_F^{\max} \right] c}{a_c^I + c} \right\} [1 - \kappa_F F] M^{1+q} + k_F c N - \delta_M M. \tag{5.6}$$

Here r_F is the cell division rate, $r_F^{\max}$ is the maximum factor with which the cell division rate can be enhanced due to the presence of the signaling molecule, a_c^I is the concentration of the signaling molecule that causes the half-maximum enhancement of the cell division rate, $\kappa_F F$ represents the reduction in the cell division rate due to crowding, q is a fixed constant, k_F is the signaling molecule-dependent cell differentiation rate of fibroblasts into myofibroblasts, δ_N is the apoptosis rate of fibroblasts and δ_M is the apoptosis rate of myofibroblasts.

5.2.2. THE SIGNALING MOLECULES

THE functional form for the dispersion of the generic signaling molecule and the functional forms for the release, the consumption and the removal of the generic signaling molecule are also identical to the functional forms that have been introduced in Chapter 4:

$$\mathbf{J}_c = -D_c \nabla c, \tag{5.7}$$

$$R_c = k_c \left[\frac{c}{a_c^{II} + c} \right] \left[N + \eta M \right] - \delta_c g(F, c, \rho) c. \tag{5.8}$$

The parameter D_c represents the random diffusion coefficient of the generic signaling molecule, k_c represents the maximum net secretion rate of the signaling molecule, η is the ratio of myofibroblasts to fibroblasts in the maximum net secretion rate of the signaling molecule, a_c^{II} is the concentration of the signaling molecule that causes the half-maximum net secretion rate of the signaling molecule and δ_c is the proteolytic breakdown rate of the signaling molecules. The concentration of the generic metalloproteinase (MMP) (i.e., $g(F, c, \rho)$) which is responsible for the breakdown of the signaling molecules was assumed to be proportional to the cell density of the (myo)fibroblasts, and the concentration of both the collagen molecules and the signaling molecules according to the following formula (See the accompanying paragraph of Equation (4.9) for further details):

$$g(F, c, \rho) \propto \frac{\rho F}{1 + a_c^{III} c}. \tag{5.9}$$

Here $1/[1 + a_c^{III} c]$ represents the inhibition of the secretion of the generic MMP due to the presence of the signaling molecule.

5.2.3. THE COLLAGEN MOLECULES

IT was assumed that the secreted collagen molecules are attached to the extracellular matrix (ECM) instantaneously. Hence it was assumed that no active transport of collagen molecules takes place. Furthermore, the production of collagen molecules by both fibroblasts and myofibroblasts was incorporated into the model. The secretion rate of the molecules is enhanced in the presence of the signaling molecule. Finally, the proteolytic breakdown of the collagen molecules was incorporated into the model analogously to how this has been incorporated for the breakdown of the signaling molecules. Taken together, the following was obtained:

$$\mathbf{J}_\rho = \mathbf{0}, \tag{5.10}$$

$$R_\rho = k_\rho \left\{ 1 + \left[\frac{k_\rho^{\max} c}{a_c^{IV} + c} \right] \right\} \left[N + \eta M \right] - \delta_\rho g(F, c, \rho) \rho. \tag{5.11}$$

Here k_ρ is the collagen molecule secretion rate, $k_\rho^{\max}$ is the maximum factor with which this secretion rate can be enhanced due to the presence of the signaling molecule, a_c^{IV}

is the concentration of the signaling molecules that causes the half-maximum enhancement of the secretion rate and δ_ρ is the proteolytic breakdown rate of the molecules.

5.2.4. THE FORCE BALANCE

FOR the description of the relation between the generated stresses in the modeled portion of dermal layer and the produced strains, the following stress-strain relation was chosen:

$$J\sigma = 2C_1 J^{-\frac{2}{3}} \left[\mathbf{B} - \frac{1}{3}\mathrm{tr}\,(\mathbf{B})\,\mathbf{I}\right] + 2D_1 J\,[J-1]\,\mathbf{I}, \tag{5.12}$$

$$\mathbf{B} = (-2\mathbf{e} + \mathbf{I})^{-1}, \tag{5.13}$$

$$\mathbf{e} = \frac{1}{2}\left[\nabla\mathbf{u} + (\nabla\mathbf{u})^{\mathrm{T}} - (\nabla\mathbf{u})^{\mathrm{T}}\,\nabla\mathbf{u}\right], \tag{5.14}$$

$$J = \sqrt{\det(\mathbf{B})}, \tag{5.15}$$

$$C_1 = \frac{E\rho}{4[1+\nu]}, \tag{5.16}$$

$$D_1 = \frac{E\rho}{6[1-2\nu]}. \tag{5.17}$$

Here $\mathbf{B}$ is the left Cauchy-Green deformation tensor, $\mathbf{e}$ is the Eulerian finite strain tensor, $\mathbf{I}$ is the second order identity tensor and ν is Poisson's ratio [45]. It was assumed that the Young's moduli of the tissues are dependent on the concentration of the collagen molecules [35, 36]. In this model it was assumed that this dependence is linear. Hence the Young's modulus equals $E\rho$, where E is a constant.

Please note the following. Due to the fact that it was assumed that $\partial u/\partial z = \partial v/\partial z = 0$ and $w = 0$ hold within the modeled portion of dermal layer, with $\mathbf{u} = (u, v, w)^{\mathrm{T}}$ (See also Subsection 5.2.5), the finite strain tensor $\mathbf{e}$ has rank 2. Therefore, the following can be obtained by using a theorem proven by Miller [23]:

$$(-2\mathbf{e} + \mathbf{I})^{-1} = \mathbf{I} + \frac{1}{a+b}\left[2a\mathbf{e} + 4\mathbf{e}^2\right], \tag{5.18}$$

$$a = 1 - 2\mathrm{tr}(\mathbf{e}), \tag{5.19}$$

$$b = 2[\mathrm{tr}(\mathbf{e})]^2 - 2\mathrm{tr}\left(\mathbf{e}^2\right). \tag{5.20}$$

Furthermore,

$$J^{-1} = \det\left(\mathbf{F}^{-1}\right), \tag{5.21}$$

$$\mathbf{F}^{-1} = \mathbf{I} - \nabla\mathbf{u}, \tag{5.22}$$

where $\mathbf{F}$ is the deformation gradient tensor. Taken together, the equalities presented in Equation (5.18) until Equation (5.22) have been used to transform the stress-strain relation from Equation (5.14) into a direct relation between the Cauchy stress tensor and the

components of the displacement vector in order to obtain a numerical approximation of the solution for the displacement of the dermal layer from Equation (5.1b).

Finally, the forces that are generated by the myofibroblasts due to their pulling on the ECM were incorporated into the model [11]. Identical to the model presented in Chapter 4 the pulling forces are modeled as isotropic stresses that are proportional to the product of the cell density of the myofibroblasts and a simple function of the concentration of the collagen molecules [29]. No other forces were incorporated into the model. Taken together, the following was obtained:

$$\mathbf{f} = \nabla \cdot \left\{ \xi M \left[\frac{\rho}{R^2 + \rho^2} \right] \mathbf{I} \right\}. \tag{5.23}$$

Here ξ is the generated stress per unit cell density and the inverse of the unit collagen molecule concentration, and R is a fixed constant.

5.2.5. THE DOMAIN OF COMPUTATION

As has been mentioned already, it was assumed that both $\partial u/\partial z = \partial v/\partial z = 0$ and $w = 0$ hold within the modeled portion of the dermal layer, with the xy-plane running parallel to the surface of the skin. Furthermore, it was assumed that the derivatives of the concentrations and the cell densities of the modeled constituents are equal to zero in the direction perpendicular to the surface of the skin. Hence $\partial i/\partial z = 0$ with $i \in \{N, M, c, \rho\}$. Taken together, these assumptions imply that the calculations for obtaining simulations can be performed on an arbitrary, infinitely thin slice of dermal layer oriented parallel to the surface of the skin, and that the results from these calculations are valid for every infinitely thin slice of dermal layer oriented parallel to the surface of the skin. For the generation of simulation results the computational domain depicted in Figure 5.1 was used. Using Lagrangian coordinates ($\mathbf{X} = (X, Y, Z)^{\mathrm{T}}$), the domain of computation ($\Omega_{\mathbf{X}}$) is described mathematically by

$$\Omega_X \in \{-12 \text{ cm} \leq X \leq 12 \text{ cm},\ -12 \text{ cm} \leq Y \leq 12 \text{ cm},\ Z = 0 \text{ cm}\}. \tag{5.24}$$

5.2.6. THE INITIAL CONDITIONS AND THE BOUNDARY CONDITIONS

THE initial conditions give a description of the different cell densities and concentrations at the onset of the proliferative phase of the wound healing cascade. For the generation of simulation results the following function was used to describe the shape of the burn:

$$w\left(\mathbf{X}, c^I, c^{II}\right) = \begin{cases} 0 & \text{if } \|\mathbf{X}\| < \left[c^I - c^{II}\right], \\ \frac{1}{2}\left[1 + \sin\left(\frac{\left[\|\mathbf{X}\| - c^I\right]\pi}{2c^{II}}\right)\right] & \text{if } \left|\|\mathbf{X}\| - c^I\right| \leq c^{II}, \\ 1 & \text{if } \|\mathbf{X}\| > \left[c^I + c^{II}\right]. \end{cases} \tag{5.25}$$

Here $w = 0$ corresponds to completely wounded dermis and $w = 1$ corresponds to unwounded dermis. The values for the parameters c^I and c^{II} determine respectively the radius of the initial burn and the steepness of the boundary of the wounded area (i.e., the minimum distance between completely wounded dermis and unwounded dermis). Here a circular shape has been chosen so that the shape of the burns in the computer

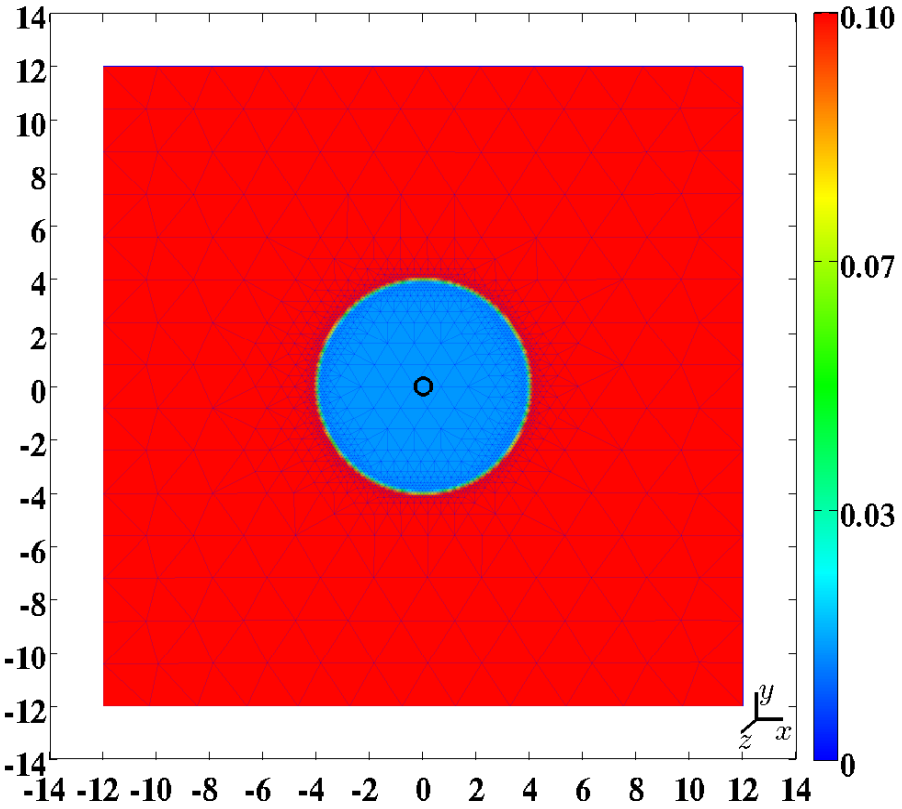

Figure 5.1: A graphical representation of the domain of computation (The scale along both axes is in centimeters). Depicted are the initial shape of the modeled portion of dermal layer and, in color scale, the initial concentration of the collagen molecules (with $I^w = 10^{-1}$), measured in g/cm^3. The black circle located more or less at the center of the wound, marks the material point within the dermal layer where the evolution of the concentrations (cell densities) of the different modeled constituents was traced over time for the generation of some of the figures in Section 5.5

simulations is equal to the shape of the burns that were created in the experimental study by Wang *et al.* [49]. Certain measurements obtained in this experimental study were used for comparison against certain outcomes of the obtained computer simulations in this study (See Section 5.5).

Based on the function for the shape of the wound, the following initial conditions were used for the modeled constituents of the dermal layer:

$$
\begin{aligned}
N(\mathbf{X},0) &= \left\{I^w + \left[1-I^w\right] w\left(\mathbf{X}, c^I, c^{II}\right)\right\} \overline{N},\\
M(\mathbf{X},0) &= \overline{M},\\
c(\mathbf{X},0) &= \left[1-w\left(\mathbf{X}, c^I, c^{II}\right)\right] c^w,\\
\rho(\mathbf{X},0) &= \left\{I^w + \left[1-I^w\right] w\left(\mathbf{X}, c^I, c^{II}\right)\right\} \overline{\rho}.
\end{aligned}
\tag{5.26}
$$

Here $\overline{N}$, $\overline{M}$ and $\overline{\rho}$ represent respectively the equilibrium cell density of the fibroblasts, the equilibrium cell density of the myofibroblasts and the equilibrium concentration of the collagen molecules, of the unwounded dermis. See Figure 5.1 for a detailed graphical representation of the initial concentration of the collagen molecules and see the leftmost column of Figure 5.2 for graphical representations of all initial cell densities and concentrations. Due to early secretion of signaling molecules by for instance macrophages, signaling molecules are present at the site of injury. The constant c^w is the maximum of the initial concentration of the signaling molecule in the wounded area. Furthermore, it was assumed that there are some fibroblasts and collagen molecules present in the wounded area; the parameter I^w determines the minimum amount of fibroblasts and collagen molecules that are present initially in the wounded area. Finally, $3.57 \leq c^I \leq 3.99$ cm and $c^{II} = 0.10$ cm.

With respect to the initial conditions for the displacement of the dermal layer, the following holds. The initial cell density of the myofibroblasts is equal to zero everywhere in the domain of computation. Looking at Equation (5.23), this implies $\mathbf{f}(\mathbf{x},0) = \mathbf{0}$. Therefore,

$$
\mathbf{u}(\mathbf{x},0) = \mathbf{0} \quad \forall \mathbf{x} \in \Omega_{\mathbf{x},0}, \tag{5.27}
$$

where $\Omega_{\mathbf{x},0}$ is the initial domain of computation in Eulerian coordinates and $\mathbf{x} = (x,y,z)^{\mathrm{T}}$ are the Eulerian coordinates.

With respect to the boundary conditions for the modeled constituents of the dermal layer, the following Dirichlet boundary conditions were used for all time t and for all $\mathbf{x} \in \partial\Omega_{\mathbf{x},t}$, where $\partial\Omega_{\mathbf{x},t}$ is the boundary of the domain of computation in Eulerian coordinates:

$$
N(\mathbf{x},t) = \overline{N}, \quad M(\mathbf{x},t) = \overline{M}, \quad c(\mathbf{x},t) = \overline{c}. \tag{5.28}
$$

Here $\overline{c}$ is the equilibrium concentration of the signaling molecules in the unwounded dermis. With respect to the boundary conditions for the mechanical component of the model, the following Robin boundary condition was used for all time t and for all $\mathbf{x} \in \partial\Omega_{\mathbf{x},t}$:

$$
\mathbf{n} \cdot \sigma(\mathbf{x},t) = -s\rho(\mathbf{x},t)\mathbf{u}(\mathbf{x},t). \tag{5.29}
$$

Here $\mathbf{n}$ is the unit outward pointing normal vector to the boundary of the domain of computation. This boundary condition implies that the boundaries experience a spring-like force per unit area in the opposite direction of the displacement of the dermal layer that is proportional to the concentration of the collagen molecules and the magnitude of this displacement.

5.2.7. THE (RANGES OF THE) VALUES FOR THE PARAMETERS

TABLE 5.1 provides an overview of the (ranges of the) values for the parameters of the model. The majority of these values were either obtained directly from previously conducted studies or estimated from results of previously conducted studies. In addition, the values for the equilibrium signaling molecule concentration of the unwounded dermis ($\overline{c}$), the constant q and the collagen molecule degradation rate (δ_ρ) could be determined due to the fact that these values are a necessary consequence of the values chosen for other parameters. See Subsection 4.2.7 for the derivation of the values for these parameters.

The ranges of the values for the free parameters δ_M, k_ρ, and I^w were chosen in such a way that there is good agreement with respect to the variability in the evolution of the surface area of burns over time between the outcomes of computer simulations obtained in this study and measurements obtained in a previously conducted experimental study by Wang *et al.* [49] (See Section 5.5). Finally, the range of the value for the radius of the initial burn (i.e., the range of the value for the parameter c^I (See Subsection 5.2.6)) was chosen in such a way that it matches with the range of the radii of the burns that were created during the experimental study of Wang *et al.* [49].

Table 5.1: An overview of the (ranges of the) values for the parameters of the model. The last column contains the references to the studies that were used for obtaining (estimates of) the values for the parameters. If (the range of) the value for a parameter has been estimated in this study, then this is indicated by the abbreviation TW. If the value for a parameter is a necessary consequence of the values chosen for the other parameters, then this is indicated by the abbreviation NC

Parameter	Value	Dimensions	Reference
D_F	10^{-7}	$cm^5/(cells\ day)$	[39]
χ_F	2×10^{-3}	$cm^5/(g\ day)$	[28]
q	-4.2×10^{-1}	–	NC
r_F	9.24×10^{-1}	$cm^{3q}/(cells^q\ day)$	[9]
r_F^{max}	2	–	[40]
a_c^I	10^{-8}	g/cm^3	[10]
κ_F	10^{-6}	$cm^3/cells$	[48]
k_F	5.4×10^6	$cm^3/(g\ day)$	[4]
δ_N	2×10^{-2}	/day	[29]
δ_M	$(1-6)\times10^{-2}$	/day	TW
D_c	2.9×10^{-3}	cm^2/day	[28]
k_c	4×10^{-13}	$g/(cells\ day)$	[29]
η	2	–	[27] & [38]
a_c^{II}	10^{-8}	g/cm^3	[29]
δ_c	5×10^{-4}	$cm^6/(cells\ g\ day)$	[29]
a_c^{III}	2×10^8	cm^3/g	[30]
k_ρ	$(1.25-2.75)\times10^{-8}$	$g/(cells\ day)$	TW
k_ρ^{max}	10	–	[29]
a_c^{IV}	10^{-9}	g/cm^3	[37]
δ_ρ	$(1.25-2.75)\times10^{-6}$	$cm^6/(cells\ g\ day)$	NC
E	1.00×10^2	$(N\ cm)/g$	[18]

Continued on the next page

Table 5.1 – *Continued from the previous page*

Parameter	Value	Dimensions	Reference
ν	4.9×10^{-1}	–	[18]
ξ	5×10^{-3}	(N g)/(cells cm^2)	[22] & [50]
R	3×10^{-1}	g/cm^3	[29]
$\overline{N}$	10^4	cells/cm^3	[29]
$\overline{M}$	0	cells/cm^3	[29]
$\overline{c}$	0	g/cm^3	NC
$\overline{\rho}$	10^{-1}	g/cm^3	[29]
I^w	$(1-2) \times 10^{-1}$	–	TW
c^w	10^{-8}	g/cm^3	[29]
s	10^3	N/g	[17]

5.2.8. A QUALITATIVE DESCRIPTION OF THE DYNAMICS OF THE MODEL

HERE a qualitative description is given of how the healing of a burn is accomplished in the presented model and how the different subprocesses that have been incorporated into the model, interact with each other. Due to the presence of the signaling molecule in the wounded area at the onset of the proliferative phase fibroblasts from the surrounding uninjured tissue are attracted toward the wounded area. Within the wounded area the fibroblasts proliferate and due to the presence of the signaling molecules, the proliferation rate is enhanced. In addition, the signaling molecules stimulate the cell differentiation of fibroblasts into myofibroblasts. This results in the emergence of a myofibroblast population in the wounded area. While there are signaling molecules present, both fibroblasts and myofibroblasts also secrete signaling molecules which results subsequently in a further enhancement of both the cell differentiation rate and the cell proliferation rate of fibroblasts and myofibroblasts and hence a further growth of the size of the myofibroblast population within the wounded area. The present (myo)fibroblasts in the wounded area produce collagen molecules in order to restore the presence of a collagen-rich ECM and due to the presence of the signaling molecules the production rate of the collagen molecules is enhanced. Furthermore, the present myofibroblasts in the wounded area pull on the ECM and as a consequence the surface area of the burn is reduced slowly over time.

During the execution of the wound healing processes the concentration of the generic MMP rises slowly in the recovering wounded area and due to this the secretion of signaling molecules becomes smaller than the proteolytic breakdown of these molecules at a certain point in time. Consequently, the signaling molecules disappear relatively fast from the wounded area and due to that the rate of production of the collagen molecules starts to decline, as does the rate of cell proliferation and cell differentiation. Slowly the cell densities and the concentrations in the recovering wound area will approach the equilibrium cell densities and the equilibrium concentrations of the unwounded area due to, respectively, cell apoptosis and proteolytic breakdown, and ultimately the properties of the recovering wounded area will become identical to the properties of the surrounding tissue. Subsequently this implies that the size of the surface area of the recovering wound area slowly returns to the surface area of the burn at the onset of the proliferative phase. The decline of the cell density of the myofibroblast population in the dermal layer, the decline of the concentrations of both the signaling molecules and

the collagen molecules, the gradual rise of the cell density of the fibroblast population in the wounded area, and the gradual retraction of the recovering wounded area are not (clearly) visible in the results presented in Section 5.5, but these phenomena are properties of the model and are clearly visible in computer simulations where longer healing times are simulated.

5.3. THE APPLIED NUMERICAL ALGORITHM

IN this section an overview of the custom-made numerical algorithm is presented. The development of this algorithm was necessary to "catch" the local dynamics of the model, obtain sufficiently accurate simulations within an acceptable amount of CPU time, and guarantee the positivity of the approximations of the solutions for the modeled constituents of the dermal layer.

For the kernel of the concrete expression of the algorithm `MATLAB` was used together with `MATLAB`'s Parallel Computing Toolbox [43]. Furthermore, this kernel was interfaced consecutively with a slightly adapted version of the mesh generator developed by Persson and Strang [32], the element resolution refinement / recoarsement tool of the computational fluid dynamics (CFD) software package `FEATFLOW2` [46], and the permutation routine `HSL_MC64` [12]. Finally, the following non-dimensionalisation was applied:

$$\begin{aligned} x &= Lx^*, & t &= \left[L^2/\left[D_F\overline{N}\right]\right]t^*, & \rho &= \overline{\rho}\rho^*, \\ N &= \overline{N}N^*, & M &= \overline{N}M^*, & c &= c^w c^*, \\ \mathbf{u} &= L\mathbf{u}^*, & \mathbf{v} &= \left[\left[D_F\overline{N}\right]/L\right]\mathbf{v}^*, & \sigma &= \left[\left[\xi\overline{N}\right]/\overline{\rho}\right]\sigma^*: \end{aligned} \tag{5.30}$$

Here $L = 1$ cm is the length scale of the model. The variables with the asterisks are the non-dimensionalised variables.

In the following two subsections a step-by-step description of the algorithm is presented. Basically the algorithm consists of two parts. The first part of the algorithm is dedicated to the generation of a proper triangulation of the domain of computation and is described in Subsection 5.3.1. The second part of the algorithm is described in Subsection 5.3.2 and is dedicated to obtaining an approximation of the solution for the displacement and the modeled constituents of the dermal layer from Equation (5.1) after application of the non-dimensionalisation.

5.3.1. GENERATION OF THE INITIAL TRIANGULATION

THE first part of the algorithm consists again of two subparts. First, a conforming base triangulation is generated and subsequently the element resolution refinement / recoarsement tool is used to adjust the resolution of the elements of this base triangulation.

In order to create a conforming base triangulation the aforementioned adapted version of the mesh generator developed by Persson and Strang is used [32]. This results in a very high quality triangulation of the domain of computation that consists mainly of equilateral triangles. Most of the triangles that are not equilateral, are located near the left and right boundary of the domain of computation. These latter triangles are nearly equilateral. Using the following measure for the quality of a triangle ABC:

$$\alpha(ABC) = 2\sqrt{3}\left[\frac{\|CA \times CB\|}{\|CA\|^2 + \|AB\|^2 + \|BC\|^2}\right], \tag{5.31}$$

it was observed that $\alpha > 0.86$ for all triangles in the generated triangulations that were used for the generation of the simulation results, where $0 \leq \alpha \leq 1$ [19].

For the generation of the simulation results presented in Figures 5.2 through 5.6, a base triangulation was used that consisted of triangles with an average initial edge length of 1.85 cm. The calculations for the generation of the simulation results presented in Figures 5.2 through 5.5 were repeated two times. The first time a base triangulation that consisted of triangles with an average initial edge length of 9.24×10^{-1} cm was used and the second time a base triangulation that consisted of triangles with an average initial edge length of 3.46 cm was used. It was observed that the difference in the simulation results with respect to the outcomes between the different calculations were small.

After generation of the conforming base triangulation the element resolution refinement / recoarsement tool is used to adjust the resolution of the elements of this base triangulation [24]. For this purpose the L_2-norm of an estimation of the error in the gradient of the numerical approximation of the function that gives a mathematical description of the shape of the wound (i.e., Equation (5.25)) per element is determined first [25]. Subsequently, the resolution of the elements is adapted in order to adjust the estimated error. For this end, the following measure is used to determine the relative error per element K_t in the gradient of the numerical approximation of the function that gives a mathematical description of the shape of the wound with respect to the other elements:

$$\beta(K_t) = \left[\frac{\left|\mathcal{T}_{h,t}\right| \|\hat{\mathbf{e}}\|^2_{L_2(K_t)}}{\sum_{K_t \in \mathcal{T}_{h,t}} \left(\|\sigma_h\|^2_{L_2(K_t)} + \|\hat{\mathbf{e}}\|^2_{L_2(K_t)}\right)}\right]^{\frac{1}{2}}. \tag{5.32}$$

Here $\mathcal{T}_{h,t}$ represents the current triangulation, $\left|\mathcal{T}_{h,t}\right|$ represents the number of elements that constitute this current triangulation, $\|\hat{\mathbf{e}}\|_{L_2(K_t)}$ represents the L_2-norm of the estimation of the error in the gradient of the numerical approximation of the function that gives a mathematical description of the shape of the wound over element K_t, and $\|\sigma_h\|_{L_2(K_t)}$ represents the L_2-norm of a low-order estimation of the gradient of the numerical approximation of the function that gives a mathematical description of the shape of the wound over element K_t [25]. If $\beta(K_t) > 0.2$, then the resolution of the element K_t is increased. If $\beta(K_t) < 0.04$, then the resolution of the element K_t is decreased. In this study the resolution of the elements in the base triangulation could be increased at most four times and the size of the elements in the base triangulation could not be increased beyond the size they had in the base triangulation.

The estimation of the error $\|\hat{\mathbf{e}}\|_{L_2(K_t)}$ and the subsequent adjustment of the resolution of the elements are repeated until either the absolute value of the relative change of the sum of the L_2-norm of the estimation of the error of the gradient over all elements is smaller than 5%, or the maximum number of allowed for iterations is reached. In this study this latter number was set to ten.

5.3.2. DETERMINATION OF THE APPROXIMATION OF THE SOLUTION

As was mentioned before, the second part of the algorithm is dedicated to obtaining an approximation of the solution for the displacement and the modeled constituents of the dermal layer from Equation (5.1). In order to solve the time-dependent problem the method of lines and the standard fixed-point defect correction method are used [47]. The two equations of the system are solved in a segregated way. Each time step approximations of the solutions for the modeled constituents of the dermal layer are determined first and subsequently an approximation of the solution for the displacement of the dermal layer is determined. This scheme is iterated until the maximum of the relative 1-norms of the residuals of the approximations is smaller than one, and the maximum of the relative 1-norms of the difference between subsequent approximations per variable is smaller than 5×10^{-2}. If the fixed-point scheme does not meet the convergence criteria within five iterations, then the scheme is interrupted, the time step is decreased to 85% of its current value, and subsequently the scheme is restarted. The required estimate of the gradient of the solution for the signaling molecule is obtained by using a variational gradient recovery projection scheme [20].

For the discretization of the system of equations the first-order backward Euler time-integration method is used together with a moving-grid finite-element method [21]. For the approximation of the individual primary variables of the model functions from the space of triangular finite-elements with linear basis functions are chosen [34]. The integrals over the interior of the elements are approximated by a second-order accurate Newton-Cotes quadrature rule and the integrals over the boundaries of the elements are approximated by a second-order accurate Gaussian quadrature rule. Furthermore, a semi-implicit flux-corrected transport (FCT) limiter developed by Möller *et al.* and a source term splitting procedure proposed by Patankar, are applied on the discretized system of equations that describe the dynamics of the modeled constituents of the dermal layer [26, 31]. Taken together, these latter two techniques enforce positivity of the approximations of the solutions for the constituents of the dermal layer.

In order to obtain approximate solutions for the resulting linear systems of equations, `MATLAB`'s backslash operator is used after using the LU factorization algorithm on scaled and permuted versions of the original linear systems [2, 43]. For the scaling and permutation of the linear systems several inbuilt scaling and permutation algorithms of `MATLAB` are used together with the permutation routine `HSL_MC64` [3, 6, 12].

The time steps are chosen by using an automatically adaptive time-stepping procedure with inbuilt local truncation error control [15]. The maximum size of the initial time step is set to 10^{-5} dimensionless units and the upper bound of the size of the time step is set to 10^{-3} dimensionless units. If a time step is accepted, then the subsequent time step is at most 1.25 times the size of the current time step. If a time step is rejected, then the subsequent time step is at least 0.25 times the size of the current time step. The absolute and relative truncation error tolerance were set to, respectively, 10^{-2} and 5×10^{-2} dimensionless units (See the article by Kavetski *et al.* for further details on this matter [14]). After obtaining and accepting an approximation for a certain time step, the local extrapolation procedure proposed by Kavetski *et al.* is used to increase the accuracy of the approximation [15].

Finally, the aforementioned element resolution refinement / recoarsement tool is

applied every ten time steps to adjust the resolution of the elements of the triangulation. For this end the L_2-norm of an estimation of the error of the gradient of the numerical approximation of the solution for the concentration of the collagen molecules per element is determined first [25]. Thereafter the resolution of the elements is adapted in a fashion identical to the procedure described in Subsection 5.3.1 in order to adjust the estimated error. For the interpolation of approximations to new vertices in the triangulation, piecewise bivariate Hermite interpolation is used [8]. The required gradients of the approximations at the existing vertices are estimated by using a polynomial preserving gradient recovery scheme [51].

5.4. DETAILS OF THE APPLIED STATISTICAL METHODS

5.4.1. THE FACTORIAL DESIGN AND THE REGRESSION ANALYSIS

IN this study a simple mixed-level full-factorial design in combination with a multiple linear regression analysis was used to quantify the individual contributions of the variations in the values for the free parameters of the model and the initial radius of the wound, to the dispersion in the surface area of healing burns [33, 41, 42]. The relative surface area of the healing burn at day 42 compared to the surface area of the burn at day 0 was chosen as the response variable (i.e., the dependent variable). The free parameters of the model and the initial radius of the wound were chosen as factors (i.e., independent variables). These latter parameters were assigned discrete values (i.e., levels) that divide the range of each factor equally. Here the radius of the initial burn (c^I) was assigned two levels, the minimum amount of fibroblasts and collagen molecules that are present initially in the wounded area (I^w) was assigned three levels, the collagen molecule secretion rate (k_ρ) was assigned four levels and the myofibroblast apoptosis rate (δ_M) was assigned six levels. For the analysis all possible combinations of the levels of the factors were examined. Hence in total 144 computer simulations were generated.

The obtained simulation data were analyzed in `IBM SPSS` by means of the aforementioned regression analysis [13]. No interactions or powers of independent variables were included in this analysis. In order to reduce the skewness and kurtosis of the data related to the relative surface area of the healing burn and to improve the normality, linearity and homoscedasticity of the residuals of the regression analysis, the Rankit rank-based normalization method was used on the data related to the response variable. Furthermore, all data related to the factors of the factorial design were transformed to standard scores (i.e., z values).

The surface areas of a the burns were determined in two steps. In the first step the displacements of the material points with coordinates $(c^I(\cos(2\pi(i-1)/40)), c^I(\sin(2\pi(i-1)/40)), 0)^{\mathrm{T}}$, where $i \in \{1,\ldots,40\}$, were determined. Subsequently, the area of the polygon with vertices located at the displaced material points was computed. This area is approximately equal to the surface area of a healing burn.

5.4.2. THE PROBABILISTIC ANALYSIS

AFTER having used a regression analysis, a probabilistic analysis was used in order to investigate in more detail the effect of variability in the values for the collagen molecule secretion rate and the myofibroblast apoptosis rate, on both the cell density of

Table 5.2: An overview of the results obtained with the multiple linear regression analysis. The regression coefficients (β) are the weights of the linear regression line. The t scores and p values are the associated statistics. The squared semipartial correlations between the dependent variable and the individual independent variables (sr^2) are displayed in the last column of the table

				95% Conf. Interval		
Variable	β	t score	p value	**Lower**	**Upper**	sr^2
c^I	0.048	2.258	0.026	0.006	0.090	0.002
I^w	-0.073	-3.463	0.001	-0.115	-0.032	0.005
δ_M	0.912	42.978	< 0.001	0.869	0.953	0.832
k_ρ	0.313	14.754	< 0.001	0.271	0.355	0.098

the myofibroblasts and the concentration of the collagen molecules at day 42, and the relative surface area of the healing burn at day 42 compared to its surface area at day 0. The collagen molecule secretion rate and the myofibroblast apoptosis rate were chosen because the multiple linear regression analysis demonstrated that varying the value for these two factors has by far the largest impact on the relative surface area of the healing burn (See the presentation of the results of the linear regression analysis in Table 5.2).

The distribution of the collagen molecule secretion rate (k_ρ) was defined as a Gaussian (normal) distribution with a mean value of 2×10^{-8} g/(cells day) and a standard deviation of 3.75×10^{-9} g/(cells day). The distribution of the myofibroblast apoptosis rate (δ_M) was defined as a Gaussian (normal) distribution with a mean value of 3.50×10^{-2} /day and a standard deviation of 1.25×10^{-2} /day. The values for the parameters related to the minimum amount of fibroblasts and collagen molecules that are present initially in the wounded area (I^w) and the radius of the initial burn (c^I) were set to, respectively 1.5×10^{-1} and 3.78 cm. The values for all remaining parameters are equal to those depicted in Table 5.1.

Sampling from the Gaussian distributions was realized by using MATLAB's function `normrnd` [43]. In this study two samples consisting of 100 observations, were drawn from each distribution. Hence in total 100 computer simulations were generated. The Anderson-Darling test was used to investigate the degree of normality of the samples [1]. Both samples did not show a significant deviation from a normally distributed sample ($p > 0.5$ for both samples).

The concentration of the collagen molecules and the cell density of the myofibroblasts were determined in two steps. In the first step the cell density and concentration at the material points with coordinates $(0,0,0)^{\mathrm{T}}$, $((c^I/2)(\cos(2\pi(i-1/2)/4)), (c^I/2)(\sin(2\pi(i-1/2)/4)),0)^{\mathrm{T}}$, and $(c^I(\cos(2\pi(i-1)/4)), c^I(\sin(2\pi(i-1)/4)),0)^{\mathrm{T}}$, where $i \in \{1,\ldots,4\}$, were determined. Subsequently, the averages of these values were calculated and these averages were used for the analysis. See Subsection 5.4.1 for a description of how the surface areas of the healing burns were determined.

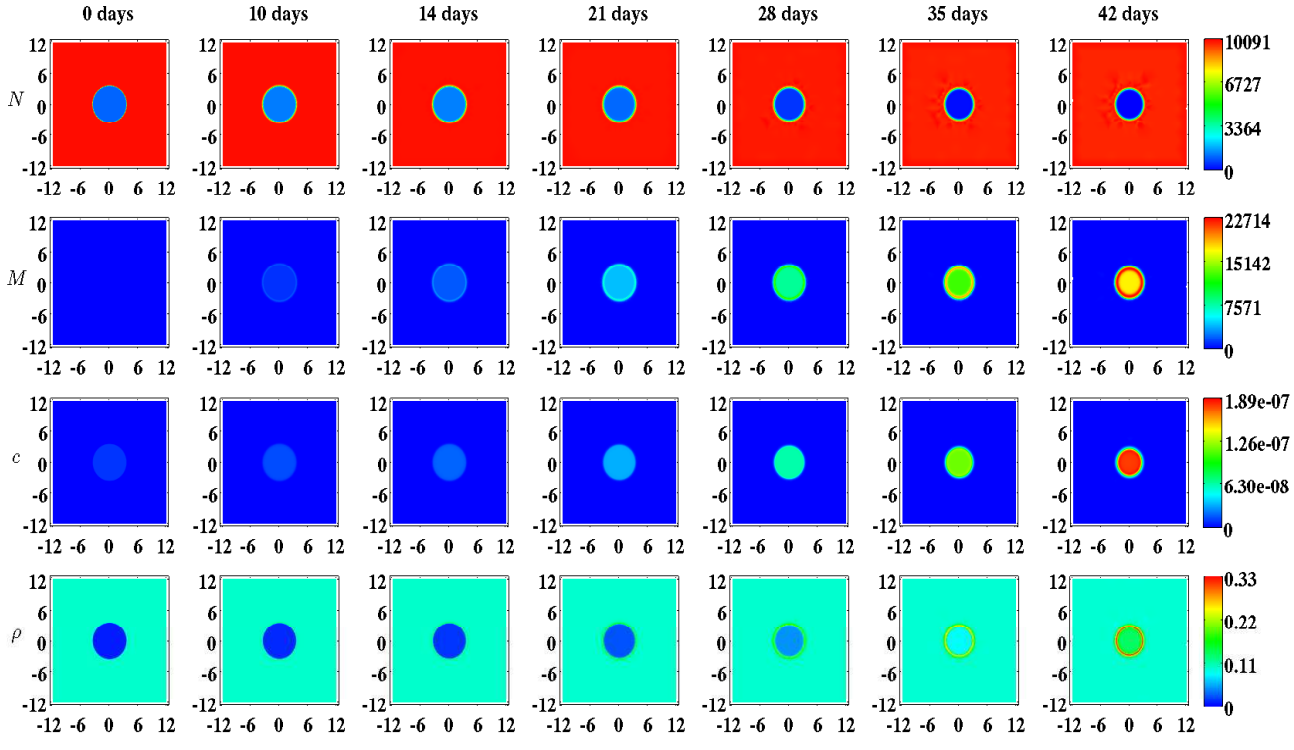

Figure 5.2: An overview of a simulation with a relatively small burn ($c^I = 3.57$ cm), a relatively low minimum initial fibroblast cell density and a relatively low minimum initial concentration of collagen molecules ($I^w = 1 \times 10^{-1}$), a relatively low apoptosis rate of myofibroblasts ($\delta_M = 2 \times 10^{-2}$ /day) and an average collagen molecule secretion rate ($k_\rho = 1.75 \times 10^{-8}$ g/(cells day)). The values for the remaining parameters are equal to those depicted in Table 5.1. The first two rows show the evolution over time of the cell density of respectively the fibroblasts and the myofibroblasts. The color scales represent the cell densities, measured in cells/cm^3. The last two rows show the evolution over time of the concentration of respectively the signaling molecules and the collagen molecules. The color scales represent the concentrations, measured in g/cm^3. Within the subfigures, the scale along both axes is in centimeters

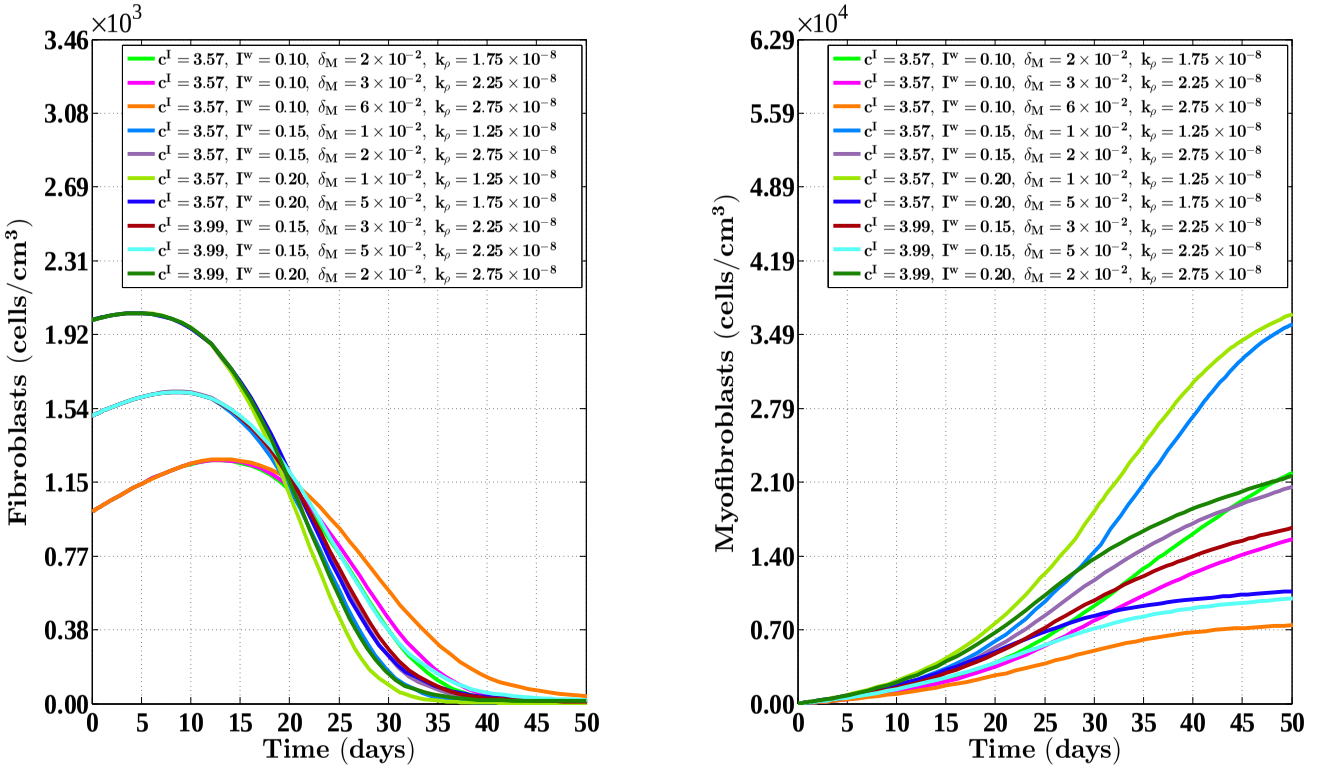

Figure 5.3: The evolution over time of the cell densities for a random selection of some combinations of the levels of the factors of the factorial design. The values for the remaining parameters are equal to those depicted in Table 5.1. See Figure 5.1 for the location where the evolution of the cell densities was traced over time

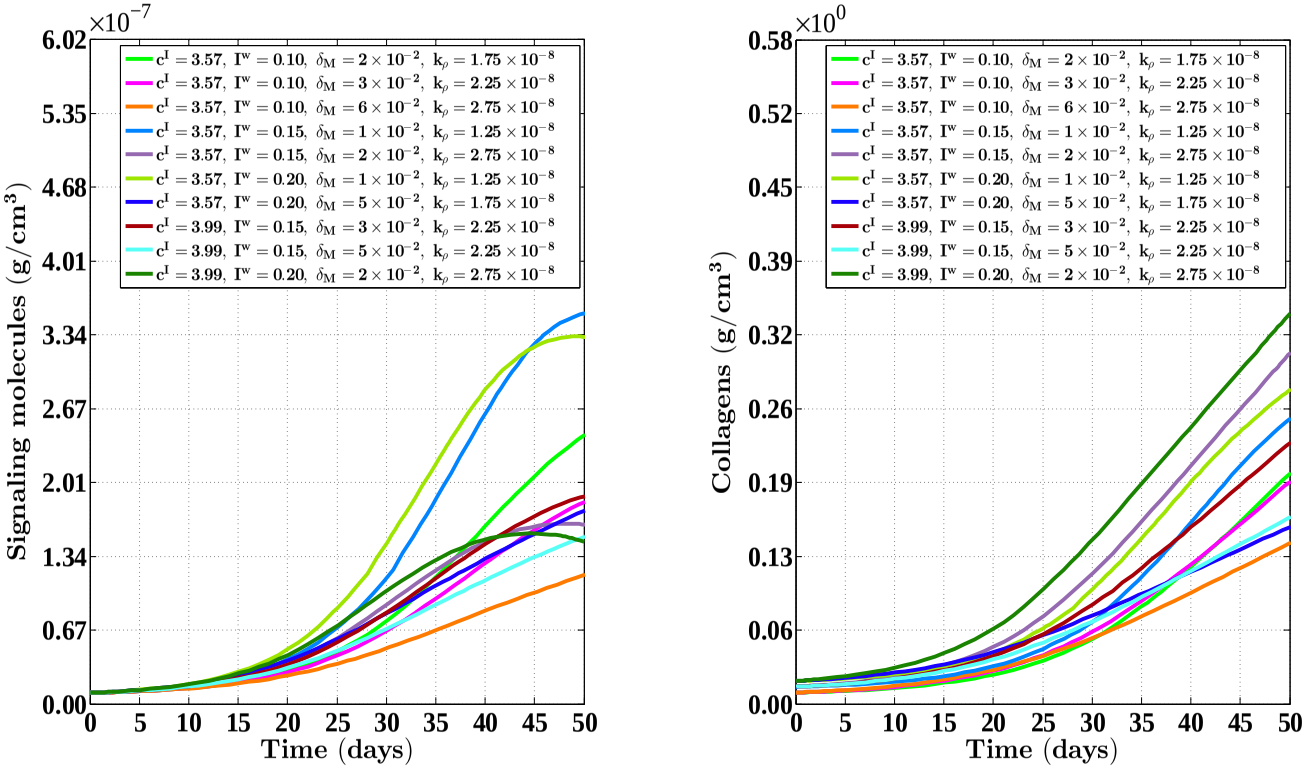

Figure 5.4: The evolution over time of the concentrations of the signaling molecules and the collagen molecules for a random selection of some combinations of the levels of the factors of the factorial design. The values for the remaining parameters are equal to those depicted in Table 5.1. See Figure 5.1 for the location where the evolution of the concentrations was traced over time

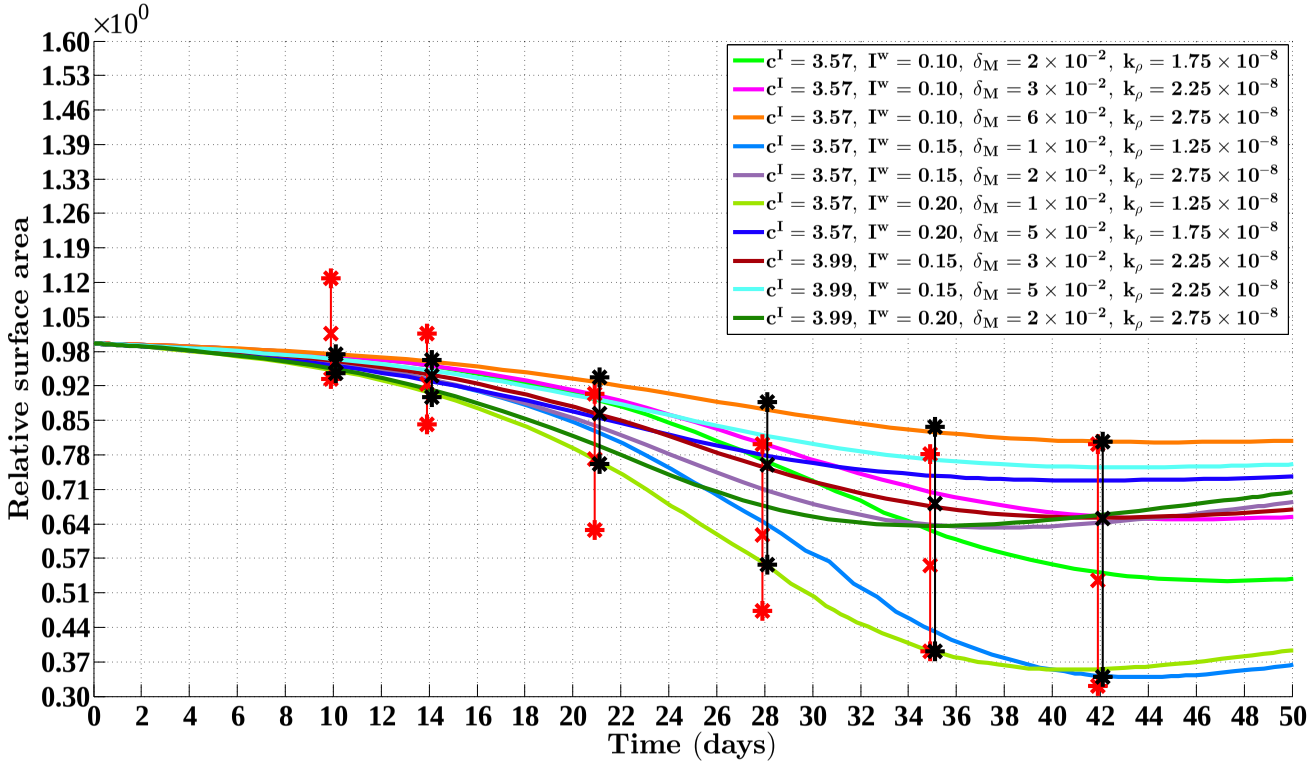

Figure 5.5: The evolution over time of the relative surface area of burns for a random selection of some combinations of the levels of the factors of the factorial design. The values for the remaining parameters are equal to those depicted in Table 5.1. The surface area of a burn was compared to its surface area at day 0 at every time point. The black bars represent the ranges of the relative surface areas of all burns at different time points after injury. The asterisks represent the extreme values of all combinations of the levels of the factors and the crosses represent the mean values of all combinations of the levels of the factors. Furthermore, the red bars represent experimental measurements of the relative surface areas of healing burns at different time points after injury in a porcine burn model [49]. The asterisks and the crosses represent, respectively, the extreme values and the mean values of these measurements

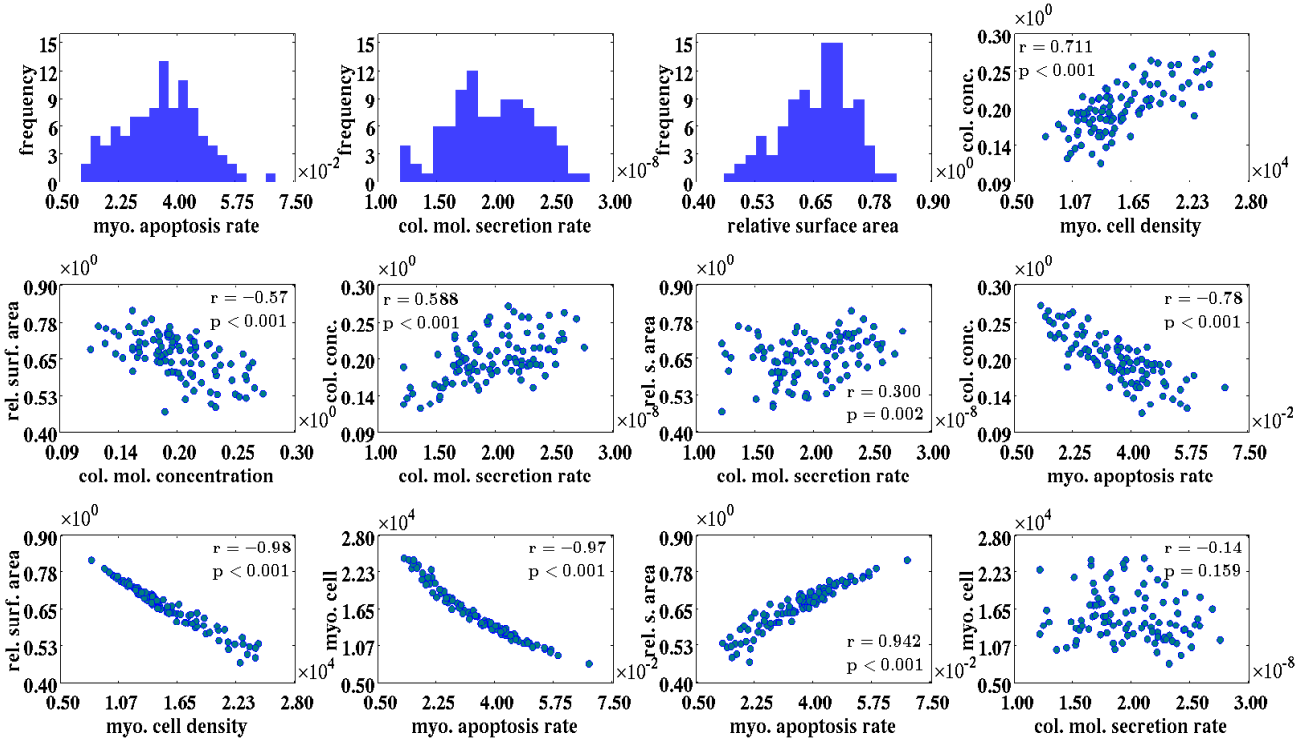

Figure 5.6: An overview of the results obtained with the probabilistic analysis. The frequency histograms display the drawn samples for the myofibroblast apoptosis rate (δ_M) and the collagen molecule secretion rate (k_ρ), and the obtained distribution of the relative surface area of the healing burns at day 42 compared to their surface areas at day 0. The scatter plots provide graphical representations of the relationships between various properties of the healing burn at day 42. Within the individual subfigures the Pearson correlation coefficients are displayed together with the associated p values

5.5. SIMULATION RESULTS

In order to obtain some insight into the dynamics of the model, an overview of a simulation is presented in Figure 5.2. Furthermore, Figure 5.3 and Figure 5.4 show, respectively, the evolution over time of the different cell densities and the evolution over time of the different concentrations for a random selection of some combinations of factor levels (i.e., some combinations of values for the initial radius of the burn, the minimum initial cell density of the fibroblasts and minimum initial concentration of the collagen molecules, the apoptosis rate of myofibroblasts and the collagen molecule secretion rate) at a certain material point within the healing burn. Finally, Figure 5.5 shows the evolution over time of the relative surface areas of the burns for the same random selection of combinations of levels as was used for the creation of Figure 5.3 and Figure 5.4.

Table 5.2 provides an overview of the outcomes of the multiple linear regression analysis. The multiple correlation (R) is significantly different from zero, $F(4,139) = 520,473$, $p < 0.001$, with the squared multiple correlation at 0.937. The adjusted squared multiple correlation of 0.936 indicates that more than 93% of the variability in the relative surface area of the healing burn at day 42 compared to the size of the burn at day 0 can be predicted from variability in the values for the factors of the factorial design.

Finally, Figure 5.6 shows an overview of the results obtained with the probabilistic analysis. The obtained distribution of the relative surface area of the healing burns at day 42 compared to their surface areas at day 0 is negatively skewed and differs significantly from a Gaussian distribution according to the Anderson-Darling test ($p < 0.04$) [1]. The mean of the relative sizes of the healing burns at day 42 is 0.657 and the standard deviation of the obtained distribution is 0.073.

5.6. CONCLUSIONS

In this chapter a continuum hypothesis-based model has been presented in order to investigate in more detail which elements of the healing response might have a substantial influence on the contraction of burns. The bars in Figure 5.5 show that the agreement with respect to the variability in the evolution of the surface area of burns over time between the outcomes of the computer simulations obtained in this study and measurements obtained in a previously conducted experimental study by Wang *et al.* [49] is quite good. There is in general a reasonably good match between the outcomes of the computer simulations and the measurements obtained in the experimental study with respect to both the ranges of the relative surface areas of the healing burns and the means of these relative surface areas, and this match becomes better as healing progresses. Furthermore, it can also be observed in the computer simulations that while some healing burns continue to contract until day 50, others stopped to contract at an earlier day and started to retract. This variability is also present in the results presented by Wang *et al.* [49].

Looking at the results depicted in Figure 5.3 and Figure 5.4, it is clear that varying the values for the free parameters of the model and the radius of the initial burn has in general a huge impact on the evolution over time of the cell densities and the concentrations of the modeled constituents of the dermal layer within the wounded area. The disper-

sion in the cell density of the myofibroblasts at the center of the healing burn becomes quite large over time, and this is also the case for the dispersion in the concentration of the signaling molecules and the collagen molecules. Figure 5.5 shows furthermore that the evolution over time of the observed dispersion in the relative surface areas of the healing burns from the experimental study by Wang *et al.* [49] can be replicated quite well by the model through the variation of the values for radius of the initial burn and the free parameters of the model.

Combined these results provide the following explanation for the observed dispersion in the relative surface areas of the healing burns in the experimental study by Wang *et al.* [49]. Variability in the values for the free parameters of the model results in an increasing dispersion over time in both the cell density of the myofibroblasts, and the concentrations of the signaling molecules and collagen molecules. Given Equation (5.23), this implies that the dispersion in the total generated stress by the myofibroblasts also increases over time, which subsequently results in an increasing dispersion in the relative surface areas of the healing burns over time. Hence the observed variability in the evolution of the surface area of the healing burns over time in the experimental study by Wang *et al.* [49] might be attributed to variability in the myofibroblast apoptosis rate, the collagen molecule secretion rate, the minimum amount of fibroblasts and collagen molecules that are present initially in the wounded area, and the radius of the initial burn.

Looking more closely at the outcomes of the multiple linear regression analysis provided in Table 5.2, it can be observed that all regression coefficients differ significantly from zero. Hence variability in the value for each factor of the factorial design contributes significantly to variability in the relative surface area of a healing burn at day 42. The sizes of the squared semipartial correlations indicate that variability in the value for the myofibroblast apoptosis rate has a very large impact on the relative surface area of the healing burn at day 42. Variability in the value for the collagen molecule secretion rate has a smaller, but still quite substantial impact on the relative surface area of a healing burn at day 42. Variability in the value for the parameter related to the minimum amount of fibroblasts and collagen molecules that are present initially in the wounded area, and variability in the value for the radius of the initial burn have only a relative small impact on the relative surface area of the healing burn. Taken together the regression analysis suggests that the observed variability in the evolution of the surface area of the healing burns over time in the experimental study by Wang *et al.* might be attributed mainly to variability in the myofibroblast apoptosis rate and the collagen molecule secretion rate and to a far lesser extent to variability in the radius of the initial burn and the minimum amount of fibroblasts and collagen molecules that are present initially in the wounded area. Interestingly, this result is in agreement with the suggestion put forward by Desmoulière *et al.* [5] that the disruption of apoptosis (i.e., a low apoptosis rate) during wound healing might be a very important factor in the development of pathological scars such as severely contracted scars.

Looking at the results obtained with the probabilistic analysis in Figure 5.6, a couple of interesting observations can be made. Firstly, there is a good agreement between the regression coefficients for the collagen molecule secretion rate and the myofibroblast apoptosis rate in the linear regression line on the one hand, and the calculated cor-

relation coefficients for the relationship between the relative surface area of a burn at day 42 and the collagen molecule secretion rate and the myofibroblast apoptosis rate on the other hand. Secondly, it is interesting to observe that the obtained distribution of the relative surface areas of the healing burns is negatively skewed and differs significantly from a Gaussian (normal) distribution, even though the samples for the collagen molecule secretion rate and myofibroblast apoptosis rate were both drawn from a Gaussian distribution. Hence, relatively speaking, only a small portion of the burns contracts severely while the majority of the burns contracts a little.

Finally, it is interesting to observe that all of the remaining individual correlations displayed in the separate scatter plots make sense intuitively with the exception of the scatter plot that displays the correlation between the collagen molecule secretion rate and the cell density of the myofibroblasts. For example, one would expect positive correlations between the concentration of the collagen molecules and the rate of secretion of these molecules, and between the concentration of the collagen molecules and the cell density of the myofibroblast population. However, taking some of the correlations together shows something peculiar; while the correlation between the collagen molecule secretion rate and the concentration of the collagen molecules, and the correlation between the collagen molecule secretion rate and the relative surface area of a burn at day 42 are both positive, the correlation between the concentration of the collagen molecules and the relative surface area of a burn at day 42 is negative.

In order to explain this phenomenon, the following is suggested. Besides influencing the total amount of generated stress directly through the relationship given in Equation (5.23), the concentration of the collagen molecules also influences the amount of generated stress indirectly through the following chain of connections. Given Equation (5.9), it is seems reasonable to expect a positive correlation between the concentration of the collagen molecules and the concentration of the generic MMP. Given Equation (5.6) and Equation (5.8), it also seems reasonable to presume a negative correlation between the concentration of the generic MMP and the concentration of the signaling molecule and a positive correlation between the concentration of the signaling molecule and the cell density of the myofibroblast population. Taken together, these correlations suggest a negative correlation between the collagen molecule secretion rate and the cell density of the myofibroblast population. Although not significantly different from zero, this is exactly what is displayed in the scatter plot that displays the correlation between the collagen molecule secretion rate and the cell density of the myofibroblasts. Figure 5.6 displays finally a very strong negative correlation between the cell density of the myofibroblast population and the relative surface area of a burn at day 42. This suggests that this chain of connections has a stronger effect on the relative surface area of a burn at day 42 than the direct connection between the concentration of the collagen molecules and the total amount of generated stress. As a consequence the correlation between the concentration of the collagen molecules and the relative surface area of a burn at day 42 is negative while the the correlation between the collagen molecule secretion rate and the relative surface area of a burn at day 42 is positive.

REFERENCES

[1] Anderson T, Darling D (1952) Asymptotic theory of certain "goodness-of-fit" criteria based on stochastic processes. Ann Math Stat 23:193–212

[2] Davis T, Duff I (1997) An unsymmetric-pattern multifrontal method for sparse LU factorization. SIAM J Matrix Anal A 18:140–158

[3] Davis T, Gilbert J, Larimore S, Ng E (2004) Algorithm 836: Colamd, a column approximate minimum degree ordering algorithm. ACM T Math Software 30:377–380

[4] Desmoulière A, Geinoz A, Gabbiani F, Gabbiani G (1993) Transforming growth factor-β1 induces α-smooth muscle actin expression in granulation tissue myofibroblasts and in quiescent and growing cultured fibroblasts. J Cell Biol 122:103–111

[5] Desmoulière A, Redard M, Darby I, Gabbiani G (1995) Apoptosis mediates the decrease in cellularity during the transition between granulation tissue and scar. Am J Pathol 146:56–66

[6] Duff I, Koster J (1999) The design and use of algorithms for permuting large entries to the diagonal of sparse matrices. SIAM J Matrix Anal A 20:889–901

[7] Enoch S, Leaper D (2007) Basic science of wound healing. Surgery 26:31–37

[8] Feng R, Zhang Y (2013) Piecewise bivariate Hermite interpolation for large sets of scattered data. J Appl Math 2013:1–10

[9] Ghosh K, Pan Z, Guan E, Ge S, Liu Y, Nakamura T, Ren ZD, Rafailovich M, Clark R (2007) Cell adaptation to a physiologically relevant ECM mimic with different viscoelastic properties. Biomaterials 28:671–679

[10] Grotendorst G (1992) Chemoattractants and growth factors. In: Cohen I, Diegelmann R, Lindblad W (eds) Wound Healing: Biochemical and Clinical Aspects, 1st edn, W.B. Saunders, Philadelphia, Pennsylvania, chap 15, pp 237–246

[11] Hinz B (2007) Formation and function of the myofibroblast during tissue repair. J Invest Dermatol 127:526–537

[12] HSL (2013) A collection of fortran codes for large scale scientific computation. URL http://www.hsl.rl.ac.uk

[13] IBM Corp (2011) IBM SPSS Statistics for Windows, Version 20.0

[14] Kavetski D, Binning P, Sloan S (2001) Adaptive time stepping and error control in a mass conservative numerical solution of the mixed form of Richards equation. Adv Water Resour 24:595–605

[15] Kavetski D, Binning P, Sloan S (2002) Adaptive backward Euler time stepping with truncation error control for numerical modelling of unsaturated fluid flow. Int J Numer Meth Eng 53:1301–1322

[16] Koppenol D, Vermolen F, Koppenol-Gonzalez G, Niessen F, Van Zuijlen P, Vuik K (2016) A mathematical model for the simulation of the contraction of burns. J Math Biol DOI: 10.1007/s00285-016-1075-4

[17] Koppenol D, Vermolen F, Niessen F, Van Zuijlen P, Vuik K (2017) A mathematical model for the simulation of the formation and the subsequent regression of hypertrophic scar tissue after dermal wounding. Biomech Model Mechanobiol 16:15–32, DOI: 10.1007/s10237-016-0799-9

[18] Liang X, Boppart S (2010) Biomedical properties of *in vivo* human skin from dynamic optical coherence elastography. IEEE T Bio-Med Eng 57:953–959

[19] Lo S (1989) Generating quadrilateral elements on plane and over curved surfaces. Comp Struct 31:421–426

[20] Lyra P (1994) Unstructured grid adaptive algorithms for fluid dynamics and heat conduction. PhD thesis, University of Wales

[21] Madzvamuse A, Wathen A, Maini P (2003) A moving grid finite element method applied to a model biological pattern generator. J Comput Phys 190:478–500

[22] Maskarinec S, Franck C, Tirrell D, Ravichandran G (2009) Quantifying cellular traction forces in three dimensions. P Natl Acad Sci USA 106:22,108–22,113

[23] Miller K (1981) On the inverse of the sum of matrices. Mathematics Magazine 54:67–72

[24] Möller M (2008) Adaptive high-resolution finite element schemes. PhD thesis, Dortmund University of Technology

[25] Möller M, Kuzmin D (2006) Adaptive mesh refinement for high-resolution finite element schemes. Int J Numer Meth Fluids 52:545–569

[26] Möller M, Kuzmin D, Kourounis D (2008) Implicit FEM-FCT algorithms and discrete Newton methods for transient convection problems. Int J Numer Meth Fluids 57:761–792

[27] Moulin V, Castilloux G, Auger F, Garrel D, O'Connor-McCourt M, Germain L (1998) Modulated response to cytokines of human wound healing myofibroblasts compared to dermal fibroblasts. Exp Cell Res 238:283–293

[28] Murphy K, Hall C, Maini P, McCue S, McElwain D (2012) A fibrocontractive mechanochemical model of dermal wound closure incorporating realistic growth factor kinetics. B Math Biol 74:1143–1170

[29] Olsen L, Sherratt J, Maini P (1995) A mechanochemical model for adult dermal wound contraction and the permanence of the contracted tissue displacement profile. J Theor Biol 177:113–128

[30] Overall C, Wrana J, Sodek J (1991) Transcriptional and post-transcriptional regulation of 72-kda gelatinase/ type IV collagenase by transforming growth factor-β1 in human fibroblasts. J Biol Chem 266:14,064–14,071

[31] Patankar S (1980) Numerical Heat Transfer and Fluid Flow, 1st edn. McGraw-Hill, New York City, New York

[32] Persson PO, Strang G (2004) A simple mesh generator in MATLAB. SIAM Rev 46:329–345

[33] Phadke M (1989) Quality Engineering Using Robust Design, 1st edn. Prentice-Hall, Englewood Cliffs, New Jersey

[34] Quarteroni A, Valli A (2008) Numerical Approximation of Partial Differential Equations, vol 23. Springer Science & Business Media, Berlin, Germany

[35] Ramtani S (2004) Mechanical modelling of cell/ECM and cell/cell interactions during the contraction of a fibroblast-populated collagen microsphere: theory and model simulation. J Biomech 37:1709–1718

[36] Ramtani S, Fernandes-Morin E, Geiger D (2002) Remodeled-matrix contraction by fibroblasts: numerical investigations. Comput Biol Med 32:283–296

[37] Roberts A, Sporn M, Assoian R, Smith J, Roche N, Wakefiled L, Heine U, Liotta L, Falanga V, Kehrl J, Fauci A (1986) Transforming growth factor type β: Rapid induction of fibrosis and angiogenesis *in vivo* and stimulation of collagen formation *in vitro*. P Natl Acad Sci USA 83:4167–4171

[38] Rudolph R, Vande Berg J (1991) The myofibroblast in Dupuytren's contracture. Hand Clin 7:683–692

[39] Sillman A, Quang D, Farboud B, Fang K, Nuccitelli R, Isseroff R (2003) Human dermal fibroblasts do not exhibit directional migration on collagen 1 in direct-current electric fields of physiological strength. Exp Dermatol 12:396–402

[40] Strutz F, Zeisberg M, Renziehausin A, Raschke B, Becker V, Van Kooten C, Muller G (2001) TGF-β1 induces proliferation in human renal fibroblasts via induction of basic fibroblast growth factor (FGF-2). Kidney Int 59:579–592

[41] Tabachnick B, Fidell L (2007) Using Multivariate Statistics, 5th edn. Pearson Education Inc, Boston, Massachusetts

[42] Taguchi G (1987) System of Experimental Design, 1st edn. UNIPUB Kraus International Publications, New York City, New York

[43] The MathWorks Inc (2014) `MATLAB` version 8.3.0.532 (R2014a)

[44] Tranquillo R, Murray J (1992) Continuum model of fibroblast-driven wound contraction: inflammation-mediation. J Theor Biol 158:135–172

[45] Treloar L (1948) Stresses and birefringence in rubber subjected to general homogeneous strain. Proc Phys Soc 60:135–144

[46] Turek S (1998) FEATFLOW Finite element software for the incompressible Navier-Stokes equations: User Manual. University of Heidelberg, Heidelberg, Germany, 1st edn

[47] Van Kan J, Segal A, Vermolen F (2014) Numerical Methods in Scientific Computing, 2nd edn. Delft Academic Press, Delft, The Netherlands

[48] Vande Berg J, Rudolph R, Poolman W, Disharoon D (1989) Comparative growth dynamics and active concentration between cultured human myofibroblasts from granulating wounds and dermal fibroblasts from normal skin. Lab Invest 61:532–538

[49] Wang XQ, Kravchuk O, Winterford C, Kimble R (2011) The correlation of in vivo burn scar contraction with the level of α-smooth muscle actin expression. Burns 37:1367–1377

[50] Wrobel L, Fray T, Molloy J, Adams J, Armitage M, Sparrow J (2002) Contractility of single human dermal myofibroblasts and fibroblasts. Cell Motil Cytoskelet 52:82–90

[51] Zhang Z, Naga A (2005) A new finite element gradient recovery method: Superconvergence property. SIAM J Sci Comput 26:1192–1213

6

IMPLICATIONS FROM A CONTINUUM MODEL FOR THE SIMULATION OF HYPERTROPHIC SCAR TISSUE FORMATION

A continuum hypothesis-based model is presented in order to investigate what might cause the formation of hypertrophic scar tissue. Solely a portion of the dermal layer of the skin is modeled explicitly and this portion is modeled as an isotropic compressible neo-Hookean solid. With respect to the constituents of the dermal layer, the following constituents were selected as primary model components: fibroblasts, myofibroblasts, a generic signaling molecule and collagen molecules. All components of the model are modeled as continuous entities. In the model pulling forces are generated by the myofibroblasts which are present in the recovering wounded area. These pulling forces are responsible for both the compaction and the increased thickness of the recovering wounded area.

A good match with respect to the evolution over time of the thickness of the dermal layer of scars between the outcomes of computer simulations and clinical measurements on both normal scars and hypertrophic scars in human subjects is demonstrated. The comparison between the outcomes of the computer simulations and the clinical measurements shows that a relatively high apoptosis rate of myofibroblasts results in scar tissue that behaves like normal scar tissue with respect to the evolution of the thickness of the tissue over time, while a relatively low apoptosis rate results in scar tissue that behaves like hypertrophic scar tissue with respect to the evolution of the thickness of the tissue over time.

This chapter is based on content of the article "A mathematical model for the simulation of the formation and the subsequent regression of hypertrophic scar tissue after dermal wounding" [7].

6.1. INTRODUCTION

THE development of the model is presented in Section 6.2. A short overview of the numerical algorithm for the generation of the computer simulations is presented in Section 6.3. The simulation results are presented in Section 6.4. Finally, the results are discussed in Section 6.5.

6.2. DEVELOPMENT OF THE MATHEMATICAL MODEL

IN order to simulate the formation and the subsequent regression of hypertrophic scar tissue, some of the processes that take place during the proliferative and the remodeling phase of the wound healing cascade were incorporated into the model [2]. With respect to he subprocesses that are executed during the proliferative phase the following subprocesses were selected: fibroplasia and wound contraction.

Solely the dermal layer of the skin is modeled explicitly and this layer is modeled as a continuum. The adjacent subcutaneous layer was incorporated implicitly into the model through a mechanical interaction between this layer and the dermal layer at their interface. The dermal layer is modeled as an isotropic compressible neo-Hookean solid [24]. With respect to the mechanical component of the model the displacement of the dermal layer ($\mathbf{u}$) was selected as primary model variable. Additionally, the following four components of the (healing) dermal layer were selected as primary model components: fibroblasts (N), myofibroblasts (M), a generic signaling molecule (c) and collagen molecules (ρ).

The continuum hypothesis-based framework of Tranquillo and Murray [23] was used as basis for the model. This framework consists of the following set of conservation equations (See Section 4.2 for more details about these equations):

$$\frac{\partial z_i}{\partial t} + \nabla \cdot [z_i \mathbf{v}] = -\nabla \cdot \mathbf{J}_i + R_i, \tag{6.1a}$$

$$-\nabla \cdot \sigma = \mathbf{f}. \tag{6.1b}$$

Within the above equations, z_i represents the cell density / concentration of constituent i, $\mathbf{v}$ represents the displacement velocity of the dermal layer, $\mathbf{J}_i$ represents the flux associated with constituent i per unit area, R_i represents the (bio)chemical kinetics associated with constituent i, σ represents the Cauchy stress tensor associated with the dermal layer, and $\mathbf{f}$ represents the total body force working on the dermal layer. Given the chosen primary model variables, $i \in \{N, M, c, \rho\}$ holds. In the remainder of the text of this chapter, z_N has been replaced by N, z_M has been replaced by M, z_c has been replaced by c and z_ρ has been replaced by ρ.

6.2.1. THE CELLS

THE functional forms for the movement of the (myo)fibroblasts and the functional forms for the biochemical kinetics associated with these cells are identical to the functional forms that have been introduced in Chapter 4. For completeness the functional forms are presented here as well. More details about the functional forms can be

found in Chapter 4. The functional forms for the cell fluxes are

$$\mathbf{J}_N = -D_F F \nabla N + \chi_F N \nabla c, \tag{6.2}$$
$$\mathbf{J}_M = -D_F F \nabla M + \chi_F M \nabla c, \tag{6.3}$$

where

$$F = N + M. \tag{6.4}$$

The parameter D_F is the cell density-dependent (myo)fibroblast random motility coefficient and χ_F is the chemotactic coefficient. The functional forms for the biochemical kinetics associated with the (myo)fibroblasts are

$$R_N = r_F \left[1 + \frac{r_F^{\max} c}{a_c^I + c} \right] [1 - \kappa_F F] N^{1+q} - k_F c N - \delta_N N, \tag{6.5}$$
$$R_M = r_F \left\{ \frac{\left[1 + r_F^{\max}\right] c}{a_c^I + c} \right\} [1 - \kappa_F F] M^{1+q} + k_F c N - \delta_M M. \tag{6.6}$$

Here r_F is the cell division rate, $r_F^{\max}$ is the maximum factor with which the cell division rate can be enhanced due to the presence of the signaling molecule, a_c^I is the concentration of the signaling molecule that causes the half-maximum enhancement of the cell division rate, $\kappa_F F$ represents the reduction in the cell division rate due to crowding, q is a fixed constant, k_F is the signaling molecule-dependent cell differentiation rate of fibroblasts into myofibroblasts, δ_N is the apoptosis rate of fibroblasts and δ_M is the apoptosis rate of myofibroblasts.

6.2.2. THE SIGNALING MOLECULES

THE functional form for the dispersion of the generic signaling molecule and the functional forms for the release, the consumption and the removal of the generic signaling molecule are also identical to the functional forms that have been introduced in Chapter 4:

$$\mathbf{J}_c = -D_c \nabla c, \tag{6.7}$$
$$R_c = k_c \left[\frac{c}{a_c^{II} + c} \right] [N + \eta M] - \delta_c g(F, c, \rho) c. \tag{6.8}$$

The parameter D_c represents the random diffusion coefficient of the generic signaling molecule, k_c represents the maximum net secretion rate of the signaling molecule, η is the ratio of myofibroblasts to fibroblasts in the maximum net secretion rate of the signaling molecule, a_c^{II} is the concentration of the signaling molecule that causes the half-maximum net secretion rate of the signaling molecule and δ_c is the proteolytic breakdown rate of the signaling molecules. The concentration of the generic metalloproteinase (MMP) (i.e., $g(F, c, \rho)$) which is responsible for the breakdown of the signaling

molecules was assumed to be proportional to the cell density of the (myo)fibroblasts, and the concentration of both the collagen molecules and the signaling molecules according to the following formula (See the accompanying paragraph of Equation (4.9) for further details):

$$g(F,c,\rho) \propto \frac{\rho F}{1+a_c^{III}c}. \tag{6.9}$$

Here $1/[1+a_c^{III}c]$ represents the inhibition of the secretion of the generic MMP due to the presence of the signaling molecule.

6.2.3. THE COLLAGEN MOLECULES

THE functional form for the dispersion of the collagen molecules and the functional forms for the secretion and the proteolytic breakdown of the collagen molecules are identical to the functional forms that have been introduced in Chapter 5:

$$\mathbf{J}_\rho = \mathbf{0}, \tag{6.10}$$

$$R_\rho = k_\rho \left\{ 1 + \left[\frac{k_\rho^{\max} c}{a_c^{IV}+c} \right] \right\} [N+\eta M] - \delta_\rho g(F,c,\rho)\rho. \tag{6.11}$$

Here k_ρ is the collagen molecule secretion rate, $k_\rho^{\max}$ is the maximum factor with which this secretion rate can be enhanced due to the presence of the signaling molecule, a_c^{IV} is the concentration of the signaling molecules that causes the half-maximum enhancement of the secretion rate and δ_ρ is the proteolytic breakdown rate of the molecules.

6.2.4. THE FORCE BALANCE

FOR the mathematical description of the relation between the stresses and the strains in the modeled portion of dermal layer, the following stress-strain relation was chosen:

$$J\sigma = 2C_1 J^{-\frac{2}{3}} \left[\mathbf{B} - \frac{1}{3}\mathrm{tr}(\mathbf{B})\,\mathbf{I} \right] + 2D_1 J[J-1]\,\mathbf{I}, \tag{6.12}$$

$$\mathbf{B} = (-2\mathbf{e}+\mathbf{I})^{-1}, \tag{6.13}$$

$$\mathbf{e} = \frac{1}{2}\left[\nabla\mathbf{u} + (\nabla\mathbf{u})^{\mathrm{T}} - (\nabla\mathbf{u})^{\mathrm{T}}\nabla\mathbf{u} \right], \tag{6.14}$$

$$J = \sqrt{\det(\mathbf{B})}, \tag{6.15}$$

$$C_1 = \frac{E\sqrt{\rho}}{4[1+\nu]}, \tag{6.16}$$

$$D_1 = \frac{E\sqrt{\rho}}{6[1-2\nu]}. \tag{6.17}$$

Here $\mathbf{B}$ is the left Cauchy-Green deformation tensor, $\mathbf{e}$ is the Eulerian finite strain tensor, $\mathbf{I}$ is the second order identity tensor and ν is Poisson's ratio [24]. It was assumed that

the Young's moduli of the tissues are dependent on the concentration of the collagen molecules [17, 18]. In this model it was assumed that this dependence is nonlinear. Here the Young's modulus equals $E\sqrt{\rho}$, where E is a constant.

Finally, the forces that are generated by the myofibroblasts due to their pulling on the extracellular matrix (ECM) were incorporated into the model. Identical to the model presented in Chapter 4 the pulling forces are modeled as isotropic stresses that are proportional to the product of the cell density of the myofibroblast population and a simple function of the concentration of the collagen molecules [14]. No other forces were incorporated into the model. Taken together, the following was obtained:

$$\mathbf{f} = \nabla \cdot \left\{ \xi M \left[\frac{\rho}{R^2 + \rho^2} \right] \mathbf{I} \right\}. \tag{6.18}$$

Here ξ is the generated stress per unit cell density and the inverse of the unit collagen molecule concentration, and R is a fixed constant.

6.2.5. THE DOMAIN OF COMPUTATION

FOR the generation of simulation results, the computational domain depicted in Figure 6.1 was used. Note that it was assumed that the exposed surface area of the wound is a perfect rectangle and that the wound extends uniformly to the boundary between the subcutaneous layer and the dermal layer of the skin. The blue box depicted in Figure 6.1b coincides with one of the planes of symmetry of the wound. Due to this symmetry $u = 0$, $\partial v/\partial x = 0$ and $\partial w/\partial x = 0$ hold within the slice of dermal layer enclosed by the blue box (with $\mathbf{u} = (u, v, w)^{\mathrm{T}}$). Furthermore, the derivatives of the concentrations and the cell densities of the individual constituents in the x-direction are also zero due to the symmetry. Using Lagrangian coordinates ($\mathbf{X} = (X, Y, Z)^{\mathrm{T}}$), the domain of computation ($\Omega_{\mathbf{X}}$) is described mathematically by

$$\Omega_X \in \{X = 0 \text{ cm},\ -15.96 \text{ cm} \leq Y \leq 15.96 \text{ cm},\ -0.15 \text{ cm} \leq Z \leq 0 \text{ cm}\}. \tag{6.19}$$

In the model the thickness of unwounded dermis is 0.15 cm. Note that this is in close agreement with the measurements of the thickness of normal skin obtained by Nedelec *et al.* [12]. Skin tissue actually consists of two layers: an epidermal layer and a dermal layer. Oliveira *et al.* [13] measured the thickness of the epidermis of normal skin tissue and their measurements showed that the epidermis of this tissue has an average thickness of less than 95 μm. Hence, the thickness of the dermis is more or less equal to the thickness of the epidermis and the dermis combined.

6.2.6. THE INITIAL CONDITIONS AND THE BOUNDARY CONDITIONS

THE initial conditions give a description of the various cell densities and the various concentrations at the onset of the proliferative phase of the wound healing cascade. For the generation of simulation results the following function was used to describe the shape of the wound:

$$w\left(\mathbf{X}, c^I, c^{II}\right) = 1 - \left[1 - I\left(Y, c^{II}, c^I\right)\right] I\left(Y, -c^{II}, c^I\right). \tag{6.20}$$

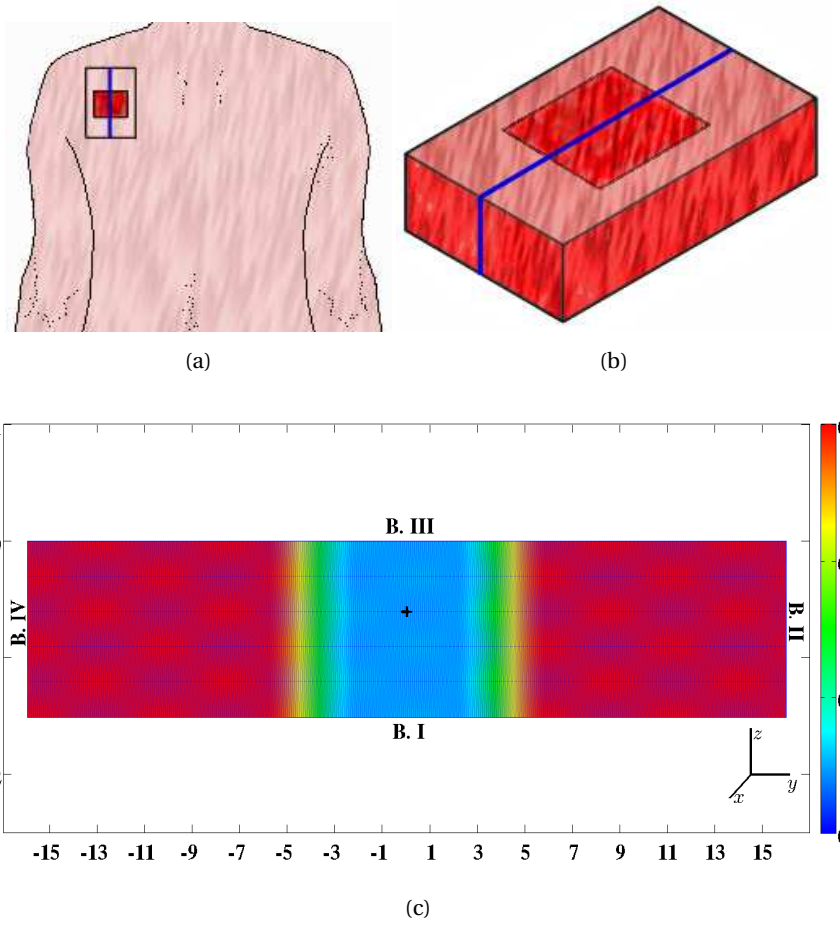

Figure 6.1: A graphical representation of the domain of computation. Figure 6.1a shows a hypothetical wound covering a portion of a shoulder. Figure 6.1b shows a close-up of a piece of the dermal layer of the shoulder from Figure 6.1a. Figure 6.1c shows a close-up of the piece of dermal layer from Figure 6.1b that is enclosed by the blue box (The scale along both axes is in centimeters). The computer simulations were created with this slice of dermal layer. Depicted are the initial shape of the slice and, in color scale, the initial concentration of the collagen molecules, measured in g/cm^3. Within Figure 6.1c, the boundaries are numbered counterclockwisely from B.I to B.IV. B.I coincides with the boundary between the subcutaneous layer and the dermal layer of the skin, B.II and B.IV border on adjacent dermal tissue, and B.III coincides with the boundary between the dermal layer and the epidermal layer (if present). Furthermore, the black plus sign located more or less at the center of the wound, marks the material point within the dermal layer where the evolution of the individual modeled constituents were traced over time for the generation of the figures in Section 6.4

Here the function I is the indicator function that has been introduced in Equation (4.31). In this study $c^I = 2$ cm and 3 cm $\leq c^{II} \leq 5$ cm. Furthermore, $w = 0$ corresponds to fully wounded dermis and $w = 1$ corresponds to unwounded dermis.

Based on the function for the shape of the wound, the following initial conditions were used for the modeled constituents of the dermal layer:

$$\begin{aligned} N(\mathbf{X},0) &= \left\{N^w + \left[1-N^w\right] w\left(\mathbf{X}, c^I, c^{II}\right)\right\}\overline{N}, \\ M(\mathbf{X},0) &= \overline{M}, \\ c(\mathbf{X},0) &= \left[1-w\left(\mathbf{X}, c^I, c^{II}\right)\right] c^w, \\ \rho(\mathbf{X},0) &= \left\{\rho^w + \left[1-\rho^w\right] w\left(\mathbf{X}, c^I, c^{II}\right)\right\}\overline{\rho}. \end{aligned} \tag{6.21}$$

Here $\overline{N}$, $\overline{M}$ and $\overline{\rho}$ are respectively the equilibrium cell density of the fibroblasts, the equilibrium cell density of the myofibroblasts and the equilibrium concentration of the collagen molecules, of the unwounded dermis. Due to early secretion of signaling molecules by for instance macrophages, signaling molecules are present in the wounded area. The constant c^w is the maximum of the initial concentration of the signaling molecule in the wounded area. Furthermore, it was assumed that there are some fibroblasts and collagen molecules present in the wounded area; the parameters N^w and ρ^w determine,respectively, how much fibroblasts and collagen molecules are present initially in the wounded area.

With respect to the initial conditions for the displacement of the dermal layer, the following holds. The initial cell density of the myofibroblast population is equal to zero everywhere in the domain of computation. Looking at Equation (6.18), this implies $\mathbf{f}(\mathbf{x},0) = \mathbf{0}$. Hence

$$\mathbf{u}(\mathbf{x},0) = \mathbf{0} \quad \forall \mathbf{x} \in \Omega_{\mathbf{x},0}, \tag{6.22}$$

where $\Omega_{\mathbf{x},0}$ is the initial domain of computation in Eulerian coordinates and $\mathbf{x} = (x,y,z)^{\mathrm{T}}$ are the Eulerian coordinates.

With respect to the boundary conditions for the constituents of the dermal layer, the following boundary conditions were used for all time t and for all $\mathbf{x} \in \{\partial\Omega^{II}_{\mathbf{x},t}, \partial\Omega^{IV}_{\mathbf{x},t}\}$, where $\partial\Omega^{II}_{\mathbf{x},t}$ and $\partial\Omega^{IV}_{\mathbf{x},t}$ denote, respectively, the second and fourth boundary of the domain of computation in Eulerian coordinates:

$$N(\mathbf{x},t) = \overline{N}, \;\; M(\mathbf{x},t) = \overline{M}, \;\; c(\mathbf{x},t) = \overline{c}. \tag{6.23}$$

Here $\overline{c}$ is the equilibrium concentration of the signaling molecules in the unwounded dermis. The following Neumann boundary conditions were used furthermore for all time t and for all $\mathbf{x} \in \{\partial\Omega^{I}_{\mathbf{x},t}, \partial\Omega^{III}_{\mathbf{x},t}\}$, where $\partial\Omega^{I}_{\mathbf{x},t}$ and $\partial\Omega^{III}_{\mathbf{x},t}$ denote, respectively, the first and third boundary of the domain of computation in Eulerian coordinates:

$$\mathbf{n}\cdot\mathbf{J}_N(\mathbf{x},t) = 0, \;\; \mathbf{n}\cdot\mathbf{J}_M(\mathbf{x},t) = 0, \;\; \mathbf{n}\cdot\mathbf{J}_c(\mathbf{x},t) = 0. \tag{6.24}$$

Here $\mathbf{n}$ is the unit outward pointing normal vector to the boundary of the domain of computation.

With respect to the mechanical component of the model, the following Robin boundary conditions were used

$$\text{B.I: } \mathbf{n}\cdot\sigma = \begin{bmatrix} 0 \\ 0 \\ -s^I \rho w \end{bmatrix}, \;\; \text{B.III: } \mathbf{n}\cdot\sigma = \begin{bmatrix} 0 \\ 0 \\ 0 \end{bmatrix}, \;\; \text{B.II \& B.IV: } \mathbf{n}\cdot\sigma = \begin{bmatrix} 0 \\ -s^{II}\rho v \\ 0 \end{bmatrix}. \tag{6.25}$$

These boundary conditions imply that the first boundary is free to move in the direction of the x-axis and the y-axis, while it experiences an opposing spring-like force per unit area in the direction of the z-axis that is proportional to the concentration of the collagen molecules and the displacement in the direction of the z-axis. With respect to the second and fourth boundary, the boundary conditions imply that these boundaries are free to move in the direction of the x-axis and the z-axis, while they experience an opposing spring-like force per unit area in the direction of the y-axis that is proportional to the concentration of the collagen molecules and the displacement in the direction of the y-axis. The boundary condition for the third boundary implies that this boundary is free to move in any direction.

6.2.7. THE (RANGES OF THE) VALUES FOR THE PARAMETERS

TABLE 6.1 provides an overview of the (ranges of the) values for the parameters of the model. The majority of these values were either obtained directly from previously conducted studies or estimated from results of previously conducted studies. In addition, the values for the equilibrium signaling molecule concentration of the unwounded dermis ($\overline{c}$), the constant q and the collagen molecule degradation rate (δ_ρ) could be determined due to the fact that these values are a necessary consequence of the values chosen for other parameters. See Subsection 4.2.7 for the derivation of the values for these parameters.

Table 6.1: An overview of the (ranges of the) values for the parameters of the model. The last column contains the references to the studies that were used for obtaining (estimates of) the values for the parameters. If (the range of) the value for a parameter has been estimated in this study, then this is indicated by the abbreviation TW. If the value for a parameter is a necessary consequence of the values chosen for the other parameters, then this is indicated by the abbreviation NC

Parameter	Value	Dimensions	Reference
D_F	10^{-7}	cm^5/cells day	[21]
χ_F	2×10^{-3}	cm^5/g day	[11]
q	-4.2×10^{-1}	–	NC
r_F	9.24×10^{-1}	cm^{3q}/(cells^q day)	[3]
$r_F^{\max}$	2	–	[22]
a_c^I	10^{-8}	g/cm^3	[4]
κ_F	10^{-6}	cm^3/(cells)	[25]
k_F	5.4×10^6	cm^3/(g day)	[1]
δ_N	2×10^{-2}	/day	[14]
δ_M	$(2-60)\times10^{-3}$	/day	TW
D_c	2.9×10^{-3}	cm^2/day	[11]
k_c	4×10^{-13}	g/(cells day)	[14]
η	2	–	[10] & [20]
a_c^{II}	10^{-8}	g/cm^3	[14]
δ_c	5×10^{-4}	cm^6/(cells g day)	[14]
a_c^{III}	2×10^8	cm^3/g	[15]
k_ρ	6×10^{-8}	g/(cells day)	NC
$k_\rho^{\max}$	10	–	[14]

Continued on the next page

Table 6.1 – *Continued from the previous page*

Parameter	Value	Dimensions	Reference
a_c^{IV}	10^{-9}	g/cm^3	[19]
δ_ρ	6×10^{-6}	cm^6/(cells g day)	TW
E	3.2×10	(N)/((g cm)$^{1/2}$)	[8]
ν	4.9×10^{-1}	–	[8]
ξ	2×10^{-3}	(N g)/(cells cm^2)	[9] & [27]
R	3×10^{-1}	g/cm^3	[14]
$\overline{N}$	10^4	cells/cm^3	[14]
$\overline{M}$	0	cells/cm^3	[14]
$\overline{c}$	0	g/cm^3	NC
$\overline{\rho}$	10^{-1}	g/cm^3	[14]
N^w	2×10^{-1}	–	TW
ρ^w	2×10^{-1}	–	TW
c^w	10^{-8}	g/cm^3	[14]
s^I	10^6	N/g	[6]
s^{II}	10^3	N/g	TW

6.3. THE APPLIED NUMERICAL ALGORITHM

FOR the generation of the computer simulations the numerical algorithm that has been presented in Section 5.3 was used without the element resolution refinement / recoarsement tool. Furthermore, the non-dimensionalisation presented in Equation (5.30), was also applied here.

In order to generate conforming triangulations of the domain of computation, the slightly adapted version of the mesh generator developed by Persson and Strang was used again [16]. This resulted in high-quality meshes that consisted mainly of equilateral triangles. The only triangles that were not equilateral were located near the second and fourth boundary of the domain of computation. These latter triangles were nearly equilateral. Using the measure from Equation (5.31), it was observed that $\alpha > 0.85$ for all triangles in the triangulation. For the generation of the simulation results presented in Section 6.4, a triangulation consisting of triangles with an average initial edge length of 3.46×10^{-2} cm was used. The calculations were repeated two times. The first time a triangulation consisting of triangles with an average initial edge length of 5.77×10^{-2} cm was used, and the second time a triangulation consisting of triangles with an average initial edge length of 1.73×10^{-2} cm was used. It was observed that the difference in the simulation results between the different calculations was negligible.

6.4. SIMULATION RESULTS

FIGURE 6.2 shows an overview of simulation results when the value for the apoptosis rate of myofibroblasts is relatively high. Figure 6.3 shows an overview of simulation results when the value for the apoptosis rate of myofibroblasts is relatively low. Furthermore, Figures 6.4 through 6.7 show the evolution over time of the different cell densities and the different concentrations for either a relatively high value for the apoptosis rate of myofibroblasts or a relatively low value for the apoptosis rate of myofibroblasts, and various widths of the wound, at a certain material point within the wounded area. In

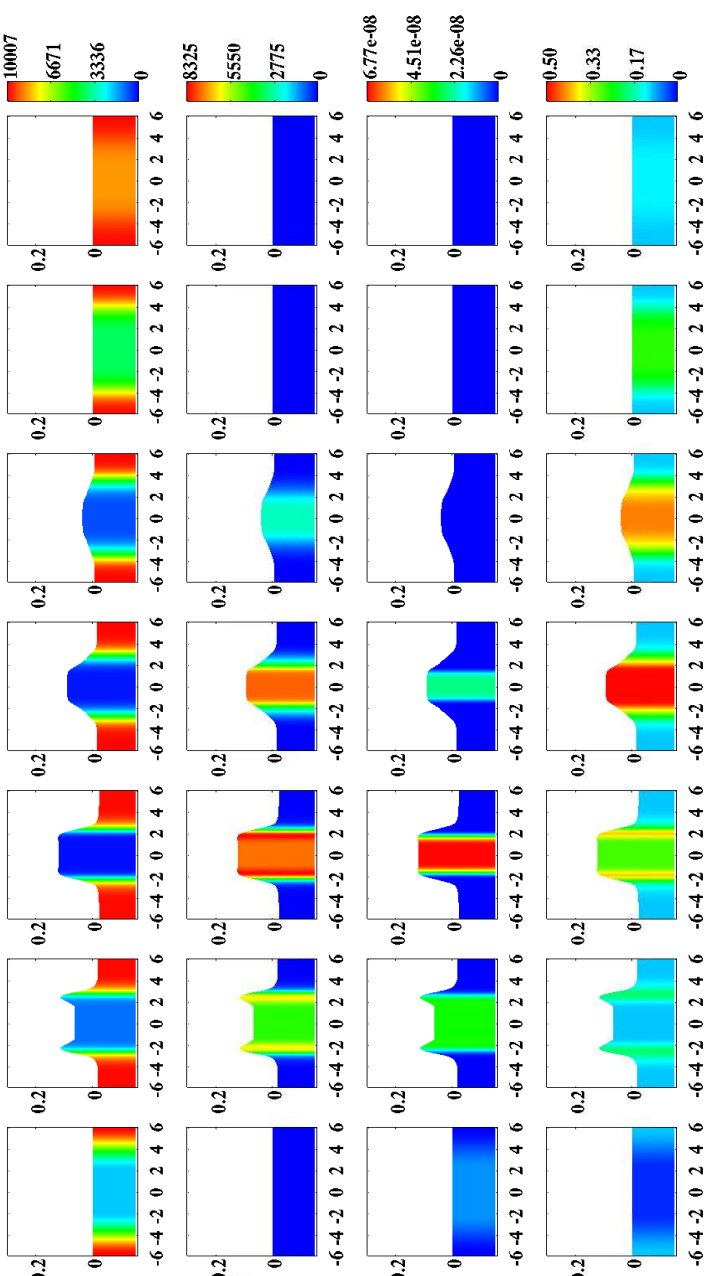

Figure 6.2: An overview of a simulation with a relatively high value for the apoptosis rate of myofibroblasts ($\delta_M = 6 \times 10^{-2}$ /day). All other parameter values are equal to those depicted in Table 6.1. With respect to the width of the wound, $c^{II} = 4$ cm in this simulation. The first two rows show the evolution over time of the cell density of, respectively, the fibroblasts and the myofibroblasts. The color scales represent the cell densities, measured in cells/cm^3. The last two rows show the evolution over time of the concentration of, respectively, the signaling molecules and the collagen molecules. The color scales represent the concentrations, measured in g/cm^3. Within the subfigures, the scale along both axes is in centimeters

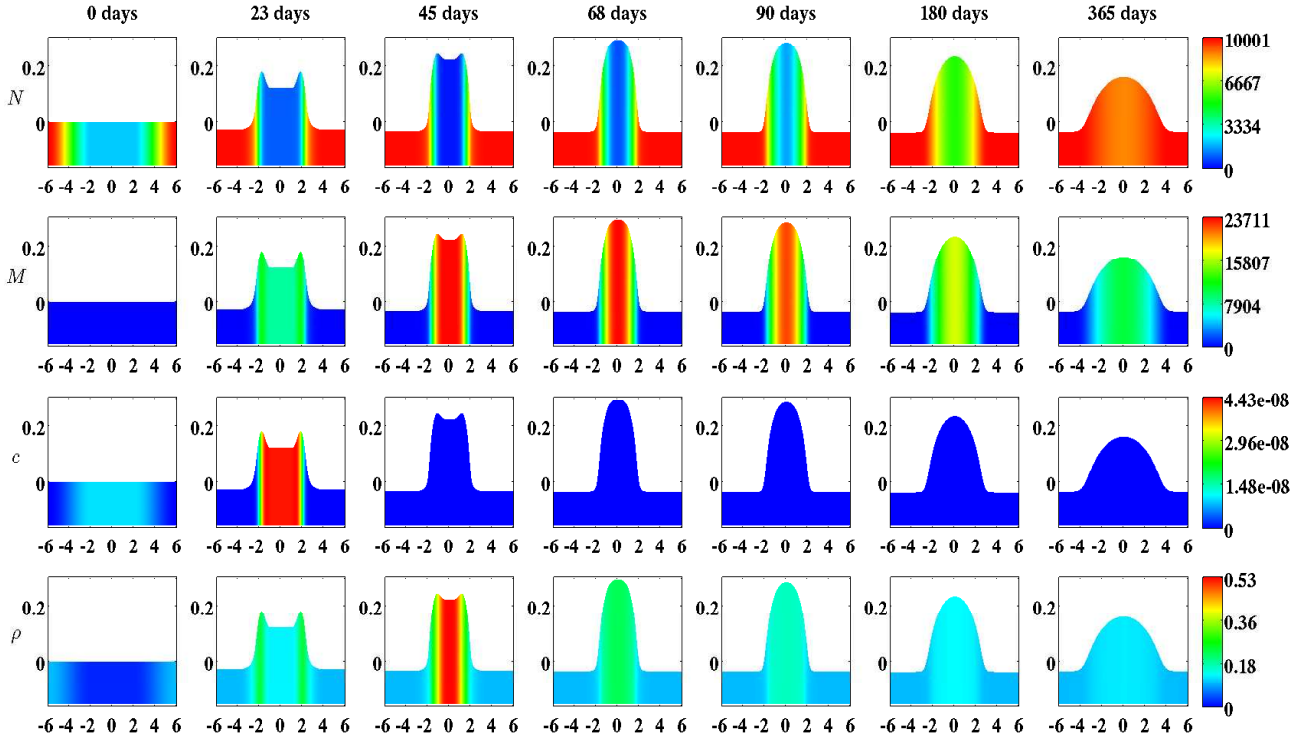

Figure 6.3: An overview of a simulation with a relatively low value for the apoptosis rate of myofibroblasts ($\delta_M = 2 \times 10^{-3}$ /day). All other parameter values are equal to those depicted in Table 6.1. With respect to the width of the wound, $c^{II} = 4$ cm in this simulation. The first two rows show the evolution over time of the cell density of, respectively, the fibroblasts and the myofibroblasts. The color scales represent the cell densities, measured in cells/cm^3. The last two rows show the evolution over time of the concentration of, respectively, the signaling molecules and the collagen molecules. The color scales represent the concentrations, measured in g/cm^3. Within the subfigures, the scale along both axes is in centimeters

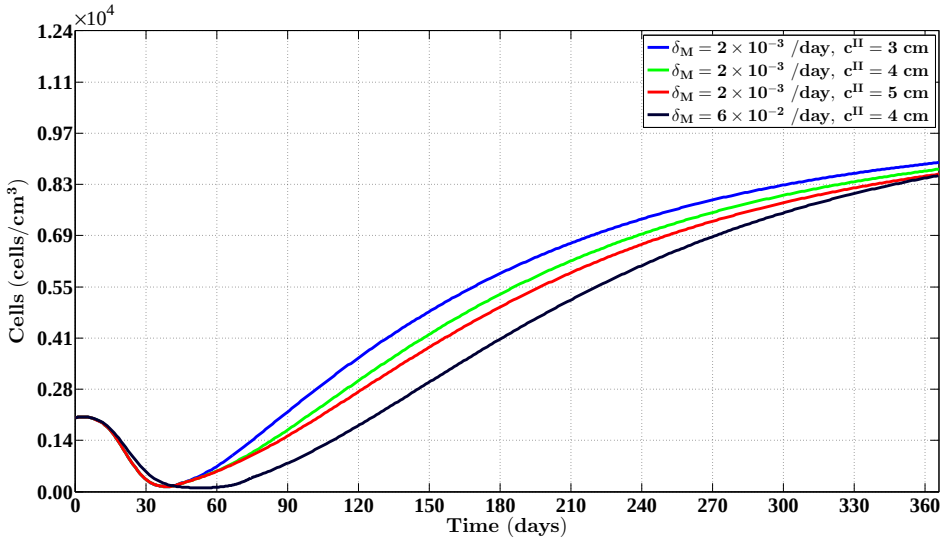

Figure 6.4: The evolution over time of the cell density of the fibroblast population for different values of the apoptosis rate of myofibroblasts and various widths of the wound. All other parameter values are equal to those depicted in Table 6.1. See Subfigure 6.1c for the location where the evolution of the cell density was traced over time

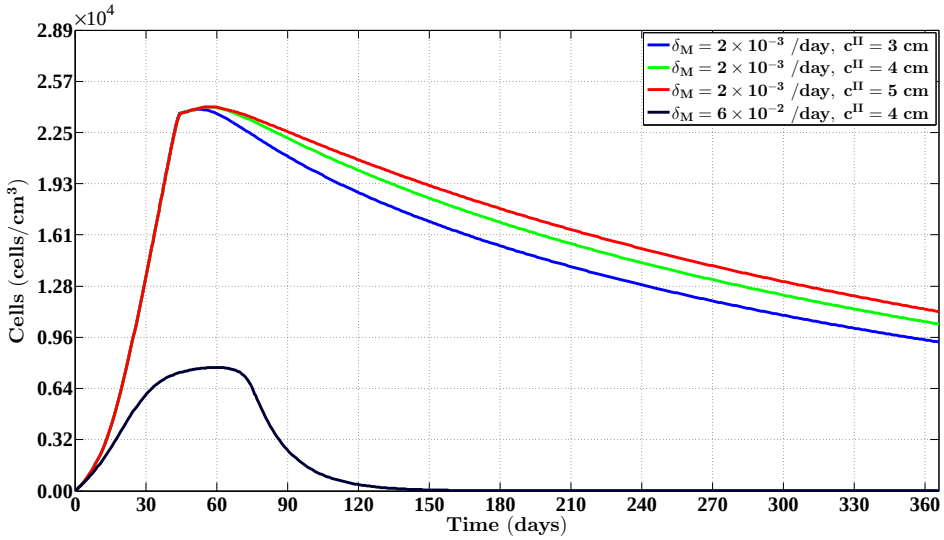

Figure 6.5: The evolution over time of the cell density of the myofibroblast population for different values for the apoptosis rate of myofibroblasts and various widths of the wound. All other parameter values are equal to those depicted in Table 6.1. See Subfigure 6.1c for the location where the evolution of the cell density was traced over time

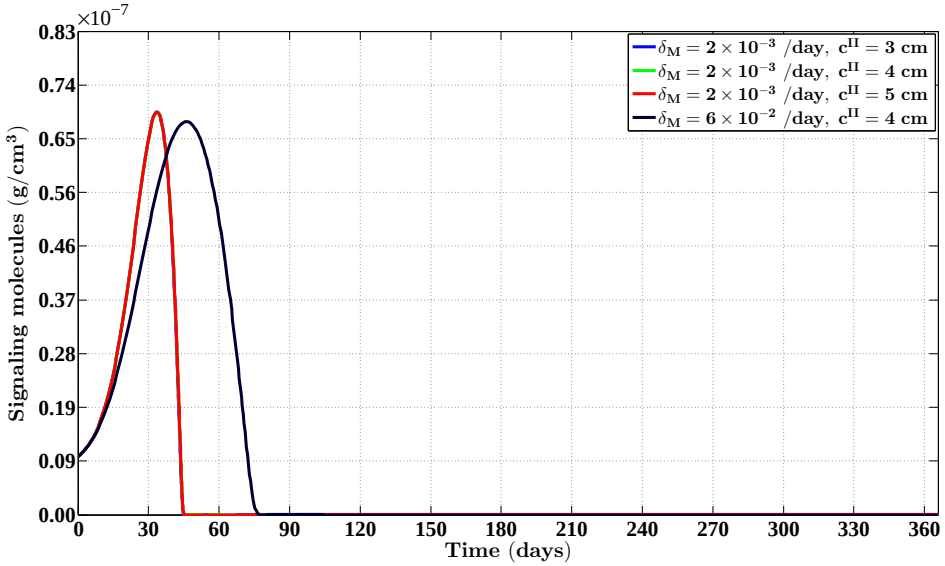

Figure 6.6: The evolution over time of the concentration of the signaling molecules for different values for the apoptosis rate of myofibroblasts and various widths of the wound (The blue curve and the green curve are situated underneath the red curve). All other parameter values are equal to those depicted in Table 6.1. See Subfigure 6.1c for the location where the evolution of the concentration was traced over time

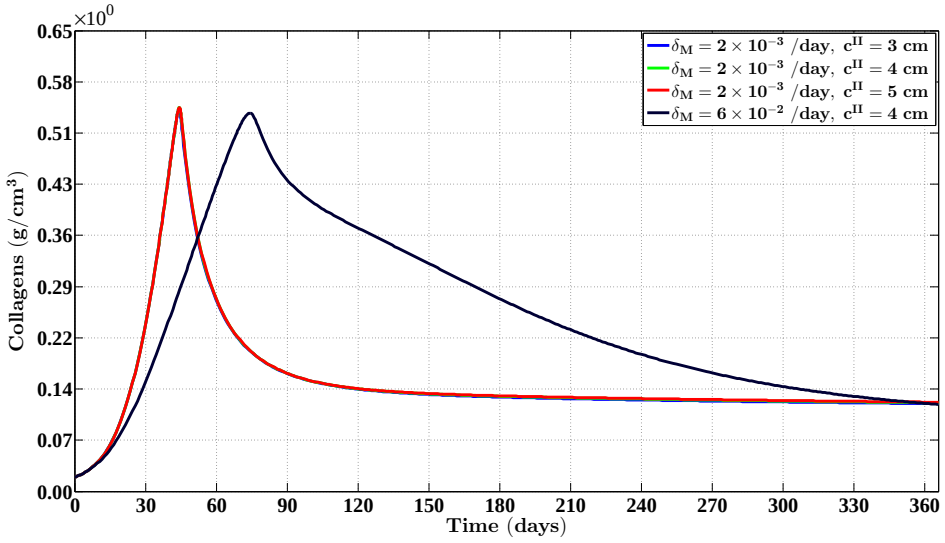

Figure 6.7: The evolution over time of the concentration of the collagen molecules for different values for the apoptosis rate of myofibroblasts and various widths of the wound (The blue curve and the green curve are situated underneath the red curve). All other parameter values are equal to those depicted in Table 6.1. See Subfigure 6.1c for the location where the evolution of the concentration was traced over time

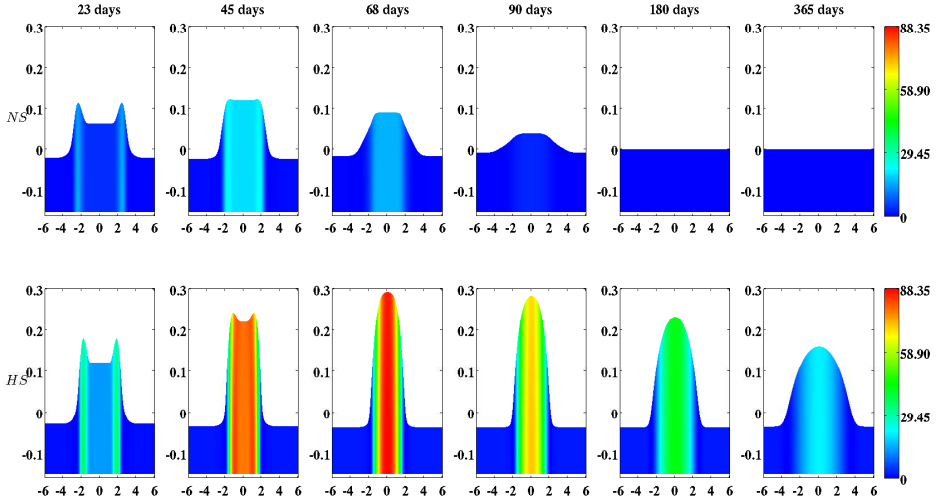

Figure 6.8: The evolution over time of the strain energy density. The first row shows the evolution when the value for the apoptosis rate of myofibroblasts is relatively high ($\delta_M = 6 \times 10^{-2}$ /day). The second row shows the evolution when the value for the apoptosis rate of myofibroblasts is relatively low ($\delta_M = 2 \times 10^{-3}$ /day). All other parameter values are equal to those depicted in Table 6.1. With respect to the width of the wound, $c^{II} = 4$ cm in both cases. The color scales represent the strain energy density, measured in J/cm^3. Within the subfigures, the scale along both axes is in centimeters

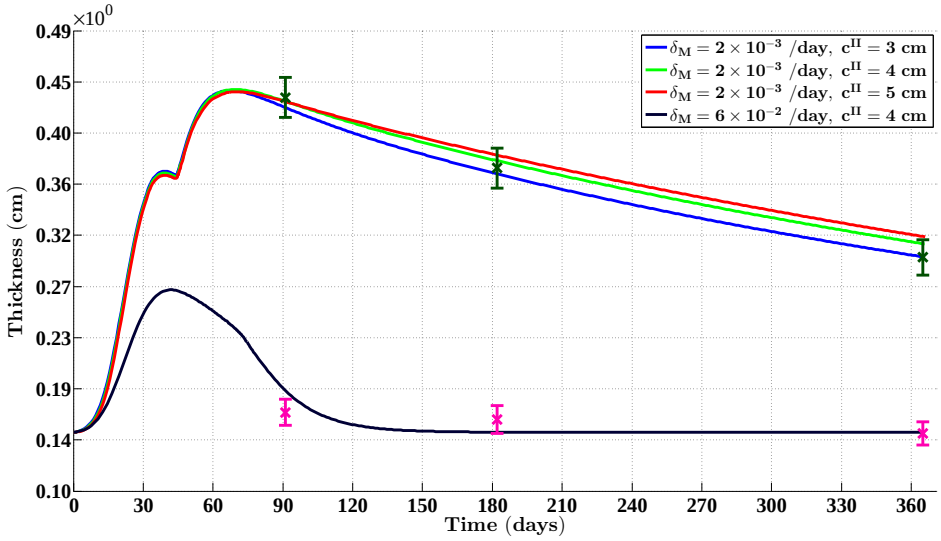

Figure 6.9: The evolution over time of the thickness of the dermal layer for different values for the apoptosis rate of myofibroblasts and various widths of the wound. All other parameter values are equal to those depicted in Table 6.1. In the simulations the thickness of the dermal layer was computed at $y = 0$ cm. The dark green error bars and the magenta error bars represent clinical measurements of the thickness of respectively hypertrophic scars and normal scars in human subjects at different time points after injury [12]. Displayed are the means (with a cross sign) plus / minus one standard deviation

order not to clutter the figures too much, the simulation results where the value for the apoptosis rate is relatively high and the width of the wound is either relatively small (i.e. $c^{II} = 3$ cm) or relatively large (i.e. $c^{II} = 5$ cm), were not included into these latter figures. These results are actually very similar to the presented results where the value for the apoptosis rate of myofibroblasts is relatively high and $c^{II} = 4$ cm.

Figure 6.8 shows the evolution over time of the strain energy density for both a relatively high value for the apoptosis rate of myofibroblasts and a relatively low value for the apoptosis rate of myofibroblasts. The strain energy density (W) was determined by computing at various time points (with $\overline{I}_1 = J^{-\frac{2}{3}} \operatorname{tr}(\mathbf{B})$):

$$W = C_1 \left(\overline{I}_1 - 3 \right) + D_1 (J-1)^2 . \tag{6.26}$$

Figure 6.9 shows the evolution over time of the thickness of the dermal layer for either a relatively high value for the apoptosis rate of myofibroblasts or a relatively low value for the apoptosis rate of myofibroblasts, and various widths of the wound. Once more, in order not to clutter the figure too much, the simulation results where the apoptosis rate is relatively high, and the width of the wound is either relatively small or relatively large, were not included into the figure. These results are actually very similar to the presented results where the value for the apoptosis rate of myofibroblasts is relatively high and $c^{II} = 4$ cm.

Figures 6.2 through 6.9 show clearly that changing the value for the apoptosis rate of myofibroblasts has a huge impact on the healing response. That is, if the value for the apoptosis rate is relatively high, then simulations show gentle healing; the maximum myofibroblasts cell density in the wounded area is relatively low and the restoration of the presence of a collagen-rich ECM in the wounded area is more gradual. The degree of compaction (i.e. the degree of wound contraction) remains relatively low and the dermal layer remains relatively thin. If the value for the apoptosis rate is relatively low, then simulations show an excessive healing response; the maximum myofibroblasts cell density in the wounded area is relatively high and the restoration of the presence of a collagen-rich ECM in the wounded area is accomplished faster. During the remodeling of the evolving ECM, the cell density of the myofibroblast population diminishes slowly while the cell density of the fibroblast population increases slowly toward the equilibrium cell density. The degree of temporary compaction is relatively high during the execution of the wound healing processes compared to the situation where the value for the apoptosis rate is relatively high, as is demonstrated in Figure 6.8 by the relatively high strain energy density in the wounded area. Furthermore, the restoring dermal tissue becomes quite a bit thicker than the unaffected surrounding tissue. Over time, the thickness of the dermal layer declines slowly toward the thickness of the unwounded dermis. Finally, the figures also show that the width of the wounded area has a relatively small, but clear effect on the evolution of the cell densities within the wounded area, and on the evolution of the thickness of the dermal layer in the case of a relatively low value for the apoptosis rate of myofibroblasts.

Figure 6.9 also shows a good match with respect to the evolution over time of the thickness of the dermal layer between the outcomes of different simulations with different values for the apoptosis rate of myofibroblasts, and clinical measurements of the thickness of both hypertrophic and normal scars at different time points after injury in

humans. Oliveira *et al.* [13] measured the thickness of the epidermises of both normal and hypertrophic scar tissue and their measurements showed that the epidermises of these tissues have an average thickness of, respectively, less than 121 μm and less than 166 μm. Hence, the thickness of the dermises of these tissues is more or less equal to the thickness of their epidermis and dermis combined.

6.5. CONCLUSIONS

IN this chapter a mathematical model has been presented in order to investigate what might cause the formation of hypertrophic scar tissue. Looking at the results obtained with the computer simulations, the following can be observed. Figure 6.5 shows that there exists a strong connection between the size of the value for the apoptosis rate of myofibroblasts and the maximum cell density of the myofibroblasts in the wounded area. Furthermore, Figure 6.7 shows that the size of the value for the apoptosis rate of myofibroblasts also strongly influences the dynamics related to the collagen molecules. Given Equation (6.18), this implies that the size of the value for the apoptosis rate of myofibroblasts has a huge impact on the total generated stress by the myofibroblast population and hence the stored strain energy in the wounded area. Consequently, there exists a strong connection between the size of the value for the apoptosis rate of myofibroblasts and the thickness of the wounded area, as is confirmed by the results depicted in Figure 6.9.

Figure 6.9 also displays a good match with respect to the evolution over time of the thickness of the dermal layer between the outcomes of different simulations with different values for the apoptosis rate of myofibroblasts and clinical measurements of the thickness of both hypertrophic and normal scars at different time points after injury in humans [12]; a relatively high value for the apoptosis rate of myofibroblasts results in scar tissue that behaves like normal scar tissue with respect to the evolution of the thickness of the tissue over time, while a relatively low value for the apoptosis rate results in scar tissue that behaves like hypertrophic scar tissue with respect to the evolution of the thickness of the tissue over time. Furthermore, several studies have demonstrated previously that the cell density of myofibroblasts in hypertrophic scar tissue is elevated in comparison to the cell density of myofibroblasts in normal scar tissue [26]. Figure 6.5 shows that the cell density of the myofibroblasts in the computer simulations is also elevated in the case where the evolution of the thickness of the tissue resembles the evolution of the thickness of hypertrophic scar tissue.

Irrespective of the value for the apoptosis rate of myofibroblasts, the thickness of the scar tissue will start to decline gradually as the cell density of the myofibroblast population diminishes slowly, and ultimately, the properties of the scar tissue will become identical to the properties of the surrounding tissue. This makes perfect sense from a mathematical point of view and is more or less in agreement with clinical observations [5]. A simple mathematical analysis demonstrates that the only stable equilibrium solutions for the cell densities and the concentrations of the individual constituents of the dermal layer are constant over the domain of computation (i.e. the equilibrium solutions are not dependent on the spatial variable). This implies that the "body force" in the mechanical force balance vanishes when the solutions related to the constituents of the dermal layer reach their equilibrium solutions. Subsequently, this implies that the

displacement field of the dermal layer becomes zero when the solutions related to the constituents of the dermal layer reach their equilibrium solutions. Consequently, the properties of the scar tissue will indeed become identical to the properties of the surrounding tissue. However, note that the cell density of the myofibroblasts declines very slowly toward the equilibrium cell density when the value for the apoptosis rate is relatively low (See Figure 6.5). Given Equation (6.18), this implies that the dermal layer remains relatively thick for a prolonged period of time.

REFERENCES

[1] Desmoulière A, Geinoz A, Gabbiani F, Gabbiani G (1993) Transforming growth factor-β1 induces α-smooth muscle actin expression in granulation tissue myofibroblasts and in quiescent and growing cultured fibroblasts. J Cell Biol 122:103–111

[2] Enoch S, Leaper D (2007) Basic science of wound healing. Surgery 26:31–37

[3] Ghosh K, Pan Z, Guan E, Ge S, Liu Y, Nakamura T, Ren ZD, Rafailovich M, Clark R (2007) Cell adaptation to a physiologically relevant ECM mimic with different viscoelastic properties. Biomaterials 28:671–679

[4] Grotendorst G (1992) Chemoattractants and growth factors. In: Cohen I, Diegelmann R, Lindblad W (eds) Wound Healing: Biochemical and Clinical Aspects, 1st edn, W.B. Saunders, Philadelphia, Pennsylvania, chap 15, pp 237–246

[5] Hawkins H, Finnerty C (2012) Pathophysiology of the burn scar. In: Herndon D (ed) Total Burn Care, 4th edn, Elsevier Inc, Philadelphia, Pennsylvania, chap 45, pp 507–516.e3

[6] Javierre E, Moreo P, Doblaré M, García-Aznar J (2009) Numerical modeling of a mechanochemical theory for wound contraction analysis. Int J Solids Struct 46:3597–3606

[7] Koppenol D, Vermolen F, Niessen F, Van Zuijlen P, Vuik K (2017) A mathematical model for the simulation of the formation and the subsequent regression of hypertrophic scar tissue after dermal wounding. Biomech Model Mechanobiol 16:15–32, DOI: 10.1007/s10237-016-0799-9

[8] Liang X, Boppart S (2010) Biomedical properties of *in vivo* human skin from dynamic optical coherence elastography. IEEE T Bio-Med Eng 57:953–959

[9] Maskarinec S, Franck C, Tirrell D, Ravichandran G (2009) Quantifying cellular traction forces in three dimensions. P Natl Acad Sci USA 106:22,108–22,113

[10] Moulin V, Castilloux G, Auger F, Garrel D, O'Connor-McCourt M, Germain L (1998) Modulated response to cytokines of human wound healing myofibroblasts compared to dermal fibroblasts. Exp Cell Res 238:283–293

[11] Murphy K, Hall C, Maini P, McCue S, McElwain D (2012) A fibrocontractive mechanochemical model of dermal wound closure incorporating realistic growth factor kinetics. B Math Biol 74:1143–1170

[12] Nedelec B, Correa J, De Oliveira A, LaSalle L, Perrault I (2014) Longitudinal burn scar quantification. Burns 40:1504–1512

[13] Oliveira G, Chinkes D, Mitchell C, Oliveras G, Hawkins H, Herndon D (2005) Objective assessment of burn scar vascularity, erythema, pliability, thickness, and planimetry. Dermatol Surg 31:48–58

[14] Olsen L, Sherratt J, Maini P (1995) A mechanochemical model for adult dermal wound contraction and the permanence of the contracted tissue displacement profile. J Theor Biol 177:113–128

[15] Overall C, Wrana J, Sodek J (1991) Transcriptional and post-transcriptional regulation of 72-kda gelatinase/ type IV collagenase by transforming growth factor-β1 in human fibroblasts. J Biol Chem 266:14,064–14,071

[16] Persson PO, Strang G (2004) A simple mesh generator in MATLAB. SIAM Rev 46:329–345

[17] Ramtani S (2004) Mechanical modelling of cell/ECM and cell/cell interactions during the contraction of a fibroblast-populated collagen microsphere: theory and model simulation. J Biomech 37:1709–1718

[18] Ramtani S, Fernandes-Morin E, Geiger D (2002) Remodeled-matrix contraction by fibroblasts: numerical investigations. Comput Biol Med 32:283–296

[19] Roberts A, Sporn M, Assoian R, Smith J, Roche N, Wakefiled L, Heine U, Liotta L, Falanga V, Kehrl J, Fauci A (1986) Transforming growth factor type β: Rapid induction of fibrosis and angiogenesis *in vivo* and stimulation of collagen formation *in vitro*. P Natl Acad Sci USA 83:4167–4171

[20] Rudolph R, Vande Berg J (1991) The myofibroblast in Dupuytren's contracture. Hand Clin 7:683–692

[21] Sillman A, Quang D, Farboud B, Fang K, Nuccitelli R, Isseroff R (2003) Human dermal fibroblasts do not exhibit directional migration on collagen 1 in direct-current electric fields of physiological strength. Exp Dermatol 12:396–402

[22] Strutz F, Zeisberg M, Renziehausin A, Raschke B, Becker V, Van Kooten C, Muller G (2001) TGF-β1 induces proliferation in human renal fibroblasts via induction of basic fibroblast growth factor (FGF-2). Kidney Int 59:579–592

[23] Tranquillo R, Murray J (1992) Continuum model of fibroblast-driven wound contraction: inflammation-mediation. J Theor Biol 158:135–172

[24] Treloar L (1948) Stresses and birefringence in rubber subjected to general homogeneous strain. Proc Phys Soc 60:135–144

[25] Vande Berg J, Rudolph R, Poolman W, Disharoon D (1989) Comparative growth dynamics and active concentration between cultured human myofibroblasts from granulating wounds and dermal fibroblasts from normal skin. Lab Invest 61:532–538

[26] Van der Veer W, Bloemen M, Ulrich M, Molema G, Van Zuijlen P, Middelkoop E, Niessen F (2009) Potential cellular and molecular causes of hypertrophic scar formation. Burns 35:15–29

[27] Wrobel L, Fray T, Molloy J, Adams J, Armitage M, Sparrow J (2002) Contractility of single human dermal myofibroblasts and fibroblasts. Cell Motil Cytoskelet 52:82–90

7

IMPLICATIONS FROM A MORPHOELASTIC CONTINUUM MODEL FOR THE SIMULATION OF CONTRACTURE FORMATION IN GRAFTS THAT COVER BURNS

A morphoelastic continuum hypothesis-based model is presented for the simulation of contracture formation in skin grafts that cover excised burns in order to obtain suggestions regarding the ideal length of splinting therapy and when to start with this therapy such that the therapy is effective optimally. Solely a portion of the dermal layer is modeled explicitly and this portion is modeled as an isotropic morphoelastic solid. With respect to the constituents of the tissue, the following constituents were selected as primary model components: fibroblasts, myofibroblasts, collagen molecules and a generic signaling molecule. All components of the model are modeled as continuous entities. In the model pulling forces are generated by the myofibroblasts which are present in the skin graft. These pulling forces are responsible for the compaction of the skin graft. Furthermore, the rate of active change of the effective strain, which determines the degree of contracture formation in the skin graft, is proportional to the product of the amount of effective strain, the local concentration of metalloproteinases, the local concentration of the signaling molecule and the inverse of the local concentration of the collagen molecules. The directions in which the effective strain changes, are determined by both the signs of the eigenvalues related to the effective strain tensor, and the directions of the associated eigenvectors.

This chapter is based on content of the article "Biomedical implications from a morphoelastic continuum model for the simulation of contracture formation in skin grafts that cover excised burns" [9].

After the presentation of the model and a more detailed presentation of the custom-made numerical algorithm for the generation of simulations, good agreement is demonstrated with respect to the evolution over time of the surface area of unmeshed skin grafts that cover excised burns between outcomes of computer simulations obtained in this study and scar assessment data gathered previously in a clinical study. Based on the simulation results obtained with the presented model it is suggested that the optimal point in time to start with splinting therapy is directly after placement of the skin graft on its recipient bed. Furthermore, the simulation results suggest that it is desirable to continue with splinting therapy until the concentration of the signaling molecules in the grafted area has become negligible such that the formation of contractures can be prevented. The chapter is concluded with a presentation of some alternative ideas on how to diminish the degree of contracture formation that are not based on a mechanical intervention.

7.1. INTRODUCTION

THE development of the model is presented in Section 7.2. Subsequently, an overview of the custom-made numerical algorithm that had to be developed for the generation of the computer simulations is presented in Section 7.3. The simulation results are presented in Section 7.4. Finally, the simulation results are discussed in Section 7.5.

7.2. DEVELOPMENT OF THE MATHEMATICAL MODEL

GIVEN that contraction mainly takes place in the dermal layer of skin tissues, solely a portion of this layer was incorporated into the model. The layer is modeled as an isotropic morphoelastic continuous solid with a modulus of elasticity that is dependent on the local concentration of the collagen molecules. With respect to the mechanical component of the model, the displacement of the dermal layer ($\mathbf{u}$), the displacement velocity of the dermal layer ($\mathbf{v}$) and the infinitesimal effective strain present in the dermal layer (ϵ) were chosen as primary model variables. The latter variable represents a local measure for the difference between the current configuration of the dermal layer and a hypothetical configuration of the dermal layer where the tissue is mechanically relaxed (See Subsection 2.5 for further details) [5]. Furthermore, the following four constituents of the dermal layer were selected as primary model variables: fibroblasts (N), myofibroblasts (M), a generic signaling molecule (c) and collagen molecules (ρ).

The general conservation equations for mass and linear momentum together with the evolution equation that describes how the infinitesimal effective strain changes over time (See Subsection 2.5 for further details), were used as basis for the model:

$$\frac{\mathrm{D}z_i}{\mathrm{D}t} + z_i\,[\nabla\cdot\mathbf{v}] = -\nabla\cdot\mathbf{J}_i + R_i, \tag{7.1a}$$

$$\frac{\mathrm{D}(\rho_t\mathbf{v})}{\mathrm{D}t} + \rho_t\mathbf{v}\,[\nabla\cdot\mathbf{v}] = \nabla\cdot\sigma + \mathbf{f}, \tag{7.1b}$$

$$\frac{\mathscr{D}\epsilon}{\mathscr{D}t} + [\mathrm{tr}(\epsilon) - 1]\mathrm{sym}(\mathbf{L}) = -\mathbf{G}. \tag{7.1c}$$

Here

$$\mathbf{v} = \frac{\mathrm{D}\mathbf{u}}{\mathrm{D}t}, \tag{7.2}$$

$$\epsilon = \mathbf{I} - \mathbf{A}^{-1}, \tag{7.3}$$

and

$$\frac{\mathscr{D}\epsilon}{\mathscr{D}t} = \frac{\mathrm{D}\epsilon}{\mathrm{D}t} + \epsilon\mathrm{skw}(\mathbf{L}) - \mathrm{skw}(\mathbf{L})\epsilon. \tag{7.4}$$

Equation (7.1a) is the conservation equation for the cell density / concentration of constituent i of the dermal layer, Equation (7.1b) is the conservation equation for the linear momentum of the dermal layer and Equation (7.1c) is the evolution equation that describes how the infinitesimal effective strain changes over time.

Within the above equations z_i represents the cell density / concentration of constituent i, $\mathbf{J}_i$ represents the flux associated with constituent i per unit area due to random dispersal, chemotaxis and other possible fluxes, R_i represents the chemical kinetics associated with constituent i, ρ_t represents the total mass density of the dermal tissues, σ represents the Cauchy stress tensor associated with the dermal layer, $\mathbf{f}$ represents the total body force working on the dermal layer, $\mathbf{L}$ is the displacement velocity gradient tensor (i.e., $\mathbf{L} = \nabla\mathbf{v}$) and $\mathbf{G}$ is the tensor that describes the rate of active change of the effective strain. The tensor $\mathbf{A}$ is the locally-defined deformation gradient tensor that describes how infinitesimal line segments in a hypothetical stress-free configuration of the dermal layer are transformed into infinitesimal line segments in the current configuration of the dermal layer (See Subsection 2.5 for further details). The operator $\mathscr{D}(\cdot)/\mathscr{D}t$ is the Jaumann time derivative and the operator $\mathrm{D}(\cdot)/\mathrm{D}t$ is the material time derivative. (If the material time derivative is applied to the effective strain tensor, then it is applied to each of the scalar elements of this tensor separately.) Given the chosen primary model variables, $i \in \{N, M, c, \rho\}$ holds. In order to simplify the notation somewhat z_i has been replaced by i in the remainder of this chapter. Hence, z_N has been replaced by N, z_M has been replaced by M and so on.

7.2.1. THE CELLS

THE functional forms for the movement of the (myo)fibroblasts and the functional forms for the biochemical kinetics associated with these cells are identical to the functional forms that have been introduced in Chapter 4. More details about the functional forms can be found in Chapter 4. The functional forms for the cell fluxes are

$$\mathbf{J}_N = -D_F F\nabla N + \chi_F N\nabla c, \tag{7.5}$$
$$\mathbf{J}_M = -D_F F\nabla M + \chi_F M\nabla c, \tag{7.6}$$

where

$$F = N + M. \tag{7.7}$$

The parameter D_F is the cell density-dependent (myo)fibroblast random motility coefficient and χ_F is the chemotactic coefficient. The functional forms for the biochemical kinetics associated with the (myo)fibroblasts are

$$R_N = r_F \left[1 + \frac{r_F^{\max} c}{a_c^I + c} \right] [1 - \kappa_F F] N^{1+q} - k_F c N - \delta_N N, \tag{7.8}$$

$$R_M = r_F \left\{ \frac{\left[1 + r_F^{\max} \right] c}{a_c^I + c} \right\} [1 - \kappa_F F] M^{1+q} + k_F c N - \delta_M M. \tag{7.9}$$

Here r_F is the cell division rate, $r_F^{\max}$ is the maximum factor with which the cell division rate can be enhanced due to the presence of the signaling molecule, a_c^I is the concentration of the signaling molecule that causes the half-maximum enhancement of the cell division rate, $\kappa_F F$ represents the reduction in the cell division rate due to crowding, q is a fixed constant, k_F is the signaling molecule-dependent cell differentiation rate of fibroblasts into myofibroblasts, δ_N is the apoptosis rate of fibroblasts and δ_M is the apoptosis rate of myofibroblasts.

7.2.2. THE SIGNALING MOLECULES

THE functional form for the dispersion of the generic signaling molecule and the functional forms for the release, the consumption and the removal of the generic signaling molecule are nearly identical to the functional forms that have been introduced in Chapter 4:

$$\mathbf{J}_c = -D_c \nabla c, \tag{7.10}$$

$$R_c = k_c \left[\frac{c}{a_c^{II} + c} \right] \left[N + \eta^I M \right] - \delta_c g(N, M, c, \rho) c. \tag{7.11}$$

The parameter D_c represents the random diffusion coefficient of the generic signaling molecule, k_c represents the maximum net secretion rate of the signaling molecule, η^I is the ratio of myofibroblasts to fibroblasts in the maximum net secretion rate of the signaling molecule, a_c^{II} is the concentration of the signaling molecule that causes the half-maximum net secretion rate of the signaling molecule and δ_c is the proteolytic breakdown rate of the signaling molecules. The concentration of the generic metalloproteinase (MMP) (i.e., $g(N, M, c, \rho)$) which is responsible for the breakdown of the signaling molecules was assumed to be proportional to the cell density of the (myo)fibroblasts, and the concentration of both the collagen molecules and the signaling molecules according to the following formula (See the accompanying paragraph of Equation (4.9) for further details):

$$g(N, M, c, \rho) \propto \frac{\left[N + \eta^{II} M \right] \rho}{1 + a_c^{III} c}. \tag{7.12}$$

The parameter η^{II} is the ratio of myofibroblasts to fibroblasts in the secretion rate of the MMPs, and $1/[1 + a_c^{III} c]$ represents the inhibition of the secretion of the generic MMP due to the presence of the signaling molecule.

7.2.3. THE COLLAGEN MOLECULES

THE functional form for the dispersion of the collagen molecules and the functional forms for the secretion and the proteolytic breakdown of the collagen molecules are nearly identical to the functional forms that have been introduced in Chapter 5:

$$\mathbf{J}_\rho = \mathbf{0}, \tag{7.13}$$

$$R_\rho = k_\rho \left\{ 1 + \left[\frac{k_\rho^{\max} c}{a_c^{IV} + c} \right] \right\} \left[N + \eta^I M \right] - \delta_\rho g(N, M, c, \rho) \rho. \tag{7.14}$$

Here k_ρ is the collagen molecule secretion rate, $k_\rho^{\max}$ is the maximum factor with which this secretion rate can be enhanced due to the presence of the signaling molecule, a_c^{IV} is the concentration of the signaling molecules that causes the half-maximum enhancement of the secretion rate and δ_ρ is the proteolytic breakdown rate of the molecules.

7.2.4. THE MECHANICAL COMPONENT

IN this study the following visco-elastic constitutive relation was used for the mathematical description of the relationship between the Cauchy stress tensor on the one hand, and the effective strains and displacement velocity gradients on the other hand:

$$\sigma = \mu_1 \mathrm{sym}(\mathbf{L}) + \mu_2 \left[\mathrm{tr}\left(\mathrm{sym}(\mathbf{L}) \right) \mathbf{I} \right] + \left[\frac{E\sqrt{\rho}}{1+\nu} \right] \left\{ \epsilon + \mathrm{tr}(\epsilon) \left[\frac{\nu}{1-2\nu} \right] \mathbf{I} \right\}. \tag{7.15}$$

Here μ_1 is the shear viscosity, μ_2 is the bulk viscosity, ν is Poisson's ratio, $E\sqrt{\rho}$ is the Young's modulus and $\mathbf{I}$ is the second-order identity tensor. It was assumed that the Young's moduli is dependent on the concentration of the collagen molecules [21, 22]. The parameter E is a constant.

Furthermore, the generation of an isotropic stress by the myofibroblasts due to their pulling on the ECM was incorporated into the model. Identical to the model presented in Chapter 4 this pulling stress is proportional to the product of the cell density of the myofibroblasts and a simple function of the concentration of the collagen molecules [17]. No other forces are incorporated into the model. Taken together, the following was obtained:

$$\mathbf{f} = \nabla \cdot \psi, \tag{7.16}$$

$$\psi = \xi M \left[\frac{\rho}{R^2 + \rho^2} \right] \mathbf{I}. \tag{7.17}$$

The parameter ψ represents the total generated stress by the myofibroblast population, ξ is the generated stress per unit cell density and the inverse of the unit collagen molecule concentration, and R is a fixed constant.

Finally, it was assumed that the rate of active change of the effective strain is proportional to the product of the amount of effective strain, the local concentration of the MMPs, the local concentration of the signaling molecule and the inverse of the local concentration of the collagen molecules. The directions in which the effective strain

changes, are determined by both the signs of the eigenvalues related to the effective strain tensor, and the directions of the associated eigenvectors. Taken together, the following symmetric tensor was obtained:

$$\mathbf{G} = \zeta \left[\frac{g(N, M, c, \rho) c}{\rho} \right] \epsilon = \zeta \left\{ \frac{\left[N + \eta^{II} M \right] c}{1 + a_c^{III} c} \right\} \epsilon. \tag{7.18}$$

Here ζ is the rate of morphoelastic change (i.e., the rate at which the effective strain changes actively over time).

7.2.5. THE DOMAIN OF COMPUTATION

IT was assumed that $u = 0$, $\partial v/\partial x = \partial w/\partial x = 0$, $v_1 = 0$, $\partial v_2/\partial x = \partial v_3/\partial x = 0$, $\epsilon_{11} = \epsilon_{12} = \epsilon_{21} = \epsilon_{13} = \epsilon_{31} = 0$ and $\partial \epsilon_{22}/\partial x = \partial \epsilon_{33}/\partial x = 0$ hold within the modeled portion of dermal layer for all time t, with the yz-plane running parallel to the surface of the skin and

$$\mathbf{u} = \begin{bmatrix} u \\ v \\ w \end{bmatrix}, \quad \mathbf{v} = \begin{bmatrix} v_1 \\ v_2 \\ v_3 \end{bmatrix}, \quad \text{and} \quad \epsilon = \begin{bmatrix} \epsilon_{11} & \epsilon_{12} & \epsilon_{13} \\ \epsilon_{21} & \epsilon_{22} & \epsilon_{23} \\ \epsilon_{31} & \epsilon_{32} & \epsilon_{33} \end{bmatrix}. \tag{7.19}$$

Furthermore, it was assumed that the derivatives of the cell densities and the concentrations of the modeled constituents of the dermal layer are equal to zero in the direction perpendicular to the surface of the skin. Taken together, these assumptions imply that the calculations can be performed on an arbitrary, infinitely thin slice of dermal layer oriented parallel to the surface of the skin, and that the results from these calculations are valid for every infinitely thin slice of dermal layer oriented parallel to the surface of the skin. Using Lagrangian coordinates ($\mathbf{X} = (X, Y, Z)^{\mathrm{T}}$), the domain of computation ($\Omega_{\mathbf{X}}$) is described mathematically by

$$\Omega_{\mathbf{X}} \in \{X = 0 \text{ cm}, \ -10 \text{ cm} \leq Y \leq 10 \text{ cm}, \ -10 \text{ cm} \leq Z \leq 10 \text{ cm}\}. \tag{7.20}$$

7.2.6. THE INITIAL CONDITIONS AND THE BOUNDARY CONDITIONS

THE initial conditions give a description of the cell densities and the concentrations immediately after placement of the skin graft on its recipient bed. For the generation of the simulation results the following function was used to describe the shape of the skin graft:

$$w(\mathbf{X}_r) = 1 - [1 - I(Y_r, 2.5, 0.10)] \, [1 - I(Z_r, 2.5, 0.10)] \, I(Y_r, 2.5, 0.10) \, I(Z_r, 2.5, 0.10). \tag{7.21}$$

Here the function I is the indicator function that has been introduced in Equation (4.31). Furthermore, $w = 0$ corresponds to grafted dermis and $w = 1$ corresponds to unwounded dermis. Finally, $\mathbf{X}_r = \mathbf{R}(\theta_r)\mathbf{X} = (X_r, Y_r, Z_r)^{\mathrm{T}}$ with $\mathbf{R}(\theta)$ the counterclockwise rotation matrix that rotates vectors by an angle θ about the X-axis, and $\theta_r = \pi/4$ rad.

Based on the function for the shape of the skin graft, the following initial conditions were used for the modeled constituents of the dermal layer:

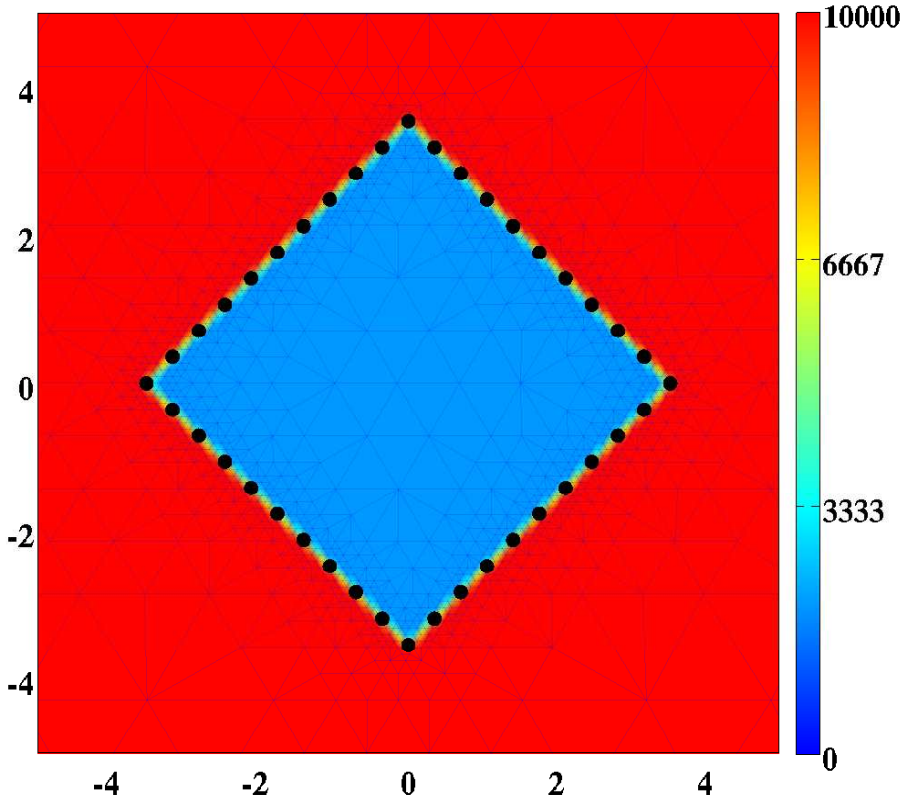

Figure 7.1: A graphical overview of the initial conditions. Depicted are the initial shape of the skin graft and, in color scale, the initial cell density of the fibroblasts (cells/cm^3). The scale along both axes is in centimeters. The X-axis points toward the reader. The black dots mark the material points that were used to trace the evolution of the surface area of the skin graft over time. That is, at each time point, the area of the polygon with vertices located at the displaced black material points was determined

$$\begin{aligned} N(\mathbf{X},0) &= \left\{I^w + \left[1 - I^w\right] w(\mathbf{X}_r)\right\} \overline{N}, \\ M(\mathbf{X},0) &= \overline{M}, \\ c(\mathbf{X},0) &= [1 - w(\mathbf{X}_r)]\, c^w, \\ \rho(\mathbf{X},0) &= \overline{\rho}. \end{aligned} \tag{7.22}$$

Here $\overline{N}$, $\overline{M}$ and $\overline{\rho}$ are respectively the equilibrium cell density of the fibroblasts, the equilibrium cell density of the myofibroblasts and the equilibrium concentration of the collagen molecules, of the unwounded dermis. Due to the secretion of signaling molecules by for instance macrophages, signaling molecules are present in the wounded area. The constant c^w represents the maximum initial concentration of the signaling molecule in the grafted area. Furthermore, it was assumed that there are some fibroblasts present in

the grafted area. The value for the parameter I^w determines how much fibroblasts are present initially in the grafted area.

With respect to the initial conditions for the mechanical component of the model, the following initial conditions are used for all $\mathbf{x} \in \Omega_{\mathbf{x},0}$ where $\Omega_{\mathbf{x},0}$ is the initial domain of computation in Eulerian coordinates:

$$\mathbf{u}(\mathbf{x},0) = \mathbf{0}, \quad \mathbf{v}(\mathbf{x},0) = \mathbf{0}, \quad \text{and} \quad \epsilon(\mathbf{x},0) = \mathbf{0}. \tag{7.23}$$

See Figure 7.1 for a graphical representation of the initial conditions that were used in this study.

With respect to the boundary conditions for the constituents of the dermal layer, the following Dirichlet boundary conditions were used for all time t and for all $\mathbf{x} \in \partial\Omega_{\mathbf{x},t}$ where $\partial\Omega_{\mathbf{x},t}$ is the boundary of the domain of computation in Eulerian coordinates:

$$N(\mathbf{x},t) = \overline{N}, \quad M(\mathbf{x},t) = \overline{M}, \quad \text{and} \quad c(\mathbf{x},t) = \overline{c}. \tag{7.24}$$

The parameter $\overline{c}$ is the equilibrium concentration of the signaling molecule in the unwounded dermis.

Finally, with respect to the boundary condition for the mechanical component of the model, the following Dirichlet boundary condition was used for all time t and for all $\mathbf{x} \in \partial\Omega_{\mathbf{x},t}$:

$$\mathbf{v}(\mathbf{x},t) = \mathbf{0}. \tag{7.25}$$

7.2.7. THE (RANGES OF THE) VALUES FOR THE PARAMETERS

TABLE 7.1 provides an overview of the (ranges of the) values for the parameters of the model. The majority of these values were either obtained directly from previously conducted studies or estimated from results of previously conducted studies. In addition, the values for the equilibrium signaling molecule concentration of the unwounded dermis ($\overline{c}$), the constant q and the collagen molecule degradation rate (δ_ρ) could be determined due to the fact that these values are a necessary consequence of the values chosen for other parameters. See Subsection 4.2.7 for the derivation of the values for these parameters.

Table 7.1: An overview of the (ranges of the) values for the parameters of the model. The last column contains the references to the studies that were used for obtaining (estimates of) the values for the parameters. If (the range of) the value for a parameter has been estimated in this study, then this is indicated by the abbreviation TW. If the value for a parameter is a necessary consequence of the values chosen for the other parameters, then this is indicated by the abbreviation NC

Parameter	Value	Dimensions	Reference
D_F	10^{-7}	$\text{cm}^5/(\text{cells day})$	[27]
χ_F	2×10^{-3}	$\text{cm}^5/(\text{g day})$	[16]
q	-4.2×10^{-1}	–	NC
r_F	9.24×10^{-1}	$\text{cm}^{3q}/(\text{cells}^q \text{ day})$	[3]
$r_F^{\max}$	2	–	[28]
a_c^I	10^{-8}	g/cm^3	[4]

Continued on the next page

Table 7.1 – *Continued from the previous page*

Parameter	Value	Dimensions	Reference
κ_F	10^{-6}	cm^3/cells	[32]
k_F	1.08×10^7	cm^3/(g day)	[1]
δ_N	2×10^{-2}	/day	[17]
δ_M	6×10^{-2}	/day	[10]
D_c	2.9×10^{-3}	cm^2/day	[16]
k_c	4×10^{-13}	g/(cells day)	[17]
η^I	2	–	[15] & [25]
a_c^{II}	10^{-8}	g/cm^3	[17]
δ_c	5×10^{-4}	cm^6/(cells g day)	[17]
η^{II}	5×10^{-1}	–	TW
a_c^{III}	$(2-2.5) \times 10^8$	cm^3/g	[18]
k_ρ	6×10^{-8}	g/(cells day)	NC
$k_\rho^{\max}$	10	–	[17]
a_c^{IV}	10^{-9}	g/cm^3	[24]
δ_ρ	6×10^{-6}	cm^6/(cells g day)	[10]
ρ_t	1.02	g/cm^3	[11]
μ_1	10^2	(N day)/cm^2	TW
μ_2	10^2	(N day)/cm^2	TW
E	3.2×10	N/((g cm)$^{1/2}$)	[11]
ν	4.9×10^{-1}	–	[11]
ξ	5×10^{-2}	(N g)/(cells cm^2)	[13] & [34]
R	9.95×10^{-1}	g/cm^3	TW
ζ	$(0-9) \times 10^2$	cm^6/(cells g day)	TW
$\overline{N}$	10^4	cells/cm^3	[17]
$\overline{M}$	0	cells/cm^3	[17]
$\overline{c}$	0	g/cm^3	NC
$\overline{\rho}$	10^{-1}	g/cm^3	[17]
I^w	2×10^{-1}	–	[10]
c^w	10^{-8}	g/cm^3	[17]

7.3. THE APPLIED NUMERICAL ALGORITHM

FOR the kernel of the concrete expression of the algorithm `MATLAB` was used together with `MATLAB`'s Parallel Computing Toolbox [29]. Furthermore, this kernel was interfaced consecutively with an adapted version of the mesh generator developed by Persson and Strang for the generation of a base triangulation of the domain of computation [20], the element resolution refinement / recoarsement tool of the computational fluid dynamics software package `FEATFLOW2` for the adjustment of the resolution of the elements of the base triangulation [30], and the permutation routine `HSL_MC64` for the permutation of the $n \times n$ matrices related to the resulting systems of linear algebraic equations after full discretization of the model equations such that the matrices have n entries on their diagonal [7]. Finally, the following non-dimensionalisation was applied to the model:

$$
\begin{aligned}
x &= Lx^*, \quad t = \left[L^2/\left[D_F\overline{N}\right]\right]t^*, \quad \rho = \overline{\rho}\rho^*, \quad N = \overline{N}N^*, \\
\mathbf{u} &= L\mathbf{u}^*, \quad \mathbf{v} = \left[\left[D_F\overline{N}\right]/L\right]\mathbf{v}^*, \quad c = c^w c^*, \quad M = \overline{N}M^*, \\
\epsilon &= \epsilon^*, \quad \sigma = \left[\left[\xi\overline{N}\right]/\overline{\rho}\right]\sigma^*.
\end{aligned} \tag{7.26}
$$

Here $L = 1$ cm is the length scale of the model. The variables with the asterisks are the non-dimensionalised variables.

In order to create conforming base triangulations of the domain of computation, the adapted version of the mesh generator developed by Persson and Strang is used [20]. This results in a high-quality triangulation of the domain of computation where most of the triangles are equilateral. The only triangles that are not equilateral, are located near the boundaries of the domain of computation. These latter triangles are nearly equilateral. Using the measure from Equation (4.31), it was observed that $\alpha > 0.86$ for all triangles in the generated triangulation. For the generation of the simulation results presented in Section 7.4, a triangulation consisting of triangles with an average initial edge length of 1.65 cm was used. After the generation of the base triangulation the element resolution refinement / recoarsement tool is used to adjust the resolution of the elements of the base triangulation. See Subsection 5.3.1 for a detailed description of this procedure.

Subsequently, an approximation of the solution for the primary model variables is determined from Equation (7.1). In order to find such an approximation the method of lines together with the standard fixed-point defect correction method are used [31]. The equations from Equation (7.1) are solved in a segregated way. That is, each fixed-point iteration within each time step approximations of the solutions for the modeled constituents of the dermal layer are determined together first, and subsequently approximations of the solutions for the displacement velocity and the effective strain are determined by solving Equation (7.1b) and Equation (7.1c) simultaneously. Finally, using the fact that the following holds

$$
\mathbf{u}(\mathbf{x}(\mathbf{X}, t), t) = \mathbf{U}(\mathbf{X}, t), \quad \text{and} \quad \mathbf{v}(\mathbf{x}(\mathbf{X}, t), t) = \mathbf{V}(\mathbf{X}, t), \tag{7.27}
$$

where $\mathbf{U}$ and $\mathbf{V}$ are, respectively the displacement and the displacement velocity of the dermal layer in Lagrangian coordinates, an approximation of the solution for the displacement of the dermal layer is determined from Equation (7.2) via post-processing in the following way:

$$
\mathbf{U}_{n+1}^{(m+1)} = \mathbf{U}_n + \Delta t\left\{[1-\theta]\mathbf{V}_n + \theta\mathbf{V}_{n+1}^{(m+1)}\right\}. \tag{7.28}
$$

Here $\mathbf{U}_n$ and $\mathbf{V}_n$ are, respectively, the final approximations of the solutions for the displacement and the displacement velocity after n time steps. Furthermore, $\mathbf{U}_{n+1}^{(m+1)}$ and $\mathbf{V}_{n+1}^{(m+1)}$ are, respectively, the new approximations of the solutions for the displacement and the displacement velocity after application of $m+1$ fixed-point iteration(s). The parameter Δt is the size of the current time step and the parameter θ is a fixed constant which was set to 0.55 in this study. After obtaining a new approximation of the solution

for the displacement of the dermal layer, the position of the vertices in the triangulation is updated in the following way:

$$\mathbf{x}_j^{(m+1)}(\mathbf{X}_j, t) = \mathbf{X}_j + \mathbf{U}_j^{(m+1)}(\mathbf{X}_j, t). \tag{7.29}$$

Here $\mathbf{x}_j^{(m+1)}(\mathbf{X}_j, t)$ is the new location of vertex j in Eulerian coordinates after application of $m+1$ fixed-point iteration(s), $\mathbf{X}_j$ is the fixed location of vertex j in Lagrangian coordinates, and $\mathbf{U}_j^{(m+1)}(\mathbf{X}_j, t)$ is the new approximation of the solution for the displacement at vertex j after application of $m+1$ fixed-point iteration(s). The fixed-point defect correction scheme is iterated until the maximum of the relative 1-norms of the residuals of the approximations is smaller than one, and the maximum of the relative 1-norms of the difference between subsequent approximations per variable is smaller than 5×10^{-2}. If the correction scheme does not meet these convergence criteria within five iterations, then the scheme is interrupted, the time step is decreased to 85% of its current value, and subsequently the scheme is restarted.

For the discretization of the system of equations from Equation (7.1), the backward Euler time-integration method together with a moving-grid finite-element method is used [12]. The derivation of the finite-element approximation of the solution for the primary model variables is presented in Appendix A. Again the flux-corrected transport (FCT) limiter and Patankar's source / sink separation technique are applied on the discretized system of equations that describes the dynamics of the modeled constituents of the dermal layer in order to enforce positivity of the approximations of the solutions for the constituents of the dermal layer [14, 19]. See Subsection 5.3.2 for more details on both the discretization of the system of equations, and how the resulting systems of linear algebraic equations are solved.

Furthermore, the individual time steps are chosen automatically again by using the automatically adaptive time-stepping method. The element resolution refinement / recoarsement tool is also applied again in order to adjust the resolution of the elements of the triangulation. See Subsection 5.3.2 for more details on both procedures.

7.4. SIMULATION RESULTS

IN order to obtain some insight into the dynamics of the model, an overview of simulation results for the modeled constituents of the dermal layer is presented in Figure 7.2. Furthermore, an overview of simulation results for the displacement field and the displacement velocity field is presented in Figure 7.3, and an overview of simulation results for the effective strain is presented in Figure 7.4. For the generation of these overviews the same set of values for the parameters of the model was used.

Figure 7.2 shows that the cell density of the myofibroblasts, and the concentrations of both the signaling molecules and the collagen molecules increase first within the skin graft. Subsequently, the concentrations of these molecules, just like the cell density of the myofibroblasts, start to decline until they reach the equilibrium concentrations and the equilibrium cell density of uninjured dermal tissue. Meanwhile, the cell density of the fibroblasts starts to increase within the skin graft until it reaches the equilibrium cell density of uninjured dermal tissue.

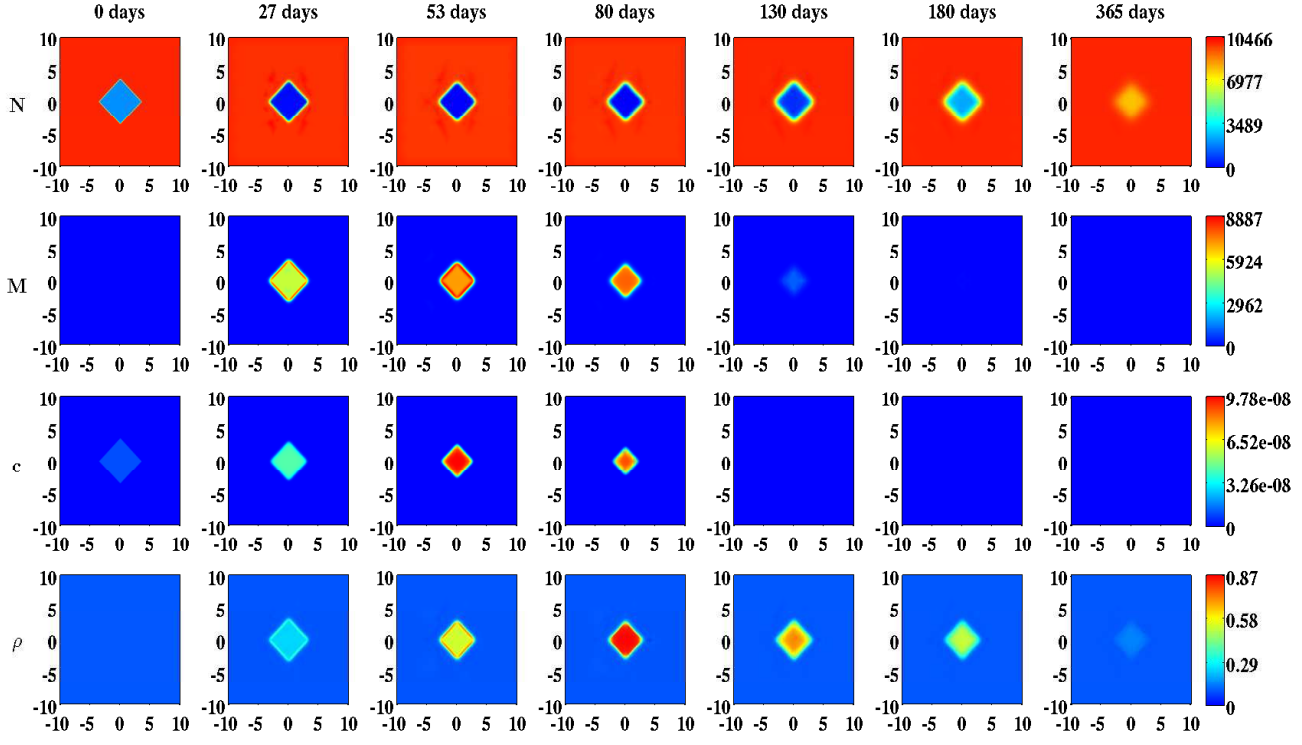

Figure 7.2: An overview of simulation results for the modeled constituents of the dermal layer when the inhibition of the secretion of MMPs due to the presence of signaling molecules is relatively low ($a_c^{III} = 2 \times 10^8$ cm^3/g) and the rate of morphoelastic change is relatively high ($\zeta = 9 \times 10^2$ cm^6/(cells g day)). The values for all other parameters are equal to those depicted in Table 7.1. The top two rows show the evolution over time of the cell density of, respectively, the fibroblast population and the myofibroblast population. The color scales represent the cell densities, measured in cells/cm^3. The bottom two rows show the evolution over time of the concentrations of, respectively, the signaling molecules and the collagen molecules. The color scales represent the concentrations, measured in g/cm^3. Within the subfigures, the scale along both axes is in centimeters

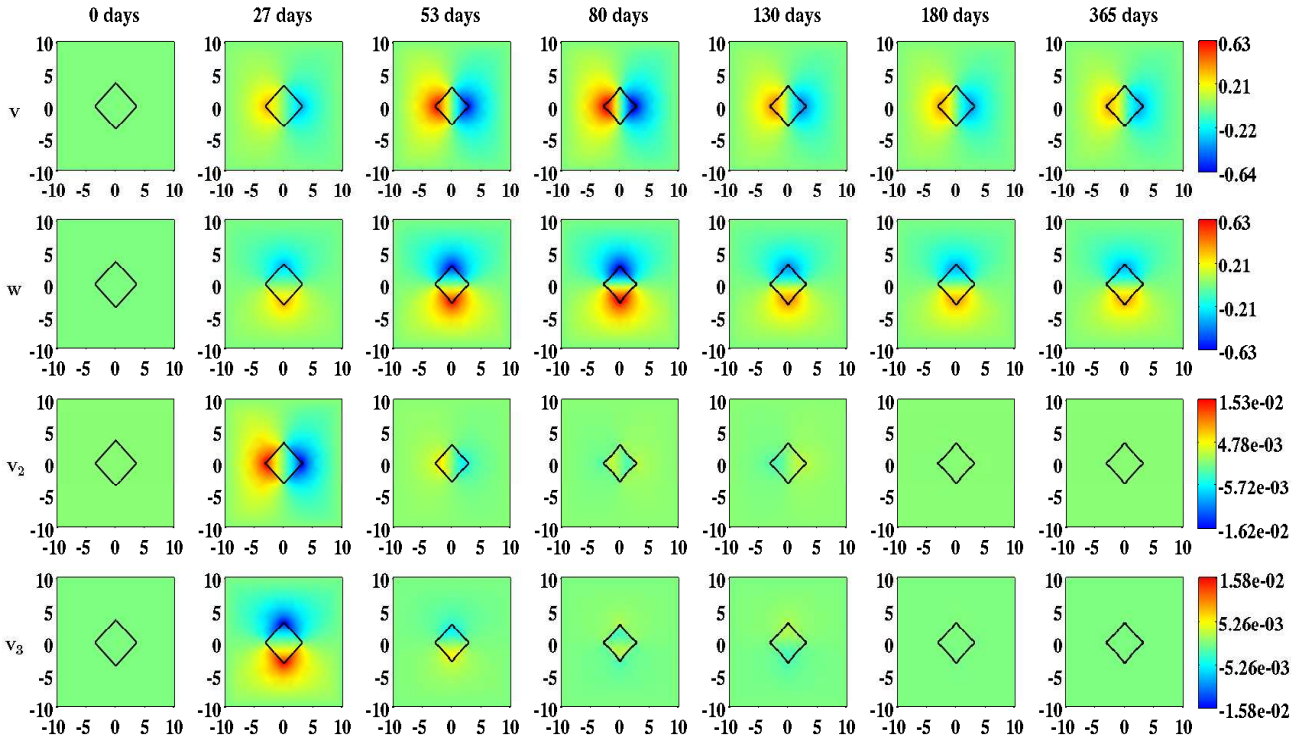

Figure 7.3: An overview of simulation results for the displacement field and the displacement velocity field when the inhibition of the secretion of MMPs due to the presence of signaling molecules is relatively low ($a_c^{III} = 2 \times 10^8$ cm^3/g) and the rate of morphoelastic change is relatively high ($\zeta = 9 \times 10^2$ cm^6/(cells g day)). The values for all other parameters are equal to those depicted in Table 7.1. The top two rows show the evolution over time of the displacement in, respectively, the horizontal direction and the vertical direction. The color scales represent the displacements, measured in centimeters. The bottom two rows show the evolution over time of the displacement velocity in, respectively, the horizontal direction and the vertical direction. The color scales represent the displacement velocities, measured in cm/day. Within the subfigures, the scale along both axes is in centimeters. The black squares within the subfigures represent the (displaced) boundaries between the skin graft and the unwounded dermis

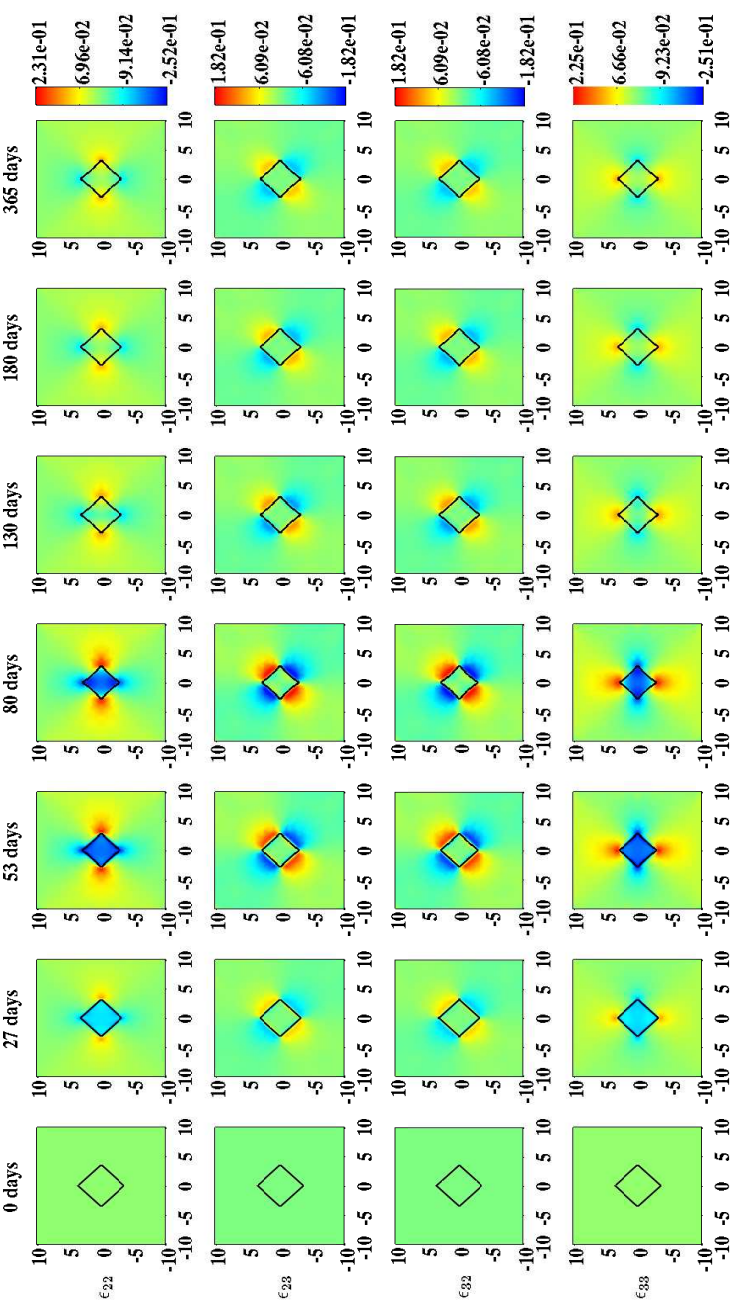

Figure 7.4: An overview of simulation results for the effective strain when the inhibition of the secretion of MMPs due to the presence of signaling molecules is relatively low ($a_c^{11} = 2 \times 10^8$ cm^3/g) and the rate of morphoelastic change is relatively high ($\zeta = 9 \times 10^2$ cm^6/(cells g day)). The values for all other parameters are equal to those depicted in Table 7.1. The separate rows show the evolution over time of the different components of the effective strain that are unequal to zero. The color scales represent the amount of effective strain. Within the subfigures, the scale along both axes is in centimeters. The black squares within the subfigures represent the (displaced) boundaries between the skin graft and the unwounded dermis

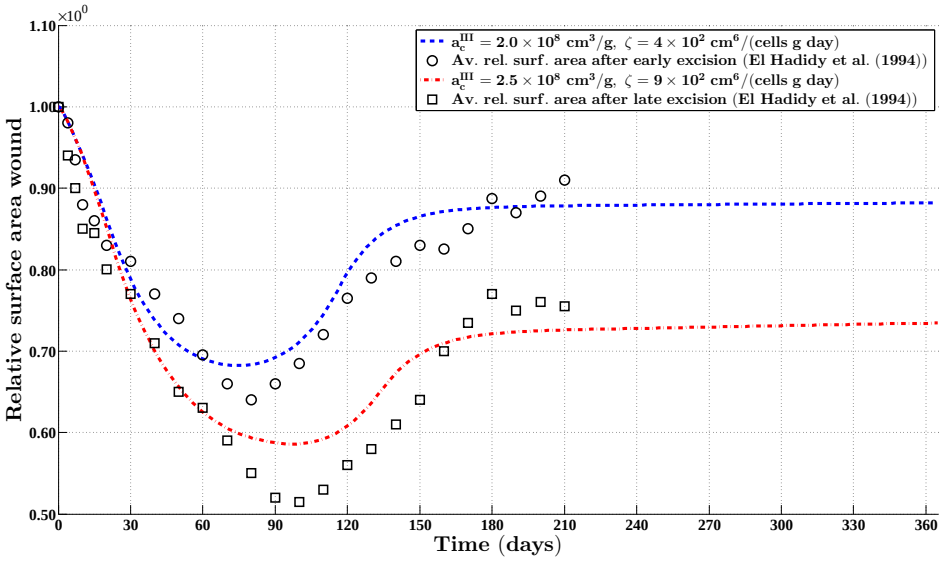

Figure 7.5: The evolution over time of the relative surface area of wounds (i.e., skin grafts) for particular combinations of values for the rate of morphoelastic change (i.e., the parameter ζ), and the parameter related to the inhibition of the secretion of MMPs due to the presence of signaling molecules (i.e., the parameter a_c^{III}). The values for all other parameters are equal to those depicted in Table 7.1. The black circles and the black squares show the evolution over time of the average of clinical measurements of the relative surface areas of placed unmeshed skin grafts after, respectively, early excision of burnt skin and late excision of burnt skin [2]

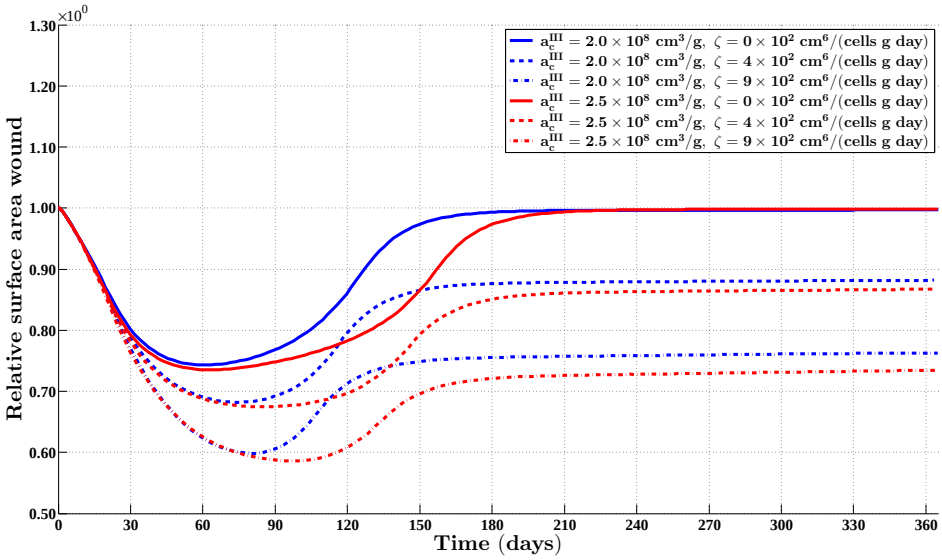

Figure 7.6: The evolution over time of the relative surface area of wounds (i.e., skin grafts) for some combinations of values for the rate of morphoelastic change (i.e., the parameter ζ), and the parameter related to the inhibition of the secretion of MMPs due to the presence of signaling molecules (i.e., the parameter a_c^{III}). The values for all other parameters are equal to those depicted in Table 7.1

Figure 7.3 shows that the boundaries between the skin graft and the uninjured tissue are pulled inward increasingly toward the center of the skin graft while the concentration of the collagen molecules and the cell density of the myofibroblasts increase. Looking at the displacement velocity field, it can be observed that the boundaries are pulled inward relatively fast initially. Subsequently, the speed with which the boundaries are pulled inward diminishes fast. Looking carefully at the displacement velocity field, it can be observed that the inward movement actually reverses from a certain time point onward. It is nice to observe that this phenomenon coincides with the gradual increase of the surface area of the skin graft, and the gradual decrease of both the cell density of the myofibroblasts and the concentration of the collagen molecules within the skin graft, as can be observed in, respectively, Figure 7.6 and Figure 7.2. Furthermore, it can be observed that the boundaries between the skin graft and the uninjured tissue hardly move anymore eventually (i.e., the individual components of the displacement velocity field become approximately equal to zero over the domain of computation), and that the surface area of the skin graft has diminished considerably after a year. This latter phenomenon is also clearly visible in Figure 7.6.

Figure 7.4 also shows something very interesting. Looking at the effective strain at day 365, it can be observed that the individual components of the effective strain tensor are not equal to zero over the domain of computation. This implies that there are residual stresses present in the grafted area. Comparing the properties of the effective strain at day 180 with the properties of the effective strain at day 365, it can be observed that these are more or less the same. Hence, the residual stresses remain present in the modeled portion of dermal layer for a prolonged period of time.

Figure 7.5 shows the evolution over time of the relative surface area of skin grafts for particular combinations of values for two parameters that are directly related to the tensor **G** (See Equation (7.18)). In addition, the figure shows averages of clinical measurements over time of the relative surface areas of placed unmeshed skin grafts in human subjects after both early excision of burnt skin and late excision of burnt skin [2].

Figure 7.6 shows the evolution over time of the relative surface area of skin grafts for some more combinations of values for the aforementioned parameters related to the tensor **G**. The figure shows that both an increase in the rate of morphoelastic change (i.e., the parameter ζ), and an increase in the inhibition of the secretion of MMPs due to the presence of signaling molecules (i.e., an increase in the value for the parameter a_c^{III}) results in a reduction of the final surface area of a skin graft. Within the chosen ranges for the values of the parameters, it can be observed that a change in the value for the rate of morphoelastic change has a large impact on the final surface area of a skin graft. Changing the value for the parameter related to the inhibition of the secretion of MMPs due to the presence of signaling molecules has a smaller impact on the final surface area of a skin graft. Note also that the value for the latter parameter has a relatively large impact on the total number of days that the boundaries between the skin graft and the uninjured tissue are pulled inward after placement of the skin graft before the retraction process starts.

Finally, it is nice to observe in Figure 7.6 that, as expected, the surface area of a skin graft returns to its initial value when the rate of morphoelastic change is equal to zero. If this rate is equal to zero, then the tensor **G** is equal to the zero tensor. In this case one

would expect an initial period during which the surface area of a skin graft diminishes due to the pulling action of the myofibroblasts, followed by a period during which this surface area slowly returns to its initial value due to the apoptosis of the myofibroblasts. This is exactly what can be observed in the figure.

7.5. CONCLUSIONS

WITH the developed model it is possible to reproduce some general qualitative features of the healing response that is initiated after the placement of a skin graft on its recipient bed [6]. The restoration of the presence of fibroblasts within the skin graft and the temporary presence of myofibroblasts during the execution of the healing response can be reproduced. Due to the initial presence of signaling molecules and the gradual increase of the cell density of the myofibroblasts in the grafted area, the secretion rate of collagen molecules is considerably larger than the proteolytic breakdown rate of these molecules in the grafted area for a prolonged period of time (See also Equation (7.14)). Consequently, the concentration of the collagen molecules in the grafted area becomes substantially higher than the concentration of the collagen molecules in the surrounding uninjured dermal tissue before it gradually decreases toward the concentration of the collagen molecules in the surrounding uninjured dermal tissue. Furthermore, it is possible to reproduce the long term contraction and subsequent retraction of a skin graft, and the development of residual stresses within the dermal layer. These phenomena can be observed, respectively, in Figure 7.3 and Figure 7.4; both the displayed components of the displacement field and the displayed components of the effective strain tensor are not equal zero over the domain of computation at day 365, and the values of the individual components over the domain of computation at day 365 are roughly equal to the values of the individual components over the domain of computation at day 180. Looking at the individual components of the displacement velocity field in Figure 7.3, it can be observed that these have become approximately equal to zero over the domain of computation at day 365.

Focusing on the simulation of the contraction of skin grafts and the formation of contractures the following can be observed. Figure 7.5 shows a good match with respect to the evolution over time of the relative surface area of skin grafts between measurements obtained in a clinical study by El Hadidy *et al.* [2] and outcomes of computer simulations obtained in this study. In this study it was assumed that the rate at which the effective strain is changing actively over time is proportional to the product of the amount of effective strain, the local concentration of the MMPs, the local concentration of the signaling molecule and the inverse of the local concentration of the collagen molecules. The directions in which the effective strain changes, are determined by both the signs of the eigenvalues related to the effective strain tensor, and the directions of the associated eigenvectors. The good match between the gathered scar assessment data and the outcomes of the computer simulations suggests that this combination of relationships might describe appropriately in mathematical terms the mechanism underlying the formation of contractures.

If the mathematical description for the mechanism underlying the formation of contractures is indeed appropriate, then this suggests the following with respect to the main therapy that is used currently for the the prevention of contracture formation in skin

grafts. The main therapy in current usage focuses on counteracting the mechanical forces generated within the contracting graft by means of static splinting of the covered wound after placement of the graft [23]. How effective splinting therapy is in preventing contracture formation is actually unclear at the moment; it is a fact that contracture formation is still a common complication despite the frequent application of splinting therapy [26]. This could be a consequence of the fact that it is unclear at present what the optimal point in time is after placement of the skin graft to start with the therapy. Furthermore, it could be a consequence of the fact that it is also unclear how long the static splints have to be worn for the therapy to be effective. Looking at Equation (7.18), it is clear that the effective strain can change solely when the local concentration of the signaling molecules is unequal to zero. Given the presence of signaling molecules within the grafted area immediately after placement of the skin graft on its recipient bed, this implies that the optimal point in time to start with splinting therapy is directly after surgery. It is interesting to note that this implication matches nicely with the finding that early mechanical restraint of tissue-engineered skin leads to a reduction in the extent of contraction [6]. Furthermore, it is also evident that it is desirable to continue with splinting therapy until the concentration of the signaling molecules in the grafted area has become negligible such that the formation of contractures can be prevented.

Furthermore, Figure 7.5 shows that the difference in the evolution over time of the average of the relative surface areas of placed unmeshed skin grafts between grafts that are placed after early excision of the burnt skin and grafts that are placed after late excision of the burnt skin might be caused by both a change in the rate of morphoelastic change and a change in the degree of inhibition of the secretion of MMPs due to the presence of signaling molecules. In itself, this is an interesting observation. In addition, it provides some alternative ideas on how to diminish the degree of contracture formation that are not based on a mechanical intervention. As demonstrated in Figure 7.6, the final surface area of a skin graft can be increased by both a reduction in the rate of morphoelastic change, and a reduction in the inhibition of the secretion of MMPs due to the presence of signaling molecules. Within the investigated ranges of values, the former reduction has a huge impact on the final surface area whereas the latter reduction has a smaller impact on the final surface area. Perhaps that the reduction in the rate of morphoelastic change can be accomplished through the local inhibition of certain cross-linking enzymes. For instance, perhaps it is possible to use the chemical β-aminopropionitrile (BAPN) for the inhibition of the cross-linking enzyme lysyl oxidase, which is crucial for the stabilization of collagen fibrils [8, 33]. The reduction in the inhibition of the secretion of MMPs due to the presence of signaling molecules can be accomplished perhaps by influencing the regulation of the transcription of MMPs by signaling molecules such as TGF-β [18].

REFERENCES

[1] Desmoulière A, Geinoz A, Gabbiani F, Gabbiani G (1993) Transforming growth factor-β1 induces α-smooth muscle actin expression in granulation tissue myofibroblasts and in quiescent and growing cultured fibroblasts. J Cell Biol 122:103–111

[2] El Hadidy M, Tesauro P, Cavallini M, Colonna M, Rizzo F, Signorini M (1994) Con-

traction and growth of deep burn wounds covered by non-meshed and meshed split thickness skin grafts in humans. Burns 20:226–228

[3] Ghosh K, Pan Z, Guan E, Ge S, Liu Y, Nakamura T, Ren ZD, Rafailovich M, Clark R (2007) Cell adaptation to a physiologically relevant ECM mimic with different viscoelastic properties. Biomaterials 28:671–679

[4] Grotendorst G (1992) Chemoattractants and growth factors. In: Cohen I, Diegelmann R, Lindblad W (eds) Wound Healing: Biochemical and Clinical Aspects, 1st edn, W.B. Saunders, Philadelphia, Pennsylvania, chap 15, pp 237–246

[5] Hall C (2009) Modelling of some biological materials using continuum mechanics. PhD thesis, Queensland University of Technology

[6] Harrison C, MacNeil S (2008) The mechanism of skin graft contraction: An update on current research and potential future therapies. Burns 34:153–163

[7] HSL (2013) A collection of fortran codes for large scale scientific computation. URL http://www.hsl.rl.ac.uk

[8] Kagan H, Li W (2003) Lysyl oxidase: Properties, specificty, and biological roles inside and outside of the cell. J Cell Biochem 88:660–672

[9] Koppenol D, Vermolen F (2017) Biomedical implications from a morphoelastic continuum model for the simulation of contracture formation in skin grafts that cover excised burns. Biomech Model Mechanobiol DOI: 10.1007/s10237-017-0881-y

[10] Koppenol D, Vermolen F, Niessen F, Van Zuijlen P, Vuik K (2017) A mathematical model for the simulation of the formation and the subsequent regression of hypertrophic scar tissue after dermal wounding. Biomech Model Mechanobiol 16:15–32, DOI: 10.1007/s10237-016-0799-9

[11] Liang X, Boppart S (2010) Biomedical properties of *in vivo* human skin from dynamic optical coherence elastography. IEEE T Bio-Med Eng 57:953–959

[12] Madzvamuse A, Wathen A, Maini P (2003) A moving grid finite element method applied to a model biological pattern generator. J Comput Phys 190:478–500

[13] Maskarinec S, Franck C, Tirrell D, Ravichandran G (2009) Quantifying cellular traction forces in three dimensions. P Natl Acad Sci USA 106:22,108–22,113

[14] Möller M, Kuzmin D, Kourounis D (2008) Implicit FEM-FCT algorithms and discrete Newton methods for transient convection problems. Int J Numer Meth Fluids 57:761–792

[15] Moulin V, Castilloux G, Auger F, Garrel D, O'Connor-McCourt M, Germain L (1998) Modulated response to cytokines of human wound healing myofibroblasts compared to dermal fibroblasts. Exp Cell Res 238:283–293

[16] Murphy K, Hall C, Maini P, McCue S, McElwain D (2012) A fibrocontractive mechanochemical model of dermal wound closure incorporating realistic growth factor kinetics. B Math Biol 74:1143–1170

[17] Olsen L, Sherratt J, Maini P (1995) A mechanochemical model for adult dermal wound contraction and the permanence of the contracted tissue displacement profile. J Theor Biol 177:113–128

[18] Overall C, Wrana J, Sodek J (1991) Transcriptional and post-transcriptional regulation of 72-kda gelatinase/ type IV collagenase by transforming growth factor-β1 in human fibroblasts. J Biol Chem 266:14,064–14,071

[19] Patankar S (1980) Numerical Heat Transfer and Fluid Flow, 1st edn. McGraw-Hill, New York City, New York

[20] Persson PO, Strang G (2004) A simple mesh generator in MATLAB. SIAM Rev 46:329–345

[21] Ramtani S (2004) Mechanical modelling of cell/ECM and cell/cell interactions during the contraction of a fibroblast-populated collagen microsphere: theory and model simulation. J Biomech 37:1709–1718

[22] Ramtani S, Fernandes-Morin E, Geiger D (2002) Remodeled-matrix contraction by fibroblasts: numerical investigations. Comput Biol Med 32:283–296

[23] Richard R, Ward R (2005) Splinting strategies and controversies. J Burn Care Rehabil 26:392–396

[24] Roberts A, Sporn M, Assoian R, Smith J, Roche N, Wakefiled L, Heine U, Liotta L, Falanga V, Kehrl J, Fauci A (1986) Transforming growth factor type β: Rapid induction of fibrosis and angiogenesis *in vivo* and stimulation of collagen formation *in vitro*. P Natl Acad Sci USA 83:4167–4171

[25] Rudolph R, Vande Berg J (1991) The myofibroblast in Dupuytren's contracture. Hand Clin 7:683–692

[26] Schouten H, Nieuwenhuis M, Van Zuijlen P (2012) A review on static splinting therapy to prevent burn scar contracture: Do clinical and experimental data warrant its clinical application? Burns 38:19–25

[27] Sillman A, Quang D, Farboud B, Fang K, Nuccitelli R, Isseroff R (2003) Human dermal fibroblasts do not exhibit directional migration on collagen 1 in direct-current electric fields of physiological strength. Exp Dermatol 12:396–402

[28] Strutz F, Zeisberg M, Renziehausin A, Raschke B, Becker V, Van Kooten C, Muller G (2001) TGF-β1 induces proliferation in human renal fibroblasts via induction of basic fibroblast growth factor (FGF-2). Kidney Int 59:579–592

[29] The MathWorks Inc (2014) `MATLAB` version 8.3.0.532 (R2014a)

[30] Turek S (1998) FEATFLOW Finite element software for the incompressible Navier-Stokes equations: User Manual. University of Heidelberg, Heidelberg, Germany, 1st edn

[31] Van Kan J, Segal A, Vermolen F (2014) Numerical Methods in Scientific Computing, 2nd edn. Delft Academic Press, Delft, The Netherlands

[32] Vande Berg J, Rudolph R, Poolman W, Disharoon D (1989) Comparative growth dynamics and active concentration between cultured human myofibroblasts from granulating wounds and dermal fibroblasts from normal skin. Lab Invest 61:532–538

[33] Wilmarth K, Froines J (1992) In vitro and in vivo inhibition of lysyl oxidase by aminopropionitriles. J Toxicol Environ Health 37:411–423

[34] Wrobel L, Fray T, Molloy J, Adams J, Armitage M, Sparrow J (2002) Contractility of single human dermal myofibroblasts and fibroblasts. Cell Motil Cytoskelet 52:82–90

8

GENERAL CONCLUSIONS

In this thesis three mathematical models have been developed in order to investigate which components of the wound healing cascade influence the degree of wound contraction and the geometrical distribution of collagen bundles in scar tissue. Furthermore, a model has been developed in order to obtain insights into which components of the wound healing cascade might get disrupted during the formation of hypertrophic scar tissue. Finally, a model has been developed in order to obtain suggestions regarding how splinting therapy should be applied such that the therapy is effective optimally. In this chapter an overview of the most important conclusions that were drawn from the results obtained with these models, is presented.

8.1. CHAPTER 3

IN Chapter 3 a hybrid model has been presented that was used to study wound contraction and the development of the distribution of the collagen bundles in relatively small, deep dermal wounds. In this model cells are modeled as discrete, inelastic spheres while the other components are modeled as continuous entities. A tensorial approach was used for the representation of the collagen bundles. Solely the dermal layer of the skin is modeled explicitly and it is modeled as an anisotropic continuous linear elastic solid. Wound contraction and the development of residual forces are caused in the model through the incorporation of both temporary pulling forces which are generated by fibroblasts, and permanent plastic forces which are caused by the remodeling of the extracellular matrix. The newly secreted collagen molecules are secreted by the fibroblasts in their direction of movement.

Parts of this chapter are based on content of the articles "A mathematical model for the simulation of the formation and the subsequent regression of hypertrophic scar tissue after dermal wounding" [7], "A biomechanical mathematical model for the collagen bundle distribution-dependent contraction and subsequent retraction of healing dermal wounds" [6], "A mathematical model for the simulation of the contraction of burns" [5] and "Biomedical implications from a morphoelastic continuum model for the simulation of contracture formation in skin grafts that cover excised burns" [4].

After obtaining baseline simulation results, which demonstrated that certain components of the healing response such as the increase in the number of collagen bundles that ends up permanently oriented toward the center of the wound and parallel to the surface of the skin, can be reproduced quite reasonably, the impact of macrophage depletion and the application of a transforming growth factor-β receptor antagonist on both the degree of wound contraction and overall distribution of the collagen bundles were investigated.

In accordance with experimental observations, depletion of the macrophages in the model during the execution of the wound healing cascade results in a delayed healing of a wound. Furthermore, the depletion of the macrophages hardly influences the geometrical distribution of the collagen bundles in the recovering wounded area. However, the depletion does result in an increase of the final surface area of the recovered wounded area. Taken together, the simulation results suggest that total depletion of macrophages in a wounded area might be beneficial if the wound environment is sterile and rapid wound repair is not a high priority.

The imitation of the application of a transforming growth factor-β receptor antagonist in the model also results in an increase of the surface area of the recovering wounded area. In addition, the application of the antagonist results in a more uniform distribution of the collagen bundles in the recovered wounded area. These observations are also in accordance with experimental observations. Hence, the simulation results support the hypothesis that the application of a transforming growth factor-β receptor antagonist results in less compaction of a recovered wounded area and in less scarring [2].

8.2. CHAPTER 4

IN Chapter 4 a continuum hypothesis-based model has been presented that was used to investigate how certain components of the wound environment and the wound healing response might influence the contraction of the wound and the development of the geometrical distribution of collagen bundles in relatively large wounds. In this model all components are modeled as continuous entities. For the representation of the collagen bundles a tensorial approach was used again. Solely a portion of the dermal layer was included explicitly into the model. This portion of dermal layer is modeled as an orthotropic continuous solid with bulk mechanical properties that are locally dependent on both the local concentration and the local geometrical distribution of the collagen bundles. Wound contraction is caused in the model by temporary pulling forces. These pulling forces are generated by myofibroblasts which are present in the recovering wounded area. With respect to the dynamic regulation of the geometrical distribution of the collagen bundles, it was assumed that a portion of the collagen molecules are deposited and reoriented in the direction of movement of the (myo)fibroblasts. The remainder of the newly secreted collagen molecules are deposited by ratio in the direction of the present collagen bundles.

The simulation results show that the distribution of the collagen bundles influences the evolution over time of both the shape of the recovering wounded area and the degree of overall contraction of the wounded area. Interestingly, these effects are solely a consequence of alterations in the initial overall distribution of the collagen bundles, and not a consequence of alterations in the evolution over time of the different cell densities

and concentrations of the modeled constituents. In addition, the evolution over time of the shape of the wound is also influenced by the orientation of the collagen bundles relative to the position of the wound while this relative orientation does not influence the evolution over time of the relative surface area of the wound.

Furthermore, the simulation results show that ultimately the majority of the collagen molecules ends up permanently oriented toward the center of the wound and in the plane that runs parallel to the surface of the skin when the dependence of the direction of deposition / reorientation of collagen molecules on the movement of cells is included into the model. If this dependence is not included, then this will result ultimately in newly generated tissue with a collagen bundle-distribution that is exactly equal to the collagen-bundle distribution of the surrounding uninjured tissue.

The fact that an increased portion of the collagen bundles ultimately ends up permanently in the plane running parallel to the surface of the skin and the fact that the majority of these bundles is oriented toward the center of the wound when the dependence of the direction of deposition / reorientation of collagen molecules on the movement of cells is included into the model, are in accordance with experimental observations [12, 13]. This is an interesting observation. It is unknown at present which wound healing mechanisms cause these experimental observations. In the presented model the dynamics related to the geometrical distribution of the collagen bundles are dependent on the speed and the direction of movement of the (myo)fibroblasts. This direction and speed of movement are dependent subsequently on the gradient of the concentration of the signaling molecule and the evolution over time of the distribution of the cell densities. Hence, the results obtained with the presented model suggest that the geometrical distribution of collagen bundles in scar tissue can be altered by changing the gradient of the concentration of the signaling molecule and / or the evolution over time of the distribution of the cell densities during wound healing. Given that the geometrical distribution of the collagen bundles has a huge impact on the response of dermal tissues to mechanical forces [3, 14], this is an interesting hypothesis. It must be possible to investigate this hypothesis further by means of an experimental study with a tissue-equivalent.

8.3. CHAPTER 5

IN Chapter 5 a continuum hypothesis-based model has been presented that was used to investigate in more detail which elements of the healing response might have a substantial influence on the contraction of burns. That is, a factorial design combined with a regression analysis were used to quantify the individual contributions of variations in the values for certain parameters of the model to the dispersion in the surface area of healing burns. In this model all components are modeled as continuous entities. Solely a portion of the dermal layer was included explicitly into the model. The dermal layer is modeled as an isotropic compressible neo-Hookean solid. Wound contraction is caused in the model by temporary pulling forces. These pulling forces are generated by myofibroblasts which are present in the recovering wounded area.

Based on the outcomes of the sensitivity analysis it was concluded that most of the variability in the evolution of the surface area of healing burns over time might be attributed to variability in the apoptosis rate of myofibroblasts and, to a lesser extent, the secretion rate of collagen molecules. Hence, if one wishes to adjust the degree of wound

contraction during the healing of a burn, then the simulation results and the associated regression analysis presented in this study suggest that this may be accomplished by adjusting the apoptosis rate of myofibroblasts and / or the secretion rate of collagen molecules.

It is expected that varying the values for most of the remaining parameters of the model that were not included into the factorial design and for which a range of values could be found in the literature, would probably also contribute significantly to variability in the relative surface area of a healing burn. Varying the values for the proliferation rate of (myo)fibroblasts (r_F), the generated stress per unit cell density and the inverse of the unit collagen molecule concentration (ξ), and the constant E related to the Young's modulus within the found ranges of values in particular would probably also contribute considerably to variability in the evolution of the relative surface area of a healing burn over time. Therefore, it would interesting to add these parameters to the factorial design in order to quantify their contribution to this variability. However, given the complexity of the model and hence the necessary complexity of the custom-made numerical algorithm, it was decided to set the values for these parameters to fixed values within the found ranges during the generation of simulation results in order to prevent the total computation time of the sensitivity analysis from rising too high. A possible solution for this problem might be to switch to a different programming language that allows for faster computations such as `Fortran`, or to use the GPU computing possibilities of `MATLAB` [11]. Another possible solution might be to use a different factorial design in which not all combinations of levels for the factors of the factorial design are simulated [9, 10].

8.4. CHAPTER 6

IN Chapter 6 a continuum hypothesis-based model has been presented that was used to investigate what might cause the formation of hypertrophic scar tissue. All components of the model are modeled as continuous entities. Solely a portion of the dermal layer of the skin is modeled explicitly and it is modeled as an isotropic compressible neo-Hookean solid. In the model pulling forces are generated by the myofibroblasts that are present in the recovering wounded area. These pulling forces are responsible for both the compaction and the increased thickness of the recovering wounded area.

The comparison between the outcomes of the computer simulations obtained in this study and clinical measurements obtained by Nedelec *et al.* [8] shows that a relatively high apoptosis rate of myofibroblasts results in scar tissue that behaves like normal scar tissue with respect to the evolution of the thickness of the tissue over time, while a relatively low apoptosis rate results in scar tissue that behaves like hypertrophic scar tissue with respect to the evolution of the thickness of the tissue over time. Interestingly, this result is in agreement with the suggestion put forward by Desmoulière *et al.* [1] that the disruption of apoptosis (i.e., a low apoptosis rate) during wound healing might be an important factor in the development of pathological scarring. Hence, the results obtained with the presented model suggest that the thickness of scar tissue can be altered by changing the apoptosis rate of myofibroblasts.

8.5. CHAPTER 7

IN Chapter 7 a continuum hypothesis-based model has been presented that was used for the simulation of contracture formation in skin grafts that cover excised burns in order to obtain suggestions regarding the ideal length of splinting therapy and when to start with this therapy such that the therapy is effective optimally. All components of the model are modeled as continuous entities. Solely a portion of the dermal layer is modeled explicitly and it is modeled as an isotropic morphoelastic solid. In the model pulling forces are generated by the myofibroblasts which are present in the skin graft. These pulling forces are responsible for the compaction of the skin graft. Furthermore, the rate of active change of the effective strain, which determines the degree of contracture formation in the skin graft, is proportional to the product of the amount of effective strain, the local concentration of metalloproteinases, the local concentration of the signaling molecules and the inverse of the local concentration of the collagen molecules. The directions in which the effective strain changes, are determined by both the signs of the eigenvalues related to the effective strain tensor, and the directions of the associated eigenvectors.

Based on the simulation results obtained with the presented model it is suggested that the optimal point in time to start with splinting therapy is directly after placement of the skin graft on its recipient bed. Furthermore, the simulation results suggest that it is desirable to continue with splinting therapy until the concentration of the signaling molecules in the grafted area has become negligible such that the formation of contractures can be prevented.

REFERENCES

[1] Desmoulière A, Redard M, Darby I, Gabbiani G (1995) Apoptosis mediates the decrease in cellularity during the transition between granulation tissue and scar. Am J Pathol 146:56–66

[2] Huang J, Wang Y, Ling T, Chuang S, Johnson F, Huang S (2002) Synthetic TGF-beta antagonist accelerates wound healing and reduces scarring. FASEB J 16:1269–1270

[3] Jor J, Nash M, Nielsen P, Hunter P (2011) Estimating material parameters of a structurally based constitutive relation for skin mechanics. Biomech Model Mechanobiol 10:767–778

[4] Koppenol D, Vermolen F (2017) Biomedical implications from a morphoelastic continuum model for the simulation of contracture formation in skin grafts that cover excised burns. Biomech Model Mechanobiol DOI: 10.1007/s10237-017-0881-y

[5] Koppenol D, Vermolen F, Koppenol-Gonzalez G, Niessen F, Van Zuijlen P, Vuik K (2016) A mathematical model for the simulation of the contraction of burns. J Math Biol DOI: 10.1007/s00285-016-1075-4

[6] Koppenol D, Vermolen F, Niessen F, Van Zuijlen P, Vuik K (2017) A biomechanical mathematical model for the collagen bundle distribution-dependent contraction and subsequent retraction of healing dermal wounds. Biomech Model Mechanobiol 16:345–361, DOI: 10.1007/s10237-016-0821-2

[7] Koppenol D, Vermolen F, Niessen F, Van Zuijlen P, Vuik K (2017) A mathematical model for the simulation of the formation and the subsequent regression of hypertrophic scar tissue after dermal wounding. Biomech Model Mechanobiol 16:15–32, DOI: 10.1007/s10237-016-0799-9

[8] Nedelec B, Correa J, De Oliveira A, LaSalle L, Perrault I (2014) Longitudinal burn scar quantification. Burns 40:1504–1512

[9] Phadke M (1989) Quality Engineering Using Robust Design, 1st edn. Prentice-Hall, Englewood Cliffs, New Jersey

[10] Taguchi G (1987) System of Experimental Design, 1st edn. UNIPUB Kraus International Publications, New York City, New York

[11] The MathWorks Inc (2014) MATLAB version 8.3.0.532 (R2014a)

[12] Van Zuijlen P, Ruurda J, Van Veen H, Van Marle J, Van Trier A, Groenevelt F, Kreis R, Middelkoop E (2003) Collagen morphology in human skin and scar tissue: no adaptation in response to mechanical loading at joints. Burns 29:423–431

[13] Welch M, Odland G, Clark R (1990) Temporal relationships of *F*-actin bundle formation, collagen and fibronectin matrix assembly, and fibronectin receptor expression to wound contraction. J Cell Biol 110:133–145

[14] Wilkes G, Brown I, Wildnauer R (1973) The biomechanical properties of skin. CRC Crit Rev Bioeng 1:453–495

9

RECOMMENDATIONS

In this chapter several possibilities are discussed to adjust the morphoelastic continuum model that has been presented in Chapter 7. In addition, several possibilities are discussed how certain components of the models developed in the previous chapters could be combined such that it becomes possible to investigate new phenomena that can be observed during the (aberrant) healing of dermal wounds. Subsequently, a short discussion is presented about the way the cell differentiation of fibroblasts into myofibroblasts has been incorporated into the presented models, and about which cell type causes the compaction of the wounded area in these models. Based on this latter discussion, recommendations are presented about what is needed for the further development of accurate computational models that can be used for the rigorous investigation of these processes.

9.1. MODEL ADAPTATIONS

THE fact that it is possible to simulate the formation of contractures with the morphoelastic continuum model presented in Chapter 7, makes this model very attractive. Obviously, the model could be adjusted in many different ways. For instance, next to the simulation of contracture formation in skin grafts, the model could also be used for the simulation of the healing of dermal wounds that heal by secondary intention alone (i.e., without the placement of a skin graft). The only element of the model that needs to be adjusted is the initial condition for the collagen molecules presented in Equation (7.22). Furthermore, it is also easy to obtain computer simulations with the presented model for wounded areas with a different shape and / or surface area. The only element of the model that needs to be altered in this case is the function presented in Equation (7.21). Especially when more detailed experimental measurement data about the evolution over time of the shapes of wounds become available in the scientific literature, it

Parts of this chapter are based on content of the articles "A biomechanical mathematical model for the collagen bundle distribution-dependent contraction and subsequent retraction of healing dermal wounds" [16], "A mathematical model for the simulation of the contraction of burns" [15] and "Biomedical implications from a morphoelastic continuum model for the simulation of contracture formation in skin grafts that cover excised burns" [14].

will become interesting to investigate to what extent the presented model can replicate such measurement data.

If the model is used for the simulation of the healing of dermal wounds that heal by secondary intention alone, then an explicit description of other subprocesses that take place during the proliferative phase of the wound healing cascade such as angiogenesis and reepithelialization could also be incorporated into the model. The incorporation of the former subprocess is probably also interesting when the formation of contractures in skin grafts is simulated. Adding angiogenesis to the model presented in Chapter 7 could be accomplished, for instance, by connecting elements of the models developed by Byrne *et al.* [4, 22, 23] with the components of the morphoelastic continuum model. Incorporation of the reepithelialization process could be accomplished, for instance, by using elements of the model developed by Mennon *et al.* [17]. Furthermore, the (bio)chemical components of the morphoelastic model could be replaced with the (bio)chemical components of the model presented in Chapter 3. This will turn the morphoelastic model into a hybrid model wherein elements of the inflammatory response are incorporated. Through the incorporation of these additional subprocesses into the model, it becomes possible to study the interactions between the components of the different subprocesses, and to investigate if an aberrant interaction between these components might result in the replication of certain characteristics of sequelae such as hypertrophic scar tissue formation and contracture formation. However, due to the incorporation of more components into the model the number of parameters usually also increases considerably. Given that it is often very complicated to obtain accurate estimates for the values of the parameters of models for the simulation of certain aspects of dermal wound healing (See also Section 9.3 for further discussion about this issue), this is a clear disadvantage of adding more components to a model.

Therefore, it is also interesting to look at how certain components of the model could be adjusted without the introduction of many new parameters. For instance, assumptions were made which made it possible to perform the calculations on an infinitely thin slice of dermal layer oriented parallel to the surface of the skin. An obvious benefit of this is that this results in a serious reduction of the computation times. Furthermore, it avoids the need to deal with a boundary that can move freely (as is the case in the model that has been presented in Chapter 6). However, it is probably very interesting to investigate in a three-dimensional portion of dermal layer what would happen to the compaction and subsequent (partial) dilatation of a wounded area. For this end, the main adaptations to the model would be the removal of the assumptions made in Section 7.2.5, and the introduction of additional boundary conditions for the interfaces between the epidermis and the dermis, and the subcutaneous tissue and the dermis. In a three-dimensional setting, the spring-like boundary conditions presented in Equation (6.25) could be used, for instance, to describe the attachment of the dermal tissue to the subcutaneous tissue and the adjacent dermal tissue. It is probably a good idea to assume first that the domain of computation is, for instance, axisymmetric (where the symmetry axis runs perpendicular to the surface of the skin) so that the calculations can be performed on a half-plane through the symmetry axis, before trying to obtain simulation results with an arbitrarily shaped three-dimensional domain of computation. In a three-dimensional setting it might also be interesting to investigate the possibility of using the

recently developed isogeometric analysis instead of a finite element analysis [5].

Sometimes the formation of hypertrophic scar tissue also coincides with the formation of contractures [11]. If a three-dimensional portion of dermal layer is simulated, then it becomes possible probably to investigate under which circumstances contractures form and under which circumstances the thickness of the dermal layer resembles the thickness of the dermal layer in hypertrophic scar tissue. Furthermore, it becomes possible to investigate under which circumstances both sequelae develop at the same time (albeit perhaps at different locations).

In the model developed in Chapter 7 it was assumed that the effective strains are small. Consequently, the evolution equation that describes the dynamic change of the infinitesimal effective strain over time was used (i.e., Equation (7.1c)). However, just like in the models developed in Chapter 5 and Chapter 6, it might actually be more appropriate to assume that the effective strains can become arbitrary large. If this assumption is made, then Equation (7.1c) can be replaced with the following evolution equation that gives a description of the dynamic change of the Eulerian finite effective strain (**e**) over time (See Section 2.5 for a definition of the tensor **A** and see Section 7.2 for a definition of the tensor **G** and the tensor **L**) [9]:

$$\frac{\mathrm{D}\mathbf{e}}{\mathrm{D}t} = \mathrm{sym}\left(\mathbf{B}^{-1}\mathbf{L} - \frac{1}{\sqrt{\det\left(\mathbf{B}^{-1}\right)}}\mathbf{B}^{-1}\mathbf{G}\right), \tag{9.1}$$

where

$$\mathbf{B} = \left[\mathbf{I} - 2\mathbf{e}\right]^{-1}, \tag{9.2}$$

and

$$\mathbf{e} = \frac{1}{2}\left\{\mathbf{I} - \left[\mathbf{A}^{-1}\right]^{2}\right\}. \tag{9.3}$$

Next, the constitutive relation presented in Equation (7.15) could be replaced with, for instance, the following constitutive relation:

$$\begin{aligned}\sigma = {} & \mu_1 \mathrm{sym}(\mathbf{L}) + \mu_2 \left[\mathrm{tr}\left(\mathrm{sym}(\mathbf{L})\right)\mathbf{I}\right] + \\ & \left\{\left\{\frac{E(\rho)}{2\left[1-2\nu\right]}\right\}\left[\sqrt{\det(\mathbf{B})} - 1\right]\right\}\mathbf{I} + \left\{\frac{E(\rho)}{2\left[1+\nu\right]}\right\}\left[\sqrt{\det(\mathbf{B})}\right]^{-\frac{5}{3}}\left[\mathbf{B} - \frac{1}{3}\mathrm{tr}(\mathbf{B})\,\mathbf{I}\right].\end{aligned} \tag{9.4}$$

Here μ_1 is the shear viscosity, μ_2 is the bulk viscosity, ν is Poisson's ratio, $E(\rho)$ is the Young's modulus and **I** is the second-order identity tensor. Please note that the elastic component of the constitutive relation is basically equal to constitutive relation presented in Equation (5.12). Whether the relation presented in Equation (9.4) is appropriate or not, remains to be seen. Unfortunately, accurate constitutive stress-strain relations for skin tissues such as granulation tissue, dermal tissue and scar tissue have not been formulated yet [6]. Looking, for instance, at the studies by Bischoff *et al.* [2] and Jor *et al.* [13], it is clear that progress is made. However, we are not there yet.

Another interesting way in which the mechanical component of the model can be adjusted in the following. Due to the organization of the collagen molecules into interconnected sheets and bundles, the geometrical distribution of the collagen bundles in particular has a huge impact on the response of dermal tissues to mechanical forces [13]. In order to incorporate this effect into the model presented in Chapter 7, the tensorial approach presented in Chapter 4 could be used for the representation of collagen bundles, and the constitutive stress-strain relation presented in Equation (7.15) could be replaced with the constitutive relation derived in Chapter 4. Furthermore, Equation (4.13) could be used for the description of the dynamic change of the geometrical distribution of the collagen bundles. Due to these adaptations to the model presented in Chapter 7, it becomes possible to study the impact of tissue anisotropy on the formation of contractures.

If the tensorial approach is used for the representation of the collagen bundles, then it is also relatively simple to make the direction of cell movement also dependent on the orientation of the collagen bundles. Previous experimental studies have demonstrated that fibroblasts align with collagen bundles, which subsequently influences the direction of movement of these cells [8]. In order to incorporate this effect into the model, Equation (7.5) and Equation (7.6) could be replaced with, for instance,

$$\mathbf{J}_N = \Omega^c \left[-D_F F \nabla N + \chi_F N \nabla c \right], \tag{9.5}$$

$$\mathbf{J}_M = \Omega^c \left[-D_F F \nabla M + \chi_F M \nabla c \right]. \tag{9.6}$$

where

$$\Omega^c = \left[1 - \frac{\mathrm{tr}\,(\Omega^\rho)}{a_\rho^I + \mathrm{tr}\,(\Omega^\rho)} \right] \mathbf{I} + \left[\frac{\mathrm{tr}\,(\Omega^\rho)}{a_\rho^I + \mathrm{tr}\,(\Omega^\rho)} \right] \hat{\Omega}^\rho. \tag{9.7}$$

Here $\mathbf{I}$ is the second-order identity tensor, the tensor Ω^ρ represents the collagen bundles, $\hat{\Omega}^\rho$ represents the tensor related to the collagen bundles with rows normalized to a length of one, and the value for the parameter a_ρ^I determines the haptotactic sensitivity of the cells.

Furthermore, Verhaegen *et al.* [26] have demonstrated that stretching of both healthy skin and scar tissue induces permanent adaptation of the orientation of the collagen bundles in these tissues. Therefore, it might be interesting to incorporate into the model the reorientation of collagen bundles due to forces. This could be accomplished perhaps by absorbing into the model some of the ideas that were used for the development of the model by Olsen *et al.* [21]. Due to this latter adjustment, it would become possible to investigate the interaction between the adaptation of the geometrical distribution of the collagen bundles due to cell fluxes and the adaptation of the geometrical distribution of the collagen bundles due to forces.

9.2. FIBROBLAST DIFFERENTIATION & PULLING FORCES

IT is interesting to look at the way that the cell differentiation of fibroblasts into myofibroblasts has been incorporated into the presented models, and to look at which cell type causes the compaction of the wounded area in these models. Just like in the

model developed by Olsen *et al.* [20], it is assumed in the models presented in Chapters 4 through 7 that the rate of cell differentiation is dependent on the concentration of the signaling molecule with no cell differentiation taking place in the absence of this signaling molecule. However, if the signaling molecule represents transforming growth factor-β, then the stimulation to differentiate by these signaling molecules is only effective in the presence of particular isoforms of fibronectin [24]. In addition, experimental studies have demonstrated that the differentiation of the cells solely takes place under conditions of sufficient mechanical stiffness [28]. At present it is actually unclear what the true stiffness is that is perceived by fibroblasts. Given that the (prolonged) presence of myofibroblasts in the wounded area probably plays an important role in the development of sequelae, it is interesting to investigate the cell differentiation of fibroblasts into myofibroblasts in more detail in order to obtain, for instance, insights regarding the perceived stiffness by fibroblasts. For this end, models such as the ones developed in this study could be used. Certain elements of the models developed by Murphy *et al.* [18] and Valero *et al.* [25], for instance, could be used for the mathematical description of the cell differentiation mechanism wherein the rate of differentiation is influenced by the mechanical environment.

In the model that has been presented in Chapter 3, wound contraction is caused by temporary pulling forces that are generated by fibroblasts, while in the models that have been presented in Chapters 4 through 7 wound contraction is caused by temporary pulling forces that are generated by myofibroblasts. Two theories exist that can both explain the compaction of a wounded area. On the one hand, there is the fibroblast theory [10] while on the other hand, there is the myofibroblast theory [7]. According to the fibroblast theory, the compaction of a wounded area is accomplished through many individual fibroblasts that exert forces on the collagen bundles as they migrate into the wounded area. According to the myofibroblast theory, the myofibroblasts within the wounded area align along the tension lines of the skin [12]. Subsequently the pseudopodia of the myofibroblasts extend, then the cytoplasmic actins of the myofibroblasts bind, with aid of integrins, to extracellular fibronectins, which are attached to the collagen bundles, and finally the pseudopodia retract. Taken together, this results in inward drawing of the collagen bundles and hence the compaction of the wounded area in the directions of the tension lines of the skin. At this moment it is impossible to determine *in vivo* which theory is correct. It might be the case that both theories are correct. Perhaps both fibroblasts and myofibroblasts are involved in the compaction of dermal wounds, but perhaps at different times and at different places. Given the impossibility to determine at present how wound contraction is realized *in vivo*, and given that a better understanding of this process probably improves the treatment of dermal wounds, it is very interesting to investigate this process in more detail with models such as the ones presented in this thesis.

9.3. VERIFICATION, CALIBRATION & VALIDATION

In order to investigate the processes discussed in the previous section rigorously with mathematical models, accurate (i.e., verified, calibrated and validated) computational (i.e., numerical) models are needed. With the results obtained in this study such as the custom-made numerical algorithms and the developed models, some progress has been

made toward the construction of such accurate computational models. However, we are not there yet. A few years ago an excellent editorial on the development of accurate computational models for the medical clinic has been written by Viceconti *et al.* [27]. Here a short summary of the most relevant parts of this editorial in the context of this thesis is presented. Based on this summary, recommendations are presented for the further development of accurate computational models.

It all starts with the selection of a proper model and the determination of the right element(s) of reality that one wishes to investigate. Basically, a model is a manifestation of a particular scientific theory cast in mathematical formulas that is intended to provide a meaningful abstraction of reality. For each theoretical framework, there are in principle infinitely many models that differ from each other with respect to such things as the number of included components, the number of parameters, boundary conditions and so on. Obviously, it is important to select that model that allows for the proper investigation of the element(s) of reality that one wishes to examine.

Subsequently, it is important to verify that the mathematical model is approximated accurately by the discrete computational model. Next, it is important to assure that the number of parameters of the model is not too large and to obtain accurate estimates for the values for these parameters. In general, it is very difficult to obtain such accurate estimates. In addition, it is often impossible to obtain estimates for some of the parameters of the model. Finally, the obtained simulation results need to be validated against controlled experimental measurements.

Based on the processes that have been discussed in the previous section, it is clear that the models that have been developed during this study need to be adjusted such that it becomes possible to investigate these processes. For instance, given that the cell differentiation of fibroblasts into myofibroblasts depends critically on the presence of particular isoforms of fibronectin and a sufficiently stiff environment, these dependencies need to be incorporated into a model.

In this study the accuracy of the developed custom-made numerical algorithms was investigated to some extent. For instance, with some of the algorithms the computations were repeated a few times with gradually refined triangulations. It was observed that the differences between the obtained results were small. This provides some confidence about the accuracy of the obtained approximations with these algorithms. However, in order to increase the confidence in the accuracy of the approximations and obtain estimates for the made approximation errors, more rigorous analyses should be performed.

Unfortunately, it was impossible to obtain accurate estimates for the values for most parameters of the models. Furthermore, it was impossible to find any value for some parameters. Likewise, it was also very difficult to find proper experimental measurement data for the validation of the obtained simulation results. As is also pointed out by Bowden *et al.* [3], this is a fundamental problem in the field of mathematical modeling of dermal wound healing processes. Some of the simulation results presented in Chapters 5 through 7 could be validated against measurement data obtained with clinical / experimental studies. However, it would have been very valuable to validate the simulation results obtained with these models against both more experimental data and against experimental data of a different kind such as cell density profiles and collagen molecule concentration profiles. If this could be done, then this would seriously increase our con-

fidence in the validity of these models. Hence, there is a clear need for suitable experimental data for the validation of the models.

In my opinion, the issues discussed in the preceding paragraphs demonstrate clearly that a close collaboration between experimental scientists, computational scientists and mathematicians is essential for the further development of accurate mathematical models: with aid of adequate experimental data generated by experimental scientists and, for instance, a Bayesian framework for the calibration and the validation of verified computational models developed by computational scientists and mathematicians, these models can be constructed [1, 19]. Once these models are there, they can assist the experimental scientist, for instance, with disentangling which cell type is responsible for the compaction of a wounded area at a certain location and at a certain point in time. The construction of such models might take a while, but I am confident that it can be done.

REFERENCES

[1] Babuška I, Nobile F, Tempone R (2008) A systematic approach to model validation based on Bayesian updates and prediction related rejection criteria. Comput Methods Appl Mech Eng 197:2517–2539

[2] Bischoff J, Arruda E, Grosh K (2004) A rheological network model for the continuum anisotropic and viscoelastic behavior of soft tissue. Biomech Model Mechan 3:56–65

[3] Bowden L, Byrne H, Maini P, Moulton D (2016) A morphoelastic model for dermal wound closure. Biomech Model Mechanobiol 15:663–681

[4] Byrne H, Chaplain M, Evans D, Hopkinson J (2000) Mathematical modeling of angiogenesis in wound healing. J Theor Med 2:175–197

[5] Cottrell J, Hughes T, Bazilevs Y (2009) Isogeometric Analysis: Toward Integration of CAD and FEA, 1st edn. John Wiley & Sons, Hoboken, New Jersey

[6] Fung Y (1993) Biomechanics, 2nd edn. Springer Science & Business Media, Berlin, Germany

[7] Gabbiani G, Ryan G, Majno G (1971) Presence of modified fibroblasts in granulation tissue and their possible role in wound contraction. Experientia 27:549–555

[8] Guido S, Tranquillo R (1993) A methodology for the systematic and quantitative study of cell contact guidance in oriented collagen gels: Correlation of fibroblast orientation and gel birefringence. J Cell Sci 105:317–331

[9] Hall C (2009) Modelling of some biological materials using continuum mechanics. PhD thesis, Queensland University of Technology

[10] Harris A, Stopak D, Wild P (1981) Fibroblast traction as a mechanism for collagen morphogenesis. Nature 290:249

[11] Hawkins H, Finnerty C (2012) Pathophysiology of the burn scar. In: Herndon D (ed) Total Burn Care, 4th edn, Elsevier Inc, Philadelphia, Pennsylvania, chap 45, pp 507–516.e3

[12] Hinz B (2007) Formation and function of the myofibroblast during tissue repair. J Invest Dermatol 127:526–537

[13] Jor J, Nash M, Nielsen P, Hunter P (2011) Estimating material parameters of a structurally based constitutive relation for skin mechanics. Biomech Model Mechanobiol 10:767–778

[14] Koppenol D, Vermolen F (2017) Biomedical implications from a morphoelastic continuum model for the simulation of contracture formation in skin grafts that cover excised burns. Biomech Model Mechanobiol DOI: 10.1007/s10237-017-0881-y

[15] Koppenol D, Vermolen F, Koppenol-Gonzalez G, Niessen F, Van Zuijlen P, Vuik K (2016) A mathematical model for the simulation of the contraction of burns. J Math Biol DOI: 10.1007/s00285-016-1075-4

[16] Koppenol D, Vermolen F, Niessen F, Van Zuijlen P, Vuik K (2017) A biomechanical mathematical model for the collagen bundle distribution-dependent contraction and subsequent retraction of healing dermal wounds. Biomech Model Mechanobiol 16:345–361, DOI: 10.1007/s10237-016-0821-2

[17] Mennon S, Flegg J, McCue S, Schugart R, Dawson R, McElwain D (2012) Modelling the interaction of keratinocytes and fibroblasts during normal and abnormal wound healing processes. Proc R Soc B 279:3329–3338

[18] Murphy K, Hall C, Maini P, McCue S, McElwain D (2012) A fibrocontractive mechanochemical model of dermal wound closure incorporating realistic growth factor kinetics. B Math Biol 74:1143–1170

[19] Oden J, Hawkins A, Prudhomme S (2010) General diffuse-interface theories and an approach to predictive tumor growth modeling. Math Models Methods Appl Sci 20:477–517

[20] Olsen L, Sherratt J, Maini P (1995) A mechanochemical model for adult dermal wound contraction and the permanence of the contracted tissue displacement profile. J Theor Biol 177:113–128

[21] Olsen L, Maini P, Sherratt J, Dallon J (1999) Mathematical modelling of anisotropy in fibrous connective tissue. Math Biosci 158:145–170

[22] Pettet G, Byrne H, McElwain D, Norbury J (1996) A model of wound-healing angiogenesis in soft tissue. Math Biosci 136:35–63

[23] Pettet G, Chaplain M, McElwain D, Byrne H (1996) On the role of angiogenesis in wound healing. Proc R Soc B 263:1487–1493

[24] Serini G, Bochaton-Piallat M, Ropraz P, Geinoz A, Borsi L, Zardi L, Gabbiani G (1998) The fibronectin domain ED-A is crucial for myofibroblastic phenotype induction by transforming growth factor-beta1. J Cell Biol 142:873–881

[25] Valero C, Javierre E, García-Aznar J, Gómez-Benito M (2014) A cell-regulatory mechanism involving feedback between contraction and tissue formation guides wound healing progression. PLoS ONE 9:e92,774

[26] Verhaegen P, Schouten H, Tigchelaar-Gutter W, Van Marle J, Van Noorden C, Middelkoop E, Van Zuijlen P (2012) Adaptation of the dermal collagen structure of human skin and scar tissue in response to stretch: an experimental study. Wound Repair Regen 20:658–666

[27] Viceconti M, Olsen S, Nolte LP, Burton K (2005) Extracting clinically relevant data from finite element simulations. Clin Biomech 20:451–454

[28] Van de Water L, Varney S, Tomasek J (2013) Mechanoregulation of the myofibroblast in wound contraction, scarring, and fibrosis: Opportunities for new therapeutic intervention. Adv Wound Care 2:122–141

A

DERIVATION OF THE GENERAL FINITE-ELEMENT APPROXIMATION

IN this appendix, the general finite-element approximation of the solution for the primary model variables from Equation (7.1) is presented. In order to derive the general finite-element approximation, Equation (7.1b) was rewritten as a systems of equations, using the assumptions described in Section 7.2.5:

$$\begin{cases} v_1 = 0, & \text{(A.1)} \\ \dfrac{\mathrm{D}(\rho_t v_2)}{\mathrm{D}t} + \rho_t v_2 \left[\nabla \cdot \mathbf{v}\right] = \nabla \cdot \sigma_{\cdot 2} + f_2, & \text{(A.2)} \\ \dfrac{\mathrm{D}(\rho_t v_3)}{\mathrm{D}t} + \rho_t v_3 \left[\nabla \cdot \mathbf{v}\right] = \nabla \cdot \sigma_{\cdot 3} + f_3, & \text{(A.3)} \end{cases}$$

where

$$\sigma = \begin{bmatrix} \sigma_{11} & \sigma_{12} & \sigma_{13} \\ \sigma_{21} & \sigma_{22} & \sigma_{23} \\ \sigma_{31} & \sigma_{32} & \sigma_{33} \end{bmatrix} = \begin{bmatrix} \sigma_{\cdot 1} & \sigma_{\cdot 2} & \sigma_{\cdot 3} \end{bmatrix}, \quad \text{and} \quad \mathbf{f} = \begin{bmatrix} f_1 \\ f_2 \\ f_3 \end{bmatrix}. \tag{A.4}$$

Equation (7.1c) was also rewritten as a system of equations, using again the assumptions described in Section 7.2.5. Furthermore, the term $\epsilon_{ij}\left[\nabla \cdot \mathbf{v}\right]$ for $i, j \in \{2,3\}$ was added to the left hand side (LHS) and the right hand side (RHS) of these evolution equations. That is, to the evolution equation that describes the dynamic change of ϵ_{22} the term $\epsilon_{22}\left[\nabla \cdot \mathbf{v}\right]$ was added to the LHS and to the RHS, to the evolution equation that describes the dynamic change of ϵ_{23} the term $\epsilon_{23}\left[\nabla \cdot \mathbf{v}\right]$ was added to the LHS and to the RHS, and so on. Finally, the individual equations of the system were rewritten (where use was made of the fact that the effective strain tensor is symmetric for all time t), in order to obtain:

A

$$\begin{cases} \epsilon_{11} = \epsilon_{12} = \epsilon_{21} = \epsilon_{13} = \epsilon_{31} = 0, & \text{(A.5)} \\ \dfrac{\mathrm{D}\epsilon_{22}}{\mathrm{D}t} + \epsilon_{22}[\nabla\cdot\mathbf{v}] = [1-\epsilon_{33}]\dfrac{\partial v_2}{\partial y} + \epsilon_{22}\dfrac{\partial v_3}{\partial z} + \dfrac{1}{2}\left[\dfrac{\partial v_2}{\partial z} - \dfrac{\partial v_3}{\partial y}\right][\epsilon_{23}+\epsilon_{32}] - G_{22}, & \text{(A.6)} \\ \dfrac{\mathrm{D}\epsilon_{23}}{\mathrm{D}t} + \epsilon_{23}[\nabla\cdot\mathbf{v}] = \epsilon_{23}\left[\dfrac{\partial v_2}{\partial y} + \dfrac{\partial v_3}{\partial z}\right] + \dfrac{1}{2}\left\{[1-2\epsilon_{22}]\dfrac{\partial v_2}{\partial z} + [1-2\epsilon_{33}]\dfrac{\partial v_3}{\partial y}\right\} - G_{23}, & \text{(A.7)} \\ \dfrac{\mathrm{D}\epsilon_{33}}{\mathrm{D}t} + \epsilon_{33}[\nabla\cdot\mathbf{v}] = [1-\epsilon_{22}]\dfrac{\partial v_3}{\partial z} + \epsilon_{33}\dfrac{\partial v_2}{\partial y} - \dfrac{1}{2}\left[\dfrac{\partial v_2}{\partial z} - \dfrac{\partial v_3}{\partial y}\right][\epsilon_{23}+\epsilon_{32}] - G_{33}, & \text{(A.8)} \\ \epsilon_{32} = \epsilon_{23}, & \text{(A.9)} \end{cases}$$

where

$$\mathbf{G} = \begin{bmatrix} G_{11} & G_{12} & G_{13} \\ G_{21} & G_{22} & G_{23} \\ G_{31} & G_{32} & G_{33} \end{bmatrix} = \begin{bmatrix} G_{11} & G_{21} & G_{31} \\ G_{21} & G_{22} & G_{32} \\ G_{31} & G_{32} & G_{33} \end{bmatrix}. \tag{A.10}$$

Next, the weak formulations of Equation (7.1a), Equation (A.2) and Equation (A.3) were derived. For this end, these equations were multiplied by a test function $\eta(\mathbf{x},t) \in H^1(\Omega_{\mathbf{x},t}),\ t\in[0,T]$, where T is the total simulation time, first. Subsequently, the equations were integrated over the domain of computation and Green's first identity was applied. Taken together this results in the following:

$$\int_{\Omega_{\mathbf{x},t}} \left\{\eta\frac{\mathrm{D}z_i}{\mathrm{D}t} + \eta z_i[\nabla\cdot\mathbf{v}]\right\}\mathrm{d}\Omega_{\mathbf{x},t} = \int_{\Omega_{\mathbf{x},t}} \left[\nabla\eta\cdot\mathbf{J}_i + \eta R_i\right]\mathrm{d}\Omega_{\mathbf{x},t} - \int_{\partial\Omega_{\mathbf{x},t}} \eta\,[\mathbf{J}_i\cdot\mathbf{n}]\,\mathrm{d}\Gamma_{\mathbf{x},t}, \tag{A.11}$$

$$\rho_t\int_{\Omega_{\mathbf{x},t}} \left\{\eta\frac{\mathrm{D}v_2}{\mathrm{D}t} + \eta v_2[\nabla\cdot\mathbf{v}]\right\}\mathrm{d}\Omega_{\mathbf{x},t} = \int_{\Omega_{\mathbf{x},t}} \left[\eta f_2 - \nabla\eta\cdot\sigma_{\cdot 2}\right]\mathrm{d}\Omega_{\mathbf{x},t} + \int_{\partial\Omega_{\mathbf{x},t}} \eta\,[\sigma_{\cdot 2}\cdot\mathbf{n}]\,\mathrm{d}\Gamma_{\mathbf{x},t}, \tag{A.12}$$

$$\rho_t\int_{\Omega_{\mathbf{x},t}} \left\{\eta\frac{\mathrm{D}v_3}{\mathrm{D}t} + \eta v_3[\nabla\cdot\mathbf{v}]\right\}\mathrm{d}\Omega_{\mathbf{x},t} = \int_{\Omega_{\mathbf{x},t}} \left[\eta f_3 - \nabla\eta\cdot\sigma_{\cdot 3}\right]\mathrm{d}\Omega_{\mathbf{x},t} + \int_{\partial\Omega_{\mathbf{x},t}} \eta\,[\sigma_{\cdot 3}\cdot\mathbf{n}]\,\mathrm{d}\Gamma_{\mathbf{x},t}, \tag{A.13}$$

with $\mathbf{n}$ the unit outward pointing normal vector to the boundary of the domain of computation. Next, the product rule of differentiation was applied on the first term of the integrands on the LHS of the above equations and Reynold's transport theorem was used on the LHS of the above equations. Taken together this results in the following weak formulations. Find $z_i(\mathbf{x},t) \in H^1(\Omega_{\mathbf{x},t}),\ t\in[0,T]$ for $i\in\{N,M,c,\rho\}$, $v_2(\mathbf{x},t)\in H^1(\Omega_{\mathbf{x},t}),\ t\in[0,T]$ and $v_3(\mathbf{x},t)\in H^1(\Omega_{\mathbf{x},t}),\ t\in[0,T]$ such that

$$\frac{\mathrm{d}}{\mathrm{d}t}\int_{\Omega_{\mathbf{x},t}} \eta z_i\mathrm{d}\Omega_{\mathbf{x},t} = \int_{\Omega_{\mathbf{x},t}} \left[\nabla\eta\cdot\mathbf{J}_i + \eta R_i + z_i\frac{\mathrm{D}\eta}{\mathrm{D}t}\right]\mathrm{d}\Omega_{\mathbf{x},t} - \int_{\partial\Omega_{\mathbf{x},t}} \eta\,[\mathbf{J}_i\cdot\mathbf{n}]\,\mathrm{d}\Gamma_{\mathbf{x},t}, \tag{A.14}$$

$$\rho_t \frac{\mathrm{d}}{\mathrm{d}t} \int\limits_{\Omega_{\mathbf{x},t}} \eta v_2 \mathrm{d}\Omega_{\mathbf{x},t} = \int\limits_{\Omega_{\mathbf{x},t}} \left[\eta f_2 - \nabla\eta \cdot \sigma_{\cdot 2} + v_2 \frac{\mathrm{D}\eta}{\mathrm{D}t} \right] \mathrm{d}\Omega_{\mathbf{x},t} + \int\limits_{\partial\Omega_{\mathbf{x},t}} \eta \left[\sigma_{\cdot 2} \cdot \mathbf{n} \right] \mathrm{d}\Gamma_{\mathbf{x},t}, \tag{A.15}$$

$$\rho_t \frac{\mathrm{d}}{\mathrm{d}t} \int\limits_{\Omega_{\mathbf{x},t}} \eta v_3 \mathrm{d}\Omega_{\mathbf{x},t} = \int\limits_{\Omega_{\mathbf{x},t}} \left[\eta f_3 - \nabla\eta \cdot \sigma_{\cdot 3} + v_3 \frac{\mathrm{D}\eta}{\mathrm{D}t} \right] \mathrm{d}\Omega_{\mathbf{x},t} + \int\limits_{\partial\Omega_{\mathbf{x},t}} \eta \left[\sigma_{\cdot 3} \cdot \mathbf{n} \right] \mathrm{d}\Gamma_{\mathbf{x},t}, \tag{A.16}$$

for all $\eta(\mathbf{x}, t) \in H^1(\Omega_{\mathbf{x},t}),\ t \in [0, T]$.

Repeating the above procedure without the application of Green's first identity results in the following weak formulations of Equation (A.6), Equation (A.7) and Equation (A.8). Find $\epsilon_{22}(\mathbf{x}, t) \in L^2(\Omega_{\mathbf{x},t}),\ t \in [0, T]$, $\epsilon_{23}(\mathbf{x}, t) \in L^2(\Omega_{\mathbf{x},t}),\ t \in [0, T]$ and $\epsilon_{33}(\mathbf{x}, t) \in L^2(\Omega_{\mathbf{x},t}),\ t \in [0, T]$ such that

$$\frac{\mathrm{d}}{\mathrm{d}t} \int\limits_{\Omega_{\mathbf{x},t}} \eta \epsilon_{22} \mathrm{d}\Omega_{\mathbf{x},t} = \int\limits_{\Omega_{\mathbf{x},t}} \left\{ \epsilon_{22} \frac{\mathrm{D}\eta}{\mathrm{D}t} - \eta \left\{ [\epsilon_{33} - 1] \frac{\partial v_2}{\partial y} + G_{22} \right\} \right\} \mathrm{d}\Omega_{\mathbf{x},t} + \int\limits_{\Omega_{\mathbf{x},t}} \eta \left\{ \epsilon_{22} \frac{\partial v_3}{\partial z} + \frac{1}{2} \left[\frac{\partial v_2}{\partial z} - \frac{\partial v_3}{\partial y} \right] [\epsilon_{23} + \epsilon_{32}] \right\} \mathrm{d}\Omega_{\mathbf{x},t}, \tag{A.17}$$

$$\frac{\mathrm{d}}{\mathrm{d}t} \int\limits_{\Omega_{\mathbf{x},t}} \eta \epsilon_{23} \mathrm{d}\Omega_{\mathbf{x},t} = \int\limits_{\Omega_{\mathbf{x},t}} \left\{ \epsilon_{23} \frac{\mathrm{D}\eta}{\mathrm{D}t} - \eta \left\{ G_{23} - \epsilon_{23} \left[\frac{\partial v_2}{\partial y} + \frac{\partial v_3}{\partial z} \right] \right\} \right\} \mathrm{d}\Omega_{\mathbf{x},t} + \frac{1}{2} \int\limits_{\Omega_{\mathbf{x},t}} \eta \left\{ [1 - 2\epsilon_{22}] \frac{\partial v_2}{\partial z} + [1 - 2\epsilon_{33}] \frac{\partial v_3}{\partial y} \right\} \mathrm{d}\Omega_{\mathbf{x},t}, \tag{A.18}$$

$$\frac{\mathrm{d}}{\mathrm{d}t} \int\limits_{\Omega_{\mathbf{x},t}} \eta \epsilon_{33} \mathrm{d}\Omega_{\mathbf{x},t} = \int\limits_{\Omega_{\mathbf{x},t}} \left\{ \epsilon_{33} \frac{\mathrm{D}\eta}{\mathrm{D}t} - \eta \left\{ [\epsilon_{22} - 1] \frac{\partial v_3}{\partial z} + G_{33} \right\} \right\} \mathrm{d}\Omega_{\mathbf{x},t} + \int\limits_{\Omega_{\mathbf{x},t}} \eta \left\{ \epsilon_{33} \frac{\partial v_2}{\partial y} - \frac{1}{2} \left[\frac{\partial v_2}{\partial z} - \frac{\partial v_3}{\partial y} \right] [\epsilon_{23} + \epsilon_{32}] \right\} \mathrm{d}\Omega_{\mathbf{x},t}, \tag{A.19}$$

for all $\eta(\mathbf{x}, t) \in L^2(\Omega_{\mathbf{x},t}),\ t \in [0, T]$.

In order to derive the finite-element approximation, the general triangulation of the domain of computation $\Omega_{\mathbf{x},t}$ is presented first. Next, the used finite-dimensional subspace of the Hilbert space $H^1(\Omega_{\mathbf{x},t}),\ t \in [0, T]$ and the Lebesgue space $L^2(\Omega_{\mathbf{x},t}),\ t \in [0, T]$ are introduced, and then the used basis functions for this finite-dimensional subspace are introduced. Finally, new versions of the above derived weak formulations are presented. These new versions of the weak formulations are the finite-element approximations of the solution for the primary model variables from Equation (7.1).

A

The following general triangulation $\mathcal{T}_{h,t}$ of the domain of computation $\Omega_{\mathbf{x},t},\ t \in [0,T]$ was used:

$$\Omega_{\mathbf{x},t} = \bigcup_{K_t \in \mathcal{T}_{h,t}} K_t, \tag{A.20}$$

where

- the elements K_t are straight triangles with the general property that $\text{meas}(K_t) \neq 0$,
- $\text{meas}(K_t^1 \cap K_t^2) = 0$ for every pair of distinct elements $K_t^1, K_t^2 \in \mathcal{T}_{h,t}$,
- if $F = K_t^1 \cap K_t^2 \neq \emptyset$, then F is either a common side or vertex of K_t^1 and K_t^2,
- $\text{diam}(K_t) \leq h$ for all $K_t \in \mathcal{T}_{h,t}$.

Each of the elements K_t of $\mathcal{T}_{h,t}$ was obtained by applying an invertible affine mapping $T_{K,t}$ on the reference triangle $\hat{K}$ with vertices $(0,0)$, $(1,0)$, and $(0,1)$.

The finite-dimensional subspace that was used is the following:

$$X_h(t) = \left\{ \eta^h \in C^0(\overline{\Omega}_{\mathbf{x},t}) \mid \hat{\eta}_K^h \in \mathbb{P}_1 \ \forall K_t \in \mathcal{T}_{h,t},\ t \in [0,T] \right\}, \tag{A.21}$$

with $\eta^h(\mathbf{x},t) = \hat{\eta}_K^h(T_{K,t}^{-1}(\mathbf{x}))$ and $\mathbb{P}_1$ the space of polynomials of degree less than or equal to one in two space variables defined on the reference triangle $\hat{K}$. (See for example Quarteroni and Valli for a proof of the fact that $X_h(t) \subset H^1(\Omega_{\mathbf{x},t}),\ t \in [0,T]$, and see the Sobolev embedding theorem for a proof of the fact that $H^1(\Omega_{\mathbf{x},t}),\ t \in [0,T] \subset L^2(\Omega_{\mathbf{x},t}),\ t \in [0,T]$ [2]. Note that these inclusions also imply $X_h(t) \subset L^2(\Omega_{\mathbf{x},t}),\ t \in [0,T]$.)

In this study the values of the functions $\eta_h(\mathbf{x},t)$ at the vertices of each element K_t were chosen as the degrees of freedom on each of these elements. Denoting by N_h the total number of vertices in the triangulation $\mathcal{T}_{h,t}$ and denoting by $\mathbf{a}_j,\ j \in \{1,\ldots,N_h\}$ the coordinates of these vertices within $\overline{\Omega}_{\mathbf{x},t}$, the functions $\varphi_i \in X_h(t)$ with

$$\varphi_i(\mathbf{a}_j,t) = \delta_{ij}, \quad i,j \in \{1,\ldots,N_h\} \tag{A.22}$$

were chosen as basis functions for the finite-dimensional subspace $X_h(t)$.

Hence, looked for are finite-element approximations $z_i^h(\mathbf{x},t)$, $v_2^h(\mathbf{x},t)$, $v_3^h(\mathbf{x},t)$, $\epsilon_{22}^h(\mathbf{x},t)$, $\epsilon_{23}^h(\mathbf{x},t)$, $\epsilon_{33}^h(\mathbf{x},t) \in X_h(t),\ t \in [0,T]$ for $i \in \{N,M,c,\rho\}$ with

$$\begin{aligned}
z_i^h(\mathbf{x},t) &= \sum_{j=1}^{N_h} z_i^j(t)\varphi_j(\mathbf{x},t), \quad v_2^h(\mathbf{x},t) = \sum_{j=1}^{N_h} v_2^j(t)\varphi_j(\mathbf{x},t), \\
v_3^h(\mathbf{x},t) &= \sum_{j=1}^{N_h} v_3^j(t)\varphi_j(\mathbf{x},t), \quad \epsilon_{22}^h(\mathbf{x},t) = \sum_{j=1}^{N_h} \epsilon_{22}^j(t)\varphi_j(\mathbf{x},t), \\
\epsilon_{23}^h(\mathbf{x},t) &= \sum_{j=1}^{N_h} \epsilon_{23}^j(t)\varphi_j(\mathbf{x},t), \quad \epsilon_{33}^h(\mathbf{x},t) = \sum_{j=1}^{N_h} \epsilon_{33}^j(t)\varphi_j(\mathbf{x},t),
\end{aligned} \tag{A.23}$$

such that

$$\frac{\mathrm{d}}{\mathrm{d}t}\int\limits_{\Omega_{\mathbf{x},t}} \eta^h z_i^h \mathrm{d}\Omega_{\mathbf{x},t} = \int\limits_{\Omega_{\mathbf{x},t}} \left[\nabla\eta^h \cdot \mathbf{J}_i^h + \eta h R_i^h + z_i^h \frac{\mathrm{D}\eta^h}{\mathrm{D}t}\right] \mathrm{d}\Omega_{\mathbf{x},t} - \int\limits_{\partial\Omega_{\mathbf{x},t}} \eta^h \left[\mathbf{J}_i^h \cdot \mathbf{n}\right] \mathrm{d}\Gamma_{\mathbf{x},t}, \quad \text{(A.24)}$$

$$\rho_t \frac{\mathrm{d}}{\mathrm{d}t}\int\limits_{\Omega_{\mathbf{x},t}} \eta^h v_2^h \mathrm{d}\Omega_{\mathbf{x},t} = \int\limits_{\Omega_{\mathbf{x},t}} \left[\eta^h f_2^h - \nabla\eta^h \cdot \sigma_{\cdot 2}^h + v_2^h \frac{\mathrm{D}\eta^h}{\mathrm{D}t}\right] \mathrm{d}\Omega_{\mathbf{x},t} + \int\limits_{\partial\Omega_{\mathbf{x},t}} \eta^h \left[\sigma_{\cdot 2}^h \cdot \mathbf{n}\right] \mathrm{d}\Gamma_{\mathbf{x},t}, \quad \text{(A.25)}$$

$$\rho_t \frac{\mathrm{d}}{\mathrm{d}t}\int\limits_{\Omega_{\mathbf{x},t}} \eta^h v_3^h \mathrm{d}\Omega_{\mathbf{x},t} = \int\limits_{\Omega_{\mathbf{x},t}} \left[\eta^h f_3^h - \nabla\eta^h \cdot \sigma_{\cdot 3}^h + v_3^h \frac{\mathrm{D}\eta^h}{\mathrm{D}t}\right] \mathrm{d}\Omega_{\mathbf{x},t} + \int\limits_{\partial\Omega_{\mathbf{x},t}} \eta^h \left[\sigma_{\cdot 3}^h \cdot \mathbf{n}\right] \mathrm{d}\Gamma_{\mathbf{x},t}, \quad \text{(A.26)}$$

$$\frac{\mathrm{d}}{\mathrm{d}t}\int\limits_{\Omega_{\mathbf{x},t}} \eta^h \epsilon_{22}^h \mathrm{d}\Omega_{\mathbf{x},t} = \int\limits_{\Omega_{\mathbf{x},t}} \left\{\epsilon_{22}^h \frac{\mathrm{D}\eta^h}{\mathrm{D}t} - \eta^h \left\{[\epsilon_{33}^h - 1]\frac{\partial v_2^h}{\partial y} + G_{22}^h\right\}\right\} \mathrm{d}\Omega_{\mathbf{x},t} + \int\limits_{\Omega_{\mathbf{x},t}} \eta^h \left\{\epsilon_{22}^h \frac{\partial v_3^h}{\partial z} + \frac{1}{2}\left[\frac{\partial v_2^h}{\partial z} - \frac{\partial v_3^h}{\partial y}\right]\left[\epsilon_{23}^h + \epsilon_{32}^h\right]\right\} \mathrm{d}\Omega_{\mathbf{x},t}, \quad \text{(A.27)}$$

$$\frac{\mathrm{d}}{\mathrm{d}t}\int\limits_{\Omega_{\mathbf{x},t}} \eta^h \epsilon_{23}^h \mathrm{d}\Omega_{\mathbf{x},t} = \int\limits_{\Omega_{\mathbf{x},t}} \left\{\epsilon_{23}^h \frac{\mathrm{D}\eta^h}{\mathrm{D}t} - \eta^h \left\{G_{23}^h - \epsilon_{23}^h \left[\frac{\partial v_2^h}{\partial y} + \frac{\partial v_3^h}{\partial z}\right]\right\}\right\} \mathrm{d}\Omega_{\mathbf{x},t} + \frac{1}{2}\int\limits_{\Omega_{\mathbf{x},t}} \eta^h \left\{[1 - 2\epsilon_{22}^h]\frac{\partial v_2^h}{\partial z} + [1 - 2\epsilon_{33}^h]\frac{\partial v_3^h}{\partial y}\right\} \mathrm{d}\Omega_{\mathbf{x},t}, \quad \text{(A.28)}$$

$$\frac{\mathrm{d}}{\mathrm{d}t}\int\limits_{\Omega_{\mathbf{x},t}} \eta^h \epsilon_{33}^h \mathrm{d}\Omega_{\mathbf{x},t} = \int\limits_{\Omega_{\mathbf{x},t}} \left\{\epsilon_{33}^h \frac{\mathrm{D}\eta^h}{\mathrm{D}t} - \eta^h \left\{[\epsilon_{22}^h - 1]\frac{\partial v_3^h}{\partial z} + G_{33}^h\right\}\right\} \mathrm{d}\Omega_{\mathbf{x},t} + \int\limits_{\Omega_{\mathbf{x},t}} \eta^h \left\{\epsilon_{33}^h \frac{\partial v_2^h}{\partial y} - \frac{1}{2}\left[\frac{\partial v_2^h}{\partial z} - \frac{\partial v_3^h}{\partial y}\right]\left[\epsilon_{23}^h + \epsilon_{32}^h\right]\right\} \mathrm{d}\Omega_{\mathbf{x},t}, \quad \text{(A.29)}$$

for all $\eta^h(\mathbf{x}, t) \in X_h(t),\ t \in [0, T]$. Here $\mathbf{J}_i^h$, R_i^h, $\sigma_{\cdot 2}^h$, $\sigma_{\cdot 3}^h$, f_2^h, f_3^h, G_{22}^h, G_{23}^h, and G_{33}^h are equal to, respectively, $\mathbf{J}_i$, R_i, $\sigma_{\cdot 2}$, $\sigma_{\cdot 3}$, f_2, f_3, G_{22}, G_{23}, and G_{33} where the primary model variables have been replaced by their respective finite-element approximations from Equation (A.23).

The linear systems of algebraic equations related the above weak formulations can be obtained now by applying consecutively the first-order backward Euler method and

the fixed-point defect correction method, and by replacing $\eta^h(\mathbf{x}, t)$ with $\varphi_j(\mathbf{x}, t)$ for $j \in \{1, \ldots, N_h\}$. (See for example Van Kan *et al.* for more details about these procedures [3].) Finally, note that the following holds for the chosen basis functions of the subspace $X_h(t)$ [1]:

$$\frac{\mathrm{D}\varphi_j}{\mathrm{D}t} = 0. \tag{A.30}$$

This property of the chosen basis functions simplifies the construction of the linear systems of equations.

REFERENCES

[1] Dziuk G, Elliott C (2007) Finite elements on evolving surfaces. IMA J Numer Anal 27:262–292

[2] Quarteroni A, Valli A (2008) Numerical Approximation of Partial Differential Equations, vol 23. Springer Science & Business Media, Berlin, Germany

[3] Van Kan J, Segal A, Vermolen F (2014) Numerical Methods in Scientific Computing, 2nd edn. Delft Academic Press, Delft, The Netherlands

CURRICULUM VITÆ

Daniël Cornelis KOPPENOL

2012–2017 PhD program in Applied Mathematics
Delft University of Technology, The Netherlands
Certification: PhD
Thesis: Biomedical implications from mathematical models for the simulation of dermal wound healing

2009–2012 Bachelor's program in Applied Mathematics
Delft University of Technology, The Netherlands
Certification: BSc
Remark: **Cum Laude**
Thesis: Determination of the mechanism behind the formation of spatio-temporal hexagonal activity patterns in a model neuronal network

2006–2008 Research Master's program in Brain and Cognitive Sciences
University of Amsterdam, The Netherlands
Certification: MSc
Remark: **Cum Laude**
Thesis: Models of self-organizing development of an attractor layer for entorhinal grid cells

2003–2006 Bachelor's program in Biological and Cognitive Psychology
Erasmus University Rotterdam, The Netherlands
Certification: BSc
Thesis: The etiology of schizophrenia

2000–2002 Bachelor's program in Medicine
Utrecht University, The Netherlands
Remark: Propaedeutic phase completed

1993–1999 Pre-university secondary education
Maerlant College Brielle, The Netherlands
Remark: **Cum Laude**

LIST OF PUBLICATIONS

JOURNAL PAPERS

[1] **Koppenol D**, Vermolen F (2017) Biomedical implications from a morphoelastic continuum model for the simulation of contracture formation in skin grafts that cover excised burns. Biomech Model Mechanobiol DOI: 10.1007/s10237-017-0881-y

[2] **Koppenol D**, Vermolen F, Koppenol-Gonzalez G, Niessen F, Van Zuijlen P, Vuik K (2016) A mathematical model for the simulation of the contraction of burns. J Math Biol DOI: 10.1007/s00285-016-1075-4

[3] **Koppenol D**, Vermolen F, Niessen F, Van Zuijlen P, Vuik K (2017) A biomechanical mathematical model for the collagen bundle distribution-dependent contraction and subsequent retraction of healing dermal wounds. Biomech Model Mechanobiol 16:345–361 DOI: 10.1007/s10237-016-0821-2

[4] **Koppenol D**, Vermolen F, Niessen F, Van Zuijlen P, Vuik K (2017) A mathematical model for the simulation of the formation and the subsequent regression of hypertrophic scar tissue after dermal wounding. Biomech Model Mechanobiol 16:15–32 DOI: 10.1007/s10237-016-0799-9

[5] Boon W, **Koppenol D**, Vermolen F (2016) A multi-agent cell-based model for wound contraction. J Biomech 49:1388–1401 DOI: 10.1016/j.jbiomech.2015.11.058

TALKS AT CONFERENCES

[1] Presentation of mathematical models for the simulation of the development of hypertrophic scar tissue and the contraction of burns. Annual Science Day organized by the Dutch Burns Foundation. Amersfoort, The Netherlands, 2016

[2] A novel mechanochemical continuum model for (distorted) dermal wound healing. Annual meeting for the Society for Mathematical Biology (SMB). Atlanta (Georgia), United States of America, 2015

[3] Presentation of mechano-chemical continuum models for dermal wound healing. Annual Science Day organized by the Dutch Burns Foundation. Amersfoort, The Netherlands, 2015

[4] Presentation of a general mechano-chemical hybrid model for dermal wound healing. The eleventh World Congress on Computational Mechanics (WCCM XI), the fifth European Conference on Computational Mechanics (ECCM V), and the sixth European Conference on Computational Fluid Dynamics (ECFD VI). Barcelona, Spain, 2014

[5] Determination of the mechanism behind the formation of spatio-temporal hexagonal activity patterns in a model neuronal network. The fiftieth Dutch Mathematical Congress (NMC). Delft, The Netherlands, 2014

[6] Presentation of a flux-corrected finite-element method with adaptive time stepping for mechanochemical models of wound healing. The fourteenth conference on the Mathematics of Finite Elements and Applications (MAFELAP). London, Great Britain, 2013

[7] Presentation of preliminary results obtained from analyses performed on a mechano-chemical model for dermal wound healing. Annual Science Day organized by the Dutch Burns Foundation. Amersfoort, The Netherlands, 2013

POSTER PRESENTATION

[1] A novel mechanochemical continuum model for (distorted) dermal wound healing. Encuentros Chile Global. Rotterdam, The Netherlands, 2015